LABORATOIRE NATIONAL DES CHAMPS MAGNÉTIQUES INTENSES

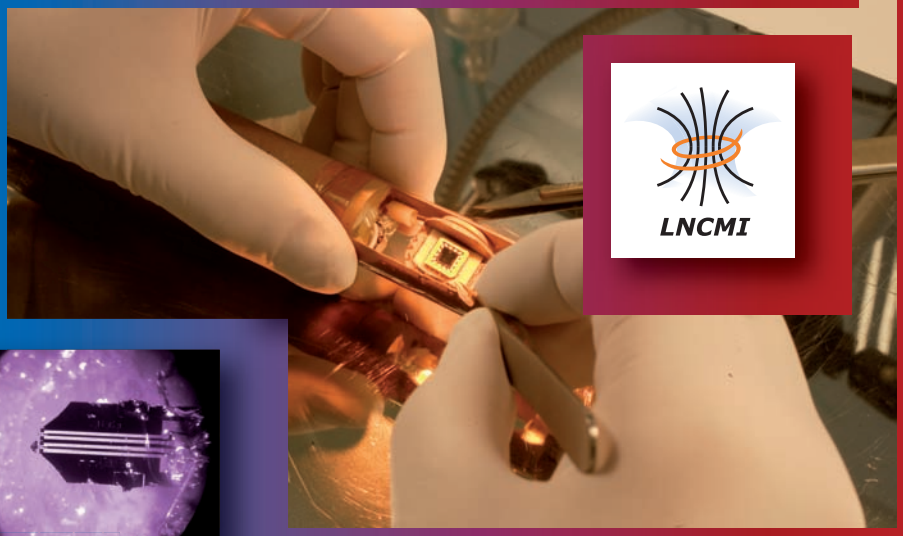

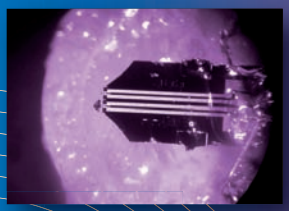

# ANNUAL REPORT 2010

# Laboratoire National des Champs Magnétiques Intenses

**Grenoble–Toulouse**

**Centre National de la Recherche Scientifique**

http://lncmi.cnrs.fr/

# Annual Report

# 2010

**LNCMI is formally associated with the "Université Joseph Fourier", Grenoble, the "Université Paul Sabatier", Toulouse and the "Institut National des Sciences Appliquées", Toulouse.**

Editors: Fabienne Duc and Duncan Maude

# Preface

Dear Reader,

You have before you the second annual report of the Laboratoire National des Champs Magnétiques Intenses (LNCMI), created on the 1st of January 2009 through the merger of the Laboratoire des Champs Magnétiques Intenses (Grenoble) and the Laboratoire National des Champs Magnétiques Pulsés (Toulouse). The LNCMI is a "Unité Propre de Recherche" of the Centre National de la Recherche Scientifique (UPR3228) and is part of the French "Très Grands Equipements". The laboratory is associated with the Université Joseph Fourier de Grenoble, the Université Paul Sabatier de Toulouse and the Institut National des Sciences Appliquées de Toulouse. Its activities are also supported by the EC FP7 "Large infrastructures" program, where it is the coordinator of the EuroMagNET2 Integrating Activity.

This report intends to provide a complete overview of the in-house and collaborative scientific and technical activities in 2010 of the LNCMI.

The 24 MW power supply of the Grenoble site, dedicated to the generation of static fields, allows either to operate simultaneously two resistive 12 MW magnets or to operate one 24 MW magnet. The highest field generated at the LNCMI-G is currently 35 T in a 34 mm bore diameter and we are working hard to increase this value. A hybrid magnet, capable of generating 43 T is currently under construction and will become available in 2013.

The 14 MJ capacitor bank generator of the Toulouse site, dedicated to the generation of pulsed fields, allows to generate fields up to 80 T. An installation to generate destructive pulsed fields has generated fields up to 150 T and we hope to increase also this value even further.

This report and the list of publications show the importance and the interest of results obtained in high magnetic fields, either on the basis of in-house research or as a result of close collaborations with several research groups from many different countries.Together with our colleagues of the HFML (Nijmegen) and the HLD (Dresden), we are performing a design study for the creation of a distributed European Magnetic Field Laboratory to serve the European high magnetic field user community even better.

In addition, the LNCMI is proud to contribute to the training of young scientists by giving them the opportunity to prepare their thesis work and/or to participate to European research activities.

Finally, a word of thanks to the scientific, technical and administrative staff of the laboratory (altogether 90 people), our post docs and PhD students (almost 30) and the numerous visitors (over 200 this year) for their contributions to the improvement of the installation and for the quality of their work.

Geert Rikken
December 2010

**CONTENTS**

## LIST OF FIGURES

# Carbon Allotropes

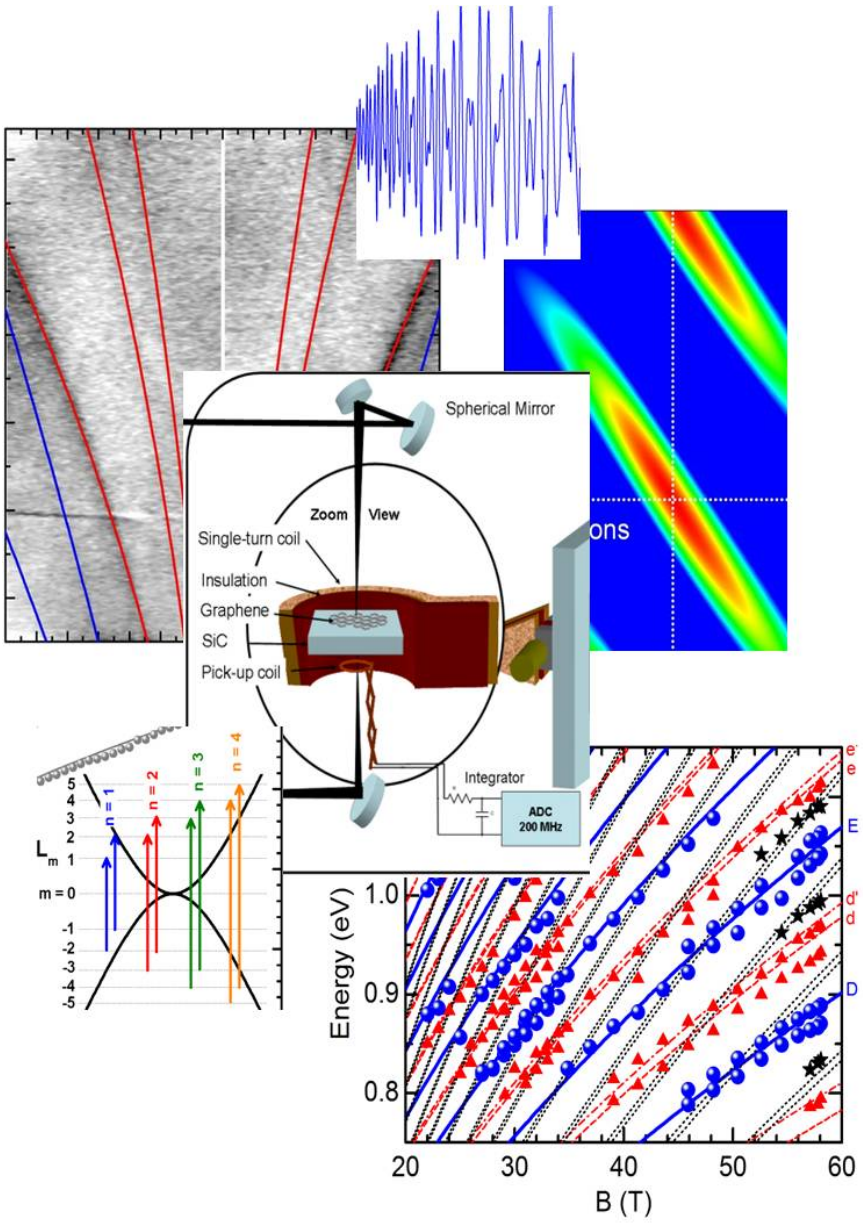

# Graphene nanoribbons under high magnetic field

Graphene nanoribbons present one of the most promising structures to be used in the new area of nanoelectronics. A graphene nanoribbon device is also a model system to understand the basic properties of Dirac fermions under a hard-wall confinement. Here we present electronic transport measurements obtained on weakly diffusive graphene nanoribbons which present a high mobility and Landau quantization which is modified by confinement effects.

Graphene nanoribbons are fabricated from mechanically exfoliated single layer graphene sheet which was deposited in $SiO_2$ substrates. The ribbons are contacted with Ti/Pd/Au metal electrodes, and the design of the etch mask was performed in PMMA (polymethyl methacrylate) e-beam resist. Oxygen plasma was used to make the etching. We describe results for two ribbons; ribbon A of $W = 100\,\mathrm{nm}$, and $L = 350\,\mathrm{nm}$, and ribbon B of $W = 70\,\mathrm{nm}$, and $L = 750\,\mathrm{nm}$. After annealing, we obtained a mobility at $4\,\mathrm{K}$ of $\mu = 2300\,\mathrm{cm}^2/\mathrm{Vs}$ (ribbon A) and $\mu = 7200\,\mathrm{cm}^2/\mathrm{Vs}$ (ribbons B). These values are considerably higher compared with previously reported mobilities for graphene nanoribbons.

Measurements of conductivity as a function of carrier density at $4\,\mathrm{K}$, for both ribbons, reveal a conductance which is relatively high, $\sim 2e^2/h$ for the narrowest ribbon at $V_g \approx -20\,\mathrm{V}$. For the shortest graphene nanoribbon, strong and reproducible conductance oscillations are observed that develop at low temperatures. At low bias voltage $\sim 50\mu\mathrm{V}$, a well define period is observed which can be associated with Fabry-Perot oscillations due to the interference of electrons which are coherently reflected at the electrodes. To clarify this point, we performed numerical simulations assuming a multichannel ballistic conductor and using as fitting parameters the length and width of the system. In the result of this numerical simulation the main period of both oscillations is consistent with experiment corresponding to $\Delta E = 4.4\,\mathrm{meV}$. Fabry-Perot oscillations are only possible in a very clean systems. In our case, the mean free path has been estimated to $\sim 100\,\mathrm{nm}$ for ribbon A, and $\sim 75\,\mathrm{nm}$ for ribbon B.

Our main results are resistance measurements as a function of magnetic field for several back gate voltages for both ribbons (see figure 1). We observe in the measurements made on ribbon A the clear presence of a plateau at $\sim 13\,\mathrm{k\Omega} = h/2e^2$ which corresponds to a filling factor of $\nu = 2$, due to Landau quantization. Also, we observe clearly the presence of a peak at $\nu = 6$. A very similar behavior can be observed for the ribbon B where we can see the presence of a peak at $\nu = 6$ but in contrast to the behavior observed for ribbon A, no plateau is observed at $\nu = 2$. Other very interesting feature in the magneto resistance measurements made on ribbon B is the observation of a double peak (blue solid arrows) where only one peak is expected. The double peak even evolves into three peaks when we change the back gate voltage (red broken arrows). A maximum of resistance in a two terminal measurement occurs when the Fermi energy matches the bottom of the magneto-electric sub-bands. Here, we are probably probing the contribution of electron correlations which lifts the degeneracy of the 1D subbands of the graphene nanoribbon. Simulations are currently underway to estimate the width of the magnetic edges in the quantum regime and the strength of the backscattering due to the disorder induced edge-current mixing.

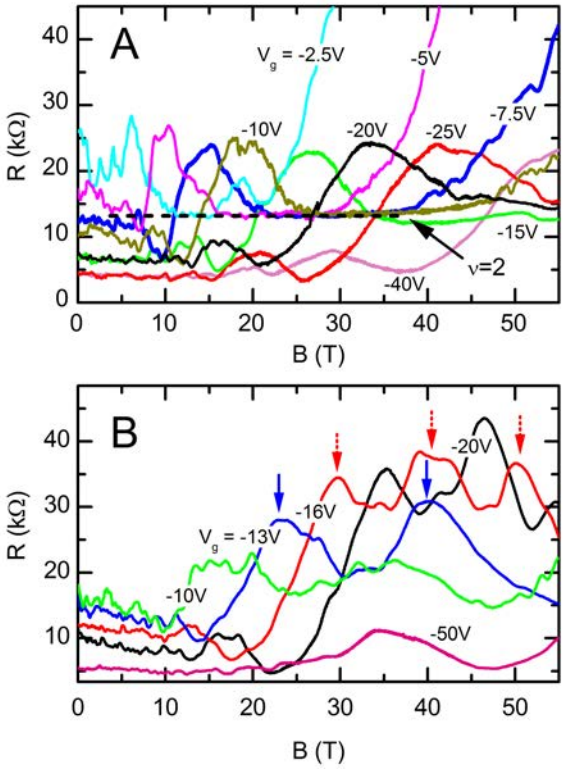


FIG. 1. *Two terminal magnetoresistance at $T = 4\,K$ for ribbons A and B. The magnetic field is applied perpendicular to the graphene plane.*

***R.L. Ribeiro, J.M. Poumirol, W. Escoffier, J.M. Broto, and B. Raquet***
***S. Roche(Universidad Autonoma de Barcelona, Spain), A. Cresti (INP-Grenoble, Grenoble, France)***

# Photoluminescence of individual carbon nanotubes in high magnetic fields

Photoluminescence (PL)experiments on semiconducting CNTs facilitate the study of a rich variety of 1D exciton physics. The predicted excitonic spectrum of a semiconducting single walled CNT consists of one optically active (bright) spin-singlet state and 15 optically forbidden (dark) states. A magnetic flux threading the tube lifts valley degeneracy which leads to the brightening of the previously dark valley antibonding spin-singlet state. The value of the splitting energy between the dark and bright spin-singlet exciton states is essential for elucidating the fine excitonic structure semiconducting CNTs. Splitting energies of 1-5meV have been inferred from low field PL of individual CNTs (Srivastava *et al.* Phys. Rev. Lett. **101**, 087402 (2008)) and from high field ensemble measurements (Mortimer *et al.* Phys. Rev. B **76**, 085404 (2007)). Using PL of *individual* CNTs in high magnetic fields, up to 28 Tesla, we have directly observed bright-dark splitting energies an order of magnitude higher than in previous experiments and have wider access to further high magnetic field effects such as the modulation of the CNT band gap due to the Aharonov-Bohm effect.

A solution of CNTs, grown using the CoMoCAT process, wrapped with regioregular poly(3-hexylthiophene) (P3HT), to prevent bundling, was prepared. The solution was then spun at 4000rpm on a quartz substrate and annealed in air. Atomic force microscopy revealed a uniform coating of the surface with dispersed, individualised CNTs. Micro-PL measurements, with a typical laser excitation spot size of $1\mu m^2$, were carried out at 4.2 K. Faraday geometry with CNTs perpendicular to the magnetic field gave sharp emission peaks with spectral line widths on the order of 1nm, typical for individual CNTs, with no change in the spectrum from zero to 28 T. This is expected as there is no magnetic field component threading the CNT.

In the Voigt geometry the excitation beam propagates perpendicular to the magnetic field,and the magnetic flux threads the carbon nanotubes. The CNTs dispersed on the quartz substrate are randomly orientated. We preferentially excite CNTs on the substrate which are aligned in the direction the magnetic field by polarising the excitation beam parallel to the field. A large depolarisation effect strongly suppresses the absorption of light polarised perpendicular to the CNT. The spatial distribution of the PL signal was found by taking spectra whilst scanning the position of the excitation across the surface using a piezo-stage. From these spectra a map can be made of the position from which the emission of specific wavelengths originates, thus we get an image of the position and orientation of the individual CNT. This was confirmed with a number of maps showing the orientation of nanotubes excited by polarised light matched that of the direction of polarisation as in figure 2a.
It is predicted that the band gap in CNTs is modulated by a magnetic field threading it due to an Aharanov-Bohm effect ([Ajiki & Ando, Physica B **201**, 349 (2002)]). The small spectral line widths and high magnetic fields used have allowed us to determine the Aharanov-Bohm shift in a number of individual CNTs. The Aharonov-Bohm shift is characterised by a redshift of the emission line, which was found typically to be on the order of 10meV at 28 T for a (6,5) chirality CNT with a diameter of 0.76 nm.

When a magnetic flux threads a carbon nanotube the dark exciton states are predicted to become optically active. It has been shown that the energy splitting varies depending on the size and local environment of each individual CNT, but all bright-dark splittings seen to date were on the order of a few meV in magnetic fields up to 7 T. We have confirmed the earlier findings but find that in higher magnetic fields it is possible to observe much larger dark-bright splitting energies of up to 33 meV.

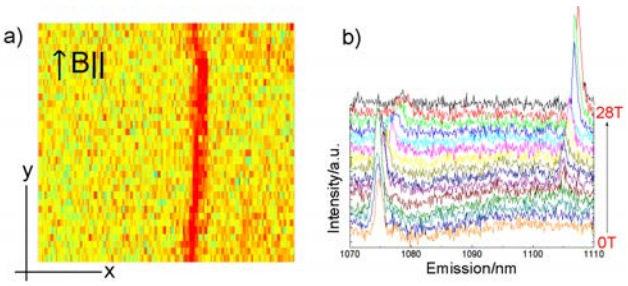


FIG. 2. ***a)*** *Spatial intensity map of emission from a carbon nanotube in the Voigt geometry with polarised excitation.* ***b)*** *Photoluminescence emission spectra from an individual carbon nanotube with increasing magnetic field. The lower energy dark exciton state becomes optically active above* 8 *T with a splitting of* 33 *meV.*

***C. Faugeras, P. Kossacki and M. Potemski***
***J. A. Alexander-Webber, R. J. Nicholas (Clarendon Laboratory, University of Oxford, UK)***

# Metal-insulator transitions in graphene

We investigate the quantum Hall effect (QHE) in a graphene sample at high magnetic fields. We have focused the study on two different metal-insulator transitions, the plateau-insulator (PI) and plateau-plateau (PP) transitions. For this purpose we have used a graphene monolayer with a Hall-bar geometry placed into a cryostat with a variable temperature insert. Four probe measurements were carried out using the standard ac lock-in technique. In the sample under study the charge neutrality point (CNP) was placed at $V_D = 4$ V. We have performed magnetotransport experiments in the range of temperatures from 4 to 230 K. By using the scaling theory of the integer QHE we obtained the associated critical exponents $\kappa$ of the transitions [Amado *et. al* New J. Phys. **12**, 053004 (2010)] . We have observed a PI transition passing from filling factor $\nu = -2$ to $\nu = 0$ as can be seen in figure 3. When the gate voltage was set 4 V away from

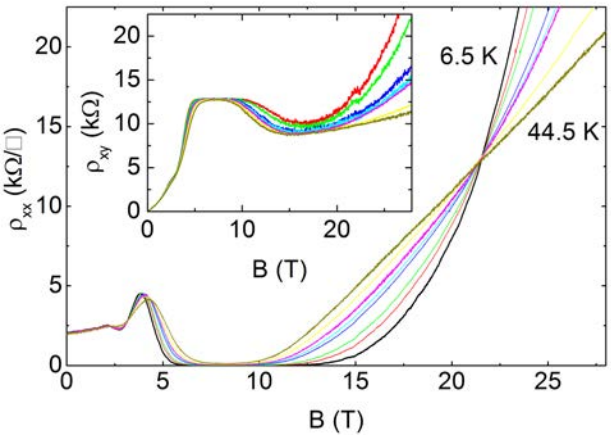


FIG. 3. *Longitudinal ($\rho_{xx}$) and Hall ($\rho_{xy}$) isotherms as a function of B, with the $V_G$ 4 V away from the CNP. A clear T-independent point separating the metallic to the insulating phase appears at $B_C = 21.65$ T.*

the CNP, the temperature dependence of the longitudinal resistance recovered the behaviour typical of a 2 dimensional electron gas (2DEG) with Anderson disorder and critical exponent $\kappa = 0.58 \pm 0.02$. Whereas when the gate voltage was set closer to the CNP the critical exponent assumes the value $0.697 \pm 0.005$ which is consistent with the expected value for the classical full percolation model. We have also noticed the existence of a maximal temperature up to which the PI transition is observable. In figure 4 we report the PI transition 2 V away from the CNP in the range of temperatures from 6.85 to 230 K. We found that at temperatures higher than 32 K the T-independent crossing point is lost, in agreement with the observation of Zhang *et al.* [Phys. Rev. Lett. **105**, 046804 (2010)].

We have also studied the plateau-plateau (PP) metal-insulator transition. We have applied a gate voltage away from the CNP to allow the observation of the plateaus $\nu = -2, -6, -10$ (figure 5). We have extracted the critical exponent of these transitions and we have found the value $\kappa = 0.254 \pm 0.006$ for the transition $\nu = -6 \rightarrow -2$ and $\kappa = 0.28 \pm 0.02$ for the $\nu = -10 \rightarrow -6$. These values are in contrast with the expected one (0.42) for 2DEGs. We conclude that further studies concerning the role of disorder in graphene samples are needed.

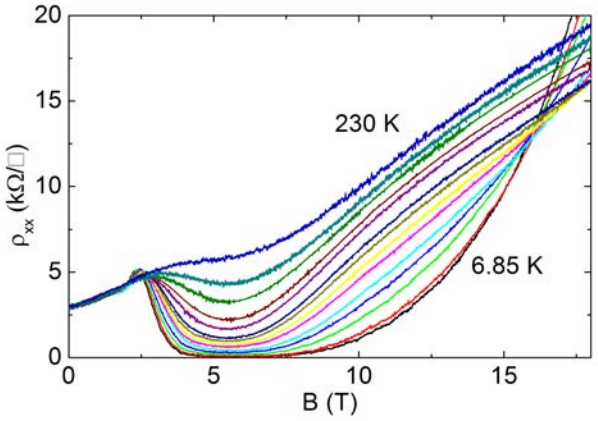


FIG. 4. *$\rho_{xx}$ isotherms as a function of B 2 V away from the CNP. A T-independent crossing point appears at $B_C = 16.05$ T. The PI transition disappears at temperatures above 32 K.*

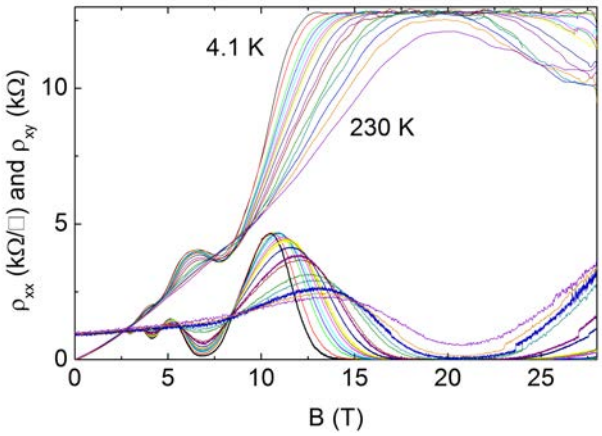


FIG. 5. *$\rho_{xx}$ and $\rho_{xy}$ isotherms as a function of B at $V_G = -8V$. Plateaus $\nu = -2, -6, -10$ are observable up to 230 K*

***D. K. Maude***
***M. Amado, E. Diez (Laboratorio de bajas temperaturas, Universidad de Salamanca, Spain), F. Rossella and V. Bellani (Universitá degli studi di Pavia, Italy) and D. López-Romero (CT-ISOM, Universidad Politécnica de Madrid, Spain)***

# Resistance deviation from $\nu = 2$ Hall plateau in disordered graphene

In the cleanest graphene samples, spin and valley degeneracy lifting has been observed at filling factors $\nu = 0, 1, 4$. While the $\nu = 1$ and $\nu = 4$ plateaus are experimentally visible in both Hall resistance and conductance, the $\nu = 0$ state responsible for the divergence of the longitudinal resistivity remains only poorly investigated. In addition, the unescapable presence of disorder (resulting in spatial inhomogeneity of carrier density) certainly plays a crucial role on the Hall resistance behaviour at very high magnetic field. In the present work, we experimentally address the impact of disorder on the low filling factor Hall quantization in a graphene flake. The main panel of figure 6 shows the

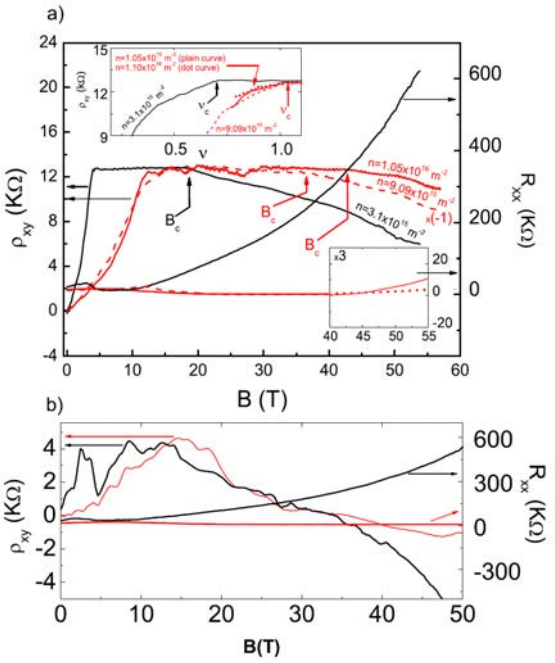


FIG. 6. *a) $\rho_{xy}(B)$ and $R_{xx}(B)$ for different electrostatically doped states. Upper left inset: the same $\rho_{xy}$ curves plotted as a function of the filling factor $\nu = n.h/e.B$, with an additional doping level at n=1.1×10$^{16}$ m$^{-2}$. (b) $\rho_{xy}(B)$ and $R_{xx}(B)$ in the vicinity of the charge neutrality point.*

Hall resistivity $\rho_{xy}$(B) and the longitudinal magnetoresistance $R_{xx}$(B) of graphene samples S1 and S2, having different disorder strength (see figure 7). Under these strong electrostatic doping conditions, only one type of carriers initially participates in the conduction. In the high magnetic field regime, we observe the expected quantized Hall plateau at $\rho_{xy} = 12.9$ kΩ ($\nu = 2$). The plateau is stable up to a magnetic field (arrows in figure 6(a)), above which the magnitude of the Hall resistance starts to decrease slowly. In the upper left inset $\rho_{xy}$ is plotted as a function of the filling factor $\nu = n.h/e.B$ for different carrier concentrations. The threshold filling factor $\nu_c$, below which the Hall resistance decreases for S1 range between 1.00 and 1.03 while it reads 0.71 for S2. Thus, for sample S1, the departures of the Hall resistance from the plateau value start at similar values of Fermi energy with respect to the Landau levels. On the other hand, $\nu_c$ seems to be related to the disorder strength in a direct way; a stronger disorder induces a decrease in the Hall resistance plateau at lower magnetic field. Figure 6(b) reports on the magnetotransport measurements in the vicinity of the charge neutrality point. We observe (i) a nonlinear increase at low magnetic field, which is the signature of a two carriers driven conduction, holes being slightly majority, (ii) after reaching a maximum, the Hall resistivity decreases and shows a sign reversal between 36 and 40 T for the two samples. One can note that large fluctuations are present up to moderate magnetic field. These fluctuations have already been seen and explained in term of a percolation process across an electron and hole puddle landscape [Poumirol *et al.*, New J. Phys. **12** 083006 (2010)]. This behavior is a fingerprint of an

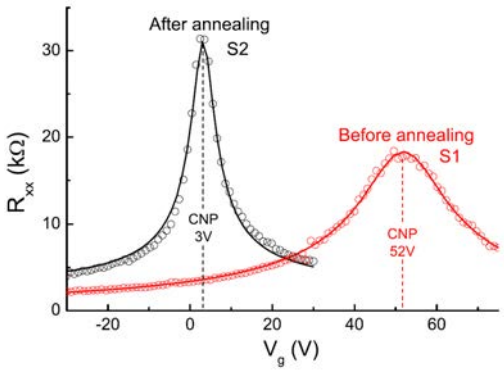


FIG. 7. *Four-probe longitudinal resistance versus backgate voltage measured at 1.6 K.*

inhomogeneous system composed by electron and hole puddles. When a magnetic field is applied perpendicular to the disordered graphene flake, the quantization of the cyclotron orbits goes along with the onset of spatially segregated Landau states, upshifted or downshifted in energy following the local variations of the charge neutrality point landscape (reference energy). At $\nu = 2$, we assume the Fermi energy to lie above the reference energy of the $n = 0$ Landau Levels in every puddles. On the other hand, as the magnetic field increases, the Fermi energy eventually decreases and lies below the reference energy for certain puddles. The straightforward consequence is the appearance of hole states. Hence, the two types of carriers are now present in the system, which is revealed by a decrease in the Hall resistance in the very high magnetic field regime. This work thus demonstrates the emergence of a novel transport regime induced by disorder in graphene under high magnetic field [Poumirol *et al.*, Phys. Rev. B **82**, 121401(R) (2010)].

***J.M. Poumirol, A. Kumar, W. Escoffier, M. Goiran, B. Raquet***

# Raman scattering from electronic excitations of Dirac fermions

Raman scattering played a crucial role in the fast development of graphene physics and technology by providing a fast and unambiguous way to identify graphene mono-layers. This is possible thanks to the second order Raman scattering spectrum of zone boundary phonons with a clear fingerprint for the monolayer for which this Raman scattering feature appears as a single component Lorentzian shaped feature. Raman scattering is also widely used to estimate doping levels of graphene specimens, their quality and the amount of strain. If phonons are, up to now, the only elementary excitation seen through Raman scattering, theorists have been interested in the possible scattering of light by electronic excitations [Kashuba *et al.*, Phys. Rev. B **80**, 241404(R), (2010)]. From these predictions, it appears that electronic excitations should contribute to the Raman scattering spectrum of graphene. The main contribution should arise from electronic excitations involving Landau levels of opposite index (symmetric transitions). Optical-like excitations should also contribute, weakly, to the Raman scattering spectrum.

We have measured the low temperature ($T = 4.2$ K), unpolarized, magneto-Raman scattering response of probably the purest graphene specimens available nowadays, graphene flakes found on the surface of natural graphite. Measurements were performed in a specially design micro-Raman probe with an excitation spot on the surface of $\approx 1\mu$m diameter and a power of 5 mW. The sample is mounted on a piezo stage which allow to move the sample under the laser spot with a sub-micrometer resolution to specifically probe the properties of the graphene flakes. These results are presented in figure 8 which shows a false color map of the magnetic field evolution of the Raman scattering response of these graphene flakes in the optical phonon range of energy. Two series of magnetic field dependent features are observed, both having a square root of the magnetic field evolution. Landau levels in graphene evolve as,

$$L_n = sgn(n)c^*\sqrt{2e\hbar B \mid n \mid} \qquad (1)$$

The most pronounced features in figure 8 can be understood as arising from symmetric excitations $2L_n$ (solid lines in figure 8). Focusing on the $L_{-1,1}$ excitation, its evolution with magnetic field can be described with a Fermi velocity $c^* = 1.02 \times 10^6 m.s^{-1}$ in line with previously reported values. This feature is characterized by a FWHM which increases as the square root of the magnetic field (*i.e.* proportional to the energy).

The weaker electronic features giving rise to a pronounced magneto-phonon effect when tuned in resonance with the $E_{2g}$ optical phonon [Faugeras *et al.*, Phys. Rev. Lett. **103**,186803, (2009)] are optical-like electronic excitations with the selection rule $\Delta|n| = \pm 1$ (dotted lines in figure 8). Due to the extremely high quality of these flakes, the electron-phonon coupling is clearly observed with a continuous transfer of the oscillator strength from electronic-like excitations to a phonon-like excitation. The parameters describing this coupling are very similar to ones determined by studying a similar effect in multi-layer epitaxial graphene specimens.

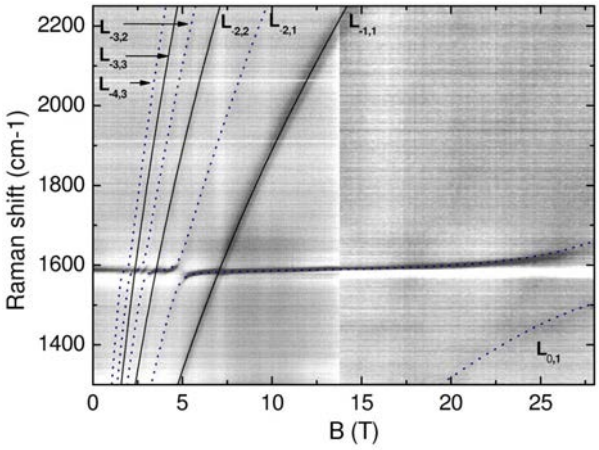


FIG. 8. *False color map of micro-Raman scattering spectra normalized to the $B = 0$ spectrum as a function of the magnetic field. Solid lines correspond to symmetric transitions $L_{-n,n}$ in graphene while dotted lines correspond to the hybrid modes involving $E_{2g}$ phonons and optical-like transitions in graphene.*

Looking in details at these electronic excitation features, it appears that symmetric transitions also couple to the optical phonon but the strength of this coupling diminishes as the magnetic field increases and is hence clearly visible for resonances characterized with a high value of the Landau level index, for magnetic fields below $B = 3$ T. The precise origin of this coupling is still an open question.

These experiments show that light can be scattered from electronic excitations in graphene and this technique appears as complementary to far infrared magneto-absorption as Raman selection rules are less strict than optical selection rules. As a result, different inter Landau-level excitations can be seen and some of these excitations couple to optical phonons, giving an insight into the rich physics of electron-phonon coupling in carbon based systems.

***C. Faugeras, P. Kossacki, M. Amado, M. Orlita, M. Potemski***

# Polarized magneto-Raman scattering of epitaxial graphene

Electronic excitations contribute to the Raman scattering response of graphene-based systems. Different inter-Landau level excitations can be observed, mainly optical-like excitation ($\Delta|n| = \pm 1$) that couple to the optical phonon and symmetric excitations ($\Delta|n| = 0$, where $n$ is the Landau level index) involving Landau levels of opposite index. These latter excitation should not couple to the optical phonon for symmetry reasons. These types of electronic excitations have different polarization rules with the optical-like excitations changing the circular polarization of light and are hence only visible in crossed circularly polarized configuration and the symmetric excitations conserving the circular polarization of light and hence only visible in co-circularly polarized configuration [Kashuba *et al.*, Phys. Rev. B **80**, 241404(R), (2010)].

To verify these selection rules, we have measured the polarization resolved Raman scattering response of an epitaxial graphene specimen grown on the carbon face of a silicon carbide substrate. These specimens consist of a high number of graphitic planes ($60 - 70$ layers) with a rotational stacking. This peculiar type of stacking strongly reduces the inter-layer interaction and these samples behave as a stacking of $N$ independent graphene layers. The polarization resolved Raman scattering response of these highly graphitized samples has been measured in a specially designed micro-Raman probe with an excitation spot of $\approx 1\mu$m diameter and an excitation power of 5 mW.

The result of such an experiment are presented in figure 9 which shows a false color map of the crossed-circular polarized (upper part of figure 9) and the co-circular polarized (lower part of figure 9) Raman scattering response as a function of the magnetic field. These spectra are normalized to the $B = 0$ T spectrum so that only magnetic field dependent features are visible. Positive and negative magnetic fields correspond to different polarization of the incoming and outgoing photons.

In the crossed circular polarization configuration, the $E_{2g}$ optical phonon is clearly visible and for increasing magnetic field, both its energy position and it line width show pronounced oscillations due to the resonant coupling with optical-like transitions (not visible in figure 9. The energy of the optical phonon is tuned over more 80 cm$^{-1}$ as a result of the excellent quality of these epitaxial samples and of the use of polarization resolved measurements. In the co-circular polarization configuration, the $E_{2g}$ optical phonon is not observed as expected from selection rules but a number of magnetic field dependent features are clearly visible. These features can be separated into two distinct series. A first series labelled L in figure 9 which are the symmetric electronic excitations across the Dirac point of a graphene monolayer, with a $\sqrt{B}$ evolution. The most pronounced feature corresponds to the the excitation involving the first Landau level in the conduction and in the valence band. Less pronounced, but still visible are symmetric transitions involving Landau levels of higher indexes. The second series, labelled B in figure 9, is identified as symmetric electronic excitations in a real graphene bilayer.

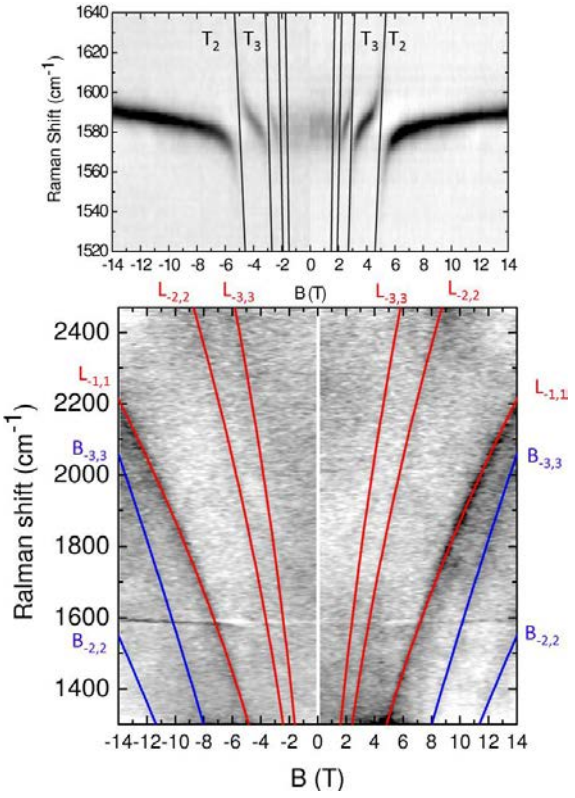


FIG. 9. *Top: False color map of crossed-circularly polarized Raman scattering spectra as a function of the magnetic field. Solid lines are the expected optical-like transition $T_i = L_{i+1} + L_i$ Bottom: False color map of co-circularly polarized Raman scattering spectra as a function of the magnetic field. Symmetric transitions $L_{-i,i}$ in a graphene monolayer and $B_{-i,i}$ are indicated.*

This second series can arise from Bernal stacked residues within an overwise rotationally stacked material, which are known to exist especially in highly graphitized specimens. Another possible explanation could be that these true graphene bilayers are of intrinsic origin, arising from the Moiré patterns that appear in rotationally stacked graphite. These experiments show that selection rules for electronic Raman scattering are well defined and can be verified experimentally.

***M. Kühne, A. L. Nicolet, M. Orlita, M. Amado, C. Faugeras, P. Kossacki, M. Potemski, M. Sprinkle, C. Berger, W.A. de Heer (Georgia Tech., Atlanta, USA)***

# Bilayer graphene inclusions in multilayer epitaxial graphene

Optical spectroscopy has played an important role in investigations of the bilayer graphene, as, for instance, it allows to directly visualize the electric-field induced energy gap in this system, [Zhang *et al.*, Nature **459**, 820 (2009)]. On the other hand, only relatively scarce information has been up to now collected from magneto-optical measurements – only a single cyclotron resonance study of bilayer graphene appeared up to now, [Henriksen *et al.*, Phys. Rev. Lett. **100**, 087403 (2009)].

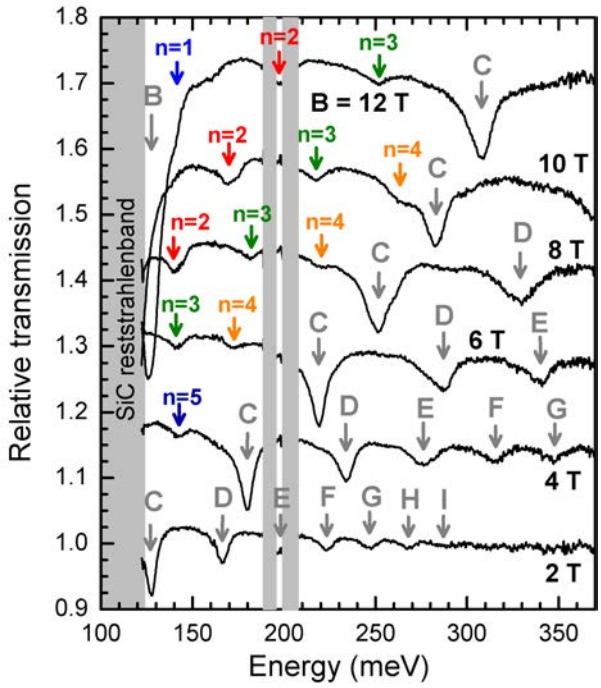


FIG. 10. *Magneto-transmission spectra of multi-layer epitaxial graphene. Whereas the transitions marked B to I correspond to electrically isolated graphene monolayers, transitions denoted $n = 1$ to 5 match to inter-LL transitions in an unperturbed graphene bilayer, following the coding* $L_{-n(-n-1)} \rightarrow L_{n+1(n)}$

Here we report on far and middle infrared magneto-transmission experiments carried out on multi-layer epitaxial graphene grown on the carbon face of 4H-SiC crystal. As reported in recent spectroscopic studies, [Sadowski *et al.*, Phys. Rev. Lett. **97**, 266405 (2006)], the dominant response of such samples in experiments is provided by graphene sheets electrically decoupled from their surrounding, with an electronic structure identical to that of an isolated graphene layer.

Nevertheless, a careful analysis of our recent data reveals significantly weaker but still well-defined response of an additional system that is present in these multi-layer graphene structures, see Fig. 10 and 11. These newly detected absorption lines scale rather linearly with the applied magnetic field instead of a $\sqrt{B}$-evolution typical of the graphene monolayer. They can be unambiguously identified as due to inter-Landau level transitions in bilayer graphene occurring between bands that touch at the charge neutrality point. Well-defined positions of individual resonances allow us to precisely estimate the inter-layer coupling as $\gamma_1 = (385 \pm 5)$ meV.

In conclusion, these bilayer inclusions embedded in multi-layer expitaxial graphene, identified in this work in magneto-transmission experiments, represent a suitable system for accurate magneto-spectroscopy studies of unperturbed bilayer graphene. For more information see [Orlita *et al.*,arXiv:1010.1767 (2010)].

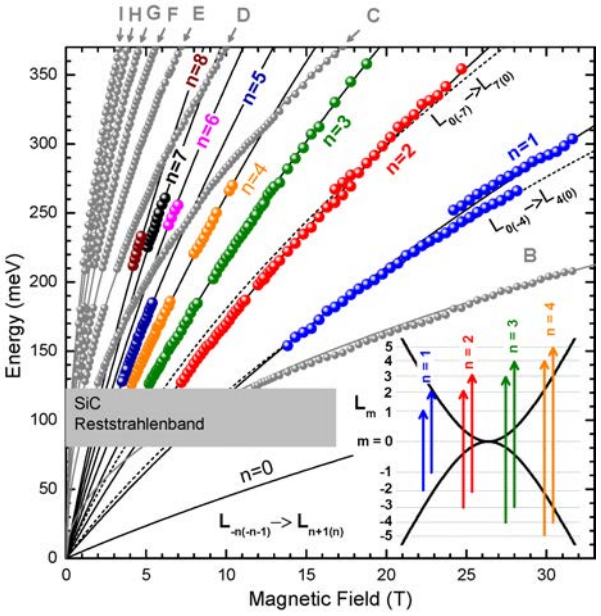


FIG. 11. *Fan chart: Points marked with Roman letters, having a characteristic $\sqrt{B}$-dependence, correspond to inter-LL transitions in electrically isolated graphene sheets. Points denoted by index $n$ represent inter-band inter-LL transitions in the graphene bilayer, see the inset.*

***M. Orlita, C. Faugeras, G. Martinez, M. Potemski***
***M. Sprinkle, C. Berger, W. A. de Heer (GeorgiaTech, Atlanta, USA), D. M. Basko (LPMMC-CNRS, Grenoble, France), J. Borysiuk, J. M. Baranowski, W. Strupinski (ITME, Warsaw, Poland)***

# Quasi-classical cyclotron resonance of Dirac fermions in highly doped graphene

Recently fabricated graphene immediately became a challenge for cyclotron resonance (CR) measurements and implied necessity to comprehend the phenomenon of cyclotron resonance in a system with massless charge carriers. Special character of CR in graphene can be exemplified using simple quasi-classical approach in which the classical cyclotron motion and consequently also the cyclotron resonance of massless Dirac fermions scale linearly with the applied magnetic field $B$, similarly to conventional massive particles, but they depend on the particle energy, which appears in a form of an energy-dependent cyclotron mass defined by the Einstein relation $|\varepsilon| = mv_F^2$.

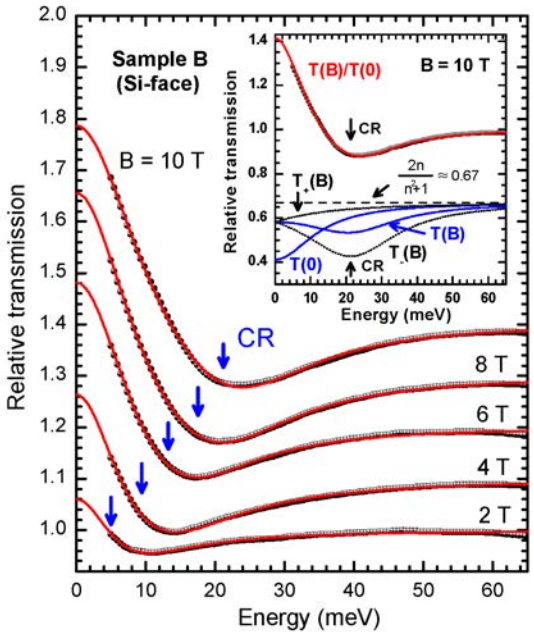


FIG. 12. *Magneto-transmission spectra of highly-doped graphene. Solid curves represent fits to experimental data according to a simple Drude-like model and vertical arrows indicate CR position. The inset shows individual transmission curves at $B = 10$ T for the CR active and inactive modes of circular polarization of light, $T_+(B)$ and $T_-(B)$, as well as the transmission at zero and non-zero field in non-polarized light, $T(0)$ and $T(B)$. All curves share a common baseline related to transmission of a dielectric slab without any conducting layer $T_{\mathrm{Slab}} = 2n/(n^2+1) \approx 0.67$.*

Surprisingly, this classical, *i.e.* linear with the magnetic field, cyclotron resonance has not been clearly observed in graphene so far. Instead, the optical response of graphene has been experimentally explored only in the quantum regime, when all detected transitions correspond to excitations between well-separated Landau levels and follow clear $\sqrt{B}$-dependence. In this work, we prove that this quasi-classical CR can be indeed observed in graphene.

In figure 12, we present spectra typical of studied samples, highly doped graphene monolayer on Si-terminated surface of SiC, which are characterized by magnetic-field-induced transmission at low energies accompanied by a relatively wide absorption minimum, which moves towards higher energies with increasing $B$. The qualitative explanation of this behavior is straightforward. The relative magneto-transmission spectrum $T(B)/T(0)$ combines two specific effects: The low-energy free carrier (Drude-like) absorption, which is gradually suppressed with the increasing field, and the cyclotron resonance itself. The former one gives rise to the field-induced transmission at low energies that decreases monotonically with the photon energy, and the latter phenomenon is manifested by an absorption minimum close to the energy of the cyclotron resonance $\omega_c$. The quantitative analysis of our data, see figure 13, allows us to find the cyclotron resonance position, which indeed evolves linearly with the applied magnetic field and find corresponding cyclotron mass of (otherwise massless) Dirac fermions at the Fermi level ($m = 0.053m_0$ in this particular case).

For more information see [Witowski *et al.*, Phys. Rev. B **82**, 165305 (2010)].

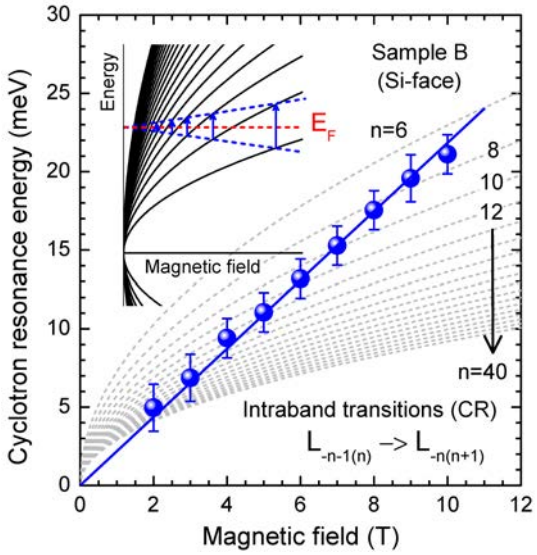


FIG. 13. *Position of cyclotron resonance as extracted from the fitting experimental curves in Fig. 12, well-following the linear in $B$ dependence plotted for the cyclotron mass of $m = 0.053m_0$ (full line).*

***M. Orlita, C. Faugeras, G. Martinez, M. Potemski***
***A. M. Witowski, R. Stępniewski, A. Wysmołek (Institute of Experimental Physics, Warsaw University, Poland) J. M. Baranowski, W. Strupiński (ITME, Warsaw, Poland)***

# Cyclotron resonance of graphene on SiC up to 120 Tesla

The Megagauss generator is now fully operational making magnetic fields in excess of 100 T available for optical experiments. The generator, previously developed at the Humboldt University in Berlin, has been initially tested by measuring the Faraday rotation on a CdS crystal. These experiments validated the performance of the Megagauss facility and associated experimental environment.

Here we described the first optical experiments on multi-layered epitaxial graphene up to 120 Tesla with a CO-laser excitation. Note that we use the magnet at only 35% of its maximum nominal energy, leaving room for improved performance of the system in the future.

The setup is presented in figure 14. We have optimized the beam path with parabolic and spherical mirrors to avoid losses due to the absorption of optical elements and to focus on the graphene sample. A chopper is used, with a high dark to light ratio (200 : 1), to limit the illumination of the sample and to prevent damage. The light source is a tunable CO-laser providing radiation between 5.2 $\mu$m to 6 $\mu$m (238 meV to 207 meV) with a maximum output power of 2 W. The acquisition is made with a fast HgCdTe photodetector connected to an 1 GHz Lecroy oscilloscope. To avoid any electrical noise due to the 100 kV trigger discharge of the generator, acquisition instruments are placed in a shielded environment.

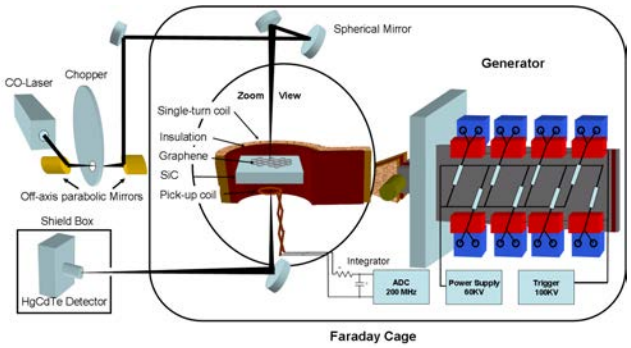


FIG. 14. *Experimental set-up for cyclotron resonance measurements of epitaxial graphene grown on SiC.*

Preliminary transmission data of graphene at an excitation energy of 229 meV as a function of time is presented in figure 15. We distinguish two different features on the experimental curve.

1. The absorption peaks marked by black arrows correspond to the cyclotron resonance of graphene, *i.e.* the energy transition from the zeroth to the first Landau level. The position of absorption lines is predicted to be square-root dependant of the magnetic field and is in good agreement with the theoretical prediction,

$$\Delta E_{(L_{-1(0)} \rightarrow L_{0(1)})} = v_f \sqrt{2\hbar e B} \qquad (2)$$

2. One broad additional absorption line, marked by grey arrows, around 100 Tesla is observed. There is no theoretical prediction for single-layer graphene at this magnetic field and this energy excitation. Further experiments are in progress in order to quantify the temperature and energy dependence of this effect.

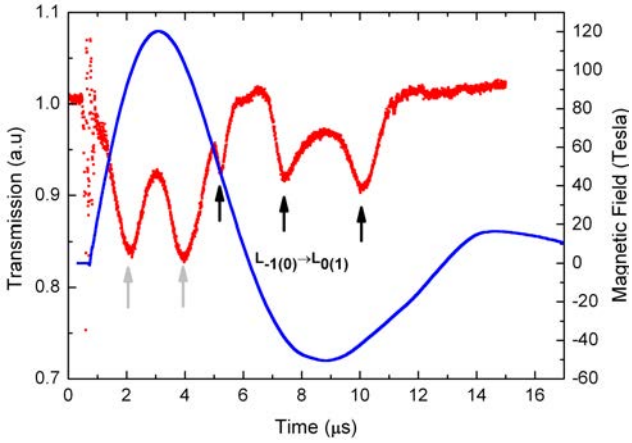


FIG. 15. *Raw data: Transmission (red points) of multi-layered epitaxial graphene grown on SiC. The incident energy is 229 meV. The magnetic field is plotted in blue and scaled on the right axis. Black arrows are the absorption for the fundamental Landau level transition and grey arrows are an additional observed absorption.*

Finally, the successful test of the cryostat, which was designed and constructed in-house, makes optical experiments down to 5 K available. Experimental setups are under development and new experiments are scheduled.

***P.Y. Solane, N. Ubrig, P. Plochocka, M. Potemski, O. Portugall***
***C. Berger, W.A. de Heer (Georgia Tech., Atlanta)***

# Magnetic-field induced electron-$K$-phonon interaction in the optical response of multi-layer epitaxial graphene

Absolute magneto-optical transmission measurements have been performed in the far-infra-red range under magnetic fields up to 32.5 T on a series of multi-layer epitaxial graphene samples. These samples are grown on the C-face of the SiC substrate, the thickness of which has been thinned down to $\sim 60\mu$m in order to minimize the contributions of the double phonon structures of SiC in the energy range of interest. We report here typical results for one sample which has 7 layers with carrier concentrations decreasing from 5 $\times 10^{12}$ cm$^{-2}$ (near the substrate) to 6 $\times 10^{10}$ cm$^{-2}$ at the surface. The relative transmission spectra are displayed in figure 16 for magnetic fields $B = 13 - 32.5$ T. Here we restrict our attention to the main optical transition corresponding to the $n = 0 \rightarrow n = 1$ and $n = -1 \rightarrow n = 0$ Landau levels respectively. As shown in this figure there is a clear additional broadening (indeed a splitting) of the transition in the energy range $150 - 153$ meV.

In a first approach, these spectra have been analyzed with a multi-layer dielectric model assuming a *single* transition which provides two parameters $\delta_{01}$ and $E_{01}$ describing the width and the position of the line respectively. The parameters $\delta_{01}$ and $E_{01}/B^{1/2}$ are plotted in figure 17 as a function of the energy ($E_{01}$). In contrast to standard two-dimensional electron gas, the scattering with impurities varies roughly linearly with the energy in graphene which is indeed observed in the top panel of figure 17 except in the range of interaction. On the other hand, $E_{01} = v_F(2e\hbar B)^{1/2}$ ( where $v_F$ is the Fermi velocity) and therefore $E_{01}/B^{1/2}$ in the bottom panel of figure 17 should be a straight horizontal line as a function of the energy which is clearly not the case. Both "anomalies" are indeed the signature of a self-energy interaction, $\Sigma(\omega)$, between the electron and the entity present in the system in the energy range $150 - 153$ meV.

In this energy range only phonons $K$ and $K'$ at the Brillouin zone boundary are present in graphene but of course not active in the infra-red. Therefore, the only possibility is that one observes the emission of such phonons occurring beyond a threshold energy. This is reminiscent of the polaronic problem and one can formally express the imaginary part of $\Sigma(\omega)$ with the corresponding polaronic expression; this is displayed as a dashed line in the top panel of figure 17. Adding this contribution to the linear variation of $\delta_{01}$ one obtain the solid line which fits quite well the experimental results at least up to 200 meV. Taking the Kramers-Krönig (KK) transform of this variation, one reproduces the variation $E_{01}/B^{1/2}$ with energy (solid line in the bottom panel of figure 17).

The agreement is acceptable although it does not tell us why or how the $K$-phonon emission process occurs. It is difficult to explain such an observation in the one-electron picture. On the other hand it is known that electron-electron interactions are important in graphene and they are also known to mix the one-electron transitions between the different valleys $K$ and $K'$ which "communicate" with $K$-phonons. Therefore, when the conservation of energy is respected, the interaction between the optical transition and $K$-phonons is possible by symmetry. However it remains to be worked out on a quantitative level, a work which is now in progress in collaboration with the group of S. Louie at Berkeley.

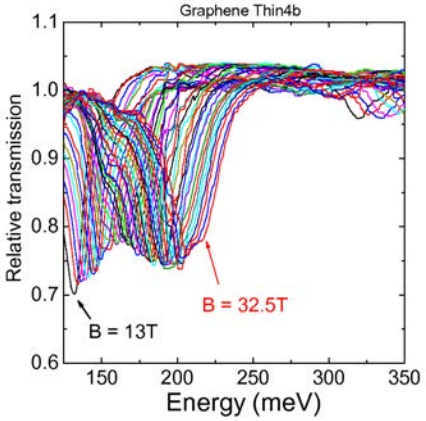


FIG. 16. *Relative transmission measured at $T = 1.8$ K as a function of the energy and different magnetic fields between 13 T and 32.5 T*

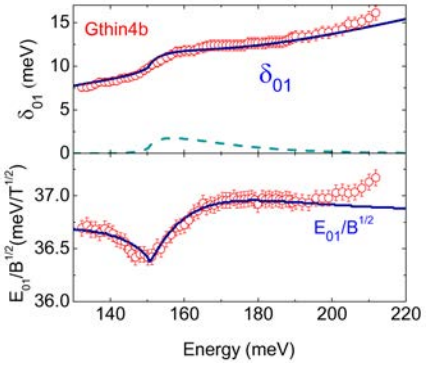


FIG. 17. *Top panel; $\delta_{01}$ (open dots) versus the energy, a simulation of the $K$-phonon emission process (dashed curve), and the total contribution to $\delta_{01}$ (solid line). Bottom panel; $E_{01}/B^{1/2}$ (open dots) versus the energy; the solid line is the KK transform of the simulated variation of $\delta_{01}$.*

***M. Orlita, G. Martinez, M. Potemski***
***M. Sprinkle, C. Berger, W. de Heer, Georgia Institute of Technology, Atlanta, USA***
***L. Tan, S. Louie, University of California at Berkeley, Berkeley, USA***

# High magnetic field induced charge density wave and sign reversal of the Hall coefficient in graphite

Graphite rapidly reaches the quantum limit at moderate magnetic field ($B > 8$ T) due to the in-plane light effective carrier mass and low carrier density (here, the magnetic field is applied parallel to the $c$-axis, *e.g.* perpendicular to the layers). On the other hand, for higher magnetic field a sharp increase of the in-plane magnetoresistance is observed for $B \approx 45$ T (not shown here). It is commonly accepted that this effect originates from a field induced electronic phase transition, where a charge density wave (CDW) instability develops along the $c$-axis. Nevertheless, up to now, this high field induced magneto-transport anomaly is not fully understood and certainly requires further investigations.

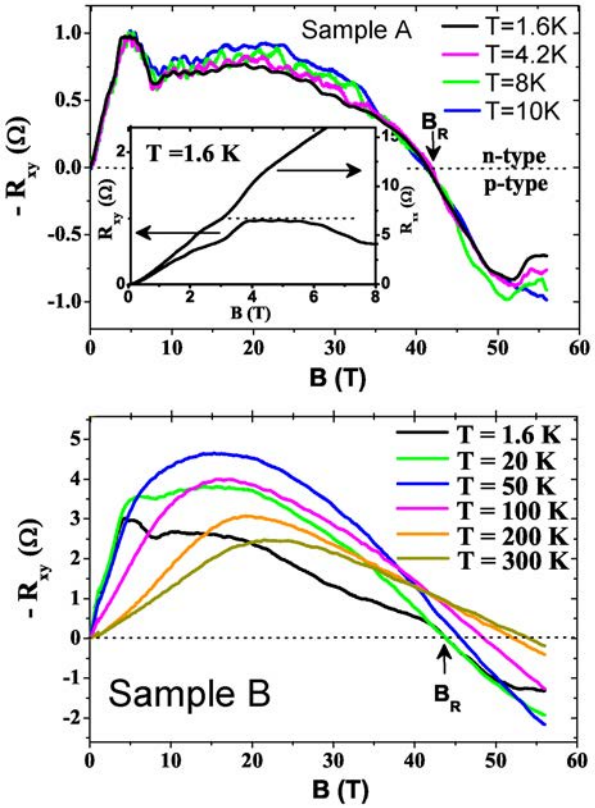


FIG. 18. *$R_{xy}(B)$ for samples A and B. The change of Hall sign coefficient from negative to positive occurs at high magnetic field, suggesting the role of hole-like quasiparticles in the the charge density wave transition observed in graphite. Inset: SdH oscillations and onset of Hall plateaus at low temperature and low magnetic field.*

To date, most of the high magnetic field experiments have been reported on Kish or natural graphite, and only few works actually report on Highly Oriented Pyrolitic Graphite (HOPG). Furthermore, the Hall resistance is not often investigated despite its usefulness to understand the charge carrier properties beyond the ultra-quantum limit. It is the purpose of this work to report on simultaneous measurements of longitudinal (in-plane) and Hall resistance in HOPG.
Two samples have been prepared and cleaved from the same source of HOPG. Their typical lateral dimensions are some hundreds of micrometers. We refer to these samples as A and B, the former being slightly bigger in size than the latter. The thickness was roughly estimated to 10 $\mu$m for both samples using scanning electron microscopy imaging. Due to experimental issues, the samples have been measured in different ranges of temperature (see figure 18).

Theoretical calculations revealed that the Fermi surface of graphite consists of majority electrons as well as two hole pockets. The band structure and Landau level formation in a magnetic field were investigated by several groups and most recently by Sugihara [Sugihara, Phys. Rev. B **29**, 6722 (1984)] who concluded that the hole levels are responsible for the CDW formation. The results presented here support this interpretation as the Hall resistance shows a sign change from negative (electrons) to positive (hole) at magnetic field in the close vicinity of the magneto-resistance jump. The Hall sign mainly depends on the ratio of charge carriers density (here, electron and hole) as well as their respective mobility. Thus, one may reasonably suppose that the hole density and/or mobility takes over the electronic-like carriers at sufficiently large magnetic field, thus providing credit to a CDW formation in the hole bands. Remarkably, the Hall resistance sign reversal is sustained up to room temperature while the CDW feature disappears above $T \approx 10$ K. Although these two phenomena take place at similar (but not exactly equal) magnetic field, the reported measurements suggest an independent origin; the former is linked to field-induced band-structure changes whereas the former requires hole-dominated transport and low temperatures [Kumar *et al.*, J. Phys.: Condens. Matter **22** 436004 (2010)].

It is interesting to note that graphite shares many similarities with other layered materials such as $NbSe_3$, 2H-$TaSe_2$, 2H-$Cu_{0.2}NbS_2$ and high temperature superconductors. Such CDW bearing compounds exhibit a change in sign of the Hall coefficient as well as a CDW transition. All these common features (occurrence of CDWs, the pseudo-gap and Hall sign reversal) point towards a generic property of highly anisotropic layered materials to which graphite belongs. Clearly, the revisited high magnetic field behaviour of HOPG continues to surprise and further experimental investigations as well as dedicated theoretical calculations are required to clarify its underlying electronic properties.

***J.M. Poumirol, A. Kumar, W. Escoffier, M. Goiran, B. Raquet***
***J.C. Pivin (Centre de Spectrométrie Nucléaire et de Spectrométrie de Masse (CSNSM), Orsay, France)***

# Probing the Fermi surface of graphite using dHvA oscillations

Graphite can be considered as a quasi-two-dimensional (2D) system consisting of stacked graphene layers. Nevertheless, the coupling between the layers, taking into account in the Slonczewski, Weiss and McClure model, leads to a band structure of graphite with resolutely 3D origins, *i.e.*, graphite has a $k_z$ dependent in-plane dispersion relation, with $z$ being the direction perpendicular to the layers. From the calculated Fermi surface of graphite we expect two majority carriers, electrons and holes, with maximal cross-section areas. Here we report on de Haas-van Alphen (dHvA) measurements at $T \approx 0.4$ K.

Figure 19 shows the torque voltage $\Delta V$ as a function of the magnetic field for $B = 0 - 0.21$ T, after removing the monotonic background by subtracting a smoothed data curve. The onset magnetic field of the quantum oscillations is $B_0 = 66$ mT which translates to $B_0 \cdot \cos(\theta) \approx 63$ mT in the $\theta = 0°$ configuration. The onset magnetic field of the quantum oscillations is comparable to the value of $B_0 = 70$ mT of the Shubnikov-de Haas (SdH) data measured at $T = 10$ mK. This suggests that the torque method is more sensitive to quantum oscillations than SdH measurements. Compared to the dHvA measurements, which probe pure thermodynamics, the magnetotransport is influenced by scattering processes at the Fermi energy, which can reduce the signal of the oscillations and also complicates the phase analysis.

Here we make a detailed phase/frequency analysis of the dHvA oscillations. Both parameters are crucial for the understanding of the topology of the Fermi surface. To extract the phase from the complex Fourier transform $\hat{f}(B)$ of $\Delta V(1/B)$ we introduce the phase shift function $K(\varphi, B) = \Re[e^{i\varphi}\hat{f}(B)] = \cos(\varphi - \varphi_0)f(B)$. Both the frequency $B_F$ and the phase $\varphi_0$ can be detected simultaneously as the position of the maximum in the $\varphi - B$ plane. $K(\varphi, B)$ is plotted in figure 20 in the regions of the fundamental frequencies of the electron and hole pockets. The phase and frequency values (corrected for the tilt angle) are $B_{F,h} = 4.44$ T, $\varphi_{0,h} = -0.56 \pm 0.05$ and $B_{F,e} = 6.08$ T, $\varphi_{0,e} = -0.48 \pm 0.05$. They are very similar to values found in our previous magnetotransport investigation ($B_{F,h} = 4.51$ T, $\varphi_{0,h} = -0.43 \pm 0.05$ and $B_{F,e} = 6.14$ T, $\varphi_{0,e} = -0.28 \pm 0.05$) [Schneider *et al.*, Phys. Rev. Lett., **102**, 166403 (2009)].

In the Lifshitz-Kosevich theory the oscillatory part of the magnetization is described by $M_{osc} \propto \sin[2\pi(\frac{B_F}{B} - \gamma \pm \delta)]$, with $\gamma = 1/2$ for massive charge carriers and $\gamma = 0$ for massless Dirac like carriers. The phase term $\delta$ reflects the curvature of the Fermi surface in the $z$-direction. It has the value $\delta = 0$ for a 2D cylindrical Fermi surface. For a 3D corrugated Fermi surface it has the value $\delta = -1/8$, for the maximal cross sections expected in graphite. The phase values obtained here, which are, in contrast to the magnetotransport data, independent of any scattering mechanism at the Fermi surface, indicate for both types of charge carriers the phase values $\gamma = 1/2$ and $\delta = 0$, in other words *massive* charge carriers with a (nearly perfect) cylindrical Fermi surface in agreement with magnetotransport measurements [Schneider *et al.*, Phys. Rev. Lett. **104**, 119702 (2010)]

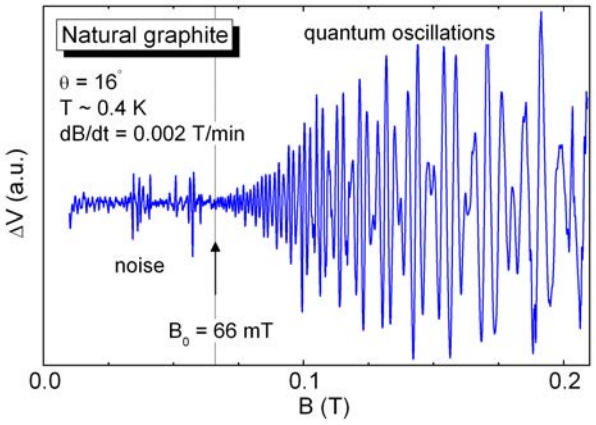


FIG. 19. *Background removed torque voltage, $\Delta V(B)$, as a function of the magnetic field ($B = 0 - 0.21$ T) measured at $T \approx 0.4$ K for a tilt angle $\theta = 16°$. The value of the onset magnetic field of the quantum oscillations is $B_0 \simeq 66$ mT.*

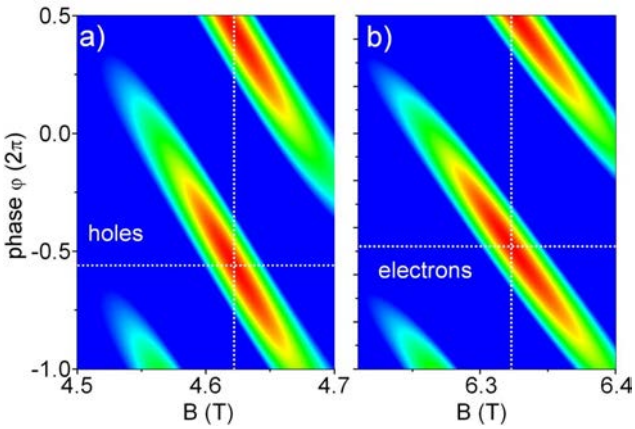


FIG. 20. *Phase shift function in the $\varphi - B$ plane. The phase and frequency values (corrected for the tilt angle) are $B_{F,h} = 4.44$ T, $\varphi_{0,h} = -0.56 \pm 0.05$ and $B_{F,e} = 6.08$ T, $\varphi_{0,e} = -0.48 \pm 0.05$ for holes and electrons, respectively. The values are characteristic for massive charge carriers with a (nearly perfect) cylindrical Fermi surface.*

***J. M. Schneider, B. A. Piot, I. Sheikin, D. K. Maude***

# High field magnetotransmission of bulk graphite

Graphite consists of Bernal stacked sheets of hexagonally arranged carbon atoms. The weak coupling between the layers transforms the single graphene layer, which is a gapless semiconductor with a linear dispersion, into a semimetal with electron and hole puddles along the $H-K-H$ edge of the hexagonal Brillouin zone. In a magnetic field the electronic structure of graphite is accurately described by the Slonczewski, Weiss and McClure (SWM) band structure calculations, with its seven tight binding parameters $\gamma_0, .., \gamma_5, \Delta$.

We have performed magneto-optical absorption measurements to probe the evolution of the $K$ and $H$ point transitions in magnetic fields up to 60 T. Typical differential magneto-absorption spectra measured at $T = 4.2$ K for magnetic fields $48-58$ T are shown in figure 21(a). All spectra show a number of absorption lines which can be assigned to dipole allowed transitions at the $H$ and $K$ points. The energetic position of the observed absorption lines is plotted as a function of the magnetic field in Figure 21(b). In order to assign the transitions we first calculate the energy of the dipole allowed transitions ($\Delta n = \pm 1$) at the $H$ and $K$-points using a greatly simplified SWM model with only two parameters $\gamma_0$ and $\lambda\gamma_1$ to describe the intra- and inter-layer coupling. Here $\lambda = 2\cos(\pi k_z)$ and $k_z$ is the momentum perpendicular to the layers. This corresponds to treating graphite as a series of graphene bi-layers whose effective coupling depends on $k_z$. The magneto-optical response is dominated by the singularities in the joint density of initial and final states which occur at the $K$-point ($\lambda = 2$) and $H$-point ($\lambda = 0$). The energy of the Landau levels is then given by,

$$E^n_{3\pm} = \pm\frac{1}{\sqrt{2}}\left[(\lambda\gamma_1)^2 + (2n+1)\varepsilon^2 - \sqrt{(\lambda\gamma_1)^4 + 2(2n+1)\varepsilon^2(\lambda\gamma_1)^2 + \varepsilon^4}\right]^{1/2}, \quad (3)$$

where $\varepsilon = \tilde{c}\sqrt{2e\hbar B}$ is the characteristic magnetic energy, $\tilde{c} = \sqrt{3}ea_0\gamma_0/2\hbar$ is the Fermi velocity, $a_0 = 0.246$ nm is the lattice constant in the $ab$ plane and $\pm$ labels the electron and hole Landau levels respectively. At the $H$-point, this reduces to the Landau level spectrum of graphene with $E^n_{3\pm} = \pm\tilde{c}\sqrt{2e\hbar Bn}$. However, the situation is complicated by the presence of the $E_1$ and $E_2$ bands which form a second Landau level spectrum which is exactly degenerate with the $E_{3\pm}$ ladder and gives rise to a series of transitions which are specific to graphite.

The energy of the dipole allowed optical transitions, calculated using Equation(3) with the tight binding parameters, $\gamma_0 = 3.15$ eV ($\tilde{c} = 1.02\times10^6$ m.s$^{-1}$) and $\gamma_1 = 0.375$ eV determined from magneto-absorption measurements at lower magnetic fields, [Orlita *et al.* Phys. Rev. Lett. **102**, 166401 (2009)] are plotted as a function of the magnetic field in Fig. 21(b). The agreement between the reduced two-parameter SWM model and experiment in Figure 21(b) is remarkable, especially taking into account that there are no adjustable parameters. The graphene like series unexpectedly shows what looks at first sight to be a splitting (see *e.g.* transition $D$), which is puzzling since such a splitting is completely absent in magneto-transmission measurements on graphene.[Plochocka *et al.* Phys. Rev. Lett. **100**, 87401 (2008)] Polarization resolved measurements confirm that the apparent splitting of the graphene like series at high magnetic field cannot be attributed to an asymmetry of the Dirac cone. The splitting resembles rather an avoided level crossing, while nevertheless remaining unexplained.

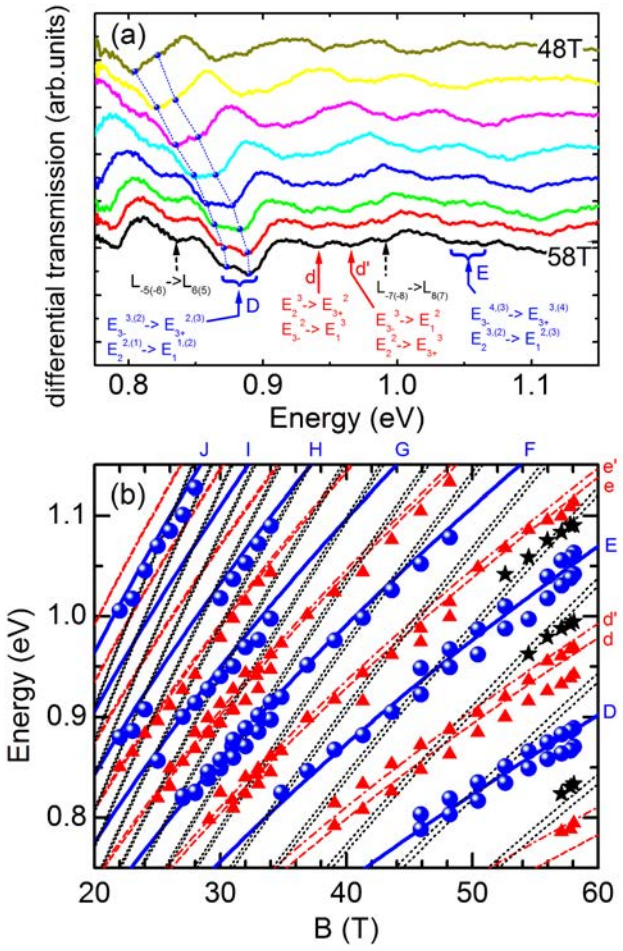


FIG. 21. *(a) Typical differential magneto-transmission spectra of natural graphite measured at magnetic fields in the range $48-58$ T at $T = 4.2$ K. (b) Magnetic field dependence of the observed transitions assigned as follows: H-point, graphene series (blue balls), graphite specific series (red triangles); K-point (black stars). The lines are calculated energies of the dipole allowed H-point (solid, dotted, and, dot-dashed lines) and K point (dashed lines) transitions as described in the text.*

# Two-Dimensional Electron Gas

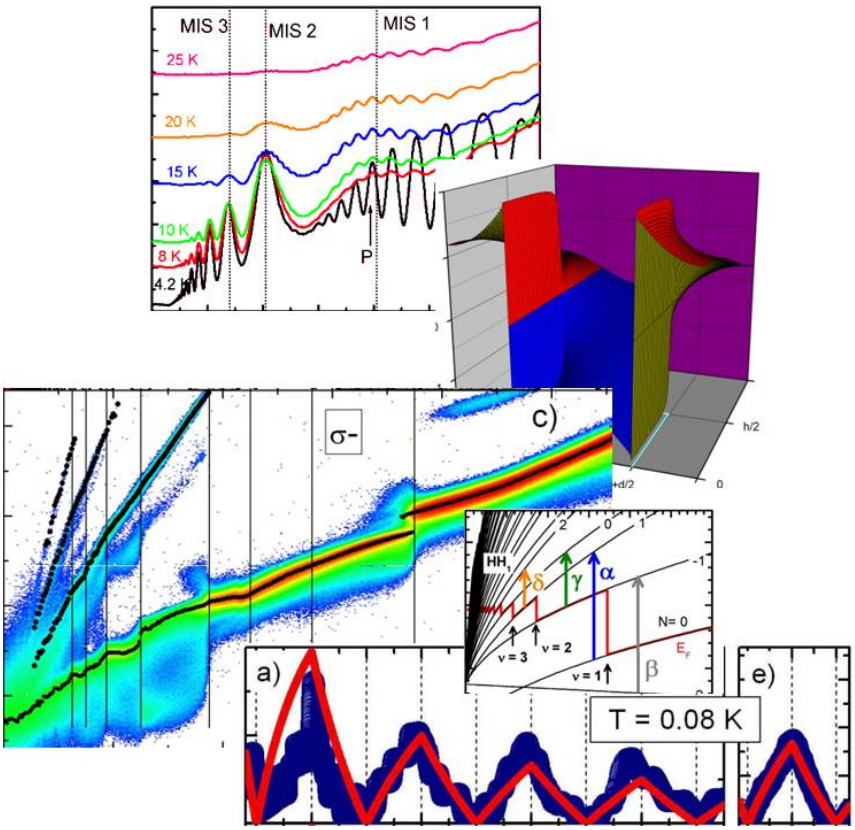

# Optical probing of the spin polarization of the $\nu = 5/2$ quantum Hall state

The fractional quantum Hall effect is the direct result of electron-electron interactions, which open energy gaps in the density of states for certain special fractional filling factors of Landau levels. In that context, the fractional quantum Hall state at $\nu = 5/2$ has been a long-standing puzzle of the field. This filling factor differs from other fractions that have so far been observed, because it violates the "odd-denominator rule" and cannot be simply described in the framework of the Laughlin wavefunction.

The interest in even denominator fractions was further intensified in 1991, when Moore and Read presented a theory that explained the existence of the quantum Hall state at 5/2 in terms of a p-wave paired state of fully spin polarized composite fermions, and predicted that the system is non-Abelian. Non-Abelian systems contain composite particles that are neither fermions nor bosons and have quantum statistics that are far richer than that offered by fermions or bosons. It was realized that the $\nu = 5/2$ state could provide experimental access to this exciting particle statistics. Additional impetus was given to this field of research when it was proposed that these non-Abelian anyons could have a real application in constructing qubits for quantum computation.

It is therefore natural that Moore-Read theory became the focus of intensive theoretical and experimental effort, trying to find evidence for the non-Abelian character of the state. The Moore-Read theory requires the electrons to be fully-polarized, *i.e.* their spins should be aligned. Hence, confirming this prediction could provide a strong experimental evidence for the validity of this theory.

In this work, we apply polarization resolved photoluminescence spectroscopy to measure the spin polarization of the two dimensional electron gas. The spin polarization is determined by considering the difference $\Delta E$ between the emission energies of the zero Landau level at the two polarizations $\sigma^+$ and $\sigma^-$. Indeed, this energy difference that we refer to as the *PL spin splitting* factors out the contributions which are equal for the two spin polarizations and is given by the sum of the Zeeman energies of the electron in the conduction band and the valence band hole, plus a term $\Delta\Sigma$ that is proportional to the interaction of the quasi-hole, which is left in the lowest Landau level after recombination, with the rest of the electrons. It can be shown that $\Delta\Sigma$ is oscillatory in $\nu$ and proportional to the spin polarization.

Let us turn now to the experimental results for the *PL spin splitting*. We first determined the energy difference, $\Delta E$, between the peak positions of the PL lines at the two polarizations at each magnetic field. We find that the *PL spin splitting* curve has an oscillatory component which is superimposed on a constant slope of 0.12 meV/T, which is the bare Zeeman splitting, $(g_h + g_e)\,\mu_B B$. Figure~ \ref{Stern1_f1}1 (c) shows the resulting $\Delta\Sigma$ as a function of filling factor for different densities. It is seen that $\Delta\Sigma$ is semi-periodic in $\nu$, with a period of $\Delta\nu = 2$,and minima at $\nu = 2, 4, 6$ and 8. Remarkably, we observe a clear dip of $\Delta\Sigma$ at $\nu = 5/2$; at this filling factor $\Delta\Sigma$ vanishes and the *PL spin splitting* is equal to the bare Zeeman splitting.

We interpret this finding as an indication that the $\nu = 5/2$ state is unpolarized. It is instructive to compare $\Delta\Sigma$ at 5/2 to that of the adjacent fraction, 7/3, the first exhibiting a minimum while the other - a maximum. This difference suggests that the spin polarization of the two fractions is different, 5/2 unpolarized and 7/3 polarized [Stern *et al.*, Phys. Rev. Lett., **105**, 096801 (2010].

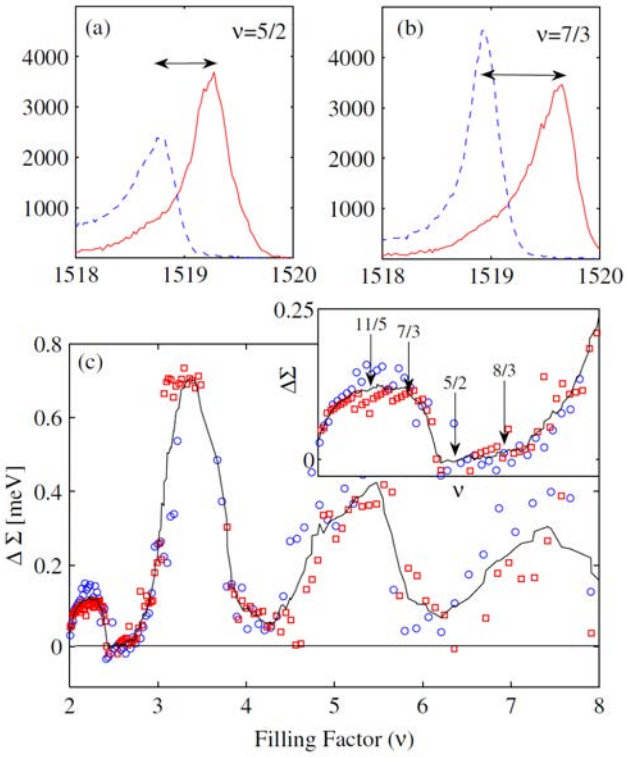


FIG. 22. *(a-b) PL spectra at both circular polarizations of the light for filling factors $\nu = 5/2$ and $\nu = 7/3$. The arrows show the difference in the PL spin splitting. (c) Enhanced spin gap as a function of filling factor. The zero enhancement observed at filling factor 5/2 is a robust signature for a non polarized state.*

***P. Plochocka, D. K. Maude, M. Potemski***
***M. Stern, V. Umansky, I. Bar-Joseph (Weizmann Institute of Science, Rehovot, Israel)***

# Static skin effect in the quantum Hall regime for high-mobility electrons on a cylindrical surface

The quantum Hall effect in a high-mobility electron gas on a cylindrical surface is dominated by a gradual change of the filling factor along the conductance path due to the gradient of the perpendicular to the surface component of the magnetic field. As a result, the current flows successively along regions with integer and non-integer filling factors, which eventually results in a transition from a quantized to a non-quantized current flow. This leads to the appearance of a finite longitudinal resistance $R^L$, which do not exist according to conventional models with a current flow along one-dimensional Landau states in an otherwise insulating bulk. We have developed a model which takes into account the current flow along incompressible stripes and compressible regions [Friedland *et al.*, Phys. Rev. B **79**, 125320 (2009)] as shown in the inset of of figure 23 (a). This model qualitatively describes the sharp peaks in $R^L$ at magnetic field values, for which the current passes from incompressible stripes to compressible bulk regions. We investigate the current flow in the compressible regions by rotating the sample around the cylinder axis by an angle $\varphi_\perp$. This is equivalent to probing the scattering of carriers into the leads as a function of distance between the leads and the position $y_\perp$, at which the magnetic field is oriented perpendicular to the surface. Here, $y_\perp = r\,\sin(\varphi_\perp)$, where $r$ denotes the radius of the cylinder. Figure 23(a) shows the longitudinal resistance. We observe resistance maxima, which do not shift their position, when the perpendicular field component is varied. Therefore, these resistance maxima are associated with the field at $y_\perp$, but decay exponentially with increasing $|y_\perp|$.

We model this using the static skin effect (SSE) developed for wave-guides [Chaplik, JETP Lett. **72**, 503 (2000)]. The essence of this effect is that the current is squeezed into a channel at only one of the wave-guide edges with a width $L_{\rm skin} = 1/(\mu\nabla_\perp B)$, where $\mu$ denotes the mobility and $\nabla_\perp B$ the field gradient, which varies along the wave guide as $\sin(\varphi_\perp)$. Consequently, we derive the following two-parameter expression for the longitudinal resistance $R^{\rm SSE}$ using the SSE theory:

$$R^{\rm SSE} = R_0^L \chi \frac{e^{-\chi}}{1-e^{-\chi}}\,, \qquad (4)$$

with $\chi_B = B_0/B_1$ for the dependence on the magnetic field $B_0$ and $\chi_{y_\perp} = y_\perp/L$ for the dependence on $y_\perp$, which is related to the rotation angle. $R_0^L$ denotes the zero-field longitudinal resistance, $B_1 = r/[\mu w \sin(\varphi_\perp)]$, $L = r^2/(B_0\mu w)$, and $w$ the Hall bar width. Using Eq. (4) for the angular dependence at low magnetic fields gives decay lengths of $L = 880$ and 390 nm for $B_0 = 0.2$ and 0.6 T, respectively. The main result of this investigation is that we can apply Eq. (4) also for the peak values of the longitudinal resistance in the quantum Hall effect regime, the results of which are shown figure 23(b). For the magnetic field values $B_0 = 4.7$ and 7.4 T, we estimate the decay lengths to be $L = 278$ and 512 nm, respectively, which are close to the values at low magnetic fields. Therefore, we conclude that also in the quantum Hall effect regime the current in the compressible regions is squeezed into a narrow channel of width $L_{\rm skin}$ as for the *metal*-state at low fields. In figure 23(c), we present the dependence of the characteristic decay length $L$ as a function of the magnetic field. $L$ is large at low magnetic fields due to narrow incompressible stripes of different filling factors, which distribute the carriers over the whole width of the wave guide. We also observe an increase of $L$ at large magnetic field, which we relate to localization, which hinders the carriers to be squeezed toward the edges by the static skin effect.

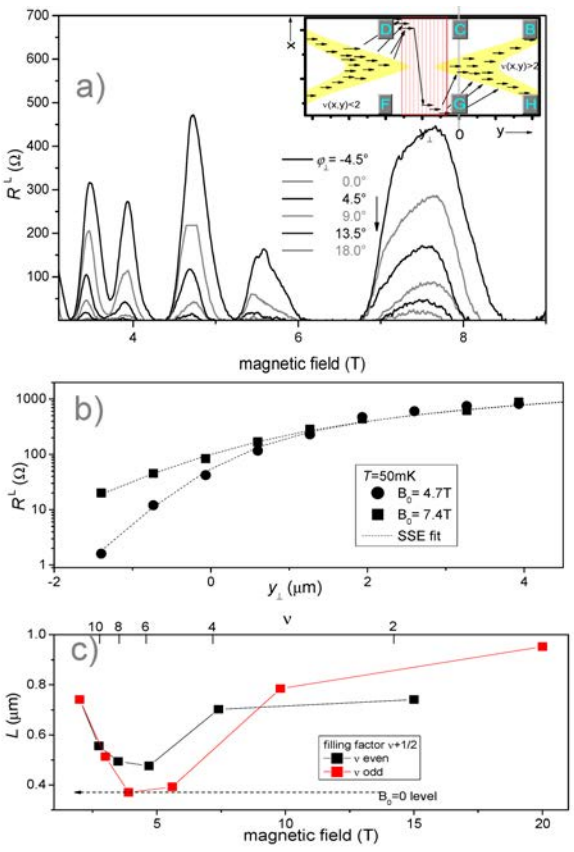


FIG. 23. *(a) Longitudinal resistance $R^L_{CB}$ as a function of the magnetic field for different rotation angles $\varphi_\perp$ at $T = 50$ mK. The spatial distribution of local filling factors around integer values, $\nu(x,y) = 2$ incompressible (yellow) and compressible (white). (b) Resistance peak values $R^L$ as a function of distance $y_\perp$ for two magnetic fields and (c) characteristic length $L$ for different filling factors.*

***D. K. Maude***
***K.-J. Friedland, R. Hey, A. Riedel (Paul-Drude-Institut für Festkörperelektronik, Berlin, Germany)***

# Magnetotransport in a wide parabolic well superimposed with superlattice

The multicomponent quantum Hall system, which consist of multiple quantum wells separated by the tunneling barriers, have exhibited many of interesting phenomena in the strong perpendicular magnetic field due to the interlayer electronic correlations. The previous theoretical works suggested several possible ground states in multilayer systems. The first class of the candidate states is the spontaneous coherent miniband state in superlattice (SL) quantum Hall system [Hanna *et al.*, Phys. Rev. B, **65**, 115323 (2002)]. This state is an analog of the interlayer coherent state at the Landau filling factor $\nu = 1$ in double well structures. The second class of the candidate states is the solid state phase (Wigner crystals) with different configurations depending on the interlayer separation. The third type of the candidate state is the staggered liquid state, which consists of independent-layer states with unequal density. Despite of considerable theoretical efforts and predictions of many exotic broken symmetry states in the quantum Hall superlattice, such states have not yet been observed.

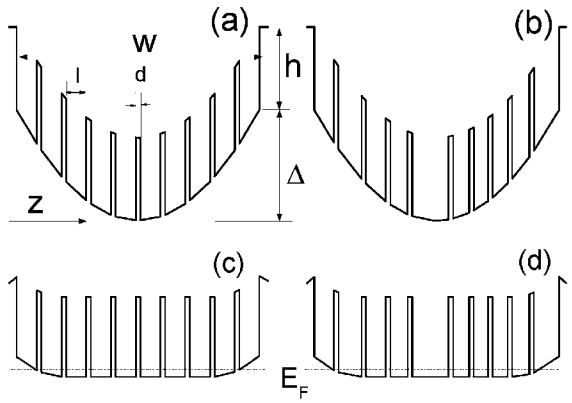


FIG. 24. *The profile of the conduction band edge of an empty (a,b) and partially fill (c,d) parabolic well with periodic (a,c) and intentionally disordered (b,d) superlattices. $E_F$ is the Fermi level.*

Here we report the magnetotransport measurements in an (AlGa)As parabolic quantum well (PQW) with periodical and intentionally disordered short-period GaAs/AlGaAs superlattice (figure 24) . In strong magnetic field we observed numerous well developed plateaus in the Hall resistance at fractional filling factors $\nu < 1$ with deep minima in the longitudinal resistance. Surprisingly, the slope of the Hall resistance is dramatically enhanced above the critical magnetic field (figure 25(b)).

We attribute this transition to a separation of the electrons into two groups, one group of electrons in the central well with highest mobility sufficient to form fractional quantum Hall effect states, and another group of low density and mobility electrons in the lateral wells,

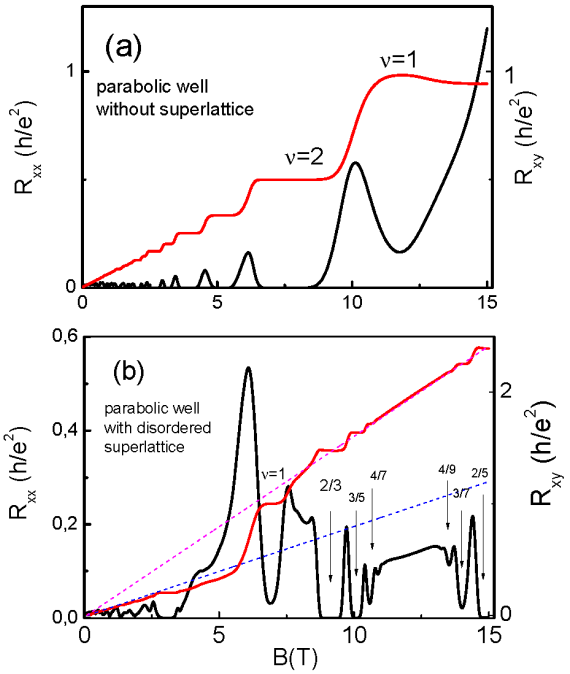


FIG. 25. *Longitudinal (black) and Hall (red) resistances as functions of the perpendicular magnetic field for a parabolic quantum well without superlattice (a) and with disordered superlattice (b). Filling factors determined from the Hall resistance are labeled. FQH states are marked with arrows. The dashed lines correspond to the linear extrapolation of the low-field (blue) and high-field (magenta) Hall resistances.*

which are localized in $X - Y$ plane and, therefore, do not contribute to the Hall resistivity. The transition occurs due to the electron-electron interaction which favours the redistribution of the electrons in the individual wells, very likely with an unequal density (staging transition), predicted by Hanna *et al.* The transition is absent in the PQW without superlattice ( figure 25(a)). A detailed description of experimental results can be found in [Gusev *et al.*, Phys. Rev. B **81**, 165302 (2010)].

***J. C. Portal***
***G. M. Gusev (Instituto de Física da Universidade de São Paulo, SP, Brazil), Yu.A.Pusep (Instituto de Física de São Carlos da Universidade de São Paulo, São Carlos, SP, Brazil), A. K. Bakarov, A.I.Toropov (Institute of Semiconductor Physics, Novosibirsk, Russia)***

# Fractional quantum Hall effect in CdTe

The fractional quantum Hall effect (FQHE) is a well-known collective phenomenon that was first seen in a two-dimensional gas of interacting electrons within GaAs heterostructures. The system behaves at very low temperatures and high magnetic fields as if it were composed of particles with fractions of the elementary charge and exhibits a series of plateaus in the Hall resistance at fractional filling factors (ratio of number of electrons to the magnetic flux quanta).

Recently, we have reported the first observation of the fractional quantum Hall effect in a high-mobility CdTe quantum well [Piot *et al*, Phys. Rev. B **82**, 081307(R) (2010)]. CdTe is a single valley, direct gap II-VI semiconductor in which the bare electronic g factor is about four times larger than in GaAs. The transport measurements performed at mK temperature reveal *fully-developed* FQH states (*i.e.* zero longitudinal resistance and exact quantization of the Hall resistance) in the upper spin branch of the lowest ($N = 0$) Landau level (LL) (see figure 26), which constitutes to our knowledge the first observation of the FQH effect in a II-VI semiconductor.

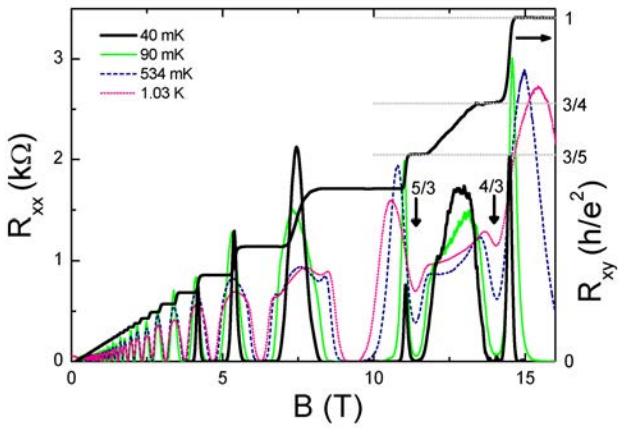


FIG. 26. *Hall resistance $R_{xy}$ and longitudinal resistance $R_{xx}$ versus perpendicular magnetic field for different temperatures.*

Tilted magnetic fields experiments up to 28 Tesla (figure 27(a)) show no significant changes of the FQH gap both at filling factor 4/3 and 5/3 (see inset), a behavior typical of spin-polarized ground states for which the lowest energy excitation is not a spin-flip. This can be accounted for by the relatively high intrinsic Zeeman energy which wins over the Coulomb energy to force the spins to align with the magnetic field. This can also be seen as the consequence of energy level crossings in the composite fermion (CF) approach for the FQH effect (see figure 27(b) and (c)). In this interpretation, the latter FQH states correspond to integer quantum Hall effect at filling factor $\nu^*_{CF} = 2$ and $\nu^*_{CF} = 1$ for composite fermions, moving in an effective field $B^*_{CF}$.

Emerging FQH minima at filling factor 7/3 and 8/3 are also observed at intermediate temperatures in the first excited ($N = 1$) LL, demonstrating the high quality of the 2DEG that it is now possible to achieve in this material. A significant advantage of CdTe systems is the possibility of incorporating magnetic ions to form a diluted magnetic semiconductor for possible applications in spintronics and also to study the many-body effects in the presence of high intrinsic Zeeman energy.

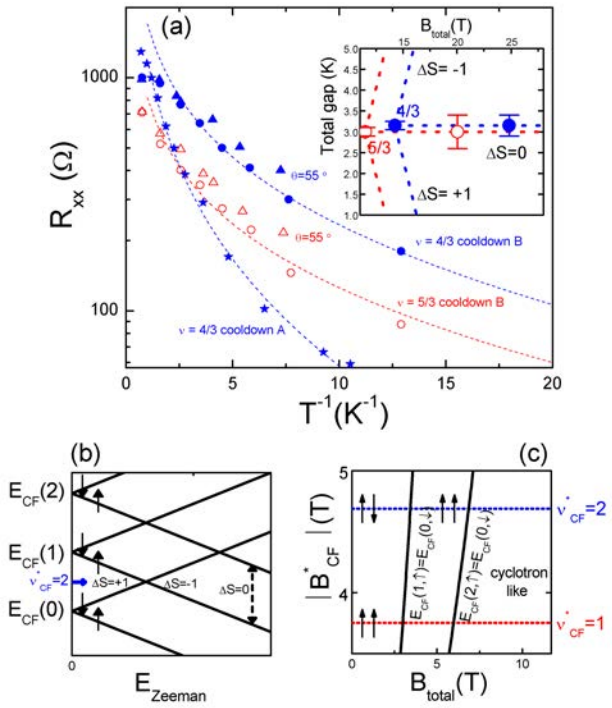


FIG. 27. *(a) Longitudinal resistance $R_{xx}$ at $\nu$=4/3 as a function of inverse temperature for cooldown A (stars) and for cooldown B at $\theta = 0°$ (circles) and $\theta = 55.6°$ (triangles). Same data for cooldown B at $\nu$=5/3 (open symbols). Simulations of the thermally activated resistance (dashed lines). Inset: Corresponding total FQH gaps at $\nu$=4/3 and $\nu$=5/3 as a function of the total field $B_{total}$. Expected evolution of the gaps for different ground states (dotted lines), $\Delta S = 0$ (constant gap) corresponding to spin polarized ground and excited states. (b) Schematic representation of the CF fan diagram at fixed CF cyclotron energy, as a function of the Zeeman energy. $E_{CF}(N)$ is the energy of the $N^{th}$ CF level. The arrows depict the spin orientation of each sub-band. (c) Position of the CF level crossings in the ($|B^*_{CF}|$,$B_{total}$) plane (thick line). The arrows depict the spin polarization of the ground state in different region.*

***B. A. Piot, J. Kunc, M. Potemski, D. K. Maude***
***C. Betthausen, A. Vogl, D. Weiss (Department of Physics, Regensburg University, Regensburg, Germany),***
***G. Karczewski, T. Wojtowicz (Institute of Physics, Polish Academy of Sciences, Warsaw, Poland)***

# Spin gap enhancement in fully occupied 2D Landau levels

Polarization-resolved magneto-photoluminescence (magneto-PL), together with simultaneous magneto-transport measurements, have been performed on a two-dimensional electron gas (2DEG) confined in CdTe quantum well in order to study the spin gap enhancement (SGE). The SGE is driven by the spin polarization of a 2DEG and is a primary manifestation of many-body electron-electron interactions in the regime of integer quantum Hall effect. However, the majority of investigations deal only with the SGE in the vicinity of the Fermi energy. In our work, we have been focused on the SGE in the fully occupied Landau levels well below Fermi energy. SGE below Fermi energy has been probed by means of magneto-PL. Because the spin gap is usually measured by means of thermally activated transport (probing SGE in the vicinity of the Fermi energy), we have measured magneto-transport and magneto-PL simultaneously in order to compare the energy of a spin gap obtained by both methods (see Fig. 28).

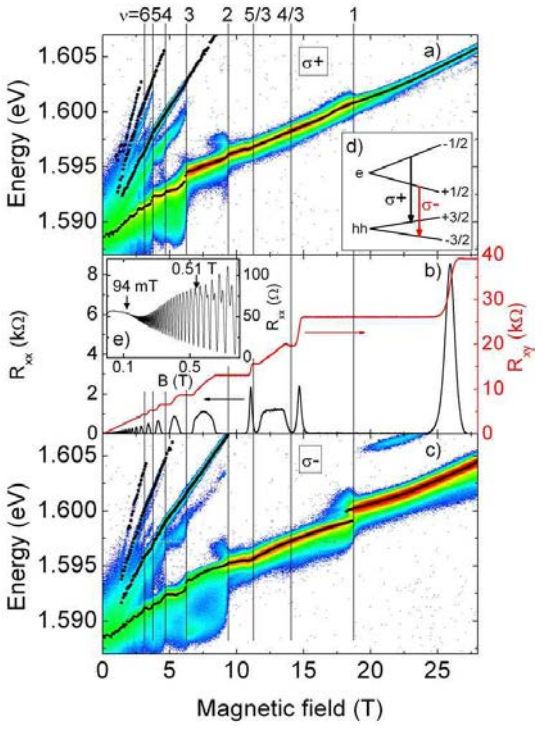


FIG. 28. *(a) and (c) color plot of $\sigma^+$ and $\sigma^-$ magneto-PL in a CdTe QW, measured at 80 mK, under low power ($\approx$ 0.5 $W/m^2$), excitation by $Ar^+$ laser at $\lambda$ = 514 nm. Black points indicate the energy of the main peaks. (b) Simultaneous magneto-transport measurements showing $R_{xx}$ and $R_{xy}$.*

The blue shifts of the energy of PL at every integer filling factor well correlate with minima in longitudinal ($R_{xx}$) and plateaux in the Hall ($R_{xy}$) resistance. The energies of the spin gap obtained by both methods agree within an experimental error for all odd filling factors. The advantage of magneto-PL is the capability to probe energy of the spin gap at intermediate magnetic field (not only at integer filling factors) and temperature. We have found that the energy of the spin splitting as a function of magnetic field consists of two contributions. The contribution linear in field is attributed to the single-particle Zeeman splitting and the oscillatory contribution is identified as a manifestation of the many-body electron-electron interactions. We have studied B-dependence of the SGE as a function of the temperature and as a function of the index of the Landau level for $N = \{0, 1\}$, see points in Fig. 29.

The oscillatory many-body contribution diminishes with increasing temperature and correlates with the filling factor (maxima/minima at odd/even filling factors). Both field and temperature dependence of the many-body contribution $\Delta E_{\uparrow\downarrow}$ can be successfully described by a simple analytical formula,

$$\Delta E_{\uparrow\downarrow} = \Delta_0' \sqrt[4]{B^2 + B_0^2}\, \frac{n_\downarrow - n_\uparrow}{n_\downarrow + n_\uparrow}. \qquad (5)$$

The good agreement between the data (points) and the model (line) is shown in the Fig. 29. Thus, the SGE appears not only in the vicinity of the Fermi energy in 2DEG, but also in fully occupied Landau levels and the amplitude of the SGE is the same for all occupied Landau levels up to the Fermi energy [Kunc **et al.**, Phys. Rev. B, **82**, 115438 (2010)].

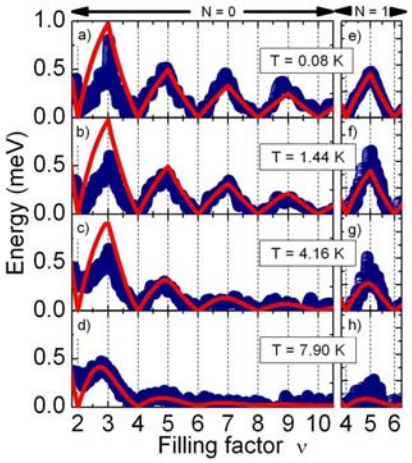


FIG. 29. *Many-body contribution to the spin gap in the $N = 0$ and $N = 1$ Landau level, extracted from magneto-PL experiments (points) and calculated using the model (solid lines).*

***J. Kunc, K. Kowalik, F. J. Teran, B. A. Piot, D. K. Maude, M. Potemski***
***V. Kolkovsky, G. Karczewski, T. Wojtowicz (Institute of Physics, Polish Academy of Sciences, Warsaw, Poland)***

# Enhancement of the RDNMR signal at $\nu = 2$

Nuclear polarization is extremely weak under thermodynamic equilibrium. The polarization of $^{75}$As nuclei in AlGaAs/GaAs heterostructures is of the order of 1% per Tesla at $T = 30$ mK. Increased polarization for a larger nuclear magnetic resonance (NMR) signal may be obtained by leaving the sample in a strong magnetic field. However the setting time is long (up to several hours) due to the long nuclear relaxation time $T_1$ and the achievable polarization is finite for a given field. Dynamic nuclear polarization (DNP) is a commonly used to generate a significant non equilibrium nuclear spin polarization via electron spin flips (flip flop process). In the quantum Hall effect (QHE) regime, several transport mechanisms lead to DNP; electron scattering between spin resolved edge channels, electron scattering between domains of different nuclear polarizations, QHE breakdown under large *dc* currents. Recently, Dean *et al.* have shown that even a relatively modest *dc* current ($I = 500$ nA) strengthens the resistively detected nuclear magnetic resonance (RDNMR) signal [Phys. Rev. B **80**, 153301 (2009)]. Here we report the enhancement of the RDNMR signal at $\nu = 2$ ($B = 3.65$ T) simply driven by a small *ac* current ($I = 20$ nA) at $4 - 6$ T magnetic fields.

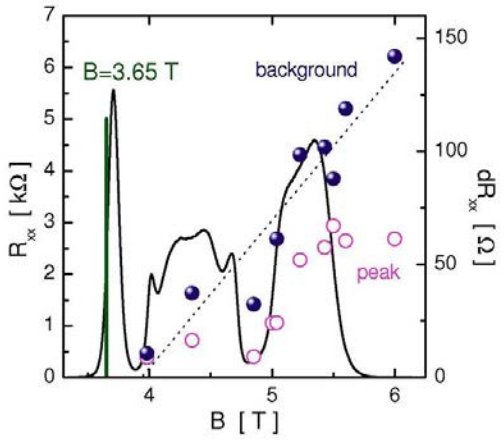


FIG. 30. *(Left axis) Magnetoresistance between $\nu = 2$ and $\nu = 1$ at $T = 90$ mK. The vertical line highlights the $B = 3.65$ T field. (Right axis) Longitudinal resistance background change $dR_{xx}^{bgnd}$ and RDNMR peak amplitude $dR_{xx}^{peak}$ (disks and circles resp.) as a function of the polarization fields. Dotted line is a guide to the eye.*

Conventional RDNMR is performed on a high mobility GaAs/AlGaAs heterojunction ($n_s = 2.1 \times 10^{11}$ cm$^{-2}$, $\mu = 5.8 \times 10^6$ cm$^2$V$^{-1}$s$^{-1}$) at $T = 40$ mK with an ac current of 20 nA. Figure 30 (left axis) shows the magnetoresistance between $\nu = 2$ and $\nu = 1$. When the magnetic field is set at $B = 3.65$ T, *i.e.* on the high field flank of $\nu = 2$ (vertical line), no resonance is detected. However if the magnetic field is set at a higher value, $B = 5.5$ T for instance, maintained for 5 minutes and then swept down to its initial value, $B = 3.65$ T, then a clear RDNMR peak signal appears at the $^{75}$As resonant radio-frequency (RF) of 26.43 MHz (upper curve in Fig. 31). Successive downward RF sweeps show a reduction of both the resonance peak amplitude and the off-resonance magnetoresistance background. After a few passages through the resonance, the longitudinal resistance reaches a stable value and the resonance signal fades out (lower curve). We stress that during the whole process the *ac* current is kept constant at 20 nA.

The observation of a nuclear resonance at $B = 3.65$ T, after the magnetic field being set at a higher value, suggests a significant increase of the nuclear polarization. A change in the nuclear polarization is confirmed by the off-resonance background resistance change $dR_{xx}^{bgnd}$ represented by the arrow in Fig. 31. It is similar to the huge longitudinal resistance effect reported at $\nu = 2/3$, where $R_{xx}$ increases versus time as DNP occurs. Figure 30 shows $dR_{xx}^{bgnd}$ for different polarization magnetic fields following the same experimental sequence; sweeping the field from $B = 3.65$ T up to the polarization field, waiting 5 mins, then sweeping the field down to $B = 3.65$ T where RDNMR scans are performed.

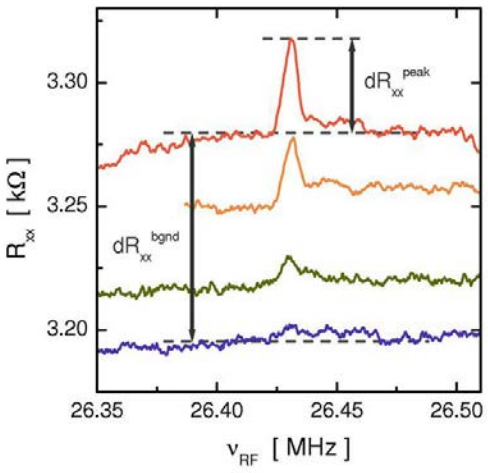


FIG. 31. *From top to bottom, successive RDNMR spectra measured at $B = 3.65$ T after setting the magnetic field at $B = 5.5$ T for 5 mins. The radio-frequency is swept downward at $0.8 - 1.3$ kHz/s for each scan. Vertical arrows represent the resistance background variation $dR_{xx}^{bgnd}$ and peak amplitude $dR_{xx}^{peak}$ of the first RDNMR scan.*

Clearly, the change in the resistance background increases as a function of the polarization field. The RDNMR peak amplitude is also enhanced in agreement with a larger nuclear polarization. Our results clearly demonstrate nuclear polarization enhancement in our sample at $\nu = 2$.

***B. A. Piot, D. K. Maude***
***W. Desrat (Groupe d'Etude des Semi-conducteurs, Université de Montpellier II, France), Z. R. Wasilewski (Institute of Microstructural Sciences, NRC, Ottawa)***

# Electron-Phonon Interactions in a single modulation doped $Ga_{0.24}In_{0.76}As$/InP Quantum Well

Absolute magneto-transmission experiments in the far-infra-red, as a function of the magnetic field B up to 28 T, have been performed on a series of single modulation doped $Ga_{0.24}In_{0.76}As$/InP Quantum Well (QW) with a width dw=10 nm. The QW is sandwiched between two InP layers. The carrier concentration $N_s$ is monitored by experimental conditions from 2 to 4.2 $10^{11}$ cm$^{-2}$ with mobilities ranging from $10^5$cm$^2$/V/sec to $2\times10^5$cm$^2$/V/sec respectively. In terms of phonons the mixed compound $Ga_xIn_{1-x}As$ is a two mode system with two transverse optical (TO) phonons varying linearly with the $x$ content between those of InAs and GaAs whereas the two longitudinal optical (LO) phonons are coupled by the macroscopic electric field. As such the "longitudinal oscillator strength" related to the Fröhlich interaction is partly transferred from the lower energy LO mode to the higher one as shown by the phonon model (Nash *et al.* Semicond. Sci. Technol. **2**, 329 (1987)). The present report is the continuation of the work reported last year which was restricted to fields below 13 T.

The relative transmission spectra are analyzed with a multi-layer dielectric model: the dielectric function of the doped QW is simulated with a Drude type contribution which for a given value of B, provides two independent fitting parameters $\delta_0$ (width of the transition) and $\hbar\omega_c$ (energy of the transition). The variations $\delta_0$ and $\hbar\omega_c$/B with the energy ($\hbar\omega_c$) are displayed, as open circles, in figure 32 for a given sample and given $N_s$ concentration. In the top panel of the figure the variation of $\delta_0$ is decomposed into different parts: the doted line simulates the electron-TO-phonons interaction, the dashed lines the electron-LO-phonons interactions and the dot-dash line the electron-interface-phonon interaction. The shape of these interactions reveal the nature of them: whereas the electron-TO-phonons interaction is driven by the deformation potential mechanism, the electron-LO-phonons interactions are characteristic of polaronic effects mediated by the Fröhlich mechanism with a threshold at the respective LO energies. The interaction with the symmetric interface mode (labelled "XP" in figure 32), active in the infra-red, is also mediated by the Fröhlich mechanism. The sum of all these interactions displayed as a continuous line is the Imaginary part of the self energy, $\Sigma(\omega)$, entering into the response function of the system. As a consequence the Kramers-Krönig (KK) transform of this variation should correspond to the real part of the self energy super-imposed to the non-parabolicity effects as displayed in the bottom panel of figure 32.

The two functions $Im(\Sigma(\omega))$ and $Re(\Sigma(\omega))$ can then be introduced in the multi-dielectric model and transmission spectra reproduced for each value of $B$ can be compared to the experimental data without any additional parameter. If the fitting is self consistent the agreement is quite good and this has been verified for different samples and different $N_s$ values. As a result we obtain for all electron-phonon interactions a set of self consistent parameters with their variation as function of $N_s$. It is shown that the polaronic contribution vanishes for $N_s$ values larger than $4.0\times10^{11}$ cm$^{-2}$ though the LO energies remain constant within the experimental errors: this is the Fröhlich interaction which is screened. This work shows as well the importance of the interaction, in this system, with the interface phonon due to the fact that it is mainly governed by the Fröhlich constant of the InP barrier.

Details of this study can be found in the recent publication of Orlita *et al.* [Eur. Phys. Lett. **92**, 37002 (2010)].

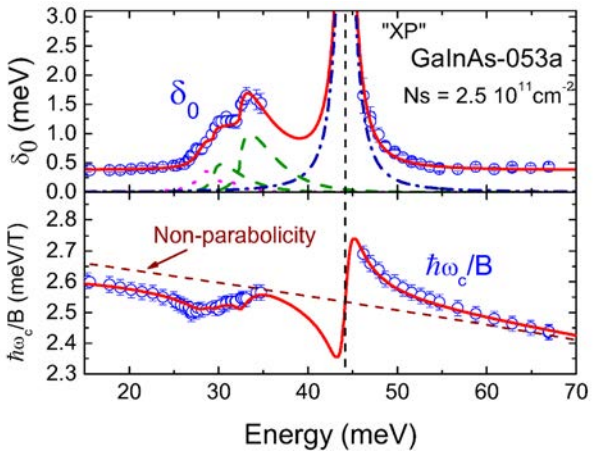


FIG. 32. *Top panel: Variation of $\delta_0$ with the energy; the open circles are values obtained from the fit of transmission data and the different dotted and dashed lines represent the different simulated contributions to $\delta_0$. The full line is the total contribution. Bottom panel: variation of $\hbar\omega_c/B$ with the energy; the open circles are values obtained from the fit of transmission data and the full line, the KK transform of the total contribution to $\delta_0$. The dashed line is the non-parabolicity contribution to $\hbar\omega_c/B$.*

***M. Orlita, C. Faugeras, G. Martinez***
***S. Studenikin, P. Poole (Institute of Microstructural Sciences, NRC, Ottawa, Canada)***

# Fine structure of "zero-mode" Landau levels in HgTe/HgCdTe quantum wells

Experimental finding of the quantum spin Hall effect (QSHE) [König *et al.*, Science **318**, 766 (2007)] in HgTe/CdTe quantum wells (QWs) affirmed the previous theoretical predictions [Bernevig *et al.*, Science **314**, 1757 (2006)] and has had a relevant impact on further development of the research on two- and three-dimensional (2D and 3D) topological insulators. Remarkably, the origin of the topological insulator phase (bulk gapped insulator with gapless conducting states at the edges or surfaces) turns out to be just the peculiar band structure, characteristic of certain class of semiconductors with an appropriate strength of spin-orbit interaction.

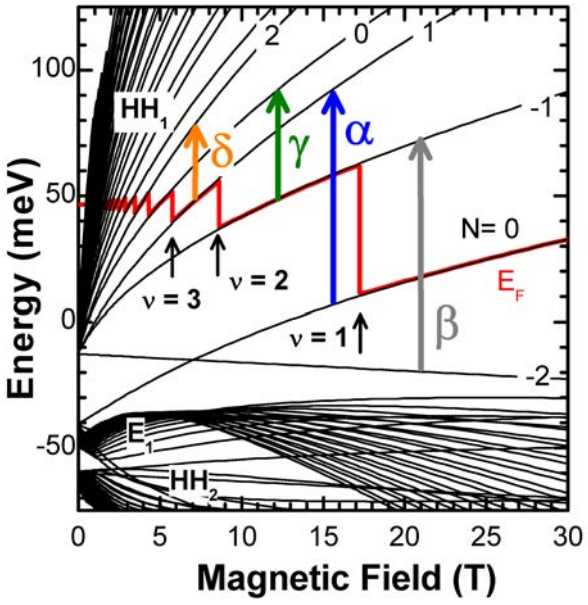


FIG. 33. *Landau level diagram calculated using k.p theory for a HgTe quantum well. Individual absorption lines are marked by arrows and Greek letters. Transitions α and β have zero-mode levels (N = −2 and 0) in their initial states.*

The 2D archetype of this phase appears in HgTe quantum wells in the regime of the so-called inverted band structure (semiconductor with a gap between the upper *p*-type and lower *s*-type energy band). The inherent property of such bands is their characteristic behavior under the applied magnetic field, i.e., the appearance of the particular pair of Landau levels which distinctly split from the upper and lower energy band. Progressively with the magnetic field, those two Landau levels merge and according to common theoretical approach (standard **k.p** theory) eventually cross at certain field $B_c$, above which the zero-field topologically insulating phase is transformed into the common quantum Hall insulator. This pair of low-lying levels is a reminiscence of the characteristic, field-independent zero-mode (zero-index) Landau levels of massless Dirac fermions, such as, for example, those found in graphene.

In this work, we inspect more closely the field evolution of these "zero-mode" Landau levels using a suitable experimental tool, namely Landau level spectroscopy (see figures 33 and 34). Essentially, we find that the zero-mode Landau levels in HgTe quantum wells with the inverted band structure do not cross, but instead display the effect of the avoided crossing. This effect might be due to the bulk inversion asymmetry which is inherently present in zinc-blend crystals but habitually neglected in band structure calculations of HgTe quantum wells. A more speculative interpretation of our experimental finding would consist of refereeing to the extended investigations of the zeromode Landau levels in graphene and pointing out the electron-electron interaction as a possible source of opening of a gap within the otherwise double degenerate Landau level at the critical field $B_c$.

For more information see Orlita *et al.* [arXiv:1011.5233v1 (2011)].

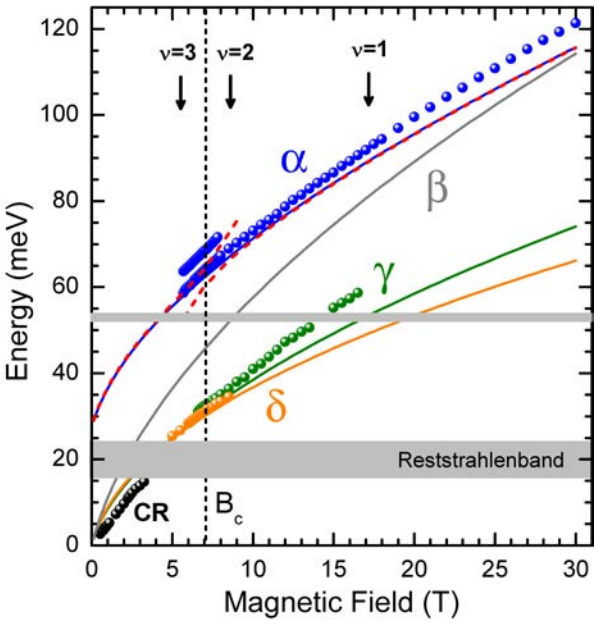


FIG. 34. *Fanchart of observed inter-Landau level transitions. The transition α, see Fig. 33, having N = −2 Landau level in its initial state has a character of a doublet around the crossing field $B_c$, which points towards avoided crossing of zero-mode levels.*

***M. Orlita, K. Masztalerz, C. Faugeras, M. Potemski***
***E. G. Novik, C. Brüne, H. Buhmann, L. W. Molenkamp (University of Würzburg, Germany)***

# Quantum Hall effect near the charge neutrality point in HgTe-based quantum wells

The quantum Hall effect (QHE) of a two-dimensional electron gas in a strong magnetic field is one of the most fascinating quantum phenomena discovered in the condensed matter physics. Its basic experimental manifestation is a vanishing longitudinal conductivity $\sigma_{xx} \approx 0$ and a quantization of the Hall conductivity $\sigma_{xx} = \nu e^2/h$, where $\nu$ is the Landau filling factor.

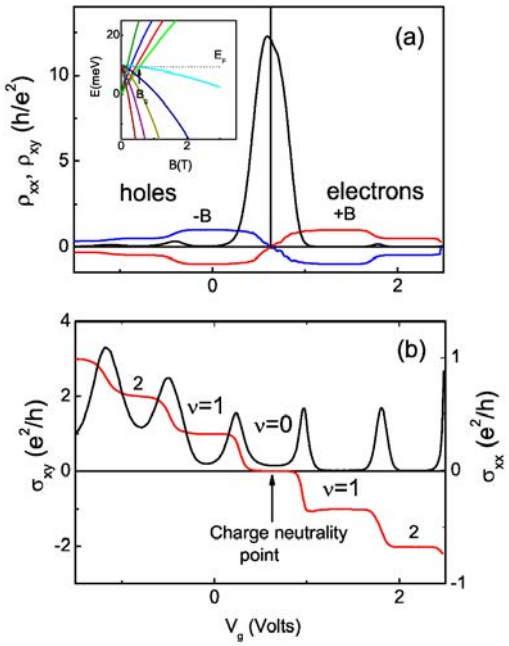


FIG. 35. *(a) Diagonal $\rho_{xx}$ (black) and Hall $\rho_{xy}$ (blue, red) resistivities as a function of the gate voltage at fixed magnetic field B=2.8 T. Hall resistivity is shown for different signs of the magnetic field. Insert -Landau level fan diagram for the electron and hole subbands. Notice that the last Landau levels from each set of subband cross at a finite $B_c$-field. $E_F$ is the Fermi level at the charge neutrality point. (b) Diagonal $\sigma_{xx}$ (black, right axis) and Hall $\sigma_{xy}$ (red, left axis) conductivities as a function of the gate voltage at the same magnetic field, T=50 mK. Arrow indicates the position of the charge neutrality point, when $n_s = p_s$.*

The origin of the conventional integer QHE lies in the existence of the spectral gap in the density of states between separated Landau levels (LL).

The discovery of a 2D electron-hole system in graphene has put a beginning to a series of studies of the properties of the special state realized when the densities of the electrons and holes are equal, the charge neutrality point (CNP) [Abanin et al, Phys. Rev. Lett. **98**, 196806 (2007)]. In a strong magnetic field the QHE near the CNP reveals a plateau with $\nu = 0$ currently associated with the resolution of the spin or the valley splitting of the lowest Landau level and deep minimum in $\sigma_{xx}$.

Recently it has been shown that a two-dimensional semi-metal exists in undoped HgTe-based quantum wells with an inverse band structure and a (013) surface orientation [Kvon et al., JETP Lett. 87, 502 (2008)]. Applying voltage to an electrostatic top gate allows the system properties to be studied at an almost arbitrary ratio of the two-dimensional electron and hole densities in the quantum well including the charge neutrality point where the densities of electrons and holes are equal. In this paper we study the transport properties of HgTe-based quantum wells containing simultaneously electrons and holes in magnetic field. In CNP, when the densities of the electrons and holes are equal, the resistance is found to increase very strongly with $B$ while the Hall resistivity turns to zero (figure 35). This behavior results in a wide plateau in the Hall conductivity $\sigma_{xy} \approx 0$ and minimum in a diagonal conductivity $\sigma_{xx}$ at $\nu = 0$ Landau filling factor. We suggest that the transport in the CNP point is determined by electron-hole "snake states" propagating along $\nu = 0$ contour (figure 36). Our observations are qualitatively similar to the quantum Hall effect in graphene as well as to the transport in random magnetic field with zero mean value.

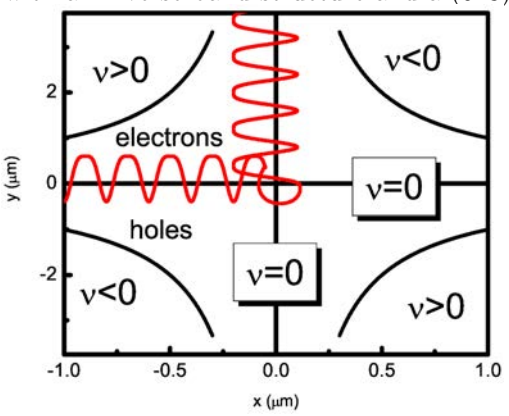


FIG. 36. *Schematic illustration of the electron-hole "snake state" percolation along $\nu = 0$ line at CNP in the strong magnetic field and geometry of the saddle point between adjacent percolation clusters.*

***J. C. Portal,***
***G.M. Gusev (Instituto de Física da Universidade de São Paulo, São Paulo, Brazil), E.B. Olshanetsky, Z.D. Kvon (Institute of Semiconductor Physics, RAS, Novosibirsk, Russia)***

# Weak antilocalization in HgTe quantum wells near a topological transition

Recently the observation of edge current-carrying states in the absence of magnetic field (Spin Hall Insulator) has been reported in HgTe quantum wells with an inverted band spectrum and a thickness slightly larger than the critical thickness of 6.3 nm. Spin-orbit effects are of critical importance for the appearance of these states. For these reasons, information on these effects is very important. However, so far they have been studied only in wide quantum wells (about 20 nm) and at high electron densities, *i.e.*, when a well has a thickness much larger than the critical value and is asymmetric. The effects in wells where a topological insulator can exist have not yet been studied except for in indirect experiments. It is well known that weak antilocalization corrections to the conductivity of systems are characteristic transport phenomena that make it possible to obtain almost direct information on the effects of the spin-orbit interaction, because this interaction results in spin relaxation, which changes the sign of the interference localization correction to the conductivity.

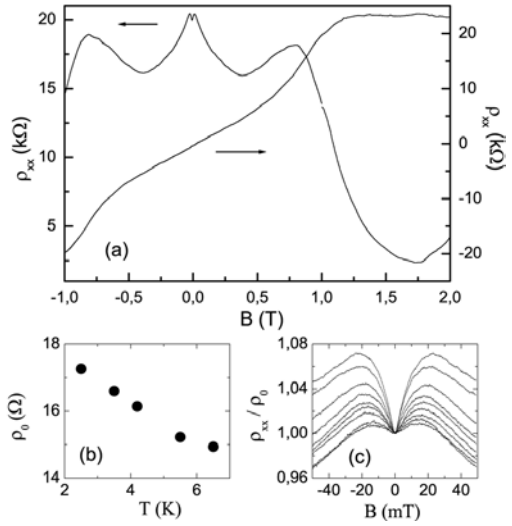


FIG. 37. *(a) The magnetic field dependence $\rho_{xx}(B)$ and $\rho_{xy}(B)$ at $T = 3$ K, (b) the temperature dependence of the resistivity $\rho_0$ at $B = 0$, and (c) the magnetic field dependence $\rho_{xx}(B)/\rho_0$ near $B = 0$ at $T =$ (from top to bottom) 1.4, 1.55, 2, 2.5, 3, 3.5, 4.2, 5.5, and 6.5 K. The results are given for the sample with a well thickness of* 8.3 *nm.*

This interaction is responsible for the anomalous magnetoresistance of two-dimensional electron systems, which is currently the most direct source of information on the spin-orbit interaction in these systems. In this work, this anomalous magnetoresistance is studied in HgTe quantum wells whose thicknesses are slightly smaller or slightly larger than the critical value $d_c =$ 6.3 nm at which the normal band quantum well is transformed into the quantum well with an inverted spectrum.The anomalous magnetoresistance in HgTe quantum wells with thicknesses of 5.8 and 8.3 nm, i.e., near the transition from the direct band spectrum to an inverted spectrum, has been observed and analyzed (figures 37 and 38). It has been shown that the observed anomalous magnetoresistance in wells with an inverted spectrum is well described by the theory developed by Iordanskii *et al.* [JETP Lett. **60**, 206 (1994)] and Knap *et al.* [Phys. Rev. B **53**, 3912 (1996)]. A detailed comparison of the experimental data with the theory indicates the presence of only the cubic term in the spin splitting of the electronic spectrum in wider quantum wells with an inverted spectrum. The applicability conditions of the mentioned theory are found not to be satisfied in narrower quantum wells with a normal (non-inverted) spectrum and, for this reason, the comparison with the theory has been impossible. The results indicate the existence of a strong spin-orbit interaction in symmetric HgTe quantum wells near the topological transition.

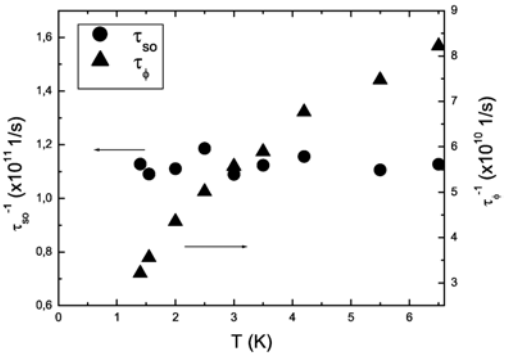


FIG. 38. *Temperature dependence (circles) $\tau_{so}(T)$ and (triangles) $\tau_\phi(T)$ obtained from the comparison of the theory with the experimental data for the sample with a well thickness of* 8.3 *nm.*

***J. C. Portal,***
***E. B. Olshanetsky, Z. D. Kvon (Institute of Semiconductor Physics, RAS, Novosibirsk, Russia)***

# Microwave-induced zero-resistance states in electronic bilayers

In the present work, we show first experimental and theoretical results on microwave-induced (MW) zero-resistance states (ZRS) in a two-dimensional electron system (2DES) with two populated 2D subbands and demonstrate that this phenomenon is not limited to single-subband systems.

We investigate GaAs wide quantum wells (WQWs) with a well width of 45 nm, which have high mobility ($\mu = 1.9 \times 10^6$ cm$^2$/V s) and a density of $n_s \simeq 9.1 \times 10^{11}$ cm$^{-2}$. Owing to charge redistribution, our WQW forms a bilayer configuration when two wells near the interface are separated by an electrostatic potential barrier and two subbands appear as a result of tunnel hybridization of 2D electron states. The corresponding symmetric (S) and asymmetric (AS) wave functions are sketched in the inset to figure 39. The two subbands are separated by an energy $\Delta_{12} = 1.4$ meV.

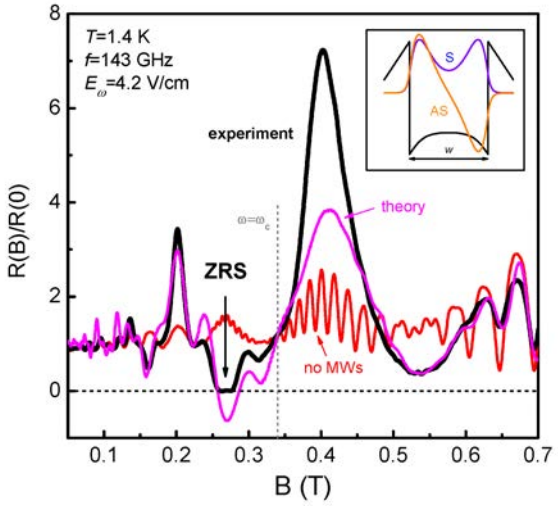


FIG. 39. *Observation of ZRS in a bilayer electron system formed by a wide quantum well: dark magnetoresistance (no MWs) and under a MW excitation of 143 GHz (experiment). The inverted MIS oscillation at B=0.27 T evolves in a ZRS. The theoretical calculation (theory) reproduces our experimental finding using an electric field of $E_\omega$=4.2 V/cm.*

The phenomenon of ZRS, which evolve in high-quality 2DES from microwave induced resistance oscillations (MIROs) with increasing MW intensity [Zudov *et al.*, Phys. Rev. Lett. **90**, 046807 (2003)] has also attracted theoretical interest. Two mechanisms of photoresistance, "inelastic" and "displacement" ones, have been proposed and widely discussed in literature. At low temperature and moderate microwave power, the inelastic mechanism is the dominant contribution due to a large value of the inelastic relaxation time $\tau_{in} \propto T^{-2}$. Both mechanisms can also lead to negative dissipative resistivity in the minima of MIROs with increasing MW power. A direct consequence of negative resistivity is the instability of homogeneous current flow and breaking of the sample into a pattern of domains. Until now, all studies of ZRS were carried out in high-quality single-subband systems.

In our experiment, which has been performed in a cryostat with a variable temperature insert using Faraday confirmation for MW experiments, we first confirm the presence of two occupied subbands by the observation of magneto-intersubband (MIS) oscillations (figure 39 - no MWs). Under a MW irradiation of 143 GHz, we find a deep minimum at $B$=0.27 T at a temperature of $T = 1.4$ K (figure 39 - experiment). In contrast to single-subband systems, the ZRS develops from the strongest minimum of combined MIS-MIRO oscillations, marked with an arrow in figure 39. The correlation between the position of ZRS and MW frequency, as well as power and temperature dependence is demonstrated in Ref. [Wiedmann *et al.*, Phys. Rev. Lett. **105**, 026804 (2010)].

Calculations of magnetoresistance exposed to MW iradiation are based on both inelastic and displacement mechanism contributions and we found that the inelastic mechanism dominates under conditions of our experiment. The effective electron temperature depending on MW power, frequency, and magnetic field has been determined by assuming energy relaxation of electrons due to their interaction with acoustic phonons. Our calculation (figure 39 - theory) reproduces all experimentally observed features, in particular the negative resistivity around $B$=0.27 T. The electric field strength, $E_\omega$=4.2 V/cm, is found by fitting experimental traces to theory.

To summarize, we have demonstrated, both experimentally and theoretically, that the phenomenon of ZRS is not limited to single-subband systems. The observed zero-resistance states are distinct from ZRS in single-layer systems and develop for inverted magneto-intersubband oscillations. We have also underlined the applicability of microscopic bulk mechanisms for the occurrence of ZRS which fully explain our experimental observations. Furthermore, additional intersubband scattering giving rise to MIS oscillations is no hindrance for this intriguing phenomenon.
This opens an opportunity for experimental and theoretical studies of ZRS in quasi-3D systems.

***S. Wiedmann, J. C. Portal***
***G. M. Gusev (Instituto de Física da Universidade de São Paulo, SP, Brazil), O. E. Raichev (Institute of Semiconductor Physics, NAS of Ukraine, Kiev, Ukraine), A. K. Bakarov (Institute of Semiconductor Physics, Novosibirsk, Russia)***

# Thermally-activated intersubband scattering in wide quantum wells

Magnetoresistance oscillations caused by Landau quantization provide important information about fundamental properties of electron system in solids. The most important examples are Shubnikov-de Haas (SdH) oscillations and magneto-intersubband (MIS) oscillations observed in two-dimensional (2D) electron systems with two or more populated 2D subbands, which are realized in single, double, and triple quantum wells [Wiedmann *et al.*, Phys. Rev. B **80**, 245306 (2009)].

In the present work we have studied magnetoresistance in GaAs wide quantum wells (WQWs) with a well width of 45 nm which have high mobility ($\mu = 1.9 \times 10^6$ cm$^2$/V s) and a density of $n_s \simeq 9.2 \times 10^{11}$ cm$^{-2}$. Such a WQW forms a bilayer electron system. In figure 40 we show magnetoresistance for different temperatures from 4.2 to 25 K. The bilayer nature of our system is confirmed by MIS oscillations with a subband splitting $\Delta$=1.4 meV. SdH oscillations are visible at 4.2 K for $B > 0.6$ T, however, they disappear with increasing temperature.

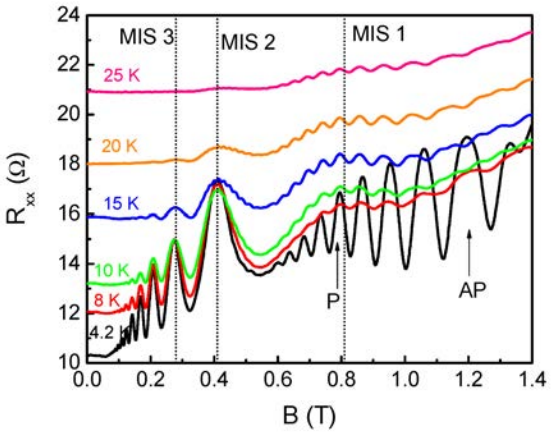


FIG. 40. *Longitudinal resistance $R_{xx}$ in a WQW at different temperatures from 4.2 to 25 K. Three MIS oscillations (marked by 1 to 3) are observed. As temperature increases, the SdH oscillations are replaced by a new kind of oscillations which have a smaller period and survive at high temperatures.*

For $B > 0.6$ T, SdH oscillations are superimposed on the first MIS peak whose maximum is placed at $B = 0.8$ T corresponding to the alignment condition $\hbar\omega_c = \Delta_{12}$. Another oscillating pattern is developed at $T > 10$ K and persists even at $T > 25$ K, when large-period MIS oscillations are strongly damped. The period of these high-temperature oscillations is close to the SdH oscillation period but does not coincide with it, *e.g.* the SdH peak at $B = 0.8$ T appears to be in phase with the high-temperature oscillations (arrow $P$ in figure 40), while the SdH peak at $B = 1.2$ T stays in antiphase. As it concerns temperature dependence of the amplitudes (peak-to-peak values) for magnetoresistance, see figure 40, those oscillations are superimposed on the maxima of the first and second large-period MIS peaks, and, for comparison, dependence for the amplitude of the second MIS peak is shown. While large-period MIS oscillations are monotonically suppressed by temperature, the small-period oscillations are characterized by a non-monotonic dependence with a maximum around $10 - 15$ K and a slower decrease with temperature.

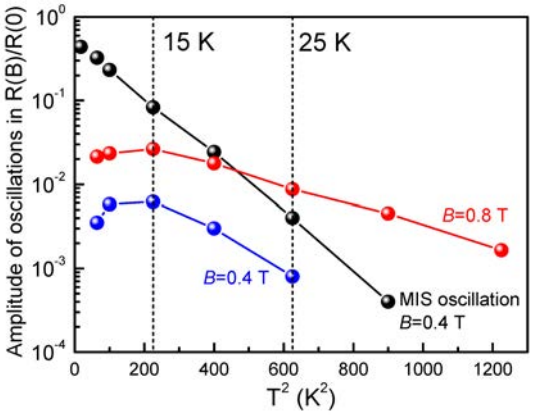


FIG. 41. *Temperature dependence of the amplitudes of small-period and large-period MIS oscillations. The solid lines are a guide to the eye.*

We attribute this observation to a thermal population of the third subband which is placed slightly above the Fermi energy ($\varepsilon_3 > \varepsilon_F$) being populated at higher $T$ and attribute the small-period oscillations to MIS oscillations owing to electron transitions between this subband and the subbands 1 and 2. The periodicity in this case is determined by the large splitting energies $\Delta_{13} = \varepsilon_3 - \varepsilon_1$ and $\Delta_{23} = \varepsilon_3 - \varepsilon_2$. We have shown in theoretical calculations that the assumption of scattering between three subbands reasonably explains our experimental observation. In addition, the widely discussed $T^2$ scaling of the broadening energy cannot be applied to the case of an almost empty subband. A detailed description of experimental results and theoretical calculations can be found in Ref. [Wiedmann *et al.*, Phys. Rev. B **82**, 165333 (2010)].

***S. Wiedmann, J. C. Portal***
***G. M. Gusev (Instituto de Física da Universidade de São Paulo, SP, Brazil), O. E. Raichev (Institute of Semiconductor Physics, NAS of Ukraine, Kiev, Ukraine), A. K. Bakarov (Institute of Semiconductor Physics, Novosibirsk, Russia)***

# Electron and hole cyclotron mass dependence in a two-dimensional semi-metal

Recently a 2D semi-metal was discovered in undoped HgTe quantum wells (QW) with an inverse band structure and (013) surface orientation. It was established that the energy spectrum of this system is determined by the overlap (about 10 meV) of electron energy dispersion curve with a minimum in the center of the Brillouin zone and the valence band with two maxima along [0-31] direction [Kvon, *et al.* JETP Lett. **87**, 502 (2008)]. A simultaneous existence of 2D electrons and holes with mobilities $\mu_n = (3-6)\times 10^5\,\mathrm{cm}^2/\mathrm{V{\cdot}s}$ for electrons and $\mu_p = (3-10)\times 10^4\,\mathrm{cm}^2/\mathrm{V{\cdot}s}$ for holes has been demonstrated in such QWs. Applying voltage to an electrostatic top gate allows the system properties to be studied at an almost arbitrary ratio of the two-dimensional electron and hole densities in the quantum well (see figure 42(a)). Here we present the results of an experimental study of electrons and holes cyclotron resonance in such a system.

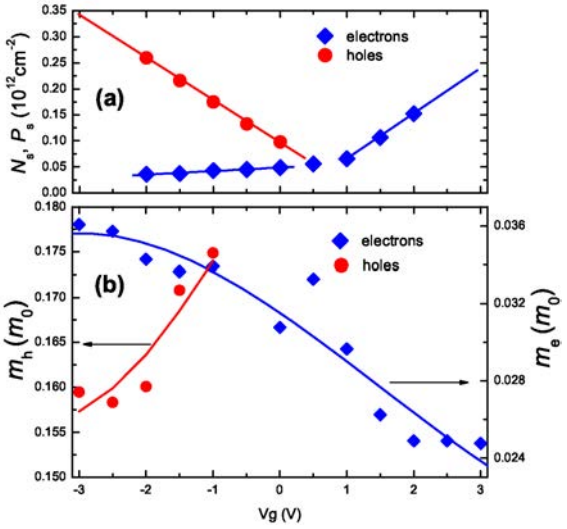


FIG. 42. *(a) Electrons (red) and holes (blue) densities versus gate voltage obtained from fitting of transport measurements at helium temperatures by standard model with two types of carriers. (b) Cyclotron effective mass dependencies for electrons and holes versus gate voltage.*

In the present work CR was studied by means of photoconductivity measurements. The experimental samples were Hall bars fabricated on the basis of undoped (013) 20 nm $Cd_xHg_{1-x}Te/HgTe/Cd_xHg_{1-x}Te$ QWs with $x = 0.75$ covered by semi-transparent top gate. These Hall bars were illuminated by microwave radiation in the frequency range 35 GHz - 170 GHz. Photoconductivity $G_{ph}$ was measured using double modulation technique in magnetic field up 0.3 T for electrons and up to 2 T for holes at temperatures from 1.4 K (mainly for electrons) to 6 K (mainly for holes). Cyclotron resonance photoconductivity in the system arises because of the heating of 2D electrons or holes caused by the resonance increase in the absorption of microwave radiation when the photon energy is equal to the distance between the Landau levels. The photoconductivity versus magnetic field dependence $G_{ph}(B)$ are curves with peak or peaks whose position depends on the photon energy and the type of carries. The sign of the resonance peaks depends on the temperature coefficient of resistance (TCR) which, in its turn, also depends both on the magnetic field and gate voltage. Frequency dependence of the position of CR peaks is determined by formula $B_{peak} = \sqrt{\omega_{pl}^2 + (2\pi m/e)^2 \times f_{MW}^2}$, where $\omega_{pl}$ corresponds to the plasmon frequency shift. As it shown in figure 43 in our system plasmon frequency is quite small for hole CR and virtually equal to zero for electron CR, most likely because of a very high dielectric constant in HgTe QWs.

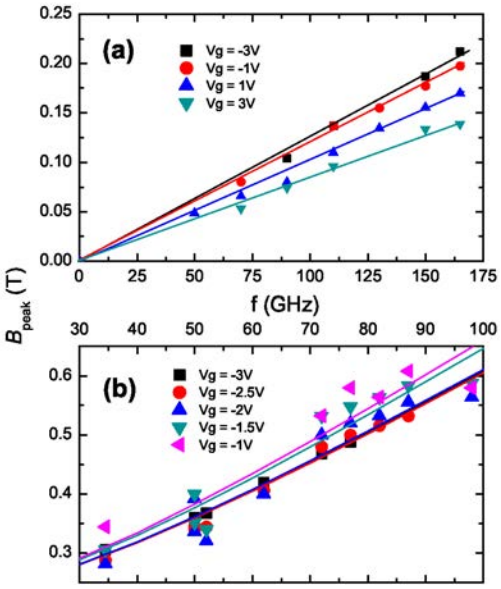


FIG. 43. *Cyclotron peaks position for electrons (a) and holes (b) for different gate voltages $V_g$ and microwave frequencies $f$.*

Electron and hole cyclotron mass dependencies on gate voltage are presented in figure 42(b). The electron effective mass decreases from $0.036m_0$ at negative gate voltages and low electron densities down to $0.024m_0$ at positive gate voltage and high electrons densities. The hole cyclotron mass lies in the range $0.16 - 0.175m_0$ but the low accuracy of this method in the case of the holes doesn't allow to make definite conclusions about this dependence.

***J. C. Portal***
***D. A. Kozlov, Z. D. Kvon (Institute of Semiconductor Physics, RAS, Novosibirsk, Russia)***

# Dipolar spin waves of magnetic superlattices

We investigate the high frequency dynamics of dysprosium and cobalt gratings fabricated at the surface of a GaAs/$Al_{0.33}Ga_{0.67}As$ heterojunction [Nogaret *et al.*, J.Phys.Cond.Mat. **22**, 253201 (2010)]. We detect the collective and localized spin wave modes of the grating by measuring the photovoltage and the photoresistance induced in the two-dimensional electron gas. The magnetic excitations couple to the 2DEG through their stray magnetic field. This allows us to perform a spectroscopy of dipolar-exchange spin waves as a function of microwave power, temperature, the tilt angle of the applied magnetic field, and by varying the structural and material parameters to change the strength of dipolar interactions.

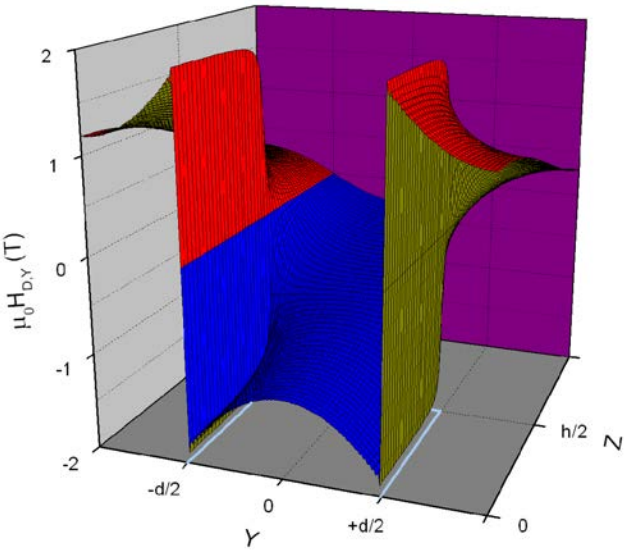


FIG. 44. *Spatial variation of the in-plane magnetic field inside a dysprosium stripe of width d=210nm and height h=80nm. There two spin wave magnetic wells near the pole surfaces at* $\pm d/2$.

The data reveal two types of spin waves. *Dipolar surface spin waves* manifest through a series of sharp resonances at lower magnetic field [J.Jorzick *et al.*, Phys.Rev.Lett. **88**, 047204 (2010)]. These waves are confined in the dips of the demagnetization field which create two spin wave magnetic wells near the pole surfaces - see figure 44. Dipolar surface spin waves are localized and interact very little with neighbouring stripes as demonstrated by the narrow resonances in figure 45 (blue circles). We calculate the eigenfrequencies of their quantized modes and obtain a qualitative explanation of the low field resonances. The fit yields a value of the exchange stiffness constant of dysprosium, $A = 1.5 \times 10^{-12}$J.m$^{-1}$. The second type of spin waves are *dipolar magnetization waves* which propagate across the grating through the magnetostatic interactions between stripes. These spin waves form a frequency band proportional to the strength of the dipolar interaction (up to 1.5 T). These are experimentally demonstrated through a huge broadening of the ferromagnetic resonance which we find to increase proportionally to the dipolar interactions between stripes when the superlattice period is reduced from 400 nm to 300 nm. The onset of the FMR corresponds to the excitation of dipolar spin waves of infinite wavelength (red dots). The FMR cutoff corresponds to spin waves at the edge of the Brillouin zone (black dots). We derive an analytical expression of their dispersion curve and obtain a good fit of the ferromagnetic resonance broadening from first principles.

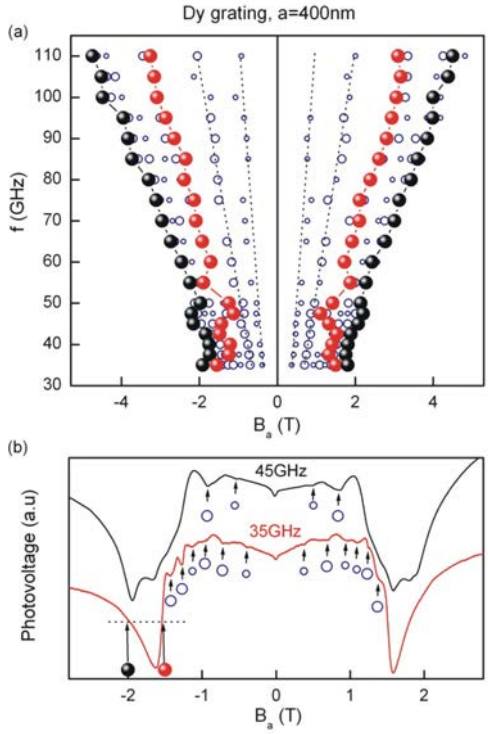


FIG. 45. *(a) Frequency dependence of microwave resonances in the photovoltage of an array of magnetic stripes. The fan diagram shows the FMR onset (red dots) and the FMR cut-off (black dots) that correspond to demagnetization waves of momentum* $q = 0$ *and* $q = \pi/a$ *where* $a$ *is the period of the 1D superlattice. The photovoltage dips at low field (blue circles) are resonances with dipolar surface spin waves quantized by the triangular magnetic wells near the pole surfaces. (b) Details of the fine resonant structure at* 35 *GHz and* 45 *GHz.*

Our experiments show that photovoltage measurements in hybrid semiconductor-ferromagnetic structures provide a sensitive and non-invasive tool for probing the spin waves of small magnets ($10 - 500$ nm).

***S. Wiedmann, J.C. Portal***
***A. Nogaret (University of Bath, UK), H. E. Beere, D. A. Ritchie (University of Cambridge, UK)***

# Semiconductors and Nanostructures

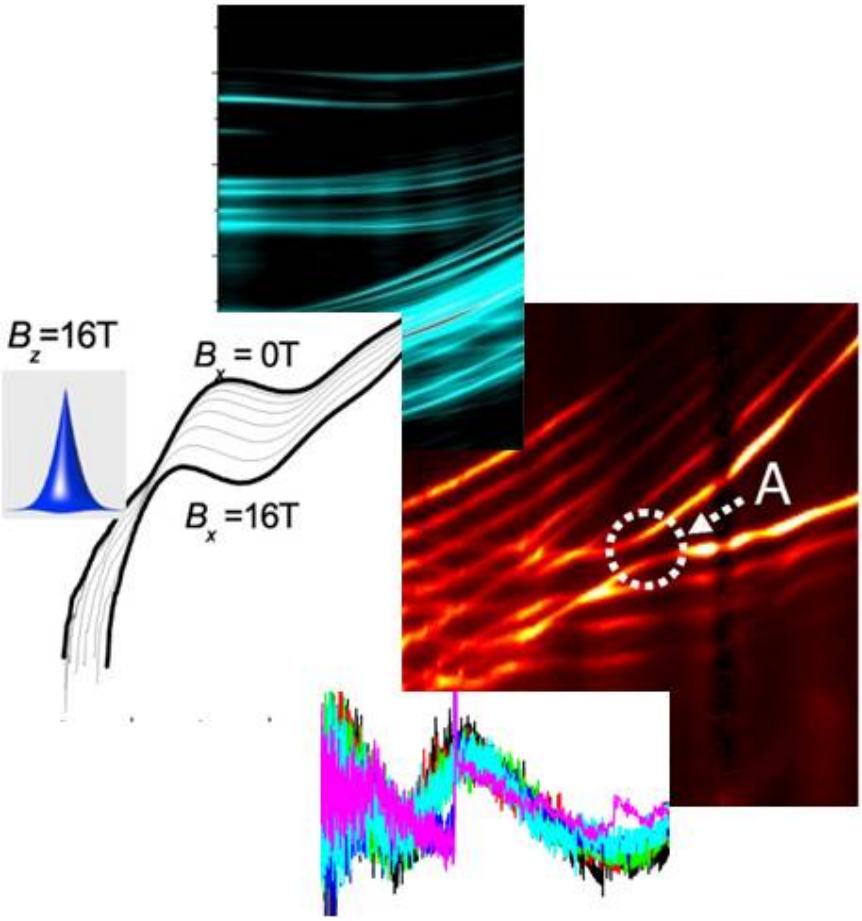

# Electrical transport phenomena in short period InAs/GaSb superlattices

The short period InAs/GaSb type-II superlattices (SL) are now considered as an interesting material system for high performance infrared (IR) p-i-n photodiodes (mid-wavelength infrared detectors) suitable for thermal imaging camera. To enhance the performances and/or temperature operation, the improvement of device technology as well as a better knowledge on material properties is still needed. In particular a better understanding of electrical transport in this material is a key point to improve the photodiodes performances. InAs/GaSb SL exhibits a reproducible change of conductivity type as a function of temperature. The SL is p-type at low temperature ($T < 150$ K) while it is n-type at room temperature. Additionally, due to the band gap structure of GaSb material the transfer of electrons from the $\Gamma$ into $L$-conduction miniband should be considered.

The preliminary experimental results of resistivity and Hall Effect measurements as a function of temperature and hydrostatic pressure suggest that in the whole investigated temperature range ($77 - 300$ K) the presence of several species of carrier (at least heavy and light holes and two types of electrons) in InAs/GaSb SL must to be taken into account in conduction process analysis. One of the methods used to detect the expected multi-carrier conduction is the measurement of the resistivity tensor as a function of magnetic field to perform a quantitative mobility spectrum analysis. Such an analysis should in particular give the information about the eventual contribution originating from the heavy electrons.

We have measured the resistivity $\rho$ and Hall resistance $\rho_H$ in the van der Pauw configuration as a function of magnetic field (step by step for both polarities of magnetic field up to 28 T) for temperatures between 284 and 360 K. The experiments have been carried out on two types of InAs/GaSb SL quantum structures: one grown on GaAs semi-insulating substrate and another grown on n-type GaSb substrate which was afterwards removed with an appropriate technological process. In such a way, for the second type of samples the unambiguous determination of carrier's properties in SL materials was possible without any parallel conduction in the substrate.

The magnetic field dependence of the resistivity and the Hall resistance are presented in Figure 46. The large magneto-resistance, together with the non linear variation of Hall resistance, indicate the presence of multi-carrier conduction in the system. To extract the mobility of all carriers present in the material the quantitative mobility spectrum analysis has been performed. This algorithm converts experimentally measured resistivity and Hall coefficient data into carrier mobility spectra. The main advantage of this algorithm is that it requires no *a priori* assumptions regarding the number and nature of carriers present in the material. The results of analysis are presented in Figure 47. The appearance of four peaks in the mobility spectrum can be considered as a signature of four types of carriers present in the sample; light and heavy holes and two species of electrons from the the $\Gamma$ and $L$ minima of the conduction band.

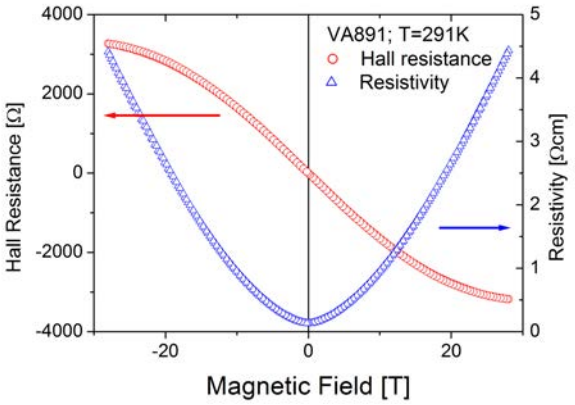


FIG. 46. *Magnetic field dependence of a resistivity and Hall resistance at 291 K for a short period InAs/GaSb type-II superlattice.*

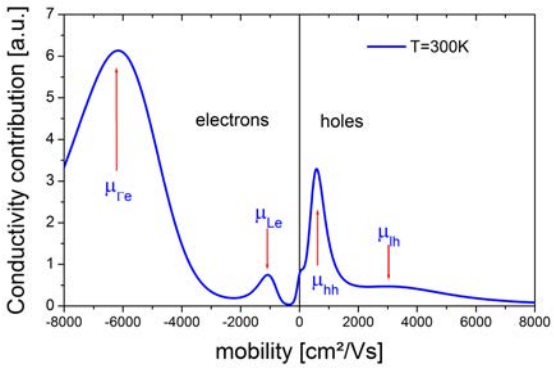


FIG. 47. *The mobility spectrum analysis for a short period InAs/GaSb type-II superlattice indicating the presence of four type of carriers at 300 K.*

***D.K. Maude***
***L. Konczewicz, S. Contreras (Groupe d'Etude des Semi-conducteurs, Université de Montpellier II, France), Ph. Christol, J-B. Rodriguez and C. Cervera (Institut d'Electronique du Sud, Université de Montpellier II, France)***

# Manipulating and imaging the shape of an electronic wave function

The possibility of fine-tuning the electronic wave function in a quantum system is of fundamental interest and has potential for applications in advanced technologies. This field is still in its infancy and requires the development of sensitive methods to image electronic wave functions. Although there have been successful examples of wave function imaging, the effect of an external force on the shape of a wave function has received less attention. Here, we use magneto-tunnelling spectroscopy to probe in situ the spatial compression of a quantum state induced by an applied magnetic field [Patane *et al.*, Phys. Rev. Lett. **105**, 236804 (2010)].

Our study focuses on the electronic wave function of a Si-donor atom in GaAs. In GaAs, the donor eigenstates are well described by the hydrogenic effective mass approximation with an effective Bohr radius $a = 10.1$ nm. In our magneto-tunnelling spectroscopy experiment, we use magnetic fields of up to $B = 22$ T, which correspond to strengths of up to $10^6$ T when scaled to the hydrogen problem. We study the current due to electron tunneling through the ground state of Si-donors within a GaAs quantum well (QW) in a magnetic field tilted at an angle to the QW plane. The component of $B$ parallel to the direction of current ($B_z$) provides us with a means of increasing the donor binding energy and hence of compressing the donor wave function in the QW plane. By measuring the current as a function of the perpendicular component of the magnetic field ($B_x$), we probe how the magneto-compression affects the spatial form of the donor wave function.

Figure 48(a) shows the $B_x$-dependence of the donor resonance peak, $D$, in the current-voltage $I(V)$ curves at various values of $B_z$. It can be seen that the $B_x$-dependence of the tunnel current becomes weaker at high $B_z$ and changes from approximately polynomial at $B_z = 0$ to Gaussian at high $B_z$, see figure 48(b). Interestingly, the semi-logarithmic plots of both the measured and calculated data reveal that; (i) at $B_z$ =0 and low $B_z$ (e.g. 4T) there is a change of curvature in the $I(B_x)$ curve at intermediate values of $B_x$ and (ii) the curvature at high $B_x$ changes from positive at low $B_z$ to negative at high $B_z$. This behaviour reflects the magneto-compression of the donor state and it is reproduced accurately by our magneto-tunneling model if we take a zero-field donor size $a = 8.5$ nm. The donor wave function exhibits only very small changes when $B_z$ is increased up to $\sim 4$ T. In this regime, the magnetic field confinement potential is weak compared to the Coulomb potential and the wave function retains its hydrogenic-like form. In contrast, when $B_z$ exceeds $\sim 10$ T, the magneto-compression becomes significant and the tail of the wave function decays as a Gaussian, thus reflecting the strong parabolic confinement induced by $B_z$ .

Our data demonstrate that magneto-tunnelling spectroscopy is a highly sensitive probe of the change in the shape of the electronic wave function due to an externally applied perturbation. By using appropriately designed tunnel diodes, magneto-tunnelling spectroscopy could be exploited to probe the effect of other types of applied perturbations on the eigenfunctions of different types of nanostructures, thus providing new insights into the manipulation and imaging of quantum systems.

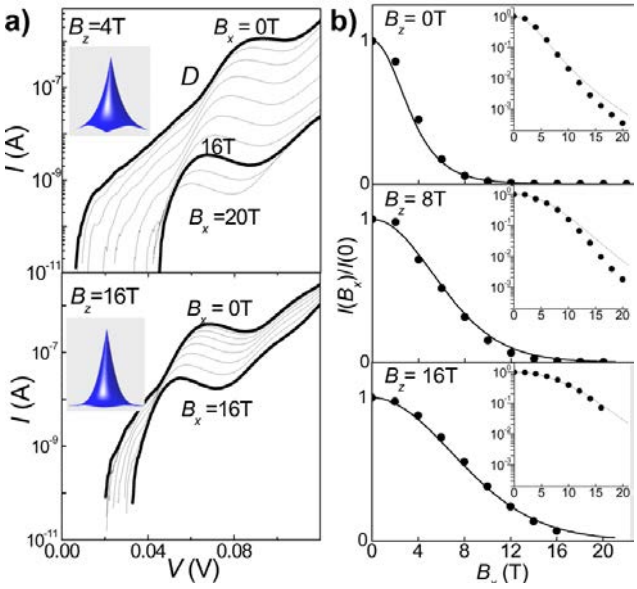


FIG. 48. *(a) $B_x$-dependence of the donor resonance peak, $D$, in $I(V)$ at various values of $B_z$. The insets illustrate the magneto-compression of the donor wave function at low and high $B_z$. (b) $B_x$-dependence of the peak current height of resonance $D$ at fixed values of $B_z$. Dots correspond to the experimental data. Continuous lines are the calculated curves. The insets show data and curves using a logarithmic scale for the vertical axis.*

***D. K. Maude***
***A. Patane, O. Makarovsky, L. Eaves, L. Dickinson (School of Physics and Astronomy, University of Nottingham, UK), N. Mori (Dept. of Electronic Engineering, University of Osaka, Japan), M. L. Zambrano, J. C. Arce (Departamento de Química, Universidad del Valle, Cali, Colombia)***

# Magnetotransport in nanocomposite $CdGeAs_2$:MnAs semiconductor

Magnetotransport properties of ferromagnetic semiconductors can be effectively studied with the use of high magnetic fields revealing a strong interplay between magnetic and electrical properties of these materials. Here we present preliminary result of magnetoresistance and Hall effect studies performed in several chalcopyrite II-IV-$V_2$ group $Cd_{1-x}Mn_xGeAs_2$ crystals with average Mn content changing between 2.1 and 5.1 at.%. All the studied samples show high temperature ferromagnetism with the Curie temperatures higher then 300 K. We prove by means of high resolution x-ray diffraction, scanning electron microscopy, and nuclear magnetic resonance techniques that ferromagnetic ordering in this alloy is due to a short range magnetic interactions, resulting from the presence of MnAs clusters.

It is well known that the presence of magnetic inclusions result in an appearance of new class of magnetotransport effects in nanocomposite materials. Substantial changes of basic transport properties were observed in the studied crystals, *i.e.*, an increase of electron concentrations (determined at $T \approx 300$ K) between $1\times10^{18} \le n \le 2\times10^{20}$ cm$^{-3}$ and carrier mobility between $0.3 \le \mu \le 233$ cm$^2$(V·s), when changing the average Mn content from 2.1 up to 5.1 at.%. A strong influence of MnAs clusters seems to be responsible for large changes in magnetotransport properties. Furthermore, the presence of cusp in the temperature

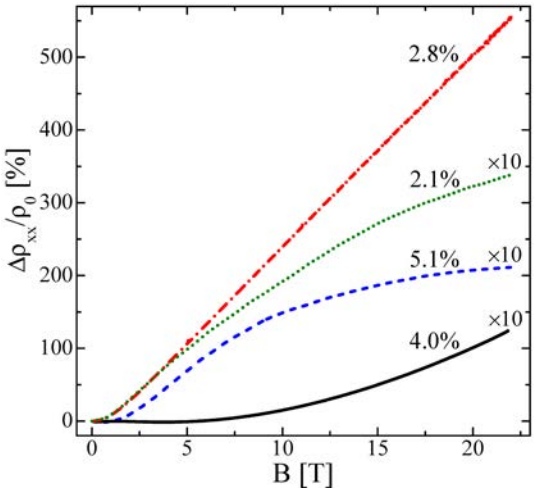


FIG. 49. *Magnetoresistance curves obtained at $T \approx 1.4$ K for selected $Cd_{1-x}Mn_xGeAs_2$ crystals with different amount of Mn (see labels).*

dependence of resistivity was detected near $T_C$ resulting from increase of scattering on magnetization fluctuations in a material. Moreover, the addition of Mn to the crystals changes the conductivity mechanism in the alloy from thermally activated ($x < 0.03$) into metallic ($x > 0.03$).

A significant positive magnetoresistance (see figure 49) was detected in all the studied crystals reaching maximum amplitudes of about 550% at $T \approx 1.5$ K, $B = 22$ T for the sample with 2.8 at.% of Mn. There seems to be no direct correlation between the magnetic properties of the crystals and the amplitude or the shape of the observed magnetoresistance effects. On the other hand the amplitude of the magnetoresistance depends on the Hall carrier mobility of the crystals. The observed magnetoresistance effects can be well explained with the use of effective medium approximation method in which we assume the two phase media with different relative mobilities in each of the phases.

The magnetic field dependence of the Hall effect measured for the studied $Cd_{1-x}Mn_xGeAs_2$ crystals (see figure 50) shows to a good approximation almost linear behavior. The absence of the anomalous Hall effect

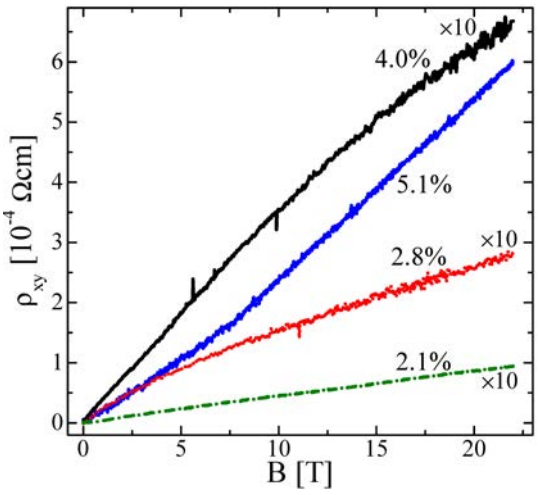


FIG. 50. *The magnetic field dependence of the Hall resistivity $\rho_{xy}$ obtained at $T \approx 1.4$ K for selected $Cd_{1-x}Mn_xGeAs_2$ crystals with different amount of Mn (see labels).*

in the studied ferromagnet indicate that the asymmetric scattering leading to this anomaly is not the only element needed for it occurrence.

The magnetoresistance effects reported here are significantly different from those observed in $Zn_{1-x}Mn_xGeAs_2$ nanocomposite (negative effect with amplitude of about -50%) [Kilanski *et al.*, J. Appl. Phys. **108**, 073925 (2010)] indicating that this class of compounds shows great promise with respect to the ability to tune their magnetotransport properties.

***D. K. Maude***
***L. Kilanski, W. Dobrowolski (Institute of Physics, Polish Academy of Sciences, Warsaw, Poland),***
***I. V. Fedorchenko, S. F. Marenkin (Kurnakov Institute of General and Inorganic Chemistry, RAS, Moscow, Russia)***

# Systematic study of Mn-doping on electronic properties of (GaMnAs)

The use of ferromagnetic semiconductors (GaMn)As opens a number of new ways for spintronic devices. However in these materials wide-spread practical use is limited by relative small Curie temperature $T_c$ (well below the room temperature). Large theoretical and experimental efforts have been devoted to an increase of $T_c$. We have performed a systematic study of the influence of Mn doping not only on the Curie temperature but also on the hole density and mobility determined from transport measurement.

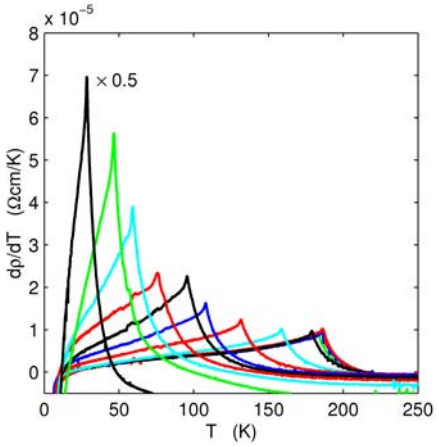


FIG. 51. *dρ/dT versus temperature to determine the Curie temperature for a series of optimized (GaMn)As samples spanning the doping range* $\simeq 1.5 - 13\%$.

Samples have been grown on semi-insulating GaAs substrate by MBE. The optimization of the epilayers in the series, which is performed individually for each nominal doping, minimizes the uncertainties in the experimental sample parameters and produces high quality materials which are as close as possible to the uniform uncompensated (Ga,Mn)As mixed crystals. Film thickness and post-growth annealing conditions are important factors determining the quality of resulting materials. For a given nominal doping, the highest attainable Curie temperature is reached only in thin films, typically thinner that approximately 50 nm. Our systematic studies therefore focus on films with thickness below 50 nm and the most extensive series of carefully optimized materials was prepared using 20 nm thick epilayers where higher uniformity can be reached as well.

The Curie temperatures have been determined from the position of the $d\rho/dT$ singularities. In figure 51 we show the $d\rho/dT$ measurements for samples spanning the doping range from 1.5 to 13% which illustrate the high quality of all epilayers within the series. For the measurement of Hall effect the samples were lithographically patterned into Hall bars of 60$\mu$m width. Measured Hall resistivities consist of an ordinary Hall component and an anomalous one. For the determination of hole densities the second component should saturate and high-field slope of the signal must be used for estimation of the hole concentration. The procedure is accurate at high doping levels but the still non-saturated magnetoresistance in samples doped below 5% leads to an overestimation of the hole density in this lower doped materials.

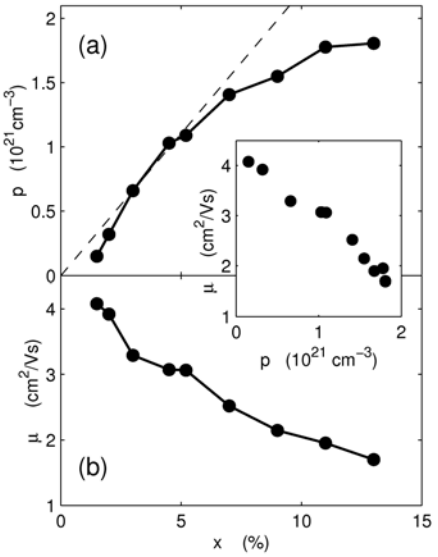


FIG. 52. *Hole concentration and mobility as function of Mn composition for a series of optimized (GaMn)As samples.*

We also emphasize that, apart from the common experimental scatter and from the correction due to the non zero magnetoresistance and due to the anomalous Hall effect, the carrier density can in principle be inferred only approximately from the slope of the Hall curve in a multi-band, spin-orbit coupled exchange-split system such as the (GaMn)As. Due to these uncertainties we can only make qualitative or at most semi-quantitative conclusions based on the measured Hall effect densities. Among these conclusions is the confirmed overall trend of increasing hole concentration with nominal doping in the optimize materials as shown in figure 52.

***D. K. Maude, M. Orlita***
***P. Vasek, P. Svoboda, L. Smrcka, V. Novak, Z. Vyborny, V. Jurka (Institute of Physics ASCR, v.v.i., Prague, Czech Rep***

# Systematic study of Mn-doping trends in optical properties of (GaMn)As

In the insulator non-magnetic regime ($x_{\mathrm{Mn}} \ll 1$ %), the (GaMn)As is readily described by localized Fermi level states residing inside a narrow impurity band separated from the valence band by an energy gap of magnitude close to the isolated MnGa impurity binding energy. Recently, a debate has been stirred by proposals, based in particular on optical spectroscopy measurements [Burch *et al.*, J. Magn. Magn. Mater. **320**, 3207 (2008)], that the narrow impurity band also persists in highly-doped (GaMn)As with metallic conduction.

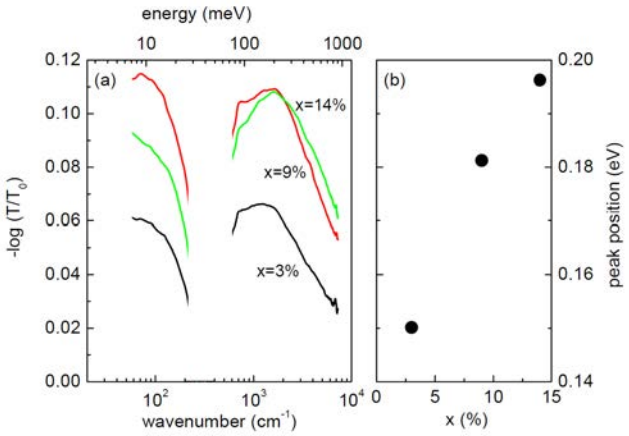


FIG. 53. *Example of low-temperature transmission measurements on (GaMn)As samples with differing Mn doping. The transmission spectra $T$ are normalized by the transmission of the substrate $T_0$ and plotted as $-\log(T/T_0)$ to emphasize the existence of broad middle infrared absorption maximum. This minimum corresponds to intra-valence band absorption and exhibits prevailing blue shift with the increasing Mn concentration.*

Motivated by this controversy, we have performed optical spectroscopy measurements on a large set of systematically prepared (GaMn)As epilayers and showed that doping trends reported previously in a limited number of samples and regarded as the key experimental evidence of the impurity band nature of Fermi level states are not generic and not even prevailing in ferromagnetic (GaMn)As materials. The experimental foundation of the impurity band model based on these optical spectroscopies is therefore invalid which corroborates the absence of a microscopic theory foundation of this model. In contrast, the valence band model, which is readily established from microscopic theory and from numerous previous comparisons to experiments, accounts qualitatively or semi-quantitatively for the measured optical data.

This work, initiated at the Institute of Physics of the Academy of Sciences of the Czech Republic, involved a number of experimental techniques, which were applied to study the optical response of investigated samples from THz frequencies up to the visible range as well as (magneto-)transport properties. The decisive transmission measurements were performed in the middle infrared region at room as well as liquid helium temperatures and demonstrated the prevailing blue shift of the broad absorption band with the increasing Mn concentration (for $x_{\mathrm{Mn}} > 0.1$ %). Selected transmission curves taken at low temperatures are presented in figure 53, part of the obtained magneto-transport data is shown in figure 54. This behavior is consistent with the description of ferromagnetic (GaMn)As based on the microscopic valence band theory and directly excludes the impurity band scenario.

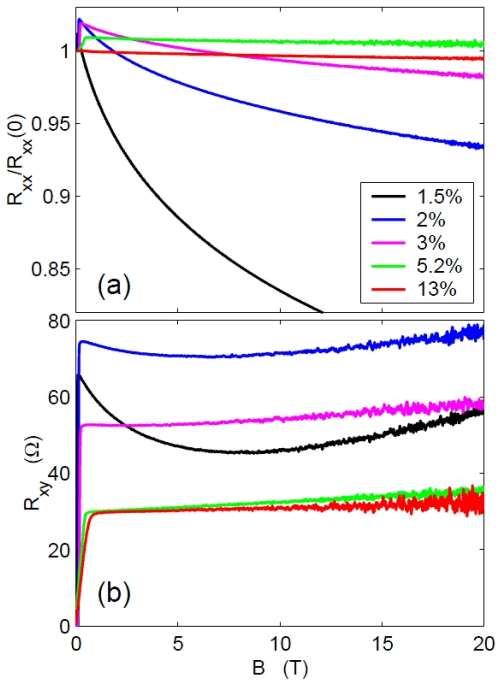


FIG. 54. *Example of longitudinal and Hall resistances measured on a set of (GaMn)As epilayers. The Hall signal includes a significant contribution of the anomalous Hall effect so that high magnetic fields are essential to correctly determine the hole concentration.*

For further information see [Jungwirth *et al.*, Phys. Rev. Lett. **105**, 227201 (2010)].

***M. Orlita***

***T. Jungwirth, P. Kužel, V. Novák, J. Mašek, C. Kadlec, K. Olejník, Z. Sobáň, P. Vašek, P. Svoboda, and Jairo Sinova (Institute of Physics ASCR,v.v.i.,Prague) P. Horodyská, N. Tesařová, P. Němec, J. Šubrt, P. Malý, I. Němec (Charles University, Prague, Czech Republic)***

# Negative magnetoresistance in polycrystalline $SnO_2$ thin films

The analysis of high-field magnetoresistance (MR) data, obtained on our samples of $SnO_2$ polycrystalline thin films, provides a possibility to justify the mechanism of electron-electron interaction (EEI) in disordered systems [Altshuler and Aronov, in Modern problems in condensed matter sciences **10**, Efros & Pollak ed., North Holland 1985] since the highly controllable degree of disorder in our samples, provides the possibility to tune the range of realization of quantum interference under applied magnetic fields (MF).

Usually, EEI in disordered structures is accompanied by weak localizations (WL) at low temperatures. We reported last year an evidence of 2D-WL in polycrystalline $SnO_2$ films [Dauzhenka, *et al.*, J. Low Temp. Phys. **159**, 2212 (2010)], the electron dephasing being due to EEI with small energy transfer. An explanation of experimental data, which is based on EEI and WL models, requires the existence of extended states at low temperatures.

The experimental MF dependences of magnetoresistance (MR), measured at different fixed temperatures, are negative over the full range of applied MF (not shown here). In the strongly localized regime, the total MR can be written as the sum of a positive component (PMR) which is induced by the MF shrinkage of the localized waves functions, and a negative part (NMR), related to the presence of the underbarrier scattering of hopping electrons by intermediate hopping sites and to interferences between different hopping trajectories (Nguyen, Spivak, Shkolvskii,- NSS-model).

Usually, for 3D semiconductors the NMR is suppressed with decrease in temperature after the crossover from Mott-type hopping to Efros-Shklovskii (ES) hopping over the states within the Coulomb gap. At the same time, the amplitude of NMR increases as the temperature decreases in the Mott-type hopping regime and decreases with the temperature in the ES hopping regime. Regarding our samples, the NMR amplitudes increases as the temperature decreases, thus excluding the ES hopping regime.

In figure 55 the MF dependences of magnetoconductance (MC) are presented in the wide range of MF. The solid lines are the extensions to high MF of the fitting curves obtained for the WL model only [Hikami *et al.*, Prog. Theor. Phys. **63**, 707 (1980)]. It is clear that these curves do not capture the behaviour of MC in high MF.

Figure 56 presents the same experimental data as in figure 55. The solid lines are now obtained by taking into account the EEI. The total MC is written as a sum of the Drude component, a term of WL and a term of EEI for 2D system [Altshuler *et al.*, in Quantum Theory of Solids, ed. by Lifshitz. Mir Publishers. Moscow 1982. pp. 130 - 237]. At vanishing field ($B < 1$ T) the fit follows the WL model. Reasonable values of obtained parameters (not shown here) and good fitting results suggest the samples we study are on the metallic side of the metal-insulator transition (MIT) and charge transport is of diffusive nature.

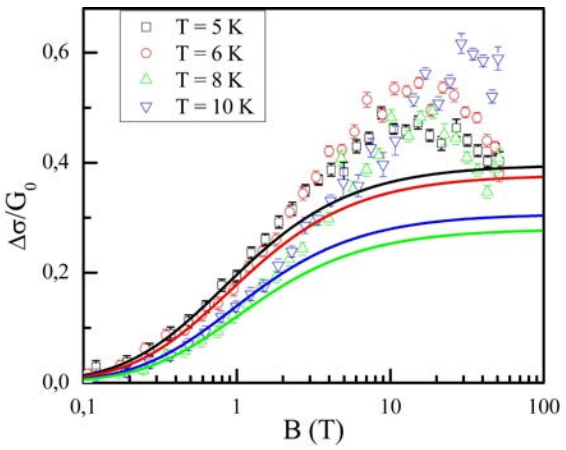


FIG. 55. *Magnetic field dependences of normalized magnetoconductance measured at different temperatures. Solid lines are the fitting results obtained by the weak localizations.*

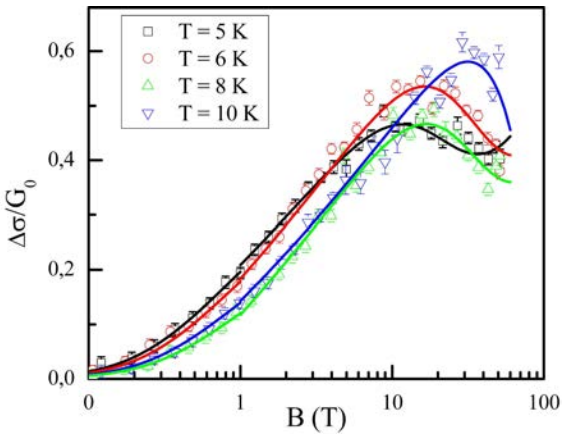


FIG. 56. *Magnetic field dependence of normalized magnetoconductance measured at different temperatures. Solid line are the fitting results obtained by the weak localizations ($B < 1$ Tesla) and the electron-electron interaction contributions ($B > 1$ Tesla).*

In conclusion, we confirm the recently reported existence of a disorder-induced MIT which involves quantum corrections to the conductivity due to EEI in not intentionally doped $SnO_2$ polycrystalline films which behave as a quasi-two dimensional electron gas.

***T.A. Dauzhenka, J. Galibert***
***V.K. Ksenevich (Belarus State Univ., Dept Phys. SC and Nanoelectronics, BY-Minsk), I.A. Bashmakov (Belarus State Univ., Research Institute of Physicochemical Problems, BY-Minsk)***

# Geometrically confined doping in $LaVO_3/SrVO_3$ superlattices

The physical properties of interfaces between two materials can differ strongly from the properties of the constituent materials as seen for the complex behaviour of polar discontinuous interfaces, showing a high mobility two dimensional (2D) electron gas at the interface of insulators, magnetic effects at the interface of non-magnetic materials or even superconductivity. While most of these effects were observed at the $SrTiO_3/LaAlO_3$ interface, another large group of systems showing polar discontinuous interface, *i.e.* $LaBO_3/SrBO_3$ (001) oriented interfaces with B being a transition metal, received much less interest, although the phase diagrams of the solid solutions can already be very complex, showing interesting effects as colossal magnetoresistance and charge ordering, metal-to-insulator transitions and complete spin-polarization of the conducting electrons. To study the effects present at interfaces in such systems, we used the system $LaVO_3/SrVO_3$, because the behaviour of the solid solution counterpart is well-known. To enhance the influence of effects at the interface, the $SrVO_3$ layer has a thickness of nominally 1uc, so our samples can be regarded as $LaVO_3$ with some LaO subplanes replaced by SrO subplanes, leading to a geometrical confinement of the doping electrons because of the insulating character of $LaVO_3$.

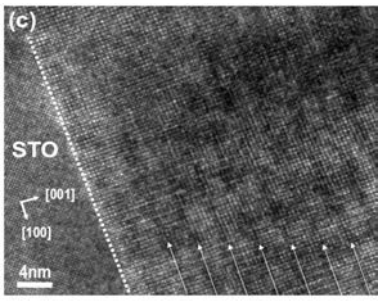


FIG. 57. *Transmission electron microscope image of a $(LaVO_3)6uc/(SrVO_3)1uc$ superlattice. The arrows indicate the dark contrast corresponding to the $SrVO_3$ layers.*

Superlattices of $(LaVO_3)_m/(SrVO_3)_1$, with m being the number of unit cells ranging from 2 to 9, of a high crystal quality were grown on $SrTiO_3$ (001) substrates (see figure 57) by pulsed laser ablation. The superlattices grow epitaxially on the substrate and show abrupt interfaces. Transmission electron microscopy demonstrated the continuity of a three unit cell-thick $SrVO_3$ layers. The bilayers were repeated up to a total thickness of around 80nm. Although none of the constituent materials, neither the solid solution, show ferromagnetism, we observe a macroscopic magnetic moment in the superlattices [Lüders *et al*, PRB **80**, 241102(R) (2009)], which was explained by the partial localization of the 3d electrons due to their lowered bandwidth as a result of the 2D character of the $SrVO_3$ layers.

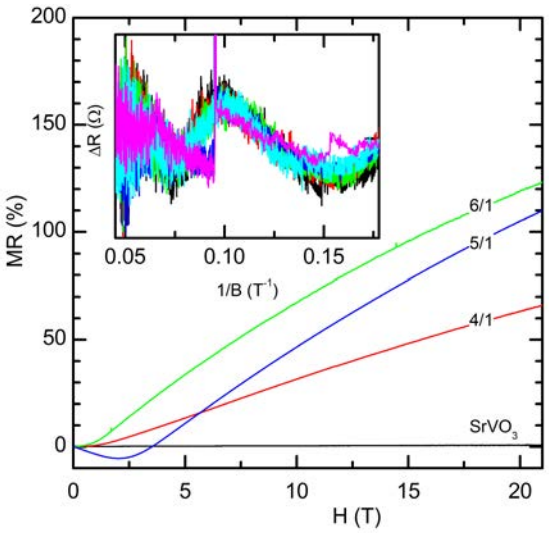


FIG. 58. *Magnetoresistance vs magnetic field for a $SrVO_3$ thin film (black line) and superlattices $(LaVO_3)muc/(SrVO_3)1uc$ with m ranging from 4 to 6uc.*

The objective of the measurements at the LNCMI was to measure the Fermi surface of the low temperature metallic phase of the superlattice samples in order to confirm the two-dimensionality of the conduction electrons as well as to gain more information on this peculiar metallic state. Shubnikov - de Haas oscillations can appear in resistance measurements in high magnetic fields and at low temperatures due to the crossing of the Landau levels across the Fermi energy, so that the absence of the oscillation in the out-of-plane direction is a simple proof of the bidimensionality of the conduction electrons. Different kinds of samples were measured: a thick $SrVO_3$ single film as a reference and several $(LaVO_3)m$uc/$(SrVO_3)$1uc superlattices with $m$ ranging from 4 to 6 to sample the dependence on the thickness of the $LaVO_3$ layer.

In figure 58, the magnetoresistance $(R(H) - R(0T))/R(0T)$ is shown for a 15 nm thick $SrVO_3$ thin film and the three superlattices is shown. The most important observation is that the superlattices show a strong positive magnetoresistance at high fields, which is not present in the $SrVO_3$ thin film. This behaviour is most probably due to orbital effects. The low field negative magnetoresistance of the $m = 5$ can be explained by the magnetic character of the sample and therefore field dependent scattering. The inset shows evidence for long period Shubnikov - de Haas oscillations in the background removed magnetoresistance up to $B = 22$ T.

***D. K. Maude***
***U. Lüders, A. David, W. Prellier (CRISMAT, CNRS, Caen, France)***

# Free Excitons of $CuInSe_2$ and $CuGaSe_2$ in Magnetic Fields

$CuInSe_2$ and $CuGaSe_2$ are chalcopyrite compounds used in the absorber layer of leading thin-film solar cell technology with conversion efficiency of 20%. To improve further the device performance, it is essential to know accurate values of such important fundamental physical parameters as the band gap $E_g$, exciton binding energy, static dielectric constant and the charge carrier effective masses.

The band gap $E_g$, exciton binding energy, static dielectric constant can be found from the spectral positions of the ground ($n = 1$) and first excited ($n = 2$) free excitons. Although the research on $CuInSe_2$ has been carried out for more than 40 years the excited states of the A and B excitons have not been observed. The applied magnetic field reduces the size of the exciton wave-function making it more stable and sharpening its line shape in the optical spectra. This effect helped to observe the A and B first excited states A' and B' in magneto-photoluminescence (MPL) spectra of $CuInSe_2$, shown in figure 59, where the A and B free excitons can also be seen resolved.

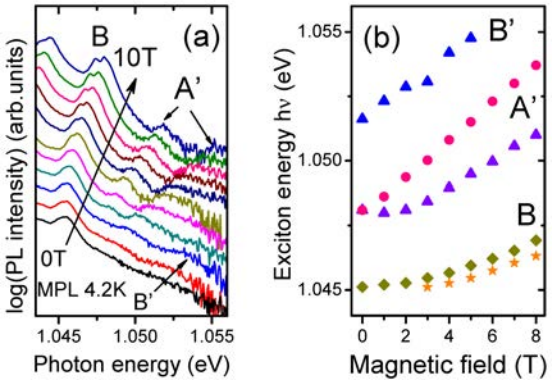


FIG. 59. *(a) The evolution of the B ground (n=1) state exciton and the A' and B' excited (n=2) states under the influence of magnetic fields at $B \perp c$ for $CuInSe_2$, (b) dependence of the spectral positions of the lines related to the ground B and A' and B' excited states of free excitons on the magnetic field strength.*

The dependence of the spectral positions of the B ($n = 1$), A' and B' ($n = 2$) lines on the magnetic field at $B \perp c$ are shown in figure 59(b). The spectral positions of the first ($n = 2$) excited states for the A and B free excitons are 1.0481 eV and 1.0516 eV, respectively, which have been used to calculate accurate values of the A and B exciton binding energies as $E_b^A = 8.5$ and $E_b^B = 8.4$ meV assuming a hydrogenic model. The model also gives values for the Bohr radii $a_B^A = 7.5$, $a_B^B = 7.5$ nm as well as the static dielectric constant $\epsilon = 11.3$. The band gaps of the A and B excitons are estimated as 1.0502 eV and 1.0537 eV, respectively, at 6 K [Yakushev et al. Appl. Phys. Lett. **97**, 152110 (2010)].

Despite the importance of $CuGaSe_2$ no reliable experimental values of the charge carrier effective masses can be found in the literature. The reduced mass of free exciton can be determined from its diamagnetic shift. Magnetic field dependencies of the free A exciton in photoluminescence spectra of $CuGaSe_2$ single crystals have been measured for the first time [(Luckert et al. Appl. Phys. Lett. **97**, 162101 (2010)].

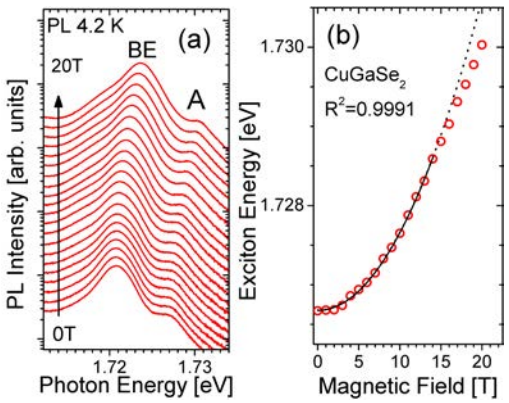


FIG. 60. *(a) Near band-gap PL spectra of $CuGaSe_2$, (b) evolution of the free A exciton PL peak position under magnetic fields from 0 to 20 T taken at 4.2 K. The solid line represents a quadratic fit up to 14 T.*

The evolution of the $CuGaSe_2$ near band gap photoluminescence (PL) spectra under magnetic fields from 0 to 20 T is shown in figure 60(a). Two peaks, A at 1.727 eV and BE at 1.721 eV, which correspond to the A free exciton and to an exciton bound to a neutral acceptor, respectively, are revealed. An increase in the magnetic field strength from 0 to 20 T results in a gradually increasing blue shift of both the bound exciton and the A free exciton, as shown in figure 60(a). From the evolution of the A free exciton PL peak position a diamagnetic shift rate $c_d = 9.82 \times 10^{-6} eV/T^2$ has been determined (figure 60(b)). A reduced mass $\mu = 0.115 m_0$ of the A free exciton has been calculated. Assuming an effective electron mass of $m_e = 0.14 m_0$ results in an effective hole mass of $m_h = 0.64 m_0$. An exciton binding energy of 12.9 meV and an exciton Bohr radius $a_B = 5.07$ nm have been calculated using the hydrogenic model.

***C. Faugeras***
***F .Luckert, M.V. Yakushev, R.W. Martin (Department of Physics, SUPA, Strathclyde University, Glasgow, UK), A.V.Karotki, A.V. Mudryi (Scientific-Practical Material Research Centre of the Belarus National Academy of Science, Minsk, Belarus)***

# Photoluminescence spectroscopy of CdMnTe quantum dots incorporated in *p-i-n* diodes

Magnetically doped quantum dots (QDs) offer an interesting possibility of combining magnetic and optical properties at nanoscale. Theoretical reports propose electrical tailoring of QD magnetization by selective tuning of the number of charge carriers in a single QD. Realization of these concepts may pave the way towards novel nanoscale memory devices as well as open a whole new field of studies of magnetic properties in confined geometries. Self assembled CdTe or CdSe QDs can be easily doped with magnetic ions; almost exclusively with Mn, providing a broad range of concentrations – from a single ion per dot to $\sim 20\%$ of magnetic cations. This proves to be a substantial advantage over the InGaAs system, where the solubility of Mn ions is very low and typically dots with only one or two ions can be found. On the other hand, charge tunability – performed routinely in InGaAs-based samples – in the II-VI system is not as straightforward. Some groups employ the procedure commonly utilized in the III-V samples - embedding the dots in Schottky diodes. We decided to investigate the feasibility of using *p-i-n* diodes. The advantage of this method is that the diode fabrication is much easier as it requires to deposit only ohmic contacts. The trade-off however is a more complicated band structure of the device (see inset to figure 61).

The samples were grown by molecular beam epitaxy on semi-insulating GaAs substrates. An *n*-type buffer layer was first deposited consisting of a $\sim 4\mu$m thick CdTe layer doped with iodine. Next, in order to provide a necessary strain for the formation of CdTe QDs, a ZnTe spacer layer was grown. Then, a single layer of CdMnTe QDs was formed by the procedure of desorption of amorphous tellurium. The QD layer was then covered with another layer of ZnTe. On top, a *p*-type ZnTe layer was grown. Ohmic contacts were made by soldering and evaporating of indium and gold contacts to *n*-type and *p*-type layers, respectively. Measurements were performed at 4 K in magnetic fields up to 14 T. The photoluminescence (PL) signal was excited with a dye laser beam in resonance with the high energy tail of the inhomogenously broadened PL band. Such excitation conditions warranted small heating related to photocreation of 2D carriers in extended excited states. PL was detected with a nitrogen-cooled CCD camera coupled to a 300 mm monochromator. Excitation and detection beams were transmitted through single mode optical fibers, which allowed for polarization selective measurements. Excellent mechanical stability of the setup facilitated measurements on single QDs.

In figure 61, we show a color-scale plot of PL versus magnetic field at a forward bias $U = +3$V. The observed transitions derive from the same QD. Transition line-widths and Zeeman shifts are more than an order of magnitude larger than in nonmagnetic CdTe QDs. Both of these effects stem from the exchange interaction between confined carriers and Mn ions. Each of

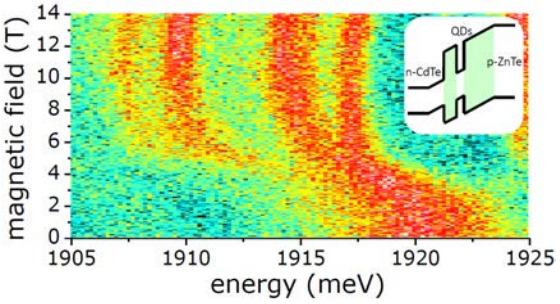


FIG. 61. *Color-scale plot of a single magnetic quantum dot photoluminescence as a function of magnetic field.*

the recombining excitons experiences a different configuration of fluctuating Mn ions giving rise to a different transition energy and hence line broadening. Single dot Zeeman shifts follow the dot magnetization. However, as seen in figure 61, the transition energy dependence on magnetic field is not described by a typical Brillouin function. In fact, at small magnetic fields, efficient heating of the Mn ion system diminishes the magnetization and thus decreases the Zeeman shift. This heating originates from the current flowing through the device. This current is mostly due to holes, since a barrier at the buffer/spacer interface hinders the injection of electrons into the space-charge region (see inset of figure 61). However, as the magnetic field is increased, the Mn spin temperature drops, which is manifested by an increase in the Zeeman shifts. We propose that the heat is transferred to the Mn system by simultaneous spin flip-flops between Mn ions and itinerant holes contributing to the current. Increasing the magnetic field leads to an increase of the hole Zeeman energy with a large $g-$factor originating from the Mn-hole exchange interaction. When this energy becomes larger than the Zeeman energy of the Mn (with $g = 2$) the flip-flops become energetically forbidden and the heating is suppressed.

We are unable to identify the transitions seen in figure 61 with specific excitonic complexes in the dot. In particular, we expect a manifestation of mixing of bright and dark exciton states and appearance of other charge states with varying bias. Understanding the behavior of the exciton transitions in magnetic field will allow to determine, whether semi-magnetic QDs in *p-i-n* diodes have a potential of becoming electrically tunable nanoscale memory devices.

***P. Plochocka, P. Kossacki, M. Potemski***
***L. Kopotowski, K. Fronc. M. Wiater, M. Król, G. Karczewski (Institute of Physics, Polish Academy of Sciences, Warsaw, Poland),***

# Quantum dot spectroscopy in strong in-plane magnetic field

Recent experiments on CdTe-based self-assembled quantum dots (QDs) doped with single Mn ions [Goryca *et al.*, Phys. Rev. Lett. **103**, 087401 (2009), Le Gall *et al.*, Phys. Rev. Lett. **102**, 127402 (2009)] boosted interest in these systems. Access to single dot properties is crucial in the QD studies due to significant variation of size and shape between different QDs. This access is usually obtained by performing microphotoluminescence ($\mu$PL) experiments. Such an experiment requires very tight focusing of a laser beam to a spot of about 1$\mu$m in diameter and simultaneously high stability of the optical setup to allow signal accumulation. Typical acquisition time ranges from seconds in usual PL spectroscopy to hours in case of single photon correlation.

Usually, magneto-spectroscopy of the QD in strong magnetic field is realized in normal Faraday configuration with magnetic field parallel to growth axis. Such an axial geometry is favored by the limited size of magnet bore and the need to use microscope objective. We performed a $\mu$PL study of self-assembled CdTe/ZnTe QDs to analyze the influence of the strong magnetic field applied parallel to QD plane. In our experiment we used the same setup as for typical Faraday configuration, however instead of placing a sample flat on the surface of the Attocube piezo stage, we mounted the sample vertically. In this configuration we were able to observe a QD photoluminescence through a cleaved edge of the sample. This configuration did not affect the stability of the setup.

Obtained results revealed presence of transitions not allowed in normal Faraday configuration. Namely, we were able to observe dark exciton emerging in the higher field and thus to determine isotropic electron-hole exchange constants in our samples. Another interesting feature of the in-plane field geometry is the splitting pattern of charged excitons. Contrary to the normal Faraday configuration, we observed four-fold splitting of these transitions. The observed splittings are influenced by both initial and the final state of the transition. In the initial state, two majority carriers are forming a singlet and only the minority carrier contributes to the splitting. The final state contains only one (majority) carrier and splits according to its g-factor. Due to mixing between heavy- and light-holes, the selection rules allow the observation of all transitions in this case. Thus, the splittings observed in the experiment are govern by correspondingly the sum and difference of electron and hole g-factors in the dot. We found that the value of the in-plane g factor of the hole may be even equal to that of the electron, which contradicts the usual assumption of pure heavy character of the hole in the QD. The use of high magnetic field allowed us also to study the diamagnetic shift of the transitions. Determined values of diamagnetic coefficient were significantly smaller than the one observed in Faraday configuration, in agreement with flat shape of the QDs known from TEM microscopy.

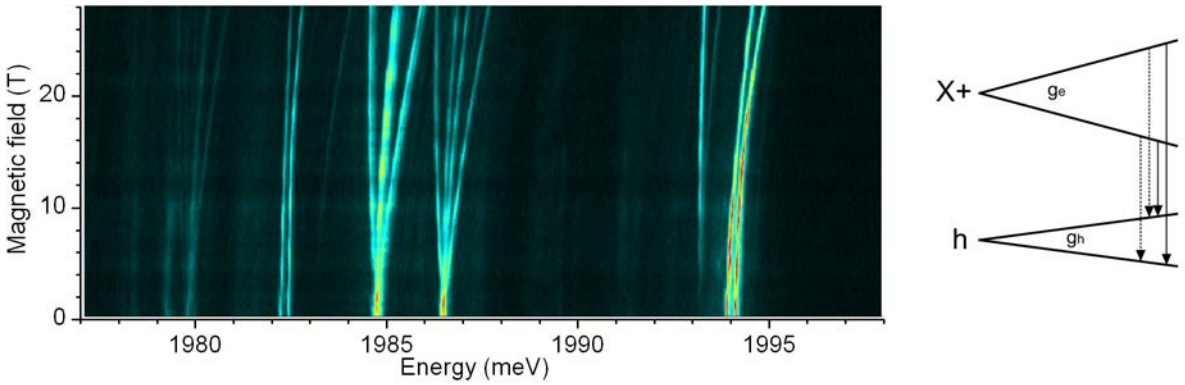


FIG. 62. *Magnetic field applied parallel to the QD plane features several transitions not observed in normal Faraday geometry,* e.g. *dark exciton branch and four-fold splitting of charge exciton recombination lines. The latter allows us to determine in-plane electron and hole g-factors separately.*

***M. Goryca, P. Płochocka, M. Potemski, P. Kossacki***
***T. Kazimierczuk (University of Warsaw, Poland), P. Wojnar (Institute of Physics, Polish Academy of Sciences, Poland)***

# Brightening of dark excitons in a single CdTe quantum dot containing a single $Mn^{2+}$ ion

It has been recently demonstrated that positioning a single magnetic ion in a single quantum dot (QD) gives unique possibilities to read and manipulate the electronic spin state of the single atom. Moreover a presence of a single magnetic ion in a QD also gives the possibility to observe certain features of excitonic states which are not readily observable in non-doped QDs. For example dark exciton states are usually inaccessible for optical spectroscopy. However, the mixing of dark and bright states, induced by the magnetic impurity, can make the observation dark excitons possible.

We have performed the micro-photoluminescence measurements in high magnetic fields to directly probe optical transitions of these dark excitons. The sample containing a single layer of self-assembled CdTe/ZnTe QDs containing a low amount of $Mn^{2+}$ ions was placed in a micro-photoluminescence setup consisting of precise piezo-electric three-dimensional stage and a microscope objective. The micro-photoluminescence system was kept at the temperature of 4.2 K in a cryostat placed in a resistive magnet producing magnetic field up to 28 T. The field was applied in the Faraday configuration, parallel to the the growth axis of the sample.

The PL of the QDs was excited using a tunable dye laser in the range $570 - 610$ nm. Both the exciting and the collected light were transmitted though a monomode fiber coupled directly to the microscope objective. The use of the monomode fiber combined with polarization optics outside the cryostat permits the control of the circular polarization of both the exciting and detected light.

Figure 63(a-b) shows the evolution of PL spectra with magnetic field for the two selected single Mn-doped QDs with diffent in-plane anisotropy. In the case of the QD with smaller anisotropy (QD1) two branches, each consisting of six lines, are clearly visible. These branches correspond to optical transitions of bright excitons ($X$). The QD with larger anisotropy (QD2) shows additional fivefold split branch in the low energy part of the spectrum. This branch is related to dark excitonic ($X_d$) transitions accompanied by a simultaneous $Mn^{2+}$ spin flip. These transitions are partially allowed by the $X$-Mn exchange interaction combined with a mixing of the heavy-light hole states induced by the QD in-plane anisotropy [M. Goryca *et al.*, Phys. Rev. B **82**, 165323 (2010)]. The anisotropy of the QD can be determined from the anticrossing of the outermost lines of $X$ branches ("A" in Fig 63(a)). A simple model, taking into account Zeeman energies of the $Mn^{2+}$ ion and the carriers trapped in the QD, their exchange interactions and heavy-light hole mixing, reproduces correctly all the key features of the PL spectra (Fig. 63(c)).

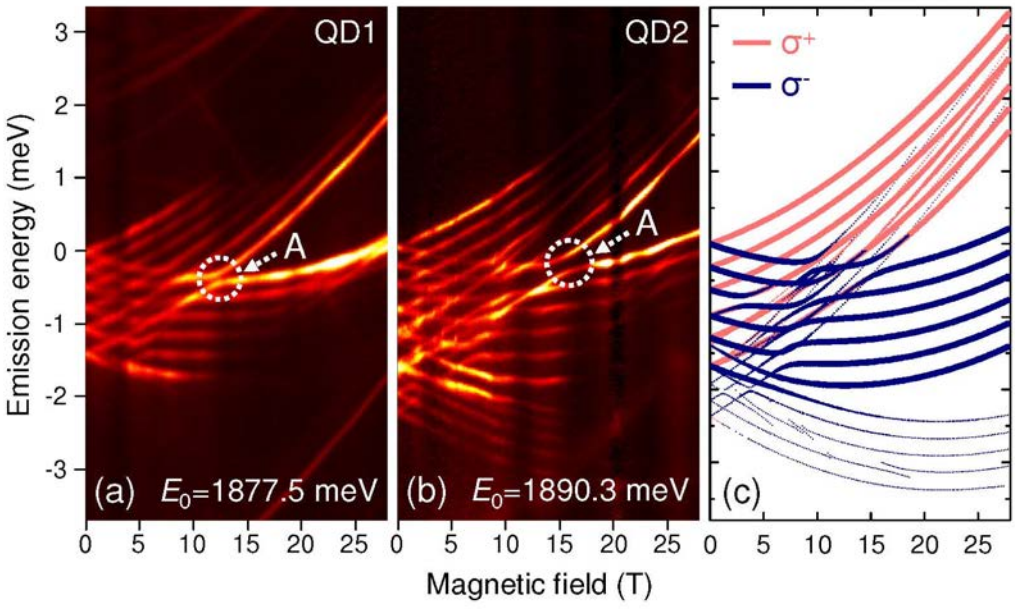


FIG. 63. *(a-b) Color-scale plots of the PL spectra of two single Mn-doped QDs with different in-plane anisotropy as a function of magnetic field. The vertical scale of each panel is shifted by $E_0$. (c) Simulation of the optical transitions in the QD2. The line thickness corresponds to the oscillator strength of the transitions.*

***M. Goryca, P. Plochocka, M. Potemski, P. Kossacki***
***T. Kazimierczuk, J.A. Gaj (Institute of Experimental Physics, Warsaw University, Poland), P. Wojnar (Institute of Physics, Polish Academy of Sciences, Warsaw, Poland)***

# Magnetophotoluminescence of prepositioned single InAs/InP quantum dots

In order to realize fibre-based quantum information processing applications, the control of photons with wavelengths in the range of 1.5 $\mu$m is required. These applications of nonclassical light generation absolutely require the need for control over electro-optical properties of the quantum dots fabricated. In this report, we review the results of our experiments where we perform magnetophotoluminescence of single InAs/InP quantum dots embedded in InP nanopyramids emitting at around 1.5 $\mu$m.

The magnetophotoluminescence of single quantum dots was measured up to 28 T. The sample was pumped with an unpolarized 632 nm laser source. Dot emission is collected through a fibre and focused onto an InGaAs detector. The spectrometer uses a 600 lines/mm grating with a spectral resolution of about 0.11nm. Data from over thirty single dots were obtained demonstrating similar behaviour in magnetic fields up to 28 T. The brightest state is the trion $X^{-1}$, followed by the neutral exciton $X^0$ at a few meV higher in energy, and the p-states and d-states at even higher energy. The $X^0$ state is very weak at 0 T and becomes brighter as a function of magnetic field. The $s-p$ splitting is approximately 20 meV and shows no trend as a function of emission energy.

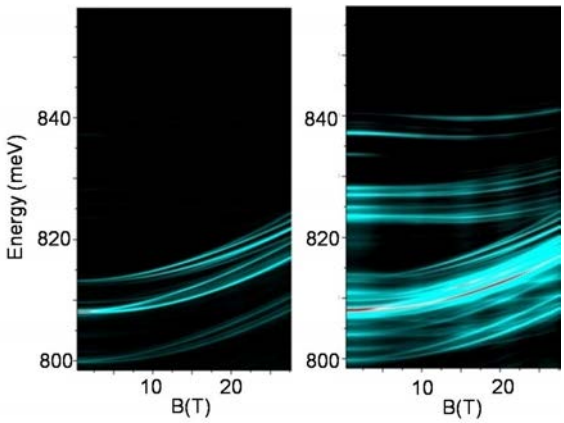


FIG. 64. *Magnetic field spectra at low and high power levels. The p and d states are clearly visible at higher pump power. Polarization-resolved measurements find a trion ($X^{-1}$) as the ground state with the neutral exciton($X^0$) at slightly higher power.*

With magnetic field, the doubly-degenerate ground state is split,

$$E_{\pm} = E_0 \pm g_{ex}\mu_B B + \gamma B^2 \qquad (6)$$

where $g_{ex}$ is the excitonic $g$-factor, $\mu_B$ is the Bohr magneton, and $\gamma$ is the diamagnetic shift. The $g$-factor of the neutral and charged exciton is given by,

$$g_{ex} = \frac{E(\sigma^+) - E(\sigma^-)}{\mu_B B}. \qquad (7)$$

where $E(\sigma^+)$ and $E(\sigma^-)$ represent the right and left circular polarized states, respectively. The $g$-factor is expected to change as an approximately linear function of emission energy [Kim et al., Phy. Rev. B. 79 045310 (2009)]. Since the energy of the quantum dot depends on its size, it is thus possible to tune the $g$-factor by controlling the area of the mesa upon which the quantum dot is grown.

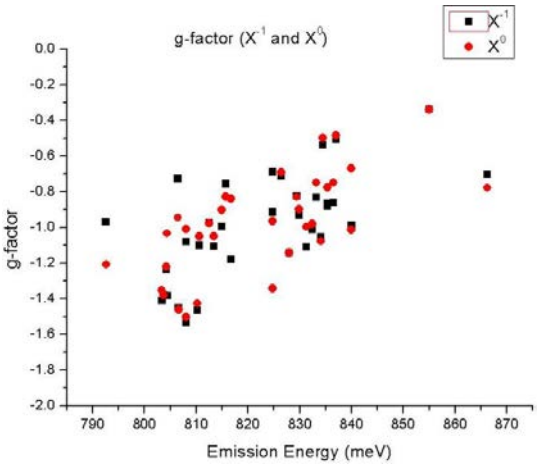


FIG. 65. *The excitonic g-factor clearly becomes less negative with increasing emission energy. Both the $X^{-1}$ and $X^0$ g-factors are similar in the majority of quantum dots examined.*

The diagmagnetic shift was calculated for both $X^{-1}$ and $X^0$. No clear difference in the diamagnetic shift are seen between the two states. Polarization-resolved spectra determined the emitted light was indeed circularly polarized.

In summary, we have demonstrated bright, consistent, and prepositioned single InAs/InP quantum dots. The $g$-factors of both $X^{-1}$ and $X^0$ were found to depend linearly from $-1.5$ to $-0.8$ on the emission energy from $800-840$ meV . The diamagnetic shift has shown no dependence on emission energy nor was significantly different for $X^{-1}$ and $X^0$ at about $10-14\,\mu\mathrm{eV/T^2}$. Future work is focused on magnetophotoluminescence with electron-number control of the quantum dots using electrostatic gating of the pyramids.

***P. Plochocka, M. Potemski***
***R. Cheriton, D. Dalacu, K. Mnaymneh, J. Lapointe, R. Williams (Institute for Microstructural Sciences, NRC, Ottawa, Canada)***

# Metals, Superconductors and Strongly Correlated Systems

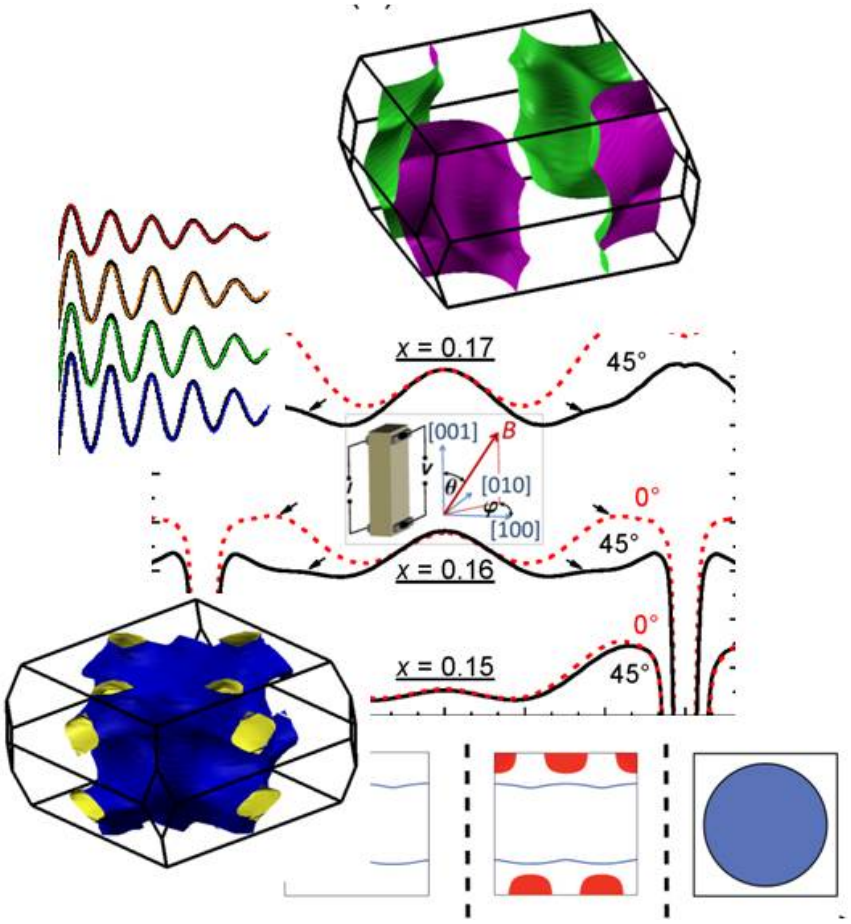

# Pressure-induced metallic state in $(BEDT\text{-}TTF)_8[Hg_4Br_{12}(C_6H_5Br)_2]$

According to band structure calculations, the Fermi surface of the isostructural organic metals $(BEDT\text{-}TTF)_8[Hg_4X_{12}(C_6H_5Y)_2]$ (where X, Y = Cl, Br and BEDT-TTF stands for bis-ethylenedithio-tetrathiafulvalene) is composed of one electron and one hole compensated orbit (labelled $a$ in figure 66). However, even though a metallic ground-state is observed for X = Cl, a metal-insulator transition occurs as the temperature is lowered for X = Br.

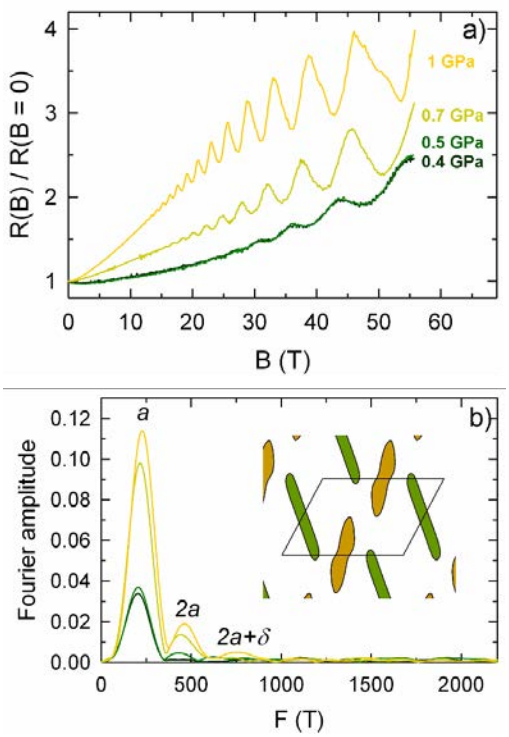


FIG. 66. *(a) Inter-layer magnetoresistance at 1.5 K of the organic metal $(BEDT\text{-}TTF)_8[Hg_4Br_{12}(C_6H_5Br)_2]$ for various applied pressures and (b) corresponding Fourier analysis. The insert displays the Fermi surface (FS) in which the labels a, corresponding to the compensated orbits area, and δ, the FS piece in-between are made explicit.*

For X = Y = Br, this transition occurs at $T_c = 125$ K at ambient pressure. X-ray diffraction data reveal that only slight structural changes occurs as the temperature is lowered. Nevertheless, the temperature-dependence of the cell parameters is non-monotonic below $T_c$ and, according to band structure calculations, a gap opening is observed in this temperature range which accounts for the low temperature insulating state observed at ambient pressure (see figure 67).

Metallic state is recovered under pressure at $P_c = 0.34$ GPa. Above $P_c$, Shubnikov-de Haas oscillations are detected which allows for the determination of Fermi surface area, through the oscillations frequency ($F$), and effective mass ($m^*$). Frequency values are in good agreement with band structure calculations. In strongly correlated systems, Fermi energy, which can be estimated as $E_F = \hbar F/m^*$, goes to zero at the metal-insulator transition. This behaviour is generally

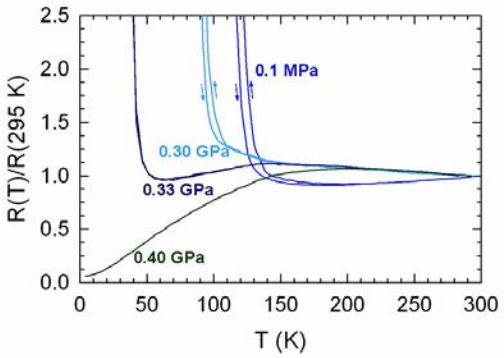


FIG. 67. *Temperature dependence of the resistance for various applied pressures. A pressure-induced metallic ground state is observed above $P_c = 0.34$ GPa.*

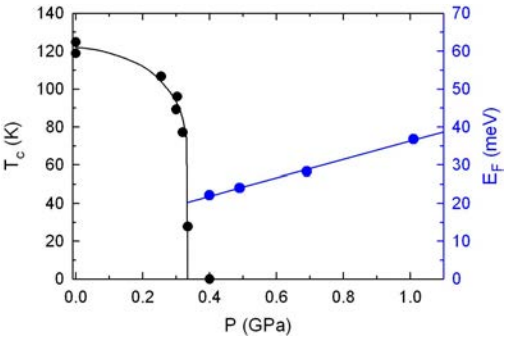


FIG. 68. *Pressure dependence of the metal-insulator transition temperature (left scale) and of the Fermi energy (right scale). The latter remains finite at the critical pressure $P_c = 0.34$ GPa.*

due to a divergence of the effective mass linked to a non-Fermi liquid state. Here, even though $m^*$ strongly decreases under pressure, $E_F$ remains finite at $P_c$ (see figure 68) which suggests that the metal-insulator transition is not driven by electron correlations. In that respect, the $T^2$ behaviour of the zero-field resistance observed in the pressure-induced metallic state at low temperature (also observed for members of this family with a metallic ground state at ambient pressure [Vignolles *et al.*, Eur. Phys. J. B **66**, 489 (2008)]), is a signature of a correlated Fermi liquid.

***A. Audouard, D. Vignolles, F. Duc***
***R.B. Lyubovskii, R.N. Lyubovskaya (IPCP, Chernogolovka, Russian Federation), E. Canadell (ICMAB, Barcelona, Spain), L. Vendier (LCC, Toulouse)***

# Magnetoresistance measurements of $YbCu_2Si_2$ single crystals under high magnetic field and pressure

The intermediate valence compound $YbCu_2Si_2$ has a well known magnetic phase transition [Alami-Yadri *et al.*, Eur. Phys. J. B **6**, 5 (1998)] induced by pressure as a control parameter. Pressure tends to drive Yb ion from its divalent nonmagnetic configuration ($4f^{14}$) to the trivalent magnetic state ($4f^{13}$). Recent *ac* calorimetry and *ac* susceptibility measurements [Colombier *et al.*, Phys. Rev. B **79**, 245113 (2009)] have shown that the magnetic order appears for pressures above the critical pressure of 8 GPa(figure 69).

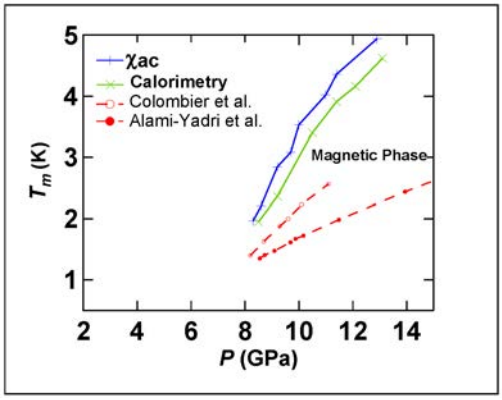


FIG. 69. *Phase diagram of high quality single crystals of $YbCu_2Si_2$ (RRR ∼ 220) grown at the CEA/Grenoble. Ac calorimetry and susceptibility measurements have permitted to determine the transition temperature of the magnetic transition ($P > 8$ GPa).*

An interesting point to investigate is whether another control parameter, other than pressure, can also induce this magnetic ordering. This was the purpose of our high field experiment. We measured the resistivity of high quality $YbCu_2Si_2$ single crystals under 5 different pressures (from almost ambient pressure to 5.8 GPa) below the critical pressure and at different temperatures (from 2 K to 10 K) in order to explore if by applying high magnetic fields up to 28 T we could induce a "metamagnetic" transition.

Figure 70 shows the field dependence of resistivity of $YbCu_2Si_2$ at several different pressures and temperatures of 2 K (upper panel) and 6 K (lower panel). The response of the resistivity at low temperatures (2 K) is quite different for $H < 12$ T and for $H > 12$ T. For $H > 12$ T, it is almost independent of the pressure and increases monotonically with the magnetic field. On the other hand, for $H < 12$ T the resistivity is quite sensitive to pressure. Below 25 kbars, it increases with the applied magnetic field, while above 25 kbars it decreases for a certain range of magnetic fields before increasing again. The position of the peak shifts to lower fields for increasing pressures.

The interpretation of the results obtained at higher temperatures is not straightforward due to the superposition of thermal effects which seem to be more important at low magnetic fields. The behaviour is

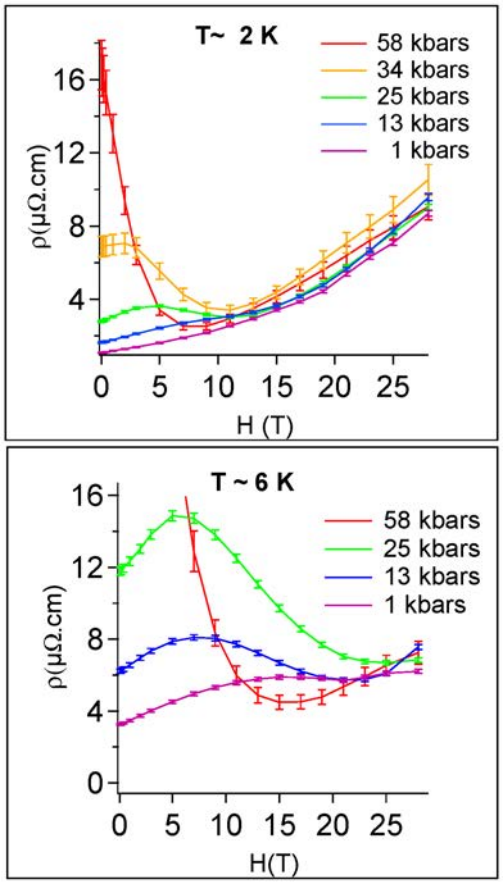


FIG. 70. *Resistivity of $YbCu_2Si_2$ single crystals under different pressures and magnetic fields up to 28 T. The measurements at 2 K (upper panel) and 6 K (lower panel) are shown.*

quite complex but there is no clear sign of a transition. In order to verify if the effect we observed is indeed the metamagnetic transition we were looking for, the present results should be compared with the magnetoresistance above the critical pressure as well as with measurements at lower temperatures. It is now clear that close to the critical pressure the necessary magnetic field is moderate. We are currently carrying out measurements in a dilution fridge at the CEA/Grenoble in the pressure range both above and below the critical pressure. These measurements should allow for a better understanding of the results obtained at high field.

***I. Sheikin***
***A. Fernandez-Panella, D. Braithwaite (CEA-SPSMS, Grenoble, France)***

# Angle-dependent magnetoresistence oscillations and Shubnikov-de Haas effect in the electron-doped superconductor $Nd_{2-x}Ce_xCuO_4$

High field magnetotransport has proved extremely helpful for elucidating the Fermiology of cuprate superconductors. Recently our group discovered angle-dependent magnetoresistance oscillations, so called AMRO, in fields up to 28 T and Shubnikov- de Haas oscillations in pulsed fields up to 64 T for single crystals of $Nd_{2-x}Ce_xCuO_4$ (NCCO) with $x$ between 0.16 to 0.17 [Helm *et al.*, Phys. Rev. Lett. **105**, 247002 (2010)]. The only other cuprate compound for which AMRO have so far been observed is $Tl_2Ba_2CuO_{6+\delta}$ in fields up to 45 T. The amplitude of the AMRO found in NCCO at 28 T was still too weak for quantitative analysis and therefore we applied the highest steady magnetic field available in Europe to shed more light onto this topic. The experiments were done on crystals with $0.15 \leq x \leq 0.17$ in a 35 T resistive magnet. *In situ* rotation was performed with a home made 2-axis-rotator at temperatures $\sim$ 25 to 1.4 K. The interlayer resistance $R_c$ was measured as a function of angle $\theta$ between the field direction and crystal axis [001], at different azimuthal angles $\varphi$, see inset in figure 71(a). Sufficiently low currents of $\sim$ 0.1 mA were applied to the samples ensuring negligibly small overheating and therefore a stable-temperature working regime.

The angle-dependent interlayer magnetoresistance (AMR) of NCCO appears to be very complex due to competing contributions from incoherent, coherent orbital, and superconducting effects. Figure 71(a) shows data of 3 different electron-dopings ranging from a nearly optimal, $x = 0.15$, to a strongly overdoped, $x = 0.17$, composition. In the range $|\theta| \leq 30°$ they display an anomalous dome which we could not relate to AMRO due to its $T$-dependence. It is more likely associated with incoherent, spin-dependent interlayer transport mechanism found also for underdoped samples. Compared to the data obtained in fields up to 28 T, the AMRO features (indicated by arrows) are stronger pronounced and we are able to trace their $\varphi$-dependence in more detail. For $x = 0.15$ above 20 T the AMR appears to be similar but without AMRO features, whereas at lower fields it is found to behave rather underdoped-like.

Encouraged by the low noise level ($10^{-5}$ of the sample resistance) and the possibility of slow field sweeps, besides AMR we have investigated the field dependence of $R_c$, applying the field perpendicular to the $CuO_2$ layers. Shubnikov-de Haas oscillations were found for $x = 0.16$, 0.165 and 0.17 at fields down to $\leq$ 20 T, see figure 71(b). Their frequencies, 290 T, 270 T and 250 T, respectively, perfectly coincide with the results obtained in pulsed fields. These low frequencies originate from small hole pockets of the reconstructed Fermi surface which are, thus, present up to highest available doping level $x = 0.17$. With increasing $x$ the frequency becomes lower, *i.e.* the Fermi pocket size shrinks. This nicely fits to the proposed magnetic breakdown scenario that explains the occurrence of fast oscillations at field above 55 T in the strongly overdoped regime. Further high-field experiments are desired for understanding why AMRO and SdH are not found below optimal doping and how the ordering responsible for the present Fermi surface reconstruction is related to superconductivity in this material class.

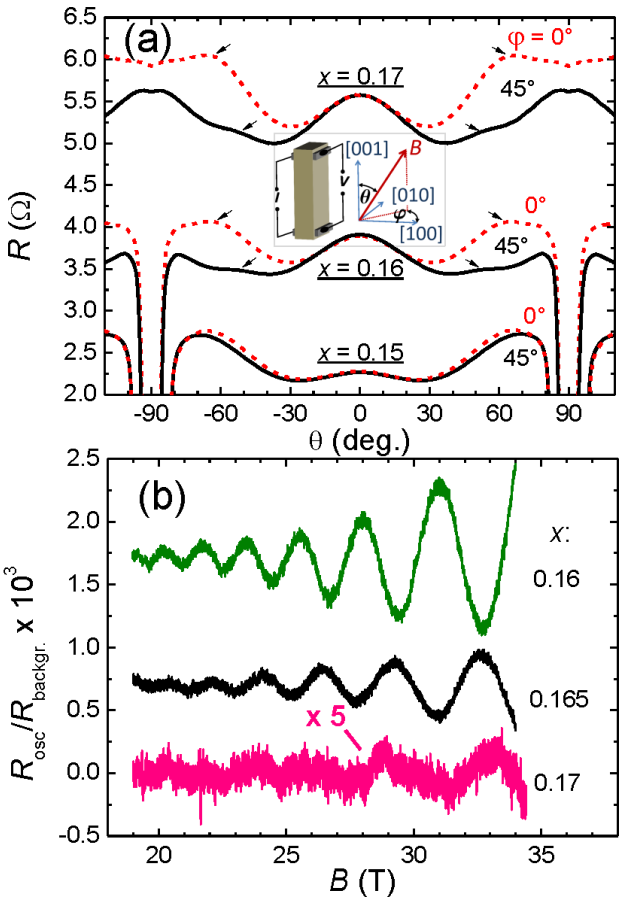


FIG. 71. *(a) Angle-dependent interlayer magnetoresistance of $Nd_{2-x}Ce_xCuO_4$ for 3 different doping levels $x$ at $B = 34$ T, $T = 1.4$ K. Arrows point to AMRO features, found in overdoped crystals, whose positions depend on azimuthal angle $\varphi$. Around $|\theta| = 90°$ the resistance drops sharply due to onset of superconductivity. (b) Shubnikov-de Haas oscillations in NCCO recorded at $T = 1.5$ K. Curves are vertically shifted for a better visibility.*

***I.Sheikin***
***T. Helm and M. V. Kartsovnik (Walther-Meissner-Institut, Garching b. München, Germany)***

# Multiple transitions and unusual magnetic phase diagram in non-centrosymmetric $CeCoGe_3$ from specific heat measurements

$CeCoGe_3$ crystallize in the tetragonal $BaNiSn_3$-type crystal structure. $CeCoGe_3$ is a moderate heavy-fermion system with a Sommerfeld coefficient of the specific heat $\gamma = 0.032$ J/molK$^2$. It undergoes an untiferromagnetic transition at $T_{N1} = 21$ K, followed by two more transitions at $T_{N2} = 12$ K and $T_{N3} = 8$ K [Thamizhavel *et al.*, J. Phys. Soc. Jpn. **74**, 1858 (2005)]. Three consecutive metamagnetic transitions were observed for magnetic field applied along the easy magnetic $c$-axis. A rather complex magnetic phase diagram was suggested by Thamizhavel *et al.* However, the authors did not discuss whether the magnetic transitions were of first or second order. Furthermore, only the transition at $T_{N1}$ was observed in their specific heat measurements.

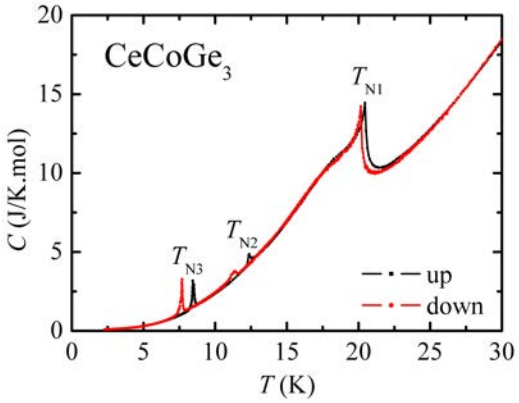


FIG. 72. *Specific heat of $CeCoGe_3$ as a function of temperature at zero magnetic field for both increasing and decreasing temperature. Hysteresis associated with the magnetic transitions suggests that all three of them are of first order.*

Figure 72 shows the temperature dependence of zero field specific heat in $CeCoGe_3$. Both the characteristic sharp peaks and hysteresis in specific heat vs temperature at the transitions imply that all of them are first order. The hysteresis is more pronounced for the transitions at $T_{N2}$ and $T_{N3}$. The transition at $T_{N1}$ is characterized by the largest specific heat anomaly and rather small hysteresis.

Upon the application of magnetic field along the [001] direction, the transitions $T_{N3}$ and $T_{N2}$ move rapidly to lower temperatures and are completely suppressed 0.2 T and 0.6 T respectively (figure 73). The highest temperature transition hardly moves up to about 2 T. Surprisingly, a new low temperature anomaly emerges slightly above 2.5 T. The anomaly moves rapidly to higher temperatures with increasing field and finally merges with the transition at $T_{N1}$ at about 3.6 T. Both anomalies then disappear at slightly higher field. This suggests the new anomaly being of the same origin as that at $T_{N1}$. Finally, a broad maximum accompanied by a hysteresis is observed on specific heat curves above 3.6 T where all transitions are suppressed. This surprising feature persists up to about 7 T. The exact origin of this peculiar behavior is not clear at present. An appealing possibility is that it is due to magnetic fluctuations which remain strong at fields much higher than that required to suppress the magnetic transitions.

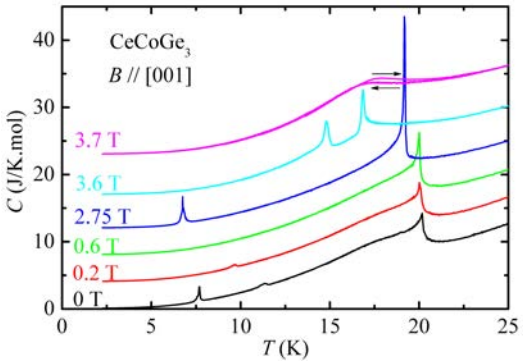


FIG. 73. *Specific heat of $CeCoGe_3$ vs temperature is shown for several values of magnetic field applied along the c-axis. All the curves are for decreasing temperature, except the one at 3.7 T, where both increasing and decreasing temperature curves are shown. The curves are shifted vertically for clarity.*

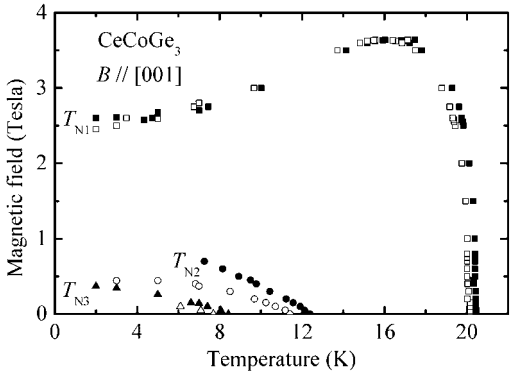


FIG. 74. *Magnetic phase diagram of $CeCoGe_3$ obtained from specific heat and magnetocaloric effect measurements. Close and open symbols correspond to increasing and decreasing temperature (field) respectively.*

The resulting $T - B$ phase diagram of $CeCoGe_3$ obtained from specific heat and magnetocaloric effect measurements is shown in figure 74.

***A. Demuer, I. Sheikin***
***R. Settai, Y. Ōnuki (Osaka University, Osaka, Japan)***

# Thermoelectricity of UCoGe

UCoGe is a heavy fermion compound and one of only a few examples of a ferromagnetic superconductor. A relatively small magnetic moment $m \sim 0.05\mu_B$ oriented along the $c$-axis is produced at the Curie temperature $T_c$ of 2.5 K and the material undergoes a superconducting transition at $T_{SC} \sim 0.6$ K [Huy *et al.*, Phys. rev. Lett. **99**, 067006 (2007)]. Resistivity measurements under field applied along the $b$-axis show an enhancement of $H_{c2}$ which leads to an 'S-shaped' $H_{c2}$ curve. In addition, the magnitude of the $T^2$ contribution to resistivity increases and peaks at H$^*$ $\sim$ 12 T with the field is applied along the hard $b$-axis [Aoki *et al*, JPSJ **78**, 113709 (2009)]. This indicates some form of instability such as in the isostructural ferromagnet URhGe where a reentrant superconducting phase is observed [Levy *et al*, Nat. Phys, **3**, 460 (2007)]. The thermopower is a very sensitive tool to observe the Fermi surface as it is related to the derivative of the density of states at the Fermi level. In this study we measure the thermopower of UCoGe in fields up to 18 T applied along the $b$-axis and down to 0.3 K in order to gain information of the Fermi surface behavior in the vicinity of H$^*$.

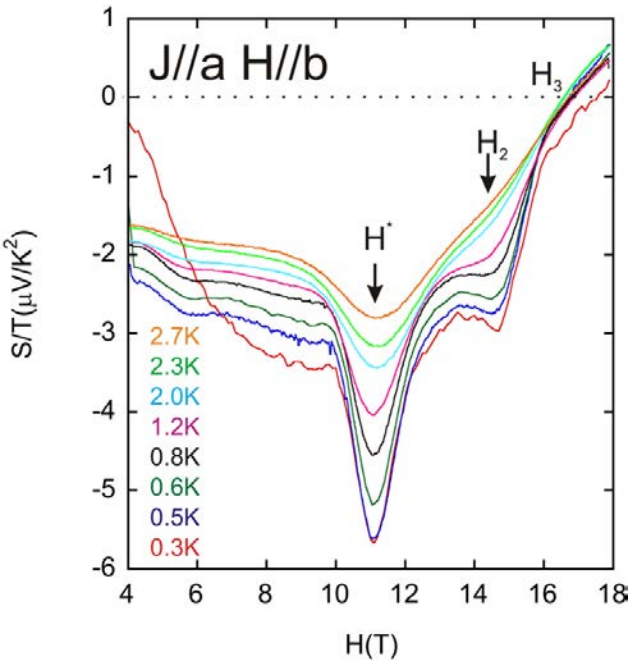


FIG. 75. *Thermopower divided by temperature $S/T$ as a function of field $H$ at several different temperatures. A large peak is observed at the instability field $H^* = 11.1$ T which becomes larger at lower temperature. An additional anomaly at $H_2 = 14.7$ T is observed at low temperature and a change of sign of the thermopower at $H_3 = 16.7$ T.*

A high quality single crystal of UCoGe was grown in the CEA, Grenoble by the Czochralski pulling method with a residual resistance ratio of 20. Thermopower measurements were performed in a custom built dilution fridge using a one heater, two thermometer setup. Figure 75 shows the thermopower of UCoGe divided by temperature $S/T$ with the heat current $j$ applied along the $a$-axis as a function of field at different temperature. The value of $S/T$ is quite large (up to $\sim 6\mu V/K$) which is expected from the large quasiparticle masses and low carrier density of UCoGe. A large peak is observed in $S/T$ at the instability field $H^*$=11.1 T. At higher temperatures the peak is less pronounced, becoming sharper at lower temperature. In addition to the $H^*$ anomaly, there are two additional features. Another, smaller peak at $H_2$=14.7 T which is only visible at the lowest measured temperatures. Finally a change of sign of sign is observed at $H_3$=16.7 T. None of the features change field as a function of temperature. From resistivity measurements it is clear that the A term (which, assuming the Kadowaki-Woods relation, is proportional to the square of the $\gamma$ term in specific heat) is increasing up to $H^*$ indicating an increase in effective mass of the system as the instability is approached. For a conventional Fermi liquid $S/T$ in the low temperature limit should be constant and proportional to the $\gamma$ term of specific heat. Therefore a peak of $S/T$ is expected at $H^*$. However the increasing amplitude of the peak at $H^*$ as a function of temperature is not expected in a simple Fermi liquid picture. This could indicate a Fermi surface instability at $H^*$ like, for example, a Lifshitz transition. In this scenario the Fermi energy is tuned to a singular point in the density of states. At zero temperature this would create a divergence in the thermopower which is smeared out at finite temperature. The anomaly at $H_2$ remains to be explained although a recent magnetoresistance and quantum oscillations study [Aoki *et al*, to be published] reveals a minimum at $H_2$. This coupled with the change of sign of $S/T$ at $H_3$ could point to a Fermi reconstruction above 18 T. One small quantum oscillation frequency is observed by Aoki *et al* above 20 T with a large effective mass ($\sim 25\,m_e$) which confirms the heavy fermion, low carrier concentration of this material but data at lower field is required to compare with the thermopower.

UCoGe offers the chance to study ferromagnetism and it's interplay with superconductivity around an instability. We have measured the thermopower as a function of field which shows a strong anomaly at the instability and could indicate a Fermi surface reconstruction at higher fields. Although more measurements are required to examine these effects.

***L. Malone, C. Proust***
***L. Howald, J. P. Brison, D. Aoki, G. Knebel, J. Flouquet (CEA-SPSMS, Grenoble, France)***

# Thermoelectricity of $URu_2Si_2$: A possible field induced Lifshitz transition

At $T_0 \sim 17\,\mathrm{K}$, $URu_2Si_2$ undergoes a second order phase transition into a hidden order (HO) state. This transition demonstrates a large drop in entropy but to date no order parameter has been conclusively observed. There are numerous theoretical suggestions for the hidden order parameter. Transport and thermodynamic probes point to a significant Fermi surface reconstruction at $T_0$, which leads to a dramatic drop in carrier density. This decrease in carrier density corresponds to a decreased Fermi temperature and furthermore this weakness is reinforced by the large effective mass of the quasiparticles. Thus a moderate field can have a large effect on the Fermi surface characteristics. Recent resistivity and Hall measurements [Shishido *et al*,PRL, **102**, 156403 (2009)] on high quality single crystals have revealed anomalies and additional quantum oscillation frequencies at $H^* \sim 23\,\mathrm{T}$ implying additional structure in the HO phase or even a possible phase transition. Thermodynamic measurements show no large anomalies in this field range which could imply a more subtle topological change in the Fermi surface or 'Lifshitz transition'. If this is the case then the interplay between the Fermi surface, the HO order parameter and magnetic field could lead to fascinating insights into this compound and a better understanding of Fermi surface changes in the presence of strong correlations.

Figure 76(a) shows the thermoelectric power divided by temperature $S/T$ as a function of magnetic field $H$ up to 28 T. The field is applied along the $c$ axis and the heat current $J$ along the $a$ axis. The thermopower is measured as the field is swept at different temperatures. The measured values of the thermopower below 12 T are in reasonable agreement with previous results [Bel *et al*, Phys. Rev. B **70**, 220501(R) (2004)]. At the lowest temperature 1.4 K, $|S/T|$ shows an increase and a broad maximum at $H_m \simeq 11\,\mathrm{T}$ followed by a decrease and minimum at $H^* \simeq 23\,\mathrm{T}$. The label $H^*$ is taken from Shishido *et al*, where it corresponds to anomalies in resistivity and Hall measurements. They occur at roughly the same fields as observed in thermopower but there is a slight difference presumably due to the broad nature of the anomalies and their angle dependence. As the temperature is increased both $H^*$ and $H_m$ are smeared out until at 10 K a monotonic increase is observed up to 28 T. Above $T_0$, in the paramagnetic state the thermopower is greatly reduced as previously reported.

There is a strong indication that the anomaly at $H^*$ is connected to a Lifshitz transition. A Lifshitz transition is not a thermodynamic phase transition in the conventional sense, rather it is a topological change in Fermi surface leading to sharp anomalies in transport coefficients only at zero temperature. In proximity to a Lifshitz transition, one of the energy bands $\epsilon(k)$ is close to a singular point. Quantities, such as the thermopower, which are related to the derivative of the density of states diverge at the singular point. The original Lifshitz paper [Lifshitz, JETP, **11**, 1130 (1960)] concentrated on a suppression of a neck in the Fermi surface and predicted thermoelectric quantities to diverge as $|z|^{-\frac{1}{2}}$ at $T = 0$ where $z$ is the tuning parameter and $z = 0$ is the transition point. However it has been shown that impurities and temperature change the form of this divergence [Varlamov *et al*, JETP, **89**,2188 (1985)]. In addition, Lifshitz assumed a particular type of singular point in a simple band structure but in a real metal the form of the divergence will depend on the details of the band structure around the singular point. It has also been shown that the resistivity will show a kink like feature close to a Lifshitz transition similar to the observed anomaly in Figure 1(d). The behavior observed in $URu_2Si_2$ is similar to what is predicted, i.e a strong, broad anomaly in thermopower with smaller anomalies in other transport properties. Therefore we conclude that the HO gap is suppressed on one band and there is a Lifshitz transition at $H^*$.

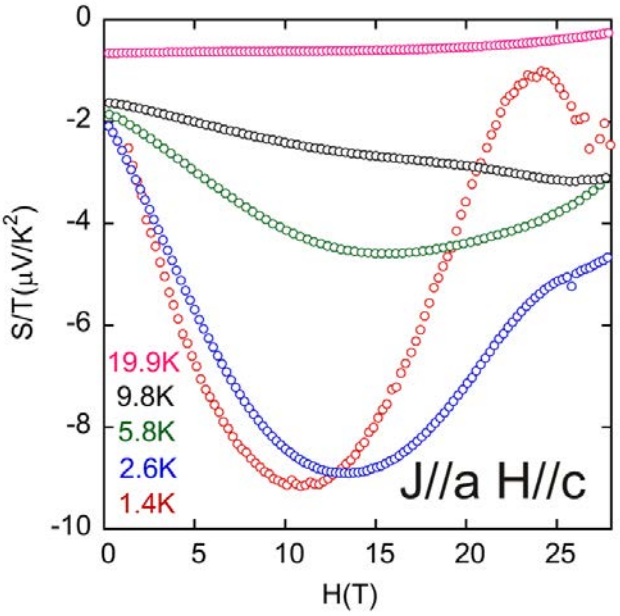


FIG. 76. *Thermopower divided by temperature $S/T$ as a function of field $H$ at several different temperatures. Below 17.5 K a large increase is observed consistent with the HO state, this increase is suppressed at lower temperatures and high fields suggesting a Fermi surface change.*

***L. Malone, C. Proust***
***T. Matsuda, V. Taufour, D. Aoki, G. Knebel, J. Flouquet (CEA-SPSMS, Grenoble), K. Behnia (ESPCI, Paris)***

# Pressure and magnetic field criticality in the heavy fermion compound $CeRu_2Si_2$

$CeRu_2Si_2$ is one of the rare heavy fermion compounds where the Fermi surface has been fully determined in the low field paramagnetic ground state. In this Ising like heavy fermion system close to antiferromagnetic (AF) quantum criticality, the new feature is that applying a magnetic field along the easy magnetization $c$-axis of this tetragonal crystal leads to spectacular pseudo-metamagnetic transition at $H = H_m$ directly linked to the occurrence of real metamagnetic transition observed by expanding the volume with La substitution.

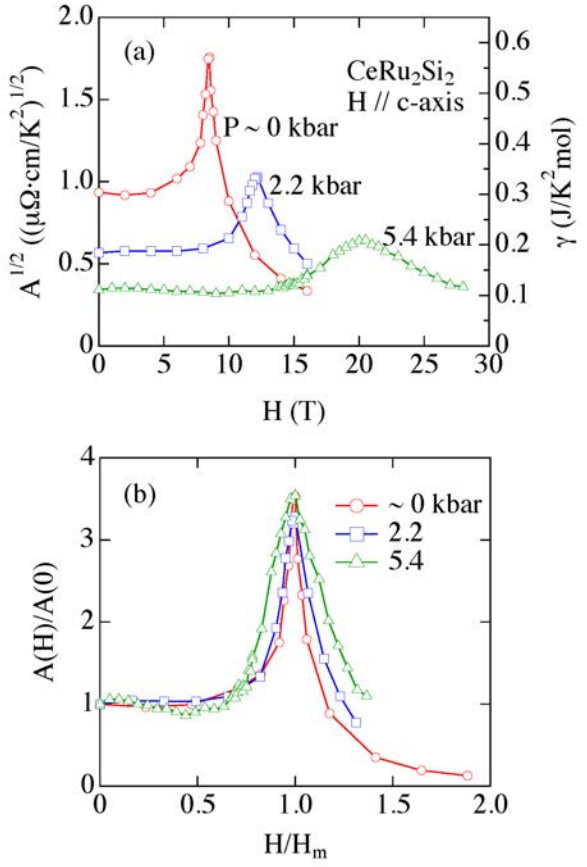


FIG. 77. *(a) Field dependence of the square root of A coefficient of resistivity for $H \parallel c$-axis under pressure in $CeRu_2Si_2$. The right axis is the corresponding Sommerfeld coefficient from Kadowaki-Woods relation. (b) Normalized A coefficient as a function of the normalized field at $H_m$.*

Our simple idea was to look how the effective mass enhancement at $H_m$ will change as a function of the pressure ($P$). Knowing that at $H = 0$, the pressure driving the system far from AF criticality is characterized by a huge electronic Grüneisen parameter $\Omega_e \sim +200$. The estimation of the effective mass $m^*$ was derived through the field variation of the square root of the $A(H, P)$ coefficient of the resistivity, assuming the Kadowaki-Woods relation $m^* \propto \sqrt{A}$.

The resistivity measurements under pressure were performed using a piston cylinder cell at temperatures down to 0.4 K and at high fields up to 28 T. The low field measurements up to 16 T were performed using a conventional superconducting magnet at temperatures down to 70 mK. The results are summarized in figure 77. In good agreement with the previous experiments [Mignot *et al.*, Phys. Rev. B **40** 10917 (1989)], the Grüneisen parameter at $H_m$ $\Omega(H_m) \sim \Omega_e$, but the new feature is that the ratio of $A(H, P)/A(0, P)$ as a function of $H/H_m$ appears quite universal at least in this low pressure range.

Through these basic experiments plus previous magnetization data, the following picture emerges:

(i) The pseudo-metamagnetic transition occurs at a constant value of the magnetization confirmed by the quasi-invariance of $\sqrt{A(0, P)} \times H_m(P)$. Basically increasing by the magnetic field, the population of the majority spin drives the pseudo-metamagneic phenomena and the individual depairing mechanism between majority and minority spin enhances the low energy ferromagnetic (FM) response.

(ii) Increasing the pressure, the decrease of the strength of AF correlation is in good agreement with the pressure moving from AF instability. That produces a P smearing of the AF pseudo-gap at $H = 0$.

(iii) However, it is known that from this AF pseudo-gap shape the FM fluctuation are built through the production of a $H$ induced magnetization. The beautiful proof of this is the pressure invariance of $A(H_m/P)/A(0, P)$ and the excellent scaling of $A(H, P)/A(0, P)$ in the reduced variable $H/H_m$.

***L. Malone***
***T. D. Matsuda, D. Aoki, J. Flouquet (CEA-SPSMS, Grenoble, France), R. Settai, Y. Ōnuki (Osaka University, Japan)***

# High-field magnetoresistance and enhancement of the effective mass in $CeRh_2Si_2$

The heavy-fermion antiferromagnet $CeRh_2Si_2$ can be driven to an antiferromagnetic-to-paramagnetic quantum phase transition either by applying magnetic field or hydrostatic pressure. Interest for this system is increased by the presence of superconductivity at the pressure-induced magnetic instability [Movshovich *et al.*, Phys. Rev. B **53**, 8241 (1996)], which indicates that magnetism and superconductivity are intimately connected.

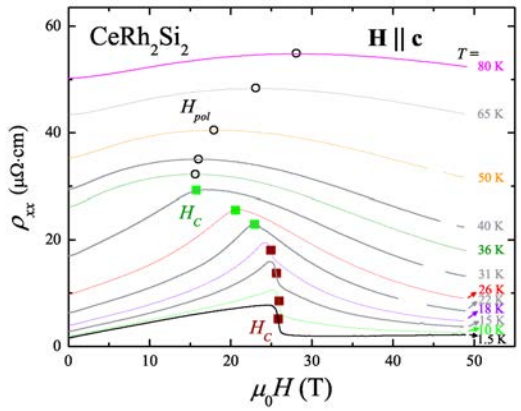


FIG. 78. *Magnetoresistivity of the antiferromagnet $CeRh_2Si_2$ for $H \parallel c$ and $1.5 \leq T \leq 80$ K.*

We have investigated the magnetic field-temperature phase diagram of $CeRh_2Si_2$ at ambient pressure, in pulsed fields $H \parallel c$ up to 50 T. Magnetoresistivity measurements (see figure 78) have been carried out between 1.5 K and 80 K and permitted to evidence different lines of the magnetic phase diagram; the transition field $H_C$ between the low-field antiferromagnetic phase and the high-field polarized regime (below $T_N$), and a crossover field $H_{pol}$ between the low-field paramagnetic phase and the high-field polarized regime (above $T_N$).

The temperature dependence of the resistivity $\rho_{x,x}(T)$ at different magnetic fields has been extracted from our measurements of $\rho_{x,x}(H)$ at different temperatures. Assuming the validity of a Fermi liquid description, the low-temperature resistivity has been fitted by $\rho(T) = \rho_0 + AT^2$ at several magnetic fields. Figure 79 shows a comparison between the field-variation of the quadratic coefficient $A$ extracted here and its hydrostatic pressure-dependence, taken from [Boursier, PhD-thesis, Université Joseph Fourier, Grenoble (2005)] and [Araki *et al.*, J. of Phys.: Condens. Matter **14**, L377 (2002)], in a $A/A_{max}$ versus $(\delta - \delta^*)/\delta^*$ plot where $A_{max}$ is the maximal value of $A$, $\delta = H$ or $p$, and $\delta^*$ corresponds to the critical value of $\delta$ ($\delta^* = \mu_0 H_c =$ 26 T or $p_c = 11$ kbar). The enhancement of $A$ is very similar at the magnetic field- and at the pressure-induced instabilities. Knowing that $A$ is proportional to the square $m^{*2}$ of the effective mass of the electrons, both kinds of instabilities are thus related to similar mass enhancements. For conventional magnetic materials, applying a magnetic field is expected to change the universality class of the magnetic phase transition. While a pressure-induced instability is expected to be associated with an enhancement of the antiferromagnetic fluctuations [Knafo *et al.*, Nature Physics **5**, 753 (2009)], a field-induced instability is believed to be related to an enhancement of the ferromagnetic fluctuations [Flouquet *et al.*, J. Magn. Magn. Mat. **272-276**, 27 (2004)]. The similar enhancements of the effective mass reported for $CeRh_2Si_2$ under pressure and magnetic field are thus not obvious and might deserve further consideration. Finally, a marked field enhancement of $A$ starts at a field near $\mu_0 H \simeq 15$ T. Despite the strong first-order nature of the quantum metamagnetic transition at $H_c$ (where the magnetization jumps by $\Delta M = 1.4\ \mu_B$/Ce-ion), the field-enhancement of $A$ occurs far below $H_c$, *i.e.* at $(H - H_c)/H_c \simeq 0.5$.

Finding a $H$- or $p$-induced singularity in the density of states to explain the common convergence of $m^*(p_c)$ with $m^*(H_M)$ is a key issue. Of course, an appealing route is to look deeper than before to the Fermi surface instability with the idea that the singularity has to be marked in the $p$ and $H$ evolution of the Fermi surface.

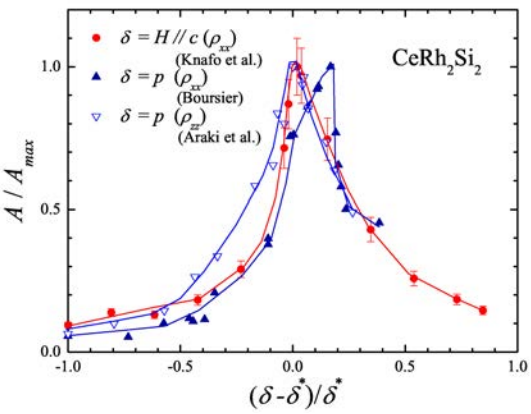


FIG. 79. *Comparison of the field- and pressure-dependence of the quadratic coefficient $A$ of the resistivity of $CeRh_2Si_2$, in a $A/A_{max}$ versus $(\delta - \delta^*)/\delta^*$ plot.*

***W. Knafo, D. Vignolles, B. Vignolle, Y. Klein, C. Jaudet, C. Proust***
***D. Aoki, J. Flouquet (SPSMS, CEA Grenoble)***

# Diamagnetic phase diagrams of Be

Quantum oscillations of the magnetization (de Haas-van-Alphen or dHvA effect) remain a powerful tool in investigation of the Fermi surface (FS) topography and quasiparticle spectra of metals. For three-dimensional metals, only the extremal cyclotron orbits in the space of wave vector **k** lead to an observable magnetization, and the quantitative treatment in this case has been known for decades. Long time ago, it was also established that the thermodynamic instability arises when a differential magnetic susceptibility $a \equiv \mu_0 \max\{\partial M/\partial B\} \geq 1$, where $M$ is the oscillatory part of the magnetization and $B$ is the magnetic induction of a sample. At this condition, the instability is avoided by stratification of the sample into domain patterns with formation of non-uniform diamagnetic structure (Condon domains).

Recently, it was shown [Kramer *et al.*, Phys. Rev B **82**, 075101 (2010)] that the measurement of the diamagnetic hysteresis and non-linear response upon entering the Condon domain phase allows to determine the phase boundary with high precision in a wide temperature and magnetic field range. This offers the possibility for a detailed comparison with the theoretical calculation of the phase diagram.

The proper calculation of the amplitude of the dHvA oscillations and phase diagram for Be relies on the knowledge of the topography of the FS. Being a compensated metal with equal densities of charge carriers, i. e. electrons and holes, Be has the simplest FS that differs essentially from the free electron model. The FS of Be consists of the second zone monster ('coronet') and the third zone 'cigar' (figure 80). In applied magnetic field **H** ∥[0001], the dHvA oscillations originate from three extremal cross-sections of 'cigar' ('waist' and 'hips') which are characterized by anomalously low curvature and slightly different cross-sectional areas. The small curvature of the extremal cross-sections results in high amplitude of the dHvA oscillations which survive at relatively high values of Dingle temperature, $T_D = \hbar/2\pi k_B \tau \approx 2.5$ K ($\hbar$ is the Planck constant, $k_B$ is the Boltzmann constant and $\tau$ is a scattering lifetime of conduction electrons), putting Be an a row of the most attractive metals in investigation of the diamagnetic instability. But long time, it has remained a puzzle in quantitative description of the diamagnetic phase transition due to the difficulties in experimental arrangements, uncertainty in the characteristic sizes of FS and absence of the reliable data on diamagnetic instability in a whole range of magnetic field, $H$, and temperature, $T$.

The starting point in the calculation of the differential magnetic susceptibility and construction of the phase diagram is the oscillatory part of the free energy density for electron gas under quantizing magnetic field

$$\Omega = \frac{(eH)^2}{(2\pi^2 c)^2 m_c} \int dk_z \cos[2\pi X(\mu, k_z)], \qquad (8)$$

where $e > 0$ is elementary charge, $c$ is the speed of the light, $k_B$ is the Boltzmann constant, $m_c$ is the electron cyclotron mass, and $\mu$ is the chemical potential. The quantity $X(\mu, k_z)$ is related to the cross-sectional area of the FS $\mathcal{A}(\mu, k_z)$ at the point $k_z$ in **k**-space according to $X(\mu, k_z) = c\hbar\mathcal{A}(\mu, k_z)/2\pi eH - \gamma$ where the phase correction $\gamma$ is typically chosen to be equal to 1/2. In case of beryllium the series expansion of electron orbit area $\mathcal{A}(\mu, k_z)$ about the extremal cross-section is not appropriate due to the vanishing curvature. The additional disadvantage arises from the fact that neither curvature factor nor its derivatives are available from the experiment. This implies the necessity of development of model representations of the FS of Be (see, figure 80). We found the satisfactory agreement with the data for $c_h = 0.35$ and $c_w = 0.625$.

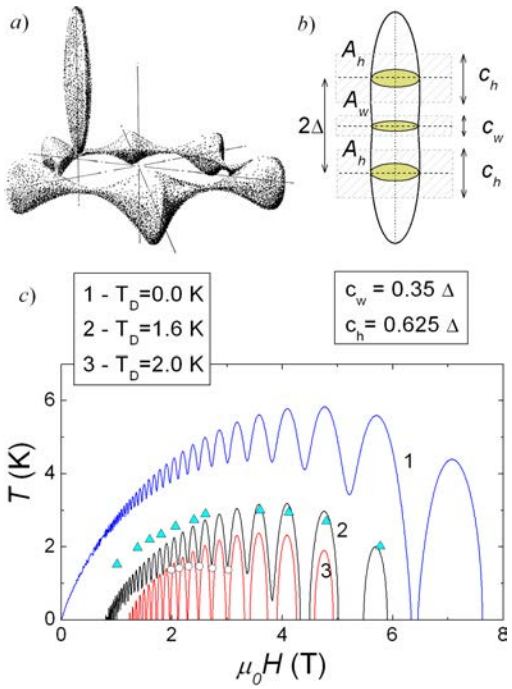


FIG. 80. *(a) Fermi-surface of beryllium (from [Loucks et al., Phys. Rev. **133**, A819 (1964)], (b) modelling of the FS ('cigar') relevant for observation of diamagnetic instability and (c) the phase boundary in $TH$-plane calculated at three different Dingle temperatures $T_D$ =0, 1.6 and 2 K (curves 1, 2 and 3). Condon domains occupy the area under the correspondent curve 1, 2 or 3. The open circles (triangles) represent the data [Kramer et al., Phys. Rev B **82**, 075101 (2010)] for beating nodes (antinodes).*

***W. Joss***
***N. Logoboy (The Racah Institute of Physics, The Hebrew University of Jerusalem, Jerusalem, Israel and The Institute of Superconductivity, Department of Physics, Bar-Ilan University, Ramat-Gan, Israel)***

# Specific heat on pnictide $FeSe_{0.5}Te_{0.5}$ superconductor

The discovery of superconductivity up to 55K in iron-based systems has generated tremendous interest. Among those, iron selenium ($FeSe_{1-\delta}$) has been reported to be superconducting with a critical temperature of 8 K at ambient pressure, rising to $34-37$ K under $7-15$ GPa. On the other hand, the substitution of tellurium on the selenium site in $Fe_{1+\delta}(Te_xSe_{1-x})$ increases $T_c$ to a maximum on the order of $14-15$ K at ambient pressure (for $x \sim 0.5$). This binary compound is very interesting as it shares the most salient characteristics of iron based systems (square-planar lattice of Fe with tetrahedral coordination) but has the simplest crystallographic structure among Fe-based superconductors. However, in contrast to iron pnictides which show only weak to moderate correlations, recent ARPES measurements suggested the existence of very large mass renormaliszation factors (up to $\sim 20$ as compared to DMFT calculations) indicating that Fe(Se,Te) is a strongly correlated metal differing significantly from iron pnictides.

In order to shed light on superconductivity in these systems, it is of fundamental importance to obtain a precise determination of the upper fields and its anisotropy. Strong deviations - associated to paramagnetic limitations - from the standard Werthamer-Helfand-Hohenberg model for $H_{c2}(T)$ have been reported but, in presence of strong thermal fluctuations, the determination of $H_{c2}$ from transport measurement becomes very hazardous and a thorough analysis was hence lacking of an unambiguous determination of $H_{c2}$ from specific heat ($C_p$) measurements.

A miniaturized high-resolution micro-calorimeter using the long-relaxation technique is used to measure $C_p$. The chip resistance used as both thermometer and heater as well as the thermal conductance of its leads have been carefully calibrated up to 28 T using a capacitance thermometer. Each relaxation provides about 1000 data points over a temperature interval of about 80% above the base temperature which has been varied between 1.8 and 20 K.

Figure 81(A) shows a well defined specific heat jump at $T_c$ for $H = 0$ ($\sim$ 20% of the total $C_p$) and this peak progressively shifts towards lower temperature with increasing magnetic field ($H \| c \leq 28$ T). The $H_{c2}$ line has been deduced from the mid-point of the $C_p/T$ anomaly. The corresponding $H_{c2}$ lines (figure 81(B)) present a very strong downward curvature for $T \to T_c$ which was not revealed by previous transport measurements. To emphasize this point, we have reported the temperatures corresponding to both $R \to 0$ and $R/R_N = 0.5$ deduced from transport measurements ($R_N$ being the normal state resistance). Such a curvature is a strong indication for paramagnetic effects and the $H_{c2}$ lines can be well fitted using a weak coupling BCS clean limit model including both orbital and Pauli limitations. This model only requires two fitting parameters (plus $T_c$); the initial slope $dH_{c2}/dT|_{T=T_c}$ and the zero temperature Pauli limit $H_p$ leading to; $\mu_0 dH_{c2}/dT|_{T=T_c} \sim 38 \pm 3$ T/K and $\sim 13 \pm 2$ T/K for $H \| ab$ and $H \| c$ respectively and $\mu_0 H_p \sim 45 \pm 2$ T and $\sim 54 \pm 4$ T/K for $H \| ab$ and $H \| c$, respectively.

Those extremely high $dH_{c2}/dT$ values are related to very small values of the coherence lengths $\xi_{ab} = \Phi_0/2\pi[0.7 \times \mu_0(dH_{c2}/dT) \times T_c] \sim 15 \pm 1\mathring{A}$ and $\xi_c = \xi_{ab} \times (H_o^{\|c}/H_o\|ab) \sim 4 \pm 1\mathring{A}$ which confirm the very strong renormalization of the Fermi velocity observed in ARPES measurements. Indeed, one gets $v_{F,ab} = \pi\Delta\xi_{ab}/\hbar \sim 1.4 \times 10^4$ m/s ($\Delta$ being the superconducting gap $\sim$ 2 meV) *i.e.* $\hbar v_{F,ab} \sim 0.09$ eV$\mathring{A}$ in perfect agreement with ARPES data hence confirm the strong correlation effects suggested by those measurements.

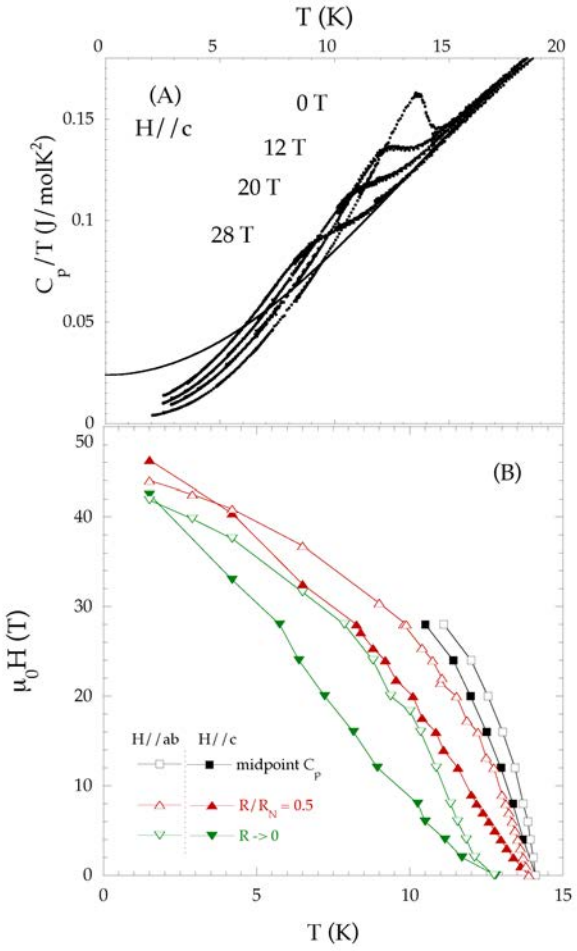


FIG. 81. *Temperature dependence and corresponding $H-T$ phase diagram in Fe(Se,Te)*

***A. Demuer, I. Sheikin***
***D. Braithwaite, C. Marcenat, G. Lapertot (SPSMS, CEA-INAC, Grenoble, France)***
***T. Klein, P. Toulemonde (Institut Neel, CNRS, Grenoble, France)***

# First observation of quantum oscillations in the ferromagnetic superconductor UCoGe

Ferromagnetism had been thought to be antagonistic to superconductivity, because the large internal field destroys the superconducting Cooper pairs easily. New superconductors, $UGe_2$, URhGe and UCoGe, which show the coexistence with ferromagnetism, thus attract much interests. The response to pressure and field, which tune the ground state between superconductivity and the ferromagnetic singularity, is different for all systems. Up to now, it is only in $UGe_2$ that the Fermi surface has been experimentally determined, since the large high quality single crystal can be easily obtained for de Haas-van Alphen experiments. Detection of quantum oscillations for the other systems will open up new perspectives.

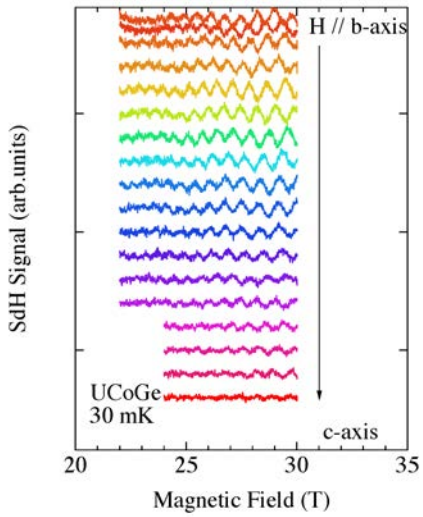


FIG. 82. *SdH oscillations for the field direction from b-axis to c-axis in UCoGe.*

The weak itinerant ferromagnet UCoGe with TiNiSi-type orthorhombic structure is an interesting case. The ordered moment directed along the $c$-axis is small, $M_0 \approx 0.05\,\mu_B$, and the Curie temperature is $T_{Curie} \approx 2.6\,K$. Superconductivity appears below $T_{sc} \approx 0.6\,K$ [Huy *et al.*, Phys. Rev. Lett. **99**, 067006 (2007)].

A striking point is the detection of huge and highly anisotropic superconducting upper critical field $H_{c2}$ [Aoki *et al.*, J. Phys. Soc. Jpn. **78**, 113709 (2009)]. When the field is applied along the hard-magnetization $b$ and $a$-axis, $H_{c2}$ reaches 17 T and 30 T, respectively. On the other hand, for the field along $c$-axis, $H_{c2}$ is only 0.6 T, which is close to the Pauli limit based on the weak coupling BCS model. This suggests that for $H \parallel a$ and $b$-axis, magnetic field induces magnetic fluctuation, and consequently enhances the effective mass, as observed for the field re-entrant superconductivity in URhGe with the identical crystal structure. It is also suggested from theory that the multi-band effect is important to explain the peculiar shape of $H_{c2}$ curve.

Magnetoresistance of a high quality single crystal of the ferromagnetic superconductor UCoGe was measured at high fields up to 34 T and temperatures down to 40 mK [Aoki *et al.*, to be published in J. Phys. Soc. Jpn. No. 1 (2011)]. The Shubnikov-de Haas (SdH) signal was observed for the first time in a U-111 system (UTGe, UTSi, T: transition metal). Figure 82 shows the SdH oscillations from $H \parallel b$-axis to $c$-axis in UCoGe. A detected frequency is relatively small ($F \sim 1\,kT$), showing no significant angular dependence, meaning a small pocket Fermi surface is detected. However, the detected cyclotron effective mass is large, $25\,m_0$ at 28 T. These results imply that UCoGe is a low carrier system with heavy quasi-particles. A similar situation is also realized in the semi-metallic heavy fermion superconductor $URu_2Si_2$.

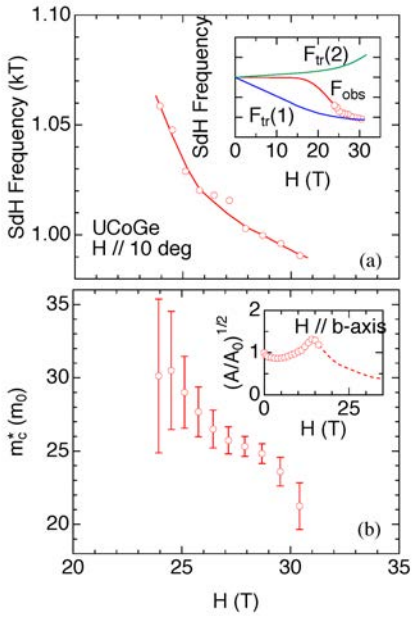


FIG. 83. *(a)Field dependence of the observed SdH frequency. The inset shows the schematic field dependence of the "true" SdH frequency $F_{tr}$ and the observed frequency $F_{obs}$. (b) Field dependence of the cyclotron mass. The inset is the field dependence of the square root of A coefficient of the resistivity.*

As shown in Fig. 83(a), the observed frequency decreases with increasing field, indicating that the volume of detected Fermi surface changes non-linearly with field. The cyclotron mass decreases as well (see Fig. 83(b)), which is consistent with the decrease of the $A$-coefficient of resistivity.

***I. Sheikin***
***D. Aoki, T. D. Matsuda, V. Taufour, G. Knebel, J. Flouquet (CEA-SPSMS, Grenoble, France)***

# Fermi-surface topology of the iron-pnictide compound $LaFe_2P_2$ and the isostructural superconductor $BaIr_2P_2$

The recent discovery of superconductivity in iron pnictides with a critical transition temperature up to $T = 55$ K has opened up a new class of high-temperature superconductors besides the long-known cuprates. The crystal structure of one class among these newly discovered superconductors contains $M_2X_2$ layers, where M is Fe, Co, or Ni and X is one of the pnictogenes which are separated by alkali metals. Suppression of spin fluctuations either by external pressure or by doping with alkali ions (K, Na, and Cs) enabled to reach superconducting transition temperatures as high as 38 K [Rotter *et al.*, Phys. Rev. Lett. **101**, 107006 (2008)]. In addition, partial substitution of the nonmagnetic 4*d* and 5*d* metals for the Fe atoms also leads to superconductivity. Despite the fact that the role of magnetism and especially that of Fe is not yet clear at this point, the full substitution of the Fe atoms by Ir and Rh is particularly interesting, since the superconductivity has also been discovered in $BaIr_2P_2$ ($T_c = 2.1$ K) and $BaRh_2P_2$ ($T_c = 1.0$ K) [Berry *et al.*, Phys. Rev. B **79**, 180502 (2009)]. Knowledge of the Fermi-surface topology is an important requirement in order to understand the mechanism responsible for superconductivity in the pnictide superconductors. In particular, topological changes upon elemental substitution may give valuable information on the importance of certain electron or hole bands for the superconducting state.

We have performed a detailed study of the Fermi-surface topology of two different samples. The first is the nonmagnetic nonsuperconducting Fe-based compound $LaFe_2P_2$, the second is a nonmagnetic superconductor without Fe, $BaIr_2P_2$. We used a torque-magnetometer setup mounted on a rotator platform to measure the angular dependence of de Haas-van Alphen oscillations (dHvA). Preliminary dHvA measurements performed in a superconducting 20 T magnet at the Dresden High Magnetic Field Laboratory in combination with band-structure calculations showed that higher fields are needed to resolve more of the predicted dHvA frequencies. The high fields and low temperatures provided by the 34 T resistive magnet and dilution refrigerator allowed us to obtain sizable oscillations and a more complete picture of the Fermi-surface topology.

For $LaFe_2P_2$, we measured for different field orientations within the *ac* plane, a plane, which is perpendicular to the FeP layers. The angular dependence of the observed dHvA frequencies allows us to identify the Fermi-surface sheets from which they originate (figure 84). Rotating away from the *c* axis we observed a $1/\cos\theta$ like behavior for the frequencies $F_\alpha$ and $F_\beta$ which can be interpreted as signatures of strongly corrugated Fermi cylinders. The existence of Fermi cylinders is a direct evidence of quasi-2D Fermi surfaces, which are a consequence of the layered structure, while the strong corrugation indicates a considerable coupling between the layers. Similar results were obtained for $BaIr_2P_2$ (figure 85). The most obvious distinction in the Fermi-surface topology of the two materials is that $BaIr_2P_2$ has significantly bigger and stronger corrugated Fermi cylinders: $F_\alpha$ and $F_\beta$ are about three times higher. The investigated compounds are somewhere between 2D and 3D metals which leads to not very large anisotropies of such properties as resistance or critical fields. The other dHvA frequencies observed evidence the existence of a truly 3D Fermi surface as suggested by band-structure calculations. From the temperature dependence of the dHvA oscillations we were able to determine the band-selective effective masses at some distinct orientations. The mass enhancement was approximately a factor of 2, which was also found for other compounds of the family.

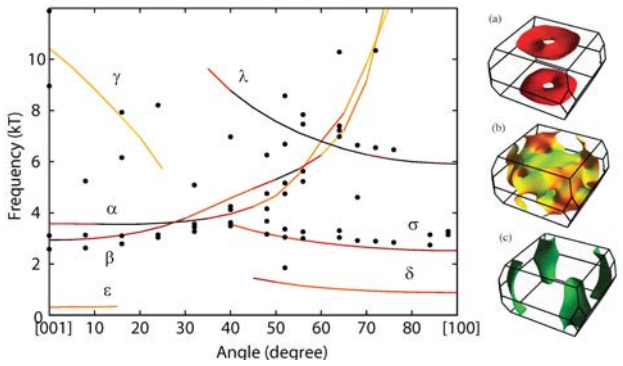


FIG. 84. *Angular dependence of the measured de Haas-van Alphen frequencies (points) with corresponding theoretical results (lines) for $LaFe_2P_2$. (a), (b) and (c) show calculated Fermi surfaces of $LaFe_2P_2$.*

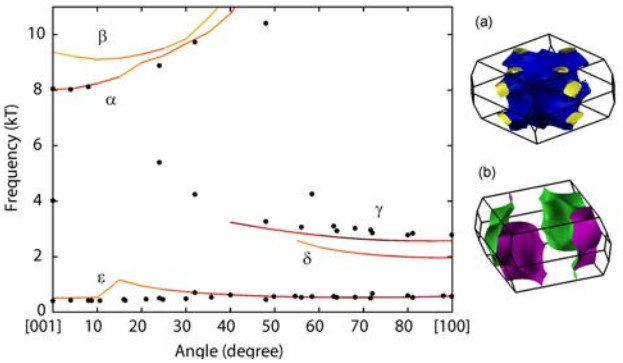


FIG. 85. *Angular dependence of the measured de Haas-van Alphen frequencies (points) with corresponding theoretical results (lines) for $BaIr_2P_2$. (a) and (b) show calculated Fermi surfaces of $BaIr_2P_2$.*

***I. Sheikin***
***O. Ignatchik (Dresden High Magnetic Field Laboratory, Dresden, Germany), M. Bartkowiak (Paul Scherrer Institut, Villigen, Switzerland)***

# Search for magnetic quantum oscillations in the electron-doped superconducting cuprate $Nd_{2-x}Ce_xCuO_4$

Knowing the exact Fermi surface and its dependence on the doping level is pivotal for understanding the mechanism of superconducting pairing in high-$T_c$ cuprate superconductors. Recently, a breakthrough in the Fermiology of high-$T_c$ superconductors was made by observation of magnetic quantum oscillations in hole-doped yttrium-barium and thallium-barium and electron-doped neodymium-cerium cuprates. The origin of the revealed Fermi surface, its shape and position in the Brillouin zone are, however, still a matter of debate. The aim of this experiment was a search and quantitative study of de Haas-van Alphen (dHvA) and Shubnikov-de Haas (SdH) oscillations in the electron-doped superconductor $Nd_{2-x}Ce_xCuO_4$ (NCCO).

Using the piezoresistive microcantilever technique, we performed measurements of magnetic torque, searching for the dHvA effect in an optimally doped, $x = 0.15$, NCCO crystal. The main problem here was a very strong anisotropic contribution of $Nd^{3+}$ moments to magnetization. One could, however, expect the magnetization to saturate at high fields, making it easier to find quantum oscillations on a flattened background. The sample chosen for the experiment had a very small size, $\sim 70 \times 20 \times 10\,\mu m^3$ ($m \approx 0.1\,\mu g$). Nevertheless, the torque signal associated with $Nd^{3+}$ was still extremely strong and the measurements could only be done at very small tilt angles (between the field and the crystal $c$-axis) $\theta \leq 2°$. At $\theta = 2.4°$ the cantilever deflection reached $\sim 60\%$ of the critical value at which the cantilever breaks.

Figure 86 shows examples of the field-dependent torque at $T = 4.2\,K$. Surprisingly, the torque shows a monotonic superlinear growth up to the highest field applied. At $\theta = 2.4°$ a kink is detected in the up-sweep, indicating that the sample holder is slightly turned in the field due to the strong torque. At lower $\theta$ we succeeded in obtaining reversible signals. However, no dHvA oscillations were found at these small angles.

Another issue addressed in the present experiment, was SdH oscillations in a slightly overdoped, $x = 0.16$, NCCO. While slow oscillations have already been reported for this composition [Helm *et al.*, Phys. Rev. Lett. **103**, 157002 (2009)], their amplitude was too small for quantitative analysis. In this experiment we have achieved a significantly higher signal-to-noise ratio, $\gtrsim 10^4$. Thus, we could resolve and analyze the oscillations in the field range down to below 30 T, see figure 87. The oscillation frequency obtained from this data is $\approx 290$ T, which originates from small hole pockets of the reconstructed Fermi surface and is consistent with that reported earlier within the experimental error bar. The effective cyclotron mass is $m_c \approx 0.72 m_e$ ($m_e$ is the free electron mass). A comparison of this result with the values obtained for other doping levels could elucidate the doping dependence of many-body interactions. Such work is in progress.

Most interestingly, new, fast oscillations emerge at fields $\gtrsim 60$ T, which is emphasized in the inset in figure 87. The oscillation frequency, 11200 T, corresponds to a Fermi surface cross section consistent with the large unreconstructed Fermi cylinder. Similar oscillations were observed in strongly overdoped samples and attributed to magnetic breakdown [Helm *et al.*, arXiv:1008.3371]. Further analysis of both the slow and fast oscillations and their evolution with doping should bring important information on the doping dependence of the superlattice potential responsible for the Fermi surface reconstruction in NCCO.

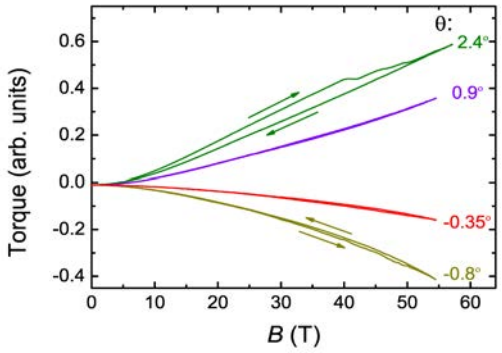


FIG. 86. *Magnetic torque of an optimally doped, $x = 0.15$, NCCO sample at 4.2 K at different tilt angles $\theta$. Signal is determined by paramagnetic $Nd^{3+}$ ions; no dHvA oscillations are seen. Arrows show the field sweep directions.*

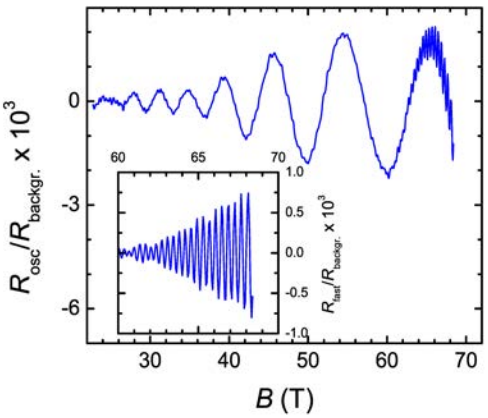


FIG. 87. *SdH oscillations normalized to the background interlayer resistance of slightly overdoped, $x = 0.16$ NCCO at $T = 2.5$ K. Inset: fast oscillations emerging at fields above $\sim 60$ T; the curve is obtained from the data in the main panel after filtering out the slow SdH oscillations.*

***S. Lepault, D. Vignolles, C. Proust***
***W. Biberacher, T. Helm, M. Kartsovnik (Walther-Meissner-Institut, Garching, Germany)***

# Lifshitz critical point in the cuprate superconductor $YBa_2Cu_3O_y$ from high-field Hall effect measurements

The Hall coefficient $R_H$ of the cuprate superconductor $YBa_2Cu_3O_y$ was measured in magnetic fields up to 60 T for a hole concentration $p$ from 0.078 to 0.152, in the underdoped regime. In fields large enough to suppress superconductivity, $R_H(T)$ is seen to go from positive at high temperature to negative at low temperature, for $p > 0.08$. This change of sign is attributed to the emergence of an electron pocket in the Fermi surface (FS) at low temperature [LeBoeuf *et al.*, Nature 450, **533** (2007)]. At $p < 0.08$, the normal-state $R_H(T)$ remains positive at all temperatures, increasing monotonically as $T \to 0$. We attribute the change of behaviour across $p = 0.08$ to a Lifshitz transition, namely a change in Fermi-surface topology occurring at a critical concentration $p_L = 0.08$, where the electron pocket vanishes. The loss of the high-mobility electron pocket across $p_L$ coincides with a ten-fold drop in the conductivity at low temperature, revealed in measurements of the electrical resistivity $\rho$ at high fields, showing that the so-called metal-insulator crossover of cuprates is in fact driven by a Lifshitz transition. For more information see [LeBoeuf *et al.*, arXiv:1009.2078].

$R_H(B)$ at $T = 10$ K is plotted in figure 88 top panel, for three different hole dopings. In the normal state beyond the flux-flow regime, $R_H$ is seen to be positive at $p = 0.078$ but negative at $p = 0.097$ and 0.120, pointing to a qualitative change in the FS occuring between $p \simeq 0.08$ and $p \simeq 0.10$. This change corresponds to a Lifshitz transition, where the electron pocket detected in quantum oscillations experiment in YBCO disappears. The loss of this high mobility electron pocket through the Lifshitz transition at $p_L \simeq 0.08$ should have a major impact on the electrical conductivity of the system. It does, as shown in figure 88 bottom panel, where $\rho$(T) at $B = 55$ T is plotted for $p = 0.11$ and $p = 0.08$. At $p = 0.08$, $\rho(B = 55\ \text{T})$ shows a pronounced upturn below 50 K, giving $\rho(B = 55\ \text{T}) \simeq 225\ \mu\Omega$cm at $T = 0.4$ K. At $p = 0.11$, there is no such upturn and $\rho(B = 55\ \text{T}) \simeq 45\ \mu\Omega$cm at $T \to 0$. The so-called metal-insulator crossover of cuprates is hence driven by a Lishitz transition causing the loss of the high mobility part of the FS.

Our data put new constrains on the possible scenarios of FS reconstruction in YBCO. Below $p_L \simeq 0.08$, where the electron pocket is gone, the conductivity [Ando *et al.*, Phys. Rev. Lett. **88**, 137005 (2002)] and the inelastic neutron scattering [Hinkov *et al.*, Science **319**, 597 (2008)] are anisotropic, indicating that the hole-like part of the reconstructed FS breaks the four-fold rotational symmetry of the $CuO_2$ planes. Such anisotropy, as well as the observed Lifshitz transition, are consistent with a FS reconstruction induced by a stripe order, i.e. a combination of charge and spin density wave. Figure 89 sketches the possible FS evolution through $p^\star$, the $T = 0$ FS reconstruction critical point, and then $p_L$ in this stripe scenario.

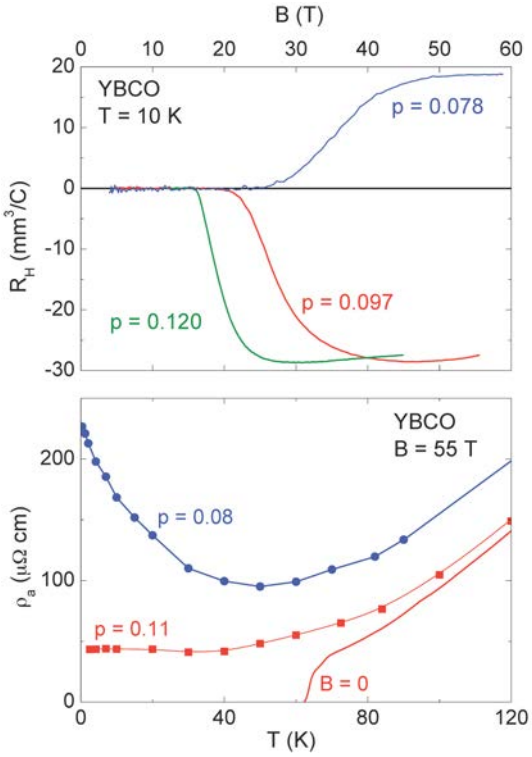


FIG. 88. *Top panel : Hall coefficient $R_H$ as a function of magnetic field at $T = 10$ K for $p = 0.120$, $p = 0.097$ and $p = 0.078$. Bottom panel : $\rho_a(T)$ for $B = 55$ T (closed symbols), for $p = 0.08$ (blue dots) and $p = 0.11$ (red squares). The continuous (red) curve is $\rho_a(T)$ in zero field.*

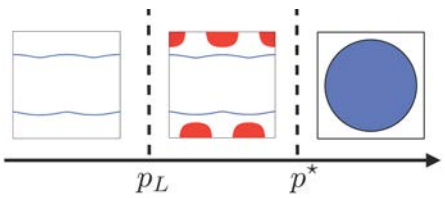


FIG. 89. *Schematic illustration of possible FS reconstruction by stripe order in cuprates. $p_L$ is the Lifshitz critical points where the reconstructed FS undergoes a change of topology: a loss of the small electron pocket. Closed blue pockets are hole-like; closed red pockets are electron-like; wavy blue lines are open FS. For $p < p^\star$, only the first quadrant of the square lattice Brillouin zone is shown.*

***B. Vignolle, J. Levallois, C. Proust***
***D. LeBoeuf, N. Doiron-Leyraud, R. Daou, F. Laliberté, O. Cyr-Choinière, J. Chang, L. Taillefer (Université de Sherbrooke, Canada), M. Sutherland (University of Cambridge, U.K.), L. Balicas, Y. J. Jo (NHMFL, USA), B. J. Ramshaw, R. Liang, D. A. Bonn, W. N. Hardy (UBC, Canada)***

# Phase fluctuations in overdoped $La_{2-x}Sr_xCuO_4$

In underdoped high-$T_c$ cuprate superconductors, phase stiffness is extremely low and long-range superconducting order is destroyed readily by thermally-generated vortices (and anti-vortices), giving rise to a broad temperature regime above the zero-field superconducting transition $T_{c0}$ in which the superconducting phase is incoherent. It has often been suggested that these vortex-like excitations are related to the normal state pseudogap or some interaction between the pseudogap state and the superconducting state. However, in order to elucidate the precise relationship between the pseudogap and superconductivity, it is important to establish whether this broad phase-fluctuation regime vanishes, along with the pseudogap, in the slightly overdoped region of the phase diagram where the superfluid pair density and correlation energy are both maximal. As it stands, there have been very few studies to date of the fluctuating superconductivity in overdoped, superconducting cuprates.

In order to address this, we studied the evolution of the upper critical field $H_{c2}$ with temperature, as determined by measurements of the in-plane resistivity $\rho_{ab}(T,H)$ in pulsed and dc magnetic fields. In this study, we make use of the well-known observation that the transverse magnetoresistance $\Delta\rho_{ab}(H)$ $(= \rho_{ab}(H)$ - $\rho_{ab}(0)$ with $\mathbf{H}\|c)$ in optimally and overdoped cuprates varies quadratically with field at temperatures well above the phase-fluctuation regime. Here, $H_{c2}$ is identified as the field at which $\rho_{ab}(H)$ recovers its quadratic field dependence. One surprising feature of the study is that while the absolute value of $H_{c2}(0)$ decreases with increasing doping, the onset temperature $T_{c2}$ for fluctuating superconductivity remains high, and even rises slightly as $x$ increases from 0.21 to 0.24. Beyond $x$ = 0.24, both $H_{c2}(0)$ and $T_{c2}$ appear to collapse as the edge of the superconducting dome is approached. The suppression of $H_{c2}(0)$ with overdoping reflects the overall reduction in the superconducting pairing strength as the system is doped further away from the parent Mott insulator.

In order to parameterize the extent of the fluctuation regime, we plot in figure 90 the ratio $T_{c2}/T_{c0}$ versus hole content $p$ (solid red squares). The ratio turns out to be surprisingly symmetrical, with a minimum at $x = p_{\rm crit} = 0.19$ where according to bulk transport and thermodymamic measurements, the normal state pseudogap energy scale collapses to zero. There is no obvious reason for amplitude fluctuations to follow such a trend. According to the original argument of Emery and Kivelson [Nature **374**, 434 (1995)], phase stiffness is determined predominantly by the superfluid density $\rho_s$; the smaller $\rho_s$, the weaker the screening and the larger the region over which classical (thermal) phase fluctuations are important. In underdoped cuprates, $\rho_s$ is found to increase monotonically with $T_c$, indicating that the condensate density drops as $p$ is reduced and the pseudogap removes low-energy spectral weight that is never recovered upon entering the full Meissner state. Significantly, in overdoped cuprates too, $\rho_s$ also falls away as $T_c$ decreases, though for different reasons, namely pair-breaking and/or phase separation.

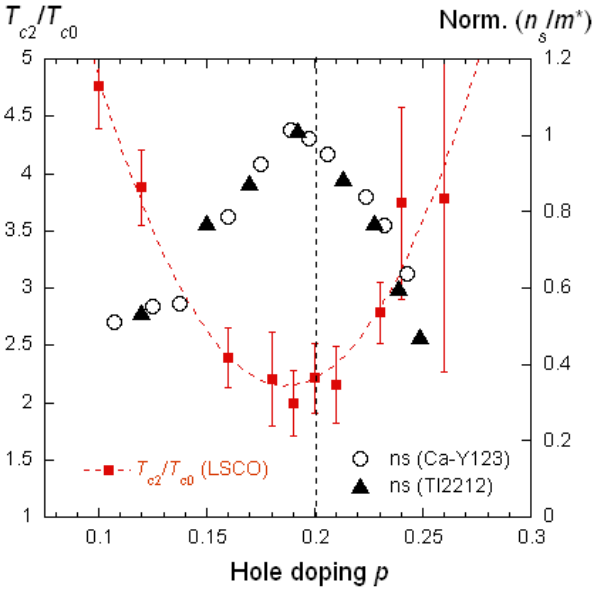


FIG. 90. *Ratio of $T_{c2}/T_{c0}$ versus hole content $p$ (solid squares) superimposed on a plot of the normalized superfluid density $\rho_s/\rho_s(p_{\rm crit})$ for Ca-doped $YBa_2Cu_3O_{6+\delta}$ (open circles) and $Tl_{0.5-y}Pb_{0.5+y}Sr_2Ca_{1-x}Y_xCu_2O_7$ (closed triangles), illustrating the anti-correlation between $\rho_s$ and the extent of the fluctuation regime.*

The open circles (closed triangles) in figure 90 correspond to estimates of the normalized superfluid density $\rho_s/\rho_s(p_{\rm crit})$ for Ca-doped $YBa_2Cu_3O_{6+\delta}$ ($Tl_{0.5-y}Pb_{0.5+y}Sr_2Ca_{1-x}Y_xCu_2O_7$) [Bernhard *et al.*, Phys. Rev. Lett. **86**, 1614 (2001)]. The clear anti-correlation between $T_{c2}/T_{c0}$ and $\rho_s(p)$ supports the Emery-Kivelson picture and provides evidence that the temperature interval $T_{c0} < T < T_{c2}$ in overdoped cuprates is characterized by the same phase fluctuations that appear on the underdoped side. The observed persistence of an extended fluctuation regime beyond $x = p_{\rm crit}$ in LSCO reveals that low phase rigidity in high-$T_c$ cuprates does not require the presence of a pseudogap in the normal state excitation spectrum and that the pseudogap itself is not a precondition for the development of an extended region of phase-fluctuating superconductivity.

***B. Vignolle, C. Proust***
***P. M. C. Rourke, N. E. Hussey (University of Bristol, UK)***

# Superconducting fluctuations, pseudogap and phase diagram in high-$T_c$ cuprates

The aim of these experiments was to suppress superconducting fluctuations in high-$T_c$ cuprates in order to reveal the underlying physical properties and to study the evolution of superconducting fluctuations with temperature and magnetic fields. All these experiments have been performed on single crystals of $YBa_2Cu_3O_{6+x}$ for different oxygen contents. Either pure and electron irradiated crystals have been studied.

We have proposed a relatively simple method based on the magnetic field dependence of the normal state magnetoresistivity to determine very accurately the threshold magnetic field above which the normal state is completely restored [Rullier-Albenque *et al.*, Phys. Rev. Lett. **99**, 027003 (2007)]. This is illustrated in figure 91 where the magnetoresistance $\delta\rho/\rho_0$ is plotted versus $H$ or $H^2$ for an optimally doped sample.

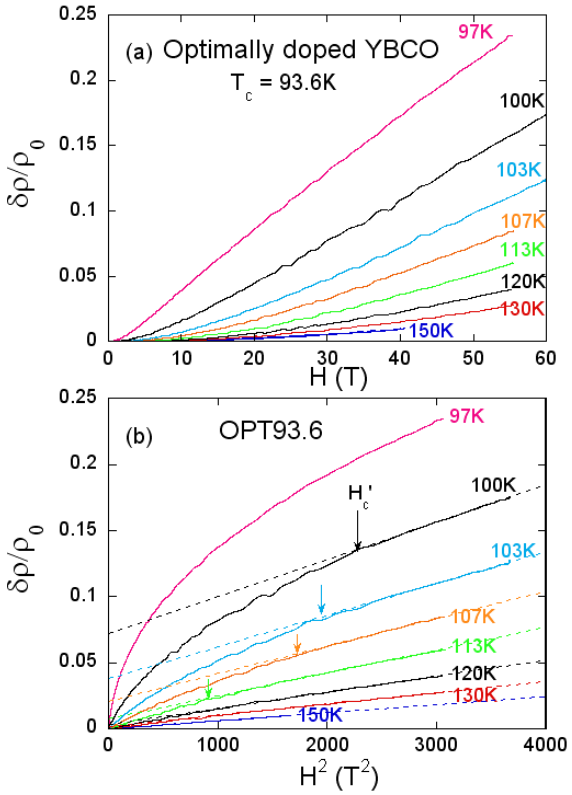


FIG. 91. *Resistivity increase normalized to its zero field value plotted versus $H$ (a) and $H^2$ (b) for decreasing temperatures in an optimally doped YBCO sample with $T_c = 93.6K$. For $T \geqslant 140K$, a $H^2$ dependence of the magnetoresistance, represented as dashed lines in (b), is observed for all values of field. For lower $T$, it is only seen above a given magnetic field $H'_c$, which is taken as the threshold field necessary to completely restore the normal state.*

We have shown that the superconducting fluctuations contribution to conductivity extends well above $T_c$, up to an onset temperature $T'_c$ larger that the onset temperature for Nernst signal. By studying samples with different hole dopings, we have been able to distinguish the effects of superconducting fluctuations (SCF) and pseudogap on the temperature dependence of the resistivity and to show that, in optimally doped samples, the onset of SCF occurs above the temperature of the pseudogap $T^*$. This definitely demonstrates that the pseudogap state cannot be considered as a precursor to superconductivity in these high-$T_c$ cuprates [Alloul *et al.*, Europhys. Lett. **91**, 37005 (2010)].

Studies of the incidence of disorder on both $T'_c$ and $T^*$ allow us to propose the phase diagram reported in figure 92 that includes disorder and explains most observations done in other cuprate families.

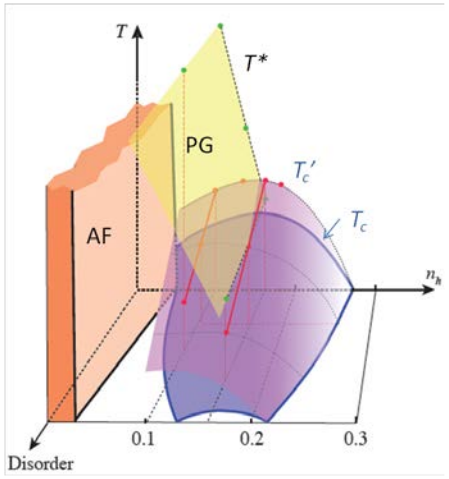


FIG. 92. *Phase diagram obtained from this study, showing the evolution of $T'_c$ the onset of superconducting fluctuations (SCF), with doping and disorder. The pseudogap and the SCF surfaces intersect each other near optimum doping in the clean limit. In the overdoped regime, data taken on Tl-2201 indicates that disorder suppresses SC without any anomalous extension of the SCF.*

On the other hand, the method developed here allowed us to determine, without any adjustable parameter, the temperature dependence of SCF in these compounds. While the SCF could be reasonably taken into account in the framework of Gaussian fluctuations in the optimally and slightly underdoped samples, this approach fails in the case of more underdoped samples.

***C. Proust, B. Vignolle***
***F. Rullier-Albenque (SPEC-CEA, Saclay, France), H. Alloul (LPS, Orsay, France)***

# Coherence crossover in the pseudogap phase of a cuprate superconductor

In a conventional metal, the electrical resistivity behaves in a similar manner whatever the direction of current. In the high-transition-temperature (high-$T_c$), copper oxide superconductors, where the electronic properties are quasi-two-dimensional, the in-plane resistivity is metallic down to $T_c$ in many underdoped cuprates while the interplane (along $c$-axis) resistivity is insulating-like. This behaviour of the $c$-axis resistivity has been ascribed to the opening of the pseudogap (the lack of well-defined quasiparticle peak in some regions of momentum space from angle resolved photoemission spectroscopy (ARPES)), but models of $c$-axis transport differ as to whether the ground state is insulating or metallic.

Here we report inter-plane transport measurements in the underdoped cuprate $YBa_2Cu_3O_y$ in magnetic field large enough to suppress superconductivity. In figure 93, we show that the incoherent inter-plane transport crosses to a coherent three-dimensional regime at low temperature. The onset of this crossover coincides with the emergence of a small electron pocket in the Fermi surface, as supported by quantum oscillations [Doiron-Leyraud *et al.*, Nature **447**, 565 (2007)] and negative Hall [LeBoeuf *et al.*, Nature **450**, 533 (2007)] and Seebeck [Chang *et al.*, Phys. Rev. Lett. **104**, 057005 (2010)] coefficients at low temperature.

The characteristic temperature scale $T_0$ of the Fermi surface reconstruction determined by Hall measurements decreases as the doping decreases and vanishes at $p = 0.08$, suggesting a Lifshitz transition [LeBoeuf *et al.*, arXiv:1009.2078 (2010)]. For the three samples studied, the temperature $T_{coh}$ below which a coherent (metallic) $c$-axis resistivity is recovered decreases as the doping decreases, closely tracking the doping evolution of temperature at which the Fermi surface reconstructs. These two phenomena are intimately linked suggesting that the Fermi surface reconstruction yields an electron pocket responsible for the coherent (metallic) $c$-axis transport, for the negative Hall and Seebeck coefficients and for quantum oscillations.

The particular in-plane momentum-dependence of the hopping integral along the $c$ axis $t_\perp$ indicates that the electron pocket is located at the anti-nodal regions of the Brillouin zone ($(\pi,0)$ and equivalent points), where ARPES do not detect a quasiparticle peak at the Fermi level but rather an energy gap above $T_c$ : the *pseudogap*.

Comparison with other quasi-2D correlated system like $Sr_2RuO_4$ [Wang *et al.*, Phys. Rev. Lett. **92**, 137002 (2004)] confirms that ARPES experiments performed above $T_{coh}$ cannot detect a quasiparticle's peak associated with the Fermi surface revealed by quantum oscillations experiments. These findings reveal the presence of a new temperature scale in the pseudogap phase of cuprates, which resolves the apparent contradiction between quantum oscillation and ARPES measurements.

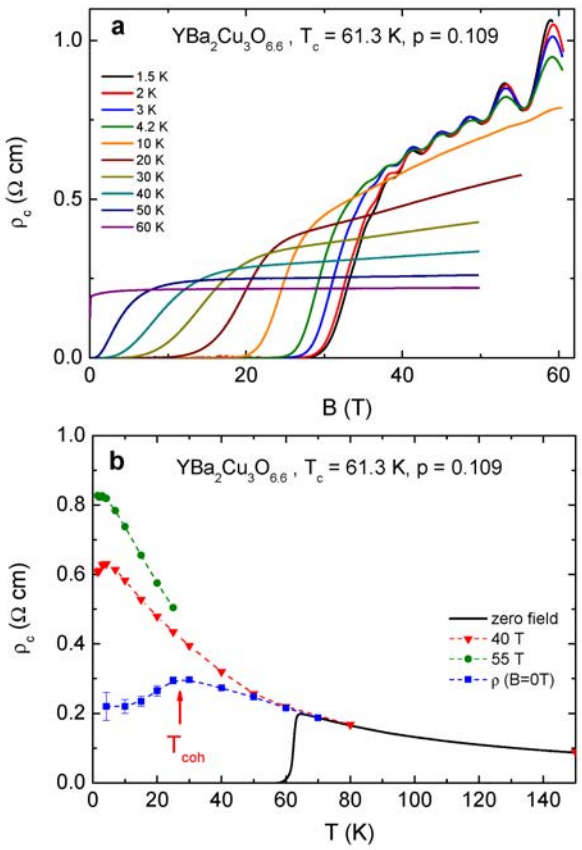


FIG. 93. *a) Electrical resistivity $\rho_c$ of $YBa_2Cu_3O_y$ for a current $I$ and a magnetic field $B$ along the c axis ($I \parallel B \parallel c$). Below 60 K, a strong positive magnetoresistance (grows with decreasing temperature. The rise of the in-field c-axis resistivity down to 4 K is followed by a clear saturation at lower temperature. This behaviour is best captured in figure b), where the resistivity is plotted as a function of temperature, in zero field (solid line) and for $B = 40$ and 55 $T$ (red and green squares). The flux-flow contribution to the resistivity is negligible above 50 T. At high temperature, the c-axis resistivity follows roughly a $1/T$ dependence, but then it crosses over to a regime where it saturates as $T \to 0$. We have used a two band model to subtract the strong magnetoresistance in order to obtain the magnetoresistance free resistivity $\rho_c(0)$ (blue squares). $\rho_c(0)$ is found to be metallic, showing that the non-superconducting ground state of $YBa_2Cu_3O_y$ is coherent in all three directions below a temperature scale $T_{coh}$.*

***B. Vignolle, D. LeBoeuf, C. Proust***
***B. J. Ramshaw, J. Day, W.N. Hardy, R. Liang, D.A. Bonn (University of British Columbia, Vancouver, Canada), L. Taillefer (University of Sherbrooke, Canada)***

# Angle-dependence of quantum oscillations in $YBa_2Cu_3O_{6.59}$ shows free spin behaviour of quasiparticles

The Fermi surface of a metal, defined as the boundary between filled and empty quasiparticle states in momentum space at zero temperature, determines almost all of the metal's measurable properties. Quantum oscillations, which are oscillations of a material property as a function of the inverse applied magnetic field, are the most direct measure of the Fermi surface in a metal. For this reason, high field measurements, and thus a determination of the Fermi surface, are of great importance when a new material is discovered. However, because the observation of quantum oscillations is only possible with very clean samples, it took almost 25 years from the time of discovery of the cuprate high temperature superconductors for the first convincing quantum oscillation measurements to be performed on the cuprate $YBa_2Cu_3O_{6+x}$ [Doiron-Leyraud *et al.* Nature **447**, 565 (2007)]. With the existence of a Fermi surface in $YBa_2Cu_3O_{6+x}$ confirmed, the next step was to determine its shape in momentum space, the mass of the quasi particles, and the difference in the response of the spin up and spin down quasiparticles to the applied magnetic field (the $g$ factor). By measuring the $c$-axis resistivity of a $YBa_2Cu_3O_{6.59}$ sample in pulsed magnetic field as a function of angle and temperature, we were able to map out the entire Fermi surface and extract the important quasiparticle parameters.

We model Fermi surface as two warped cylinders, expected for a quasi-2D system, and fit the measured oscillations to the form predicted by Lifschitz-Kosevich theory [Schoenberg, "Magnetic Oscillations in Metals", Cambridge University Press, Cambridge, 1984]. Figure 94 shows the results of the field-angle fit from 1.1 to 45.4°, taken at 4.2 K. The model is nearly indistinguishable from the data and any small differences could be due to the neglect of the contributions from higher harmonics and a very weak signal with a frequency near 660 T. This weak component is not the same as the large, extremal orbit near 600 T reported by Sebastian et al. [Sebastian *et al.*, Phys. Rev. B **81**, 214524 (2010)]; we also observe a belly orbit for a warped cylinder, but at a much lower frequency (near 515 T).

These fits indicate that within this field and temperature range, the measurements are consistent with Lifschitz-Kosevich theory, even though a drastic reorganization of the Fermi surface has occurred from what is observed in the overdoped cuprates. There are several scenarios as to how these cylinders are arranged within the Brillouin zone. One developed by Sebastian *et al.* is that they are distinct hole and electron Fermi surfaces [Phys. Rev. B **81**, 214524 (2010)], a possibility suggested by the fact that the warping of the two cylinders is rather different and that this might arise if the Fermi cylinders lie in regions of the Brillouin zone that have different $c$-axis hopping. Alternatively, they might be more closely related; if these cylinders were electron pockets, then the orthorhombicity of this material would permit somewhat different cylinders at $[\pi,0]$ and $[0,\pi]$.

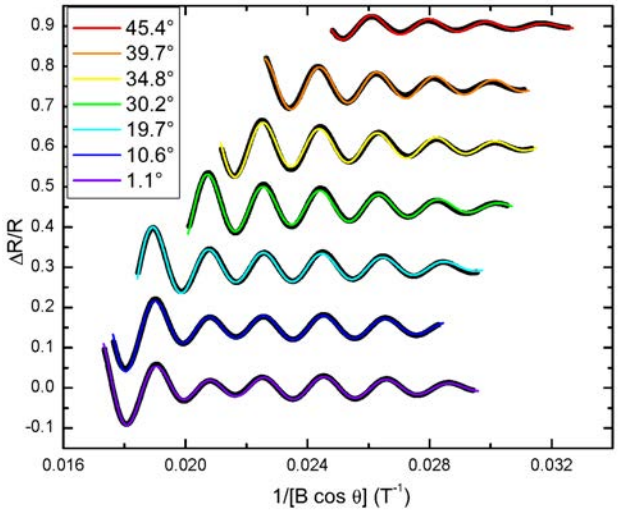


FIG. 94. *Fits to the angle and temperature dependence of the oscillatory component. $\Delta R/R$ at 4.2 K as a function of field, with the field tilted from 1.1 to 45.4° with respect to the c-axis. As the average frequency $F_0$ is expected to scale as $1/\cos\theta$, these data sets are plotted versus $1/B\cos\theta$. The fits to the angle dependence give the product of the g factor with the band mass renormalized only by electron-electron interactions: $gm_{s1} = 2.12m_e$ and $gm_{s2} = 3.18m_e$.*

The $g$ factor of the quasiparticles puts a strong constraint on which reconstruction scenarios are possible (spin density wave, $d$-density wave, *etc...*). Using the angle dependence of the oscillation amplitude and the cyclotron mass from the temperature dependence, we put a lower bound on $g$ of 1.39 and 1.86 for the smaller and larger surfaces, respectively. Since these values are far from zero, and in fact probably much closer to the free electron value of 2, this rules out a number of reconstruction scenarios involving spin order, particularly a conventional spin density wave with staggered moments perpendicular to the applied magnetic field [Garcia-Aldea *et al.* Phys. Rev. B **82**, 184526 (2010)].

***B. Vignolle, C. Proust***
***B.J. Ramshaw, J. Day, W.N. Hardy, R. Liang, D.A. Bonn (Department of Physics and Astronomy, University of British Columbia, Vancouver, Canada)***

# Zero-field resonances in $Bi_2Sr_2CaCu_2O_{8+\delta}$ Josephson junctions

Layered high-$T_c$ superconductors (HTSC) like $Bi_2Sr_2CaCu_2O_{8+\delta}$ (Bi2212) are very attractive as sources of tunable continuous electromagnetic radiation. The large value of the superconducting gap in Bi2212 allows for very high Josephson frequencies, which can be brought into the practically important THz range. However, the behavior of HTSC Josephson junctions (JJ's) is far from being totally understood. It has been recognized for low-$T_c$ superconductors that a self-excited singularities in dc current-voltage characteristic (IVC) of JJ are of interest in studies of the high-frequency properties of superconductors. If JJ is coupled with structure having electromagnetic resonances at frequencies $\nu_n$, singularities appear in dc IVC at $V_n = h\nu_n/2e$, that is, when the Josephson generation frequency $\nu_J = 2eV/h$ coincides with the frequency of one of the cavity modes $\nu_n$.

In a thin-film JJ the resonant structure is the junction itself and the cavity mode frequencies correspond to an integer number $n$ of half wavelength on the junction length $L$ and are given by the relation $\nu_n = n\bar{c}/2L$, where $\bar{c}$ is the electromagnetic wave propagation velocity in JJ called Swihart velocity. These resonances manifest itself as the self-excited a set of voltage-equidistant Fiske steps which occur only when a low magnetic field is applied parallel to the junction plane [Fiske, Rev. Mod. Phys., **36**, 221 (1964)]. There are also modes that appear in a zero field. Some evidence indicates that the current zero-field steps are due to moving Josephson vortices in the junction. These vortices are driven along the junction by the tunneling current and are reflected at the edges. Resonance occurs when the time for the vortex pattern to repeat itself equals the period of the ac supercurrent. It is suggested that the zero-field steps occur at voltages below $V \simeq n\Phi_0\bar{c}/L$, where $\Phi_0$ is the flux quantum [Fulton *et al.* Solid State Commun. **12**, 57 (1973)].

However, no detailed theory exist with which one could compare experimental results. As for HTSC, Fiske steps in IVC's of tunnel junctions was obtained only in the intrinsic JJ's in Bi2212 crystals, which behave like stacks of superconductor-insulator-superconductor JJ's with the tunneling current along $c$ axis. Evidence for zero-field steps in the intrinsic JJ's has yet to be observed which is apparently related mainly to the difficulties in synchronizing many JJ's at distances on the order of a wavelength. Whereas in case of Fiske steps, magnetic field couples JJ's and helps to synchronize them. We present the first detection of $ab$-plane zero-field current steps in the IVC's of Bi2212 JJ's. $ab$-plane tunneling experiments were performed on Bi2212 single crystal ($T_c$=84 K and $\Delta T_c$ = 1.5 K) using break junctions. Mechanically re-tuning the break junction repeatedly in liquid helium, we were able to fabricate a number of tunnel junctions at different places along the initial break of the crystal. The dc current was applied along the $ab$ plane instead of across the junctions as is done in case of the intrinsic JJ's. Previously we have argued that the tunneling in our break junctions occurs in the $ab$-plane. Figure 95 (main panel) displays the IVC's for two break junctions at $T = 4.2$ K for zero magnetic field compared with the data at $H = 3$ T (JJ #2). The IVC's show a series of six current steps at increasing values of the voltage. As is clear from figure 95 a magnetic field applied parallel to the $ab$ plane unlike Fiske steps suppresses the zero-field steps. The inset in figure 95 shows the voltage

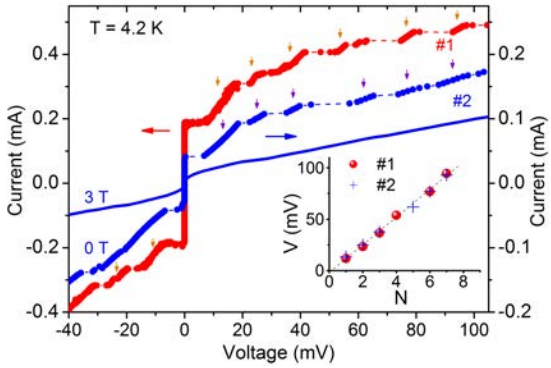


FIG. 95. *$I(V)$ characteristics for two Bi2212 break junctions at $T = 4.2$ K for zero magnetic field compared with the data at $H = 3$ T (#2). $H \parallel ab$.*

position of the steps (marked by arrows in the main panel) versus the number. It can be seen that the voltage space $\Delta V \simeq 13$ mV is to a good approximation constant over a wide range of $V$ that corresponds $\nu_J = 6.3$ THz. Since the measurements are made with a current source not all expected steps appear. If one makes the assumption that resonant structure in the break JJ represents a strip-type resonator or cylindrical resonator (microbridge), as for conventional superconductors, one can estimate the width $L$ or a diameter $D$ of JJ, respectively. Taking reasonable parameter for Bi2212 $\bar{c}/c \simeq 1 \times 10^{-3}$, we obtain $L \simeq 250$ Å or $D \simeq 360$ Å. The magnitude of the energy gap $2\Delta$ in our Bi2212 single crystals equals 45 meV at 4.2 K then our data suggest that the sources and detectors of electromagnetic radiation based on non linear Josephson current in Bi2212 JJ's can be used up to $\simeq 50$ THz. Taking into account that, the value of $2\Delta$ in Bi2212 run up to 120 meV with doping, it is clearly that this frequency range could be extended at least up to 130 THz.

***D. K. Maude, B. A. Piot***
***S. I. Vedeneev (P.N. Lebedev Physical Institute, Russian Academy of Science, Moscow, Russia)***

# Magnetic Systems

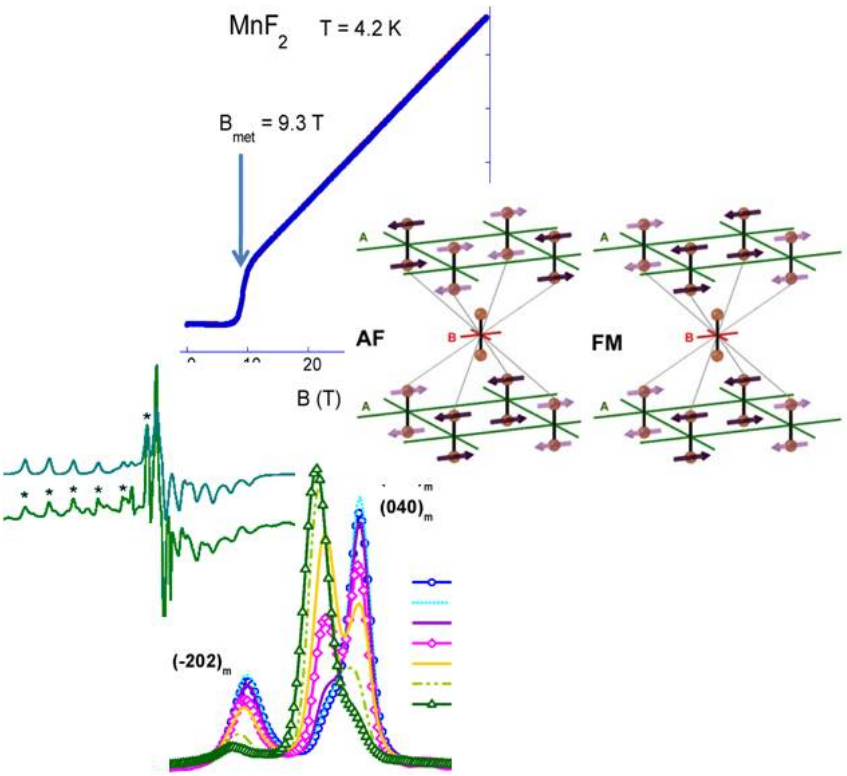

# NMR evidence for the absence of the 2/3 plateau in azurite

Since it has been recognized as a model system for a frustrated antiferromagnetic Heisenberg spin-1/2 chain of "distorted diamond" geometry, the natural mineral azurite, $Cu_3(CO_3)_2(OH)_2$, is attracting a lot of interest amongst physicists. Its most prominent feature is a large magnetization plateau at 1/3 of the saturation magnetization. Its nature is of purely quantum origin, as it is based on the spin configuration where two more strongly coupled "dimer" spins are in a singlet state, while the third spin (in a unit cell) is fully polarized. This has been confirmed for the first time by our previous NMR investigation [Aimo *et al.*, Phys. Rev. Lett. **102**, 127205 (2009)].

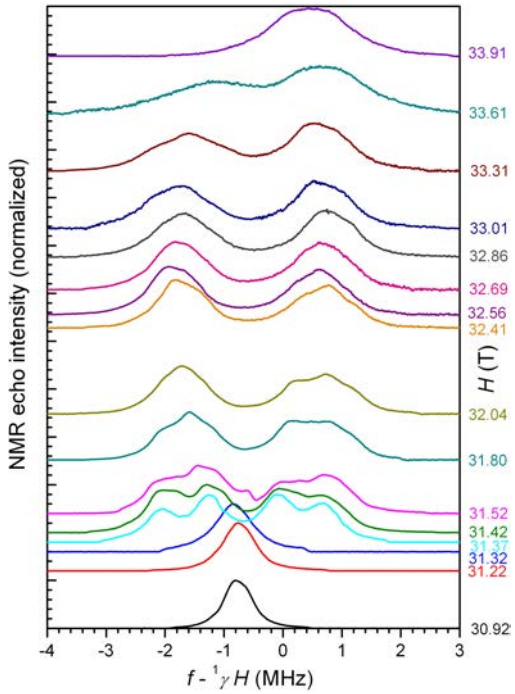


FIG. 96. *High-field proton NMR spectra of azurite covering the transition from the 1/3 plateau into the fully polarized system, taken at 0.6 K. Vertical offset of the spectra is proportional to the magnetic field, applied parallel to the c-axis. Symmetric splitting of the spectra is interpreted in terms of transverse staggered (AF) magnetization, corresponding to dimer spins in canted configuration.*

Here we focus on another interesting subject, which is the possible existence of a narrow 2/3 plateau (so far unresolved by the magnetization measurements) in the middle of the increase of magnetization from the 1/3 plateau towards the fully polarized system. Unlike the 1/3 plateau, the 2/3 plateau is expected from Oshikawa's criterion to break translational symmetry. Within the 1D (Tomonaga-Luttinger) description, where spin-spin correlation functions have power-law behaviour, it is associated to a rather exceptional situation in which the *longitudinal* spin-spin correlation function becomes dominant over the transverse one due to the so-called "$\eta$ inversion" of the corresponding exponents. In this case an incommensurate (IC) longitudinal (*i.e.*, parallel to the applied field) 3D order is expected to be stabilized at low temperature, which can generate a plateau at the commensurate point. This would *e.g.* correspond to magnetization 2/3 obtained by alternation of dimers in the singlet (zero polarization) and the triplet (fully polarized) states, while the third spin remains fully polarized. Theoretically it has been shown that the 2/3 plateau may exist in a diamond spin chain for certain values of exchange couplings $J_1, J_2, J_3$, which are compatible with experimentally quite ill-defined values. Another, much more conventional and thus less interesting situation appears when the *transverse* correlations are dominant, leading to transverse antiferromagnetic (AF, Néel) order, meaning that the dimer spins develop canted polarization.

In order to determine the microscopic nature of the spin structure of azurite above 1/3 plateau, we performed high-frequency ($1.3 - 1.45$ GHz) proton NMR at very high field ($31 - 34$ T), using specially designed ("bottom tuned") NMR probe for the narrow bore $^3$He refrigerator. In the field dependence of proton spectra shown in figure 96 one can clearly observe the end of the 1/3 plateau phase at 31.35 T where a single NMR line changes into a symmetrically split spectrum. Simple fits of the spectra by two (or 2×2) lines corresponding to a Néel state are found to be quite satisfactory, while fits to a lineshape corresponding to an IC state clearly fail. This suggests that the splitting of the spectra comes from the transverse AF order, meaning that we observe the longitudinal component of the direct dipolar field at the proton site produced by transverse staggered spin polarization on dimers. Knowing the crystallographic structure this field can be calculated, if the staggered polarization $S^{\perp}$ is know. In a model of independent dimers, $S^{\perp}$ is given by mixing the singlet and the triplet state which are degenerate at the critical field, and we obtain that it is only weakly field dependent, with the maximum $S^{\perp}_{max} = 1/\sqrt{8}$ at the point where spins are half polarized, $S^z = 1/4$. Using this value the predicted line splitting is $\pm 1.35$ MHz for the $S^{\perp}_{max}$ oriented along the $a$-axis, which is very close to the experimentally observed $\pm 1.2$ MHz. That this particular direction is favoured by the anisotropy terms can be seen from the direction of the spin polarization of dimers observed by neutrons in the zero field Néel state.

This quantitative description of the NMR line splitting permits as to conclude that a "conventional" *transverse* (canted) Néel order is realized between the 1/3 plateau and the full polarization of the system. This also means that there is no 2/3 plateau in azurite, and that the corresponding "more interesting" physics does not apply to this system [F. Aimo *et al.*, unpublished].

***F. Aimo, S. Krämer, M. Klanjšek, M. Horvatić, C. Berthier***

# NMR study of the BEC-type Quantum Critical Point in DTN

The quantum spin compound $NiCl_2$-4SC$(NH_2)_2$, abbreviated as DTN, is regarded as one of rare archetype systems for studies of the Bose-Einstein condensation (BEC) of magnons. It contains tetragonal network of Ni $S = 1$ spins which are strongly coupled along the $c$-axis by the antiferromagnetic Heisenberg exchange interaction $J_c = 2.2$ K, and subject to a strong single-ion uniaxial anisotropy $D_c = 8.9$ K. The couplings in the perpendicular directions are an order of magnitude smaller, $J_{a,b} = 0.18$ K, meaning that at temperatures above 1 K the system has 1D behaviour. Indeed, for the magnetic field $H$ applied along $c$-axis, and in the strong coupling approximation, the spin Hamiltonian of DTN is equivalent to the one of a spin 1/2 ladder, and the observed $H$-$T$ phase diagram is also equivalent. The DTN system is gapped until $H_{c1} = 2.1$ T where its magnetization starts to increase from zero up to the full polarization at $H_{c2} = 12.6$ T where the gap reopens. Between the two critical fields and at temperature below $T_{max} = 1.2$ K the system undergoes 3D ordering of the BEC type, corresponding to a canted XY ordering of the spins.

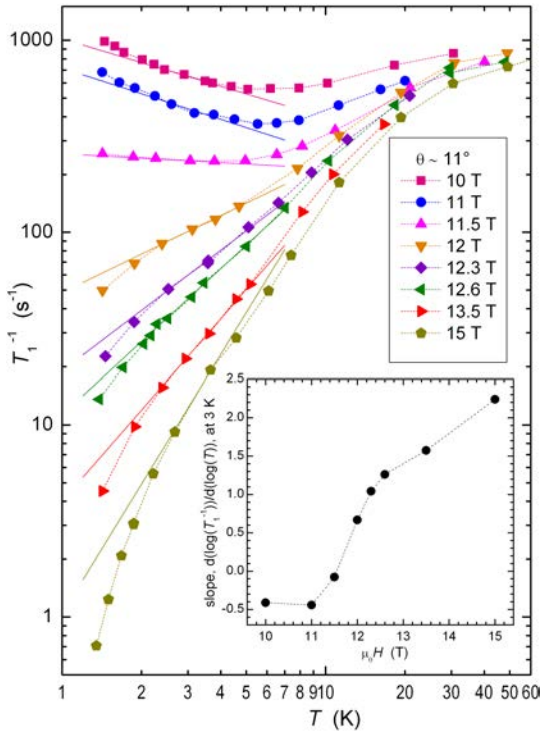


FIG. 97. *Proton NMR relaxation rate $T_1^{-1}$ in DTN for different magnetic fields tilted by $\theta = 11°$ from the c-axis. $T_1^{-1}$ measures the spin fluctuations which are strongly field dependent as the field is changed across the upper critical field $H_{c2}(\theta = 11°) \approx 12.2$ T. For $2-4$ K and below $H_{c2}$ the system is in the 1D regime where a power-law behaviour is expected (solid lines). The inset shows the field dependence of the corresponding exponent.*

In our investigation we focused on the behaviour of the system close to the upper Quantum Critical Point at $H_{c2}$ to study its dynamical properties by NMR measurements of the nuclear spin - lattice relaxation rate, $T_1^{-1}$. These measurements provide a unique possibility to access very low-energy excitations, essentially the transverse spin fluctuations. $T_1^{-1}$ data allow us to precisely follow this quantity as a function of temperature and magnetic field and to compare the observed (critical) behaviour to theoretical predictions.

The measurements in DTN have been preformed on proton NMR spectra [Mukhopadhyay *et al.*, unpublished]. Comparing the rotational dependence of the spectra to what is predicted from the dipolar field of Cu spins at high field (15 T) and low temperature (1.5 K) where they are saturated, we could assign the proton sites to the observed NMR lines, determine their hyperfine couplings and, at the same time, measure the orientation of the sample with respect to its $c$-axis. The first set of $T_1^{-1}$ measurements has been performed with the sample tilted by $\theta = 11°$ from the $c$-axis, on the highest frequency line in the spectrum. In figure 97 we see that the observed temperature dependence of $T_1^{-1}$ strongly varies as the magnetic field is changed across the critical field. This particularly applies to the $2-4$ K temperature range where the 1D behaviour is expected according to the strength of the interaction terms in the spin Hamiltonian. Above 10 K the relaxation rate increases towards its magnetic field independent, paramagnetic, high temperature limit. The 1D behaviour below $H_{c2}$ is characterized by a power-law type response functions, which indeed corresponds to the apparent linear dependence of the data plotted on a log-log scale in figure 97. The magnetic field dependence of the corresponding slope (*i.e.* the exponent) shown in the inset follows the expected behaviour; the gapless Tomonaga-Luttinger regime below $H_{c2}$ is characterized by the $1/\sqrt{T}$ divergence, while the gap opening above $H_{c2}$ leads to a progressively stronger suppression of fluctuations. As the two regimes are very different, at the critical point the change in the behaviour is very fast and continuous. This means that these data do not allow us to identify the $H_{c2}$ value, which is then taken from published data obtained by other techniques.

In further experiments we plan to investigate the angular dependence of the relaxation data. Preliminary data suggest that for small tilt angles with respect to the $c$-axis the only effect is related to the weak angle dependence of $H_{c2}$. We will also access to the very low temperature regime in the dilution refrigerator in order to define the phase boundary and thus $H_{c2}$ by NMR. $T_1^{-1}$ measurements at very low temperature will allow us to check if there is a residual gap in the system at $H_{c2}$ and to determine its angular dependence.

***S. Mukhopadhyay, M. Horvatić, C. Berthier***
***M. Grbić (University of Zagreb, Croatia), A. Paduan-Filho (Universidade de São Paulo, Brazil)***

# NMR and NQR study of the tetrahedral frustrated quantum spin system $Cu_2Te_2O_5Br_2$ in its paramagnetic phase

The tetrahedral or triangular coordination in quantum antiferromagnets is known to generate strong frustration and a wide range of exotic ground states. Among these systems, $Cu_2Te_2O_5Br_2$ consists of tetrahedral clusters of $Cu^{2+}$ ions of spin $S = 1/2$ in a distorted square planar $CuO_3X$ coordination. These tetrahedra align to form chains along the [001] direction, and are separated along [100] and [010] directions by different Te-O coordinations [Lemmens *et al.*, Phys. Rev. Lett. **87**, 227201 (2001)]. We have investigated a single crystal of this compound by $^{125}$Te and $^{79,81}$Br NMR and $^{79,81}$Br NQR. The $^{125}$Te NMR investigation showed that there is a magnetic transition around $T_N = 10.5$ K at 9 T, in agreement with previous studies. In figure 98 is shown the divergence of the spin-lattice relaxation rate above $T_N$. It extends on a very small temperature range as compared to $T_N$, which rules out the possibility that the transition could be governed by a one-dimensional divergence of the spin-spin correlation function. A detailed study of the hyperfine tensor at the $^{125}$Te site reveals an anisotropy which is shown to be due to a spin polarization of the $5s^2$ "E" doublet of the $[TeO_3E]$ tetrahedra, highlighting the importance of tellurium in the exchange paths.

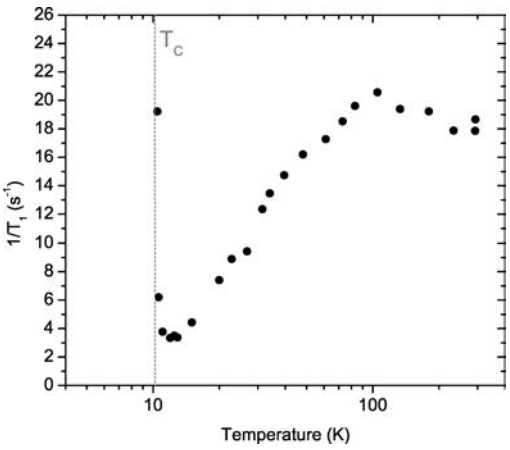


FIG. 98. *Temperature dependence of the $^{125}$Te spin-lattice relaxation rate in $Cu_2Te_2O_5Br_2$. The divergence above $T_N$ takes place in a very narrow temperature range, which cannot be due to 1D fluctuations.*

The zero field NQR frequency of the $^{79(81)}$Br was found to be $\nu_{NQR} = 87.41\,(73.02)$ MHz. Due to this very large quadrupolar coupling, some usually "forbidden transitions" can appear in the NMR spectra, and the complete determination of the hyperfine shift and the quadrupolar tensors at the Br sites required a full diagonalization of the total Hamiltonian including the intensity of all transitions, and measurements at fixed frequency (125 MHz) over a wide range of magnetic field, and at fixed field (9 and 14 T) over a wide range of frequency (figure 99) at various orientations of $H_0$ with respect to the crystalline axes. Eventually we concluded that the $Z$ axis of the local electric field gradient (EFG) tensor was along the Cu-Br direction. The hyperfine shift tensor is found to be highly anisotropic:

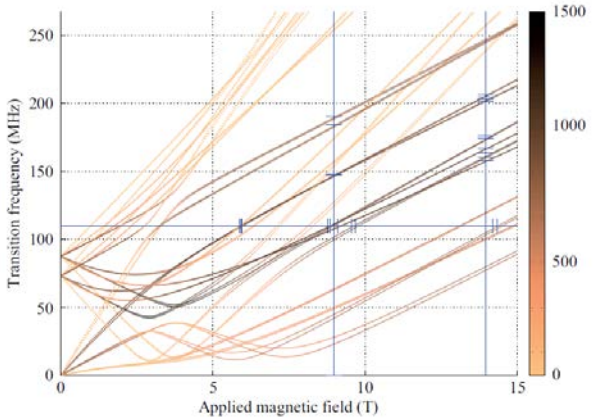


FIG. 99. *Computed Br transition frequencies and intensities as a function of the external magnetic field amplitude $|\vec{B}_0|$ for $\vec{B}_0$ oriented along [110]. The 48 possible transitions for the two Br isotopes and the four inequivalent sites are drawn. The intensities are represented on a color scale in arbitrary units: the lighter the color, the weaker the intensity. The experimental points corresponding to observed transitions are denoted by horizontal tips for spectra recorded at constant field and variable frequencies and by vertical tips for spectra recorded at fixed frequency sweeping the magnetic field.*

$A_{ZZ} = 12$ T/$\mu_B$, $A_{XX} = A_{YY} = 0.97$ T/$\mu_B$ with $X$, $Y$ and $Z$ axes being the same as those of EFG tensor. From this we deduced the fraction of spin polarization of Br $p$ orbitals amounts to 5 %. This quite large number demonstrates the crucial role of bromine in the interaction paths between Cu spins [Comment *et al.*, Phys. Rev. B **82**, 214416 (2010)].

The theoretical modelling of this frustrated spin system, topic of several recent publications, will be clearly facilitated by this new information. A complete NMR study of this material in its magnetic phase is currently in progress and is expected to shed light on its complex incommensurate magnetic phase.

***H. Mayaffre, M. Horvatić, C. Berthier***
***A. Comment (EPFL, Lausanne, Switzerland), V. Mitrović (Brown University, Providence, USA), B. Grenier (INAC/SPSMS, Grenoble, France)***

# 3D stacking of the Bose-Einstein condensate in the Han purple compound revealed by NMR

The quasi-2D, antiferromagnetic (AF) exchange coupled spin-1/2 dimer compound $BaCuSi_2O_6$ (Han purple) is considered as a prototype of the magnetic field induced Bose-Einstein Condensation (BEC) of triplet excitations on a lattice. Recently, $BaCuSi_2O_6$ has been claimed to exhibit an unusual reduction of dimensionality of the BEC from 3D to 2D when lowering the temperature, induced by frustration between adjacent planes. However, due to a structural transformation at 90 K, different intradimer exchange couplings and different gaps ($\Delta_B/\Delta_A = 1.16$) exist in every second plane along the c axis. In a first series of Nuclear Magnetic Resonance (NMR) experiments, we have shown that this leads to a population of bosons in the B planes, $n_B$, much smaller than in A planes in the field range $\Delta_A/g\mu_B < H < \Delta_B/g\mu_B$ where $n_B = 0$ is expected in a naive model of uncoupled planes [Krämer *et al.*, Phys. Rev. B **76**, 100406(R), (2007)]. More recently, a better model has been presented which takes into account both frustration and quantum fluctuations. This leads to a non-zero population $n_B$ of uncondensed bosons in the B plane, increasing quadratically with $(H - H_{c1})$, as compared to the linear dependence of $n_A$ [Laflorencie *et al.*, Phys. Rev. Lett. **102**, 060602 (2009)].

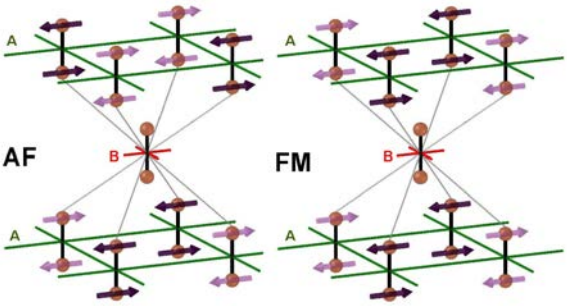


FIG. 100. *3D stacking along c-axis of modulated BEC (staggered transverse spin order on Cu dimers in A planes and empty B planes) in $BaCuSi_2O_6$ for the antiferromagnetic (AF, left) and the ferromagnetic (FM, right) case. The longitudinal component of the magnetization is not shown.*

Here we focus on a particular aspect of the problem, which is the experimental determination of the 3D stacking of the condensate along the *c*-axis. Simple models predict perfect decoupling of planes, meaning that there is no 3D coherence of the BEC layers. However, this decoupling is instable to quantum or thermal fluctuations. They lead to an effective coupling between second neighbor layers, that is suggested to be ferromagnetic (FM) or antiferromagnetic (AF), as shown in figure 100. Since modelling the 3D stacking strongly depends on parameters that are beyond the framework of the theoretical model, such as exchange coupling constants, degree of frustration and detailed structure of layers, an experimental determination of the 3D coupling is highly desirable.

In order to determine the 3D stacking of the BEC we performed $^{29}$Si NMR experiments on an isotopically enriched and c-axis oriented $BaCuSi_2O_6$ single crystal in the vicinity above $H_{c1} = 23.45$ T and at low temperature $T = 50$ mK. The field dependence of the spectra clearly shows the phase transition at $H_{c1}$ leading to split and strongly broadened component and only weakly shifted, non-split narrow component (figure 101). We assign these two components respectively to $^{29}$Si nuclei located in condensed A planes and non-condensed B planes. The spectra are compared to the expected $^{29}$Si line positions for the AF and FM 3D stacking of the BEC applying a dipolar field model and using the crystallographic structure.

From the results shown in figure 101 it can be clearly seen that the dipolar fields in the condensed A planes do not depend on the 3D stacking model. However, the observed narrow and non-split line of the B planes near zero shift is only consistent with the AF model. This experimental result will put important constraints to further theoretical modelling of the BEC in the Han purple compound [Krämer *et al.*, unpublished].

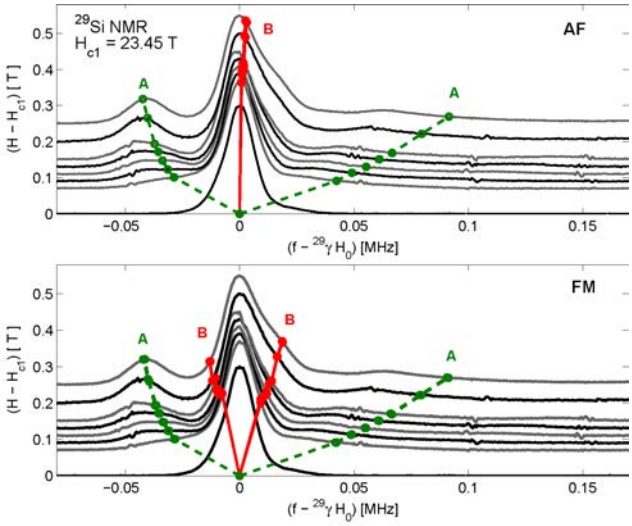


FIG. 101. *$^{29}$Si NMR spectra of $BaCuSi_2O_6$ above $H_{c1}$ at 50 mK. Vertical offset of the spectra is proportional to $(H - H_{c1})$. Expected line positions are modelled by dipolar fields using AF (top) and FM (bottom) 3D stacking model. While dipolar fields in condensed A plane (dashed lines) are model independent, the narrow line of B planes near zero shift is only consistent with the AF model (solid lines).*

***S. Krämer, F. Aimo, M. Horvatić, C. Berthier***
***R. Stern (NICPB, Tallinn, Estonia), T. Kimura (Osaka University, Osaka, Japan)***

# Direct evidence of magnetostructural phase separation in the electron-doped manganite $Ca_{0.8}Sm_{0.16}Nd_{0.4}MnO_3$

The interplay between charge, spin, lattice and orbital degrees of freedom in manganite compounds, $R_{1-x}D_xMnO_3$ ($R$ = rare-earth La, Nd, Sm; $D$ = alkaline-earth metals Sr, Ca, Ba,...) is the source of very rich phase diagrams in which several structural and magnetic phases have been observed. One of the main results of the research in manganite type compounds is the discovery of a strong tendency towards phase separation, *i.e.* the formation of inhomogeneous states. This result is very robust, appearing both in experiments and in theoretical models. The colossal magneto-resistance effect appears to be closely linked to these mixed phase tendencies and to the strong competition between the ferromagnetic (FM) metallic state and the antiferromagnetic (AF) insulating state which supports charge and orbital order.

In the present work, we have investigated the structural and magnetic behavior of the electron-doped manganite $Ca_{0.8}Sm_{0.16}Nd_{0.4}MnO_3$ at magnetic fields up to 30 T. To that end we have performed synchrotron X-ray powder diffraction under pulsed magnetic fields, combined with resistivity and magnetization measurements [Duc *et al.*, Phys. Rev. B **82**, 054105 (2010)].

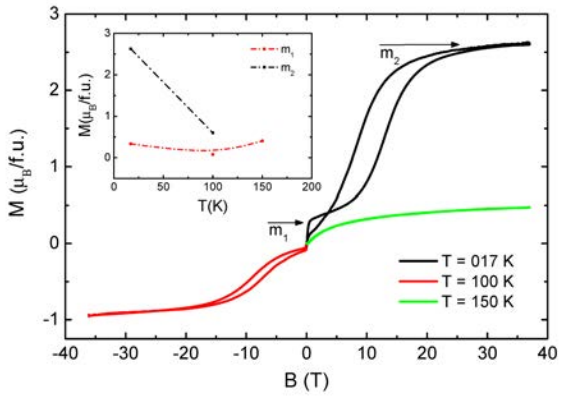


FIG. 102. *M vs. B hysteresis measurements at different temperatures ($T$ = 150 $K$, $T$ = 100 $K$ and $T$ = 17 $K$). At low temperatures, two distinct phases can be observed. The temperature dependence of their fractions are shown in the inset.*

Below 100 K, the spontaneous ($B$ = 0) low-temperature phase is found to be structurally and magnetically phase segregated, a major antiferromagnetic monoclinic $P2_1/m$ phase coexisting with a minor antiferromagnetic orthorhombic *Pnma* phase containing ferromagnetic clusters.

Upon the application of a magnetic field, two magnetic transitions occur (see figure 102); a first transition (transition $m_1$) without structural changes at low field, showing the superparamagnetic-like behavior of ferromagnetic domains, followed by a metamagnetic transition (transition $m_2$). The latter is clearly accompanied by field induced structural changes, the monoclinic $P2_1/m$ structure being gradually transformed into the orthorhombic *Pnma* phase (see figure 103).

Our experiments are consistent with earlier observations [Algarabel *et al.*, Phys. Rev. B **65**, 104437 (2002)], which in the high field region lacked the sensitivity to the structural component of the metamagnetic transition.

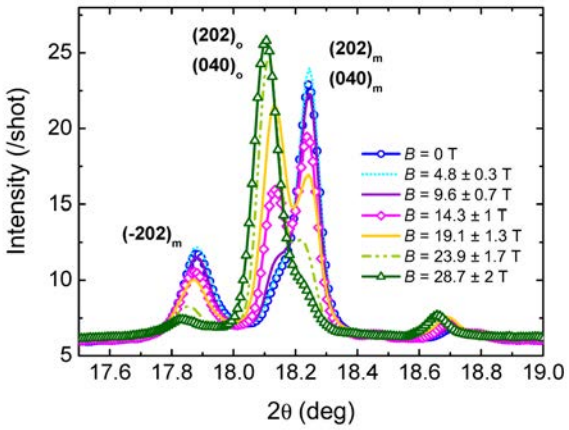


FIG. 103. *Field dependence (0 to 30 T from top to bottom) of synchrotron X-ray powder diffraction pattern observed for $Ca_{0.8}Sm_{0.16}Nd_{0.4}MnO_3$ at $T$ = 7 $K$. At this temperature, this compound is mainly monoclinic. On applying a magnetic field, the monoclinic structure is gradually transformed into an orthorhombic phase. The orthorhombic and monoclinic reflections are indicated by the subscripts "o" and "m", respectively.*

These experiments have given macroscopic and microscopic evidence of magnetic and structural phase separation in the electron-doped manganite $Ca_{0.8}Sm_{0.16}Nd_{0.4}MnO_3$. The phase separation persists for all field values investigated, crossing a maximum with 50% of both phases at 17 – 18 T.

***F. Duc, P. Frings, G.L.J.A Rikken***
***G. Zhang, W. Decelle, J. Vanacken (INPAC, Leuven, Belgium), C. Detlefs, C. Strohm, T. Roth (ESRF, Grenoble, France), J.E. Lorenzo (Institut Néel, Grenoble, France), R. Suryanarayanan (LPCES, Orsay, France)***

# Magneto-optical spectroscopy: A new tool to investigate metamagnetic transitions

We report on the first experiments aiming at mapping metamagnetic transitions in antiferromagnetic compounds by magneto-optical spectroscopies under pulsed magnetic field up to 60 T. The main interest of this new technique is its compatibility with high hydrostatic compression in a diamond anvil cell [Millot *et al.*, Phys. Rev. B **78**, 155125 (2008)]. Hence, the pressure dependence of the magnetic coupling parameter could be investigated as well as the magnetic properties of high pressure phases of magnetic compounds such as $MnF_2$ [Hernandez *et al.*, Phys. Rev. Lett. **99**, 027403 (2007)].

We demonstrate the proof of concept by a first study on $RbMnF_3$ ($T_N$ = 82 K) and $KMnF_3$ ($T_N$ = 88 K) and $MnF_2$ ($T_N$ = 67 K). The absorption photoluminescence (PL) spectra have been measured under high pulsed magnetic field conditions up to 60 T at different temperatures below the Neel temperature.

We investigated the changes of PL intensity (PL) of the red emission (620 nm) upon continuous pumping in the exciton-magnon peak in $RbMnF_3$ (557 nm), $KMnF_3$ (546 nm) and $MnF_2$ (544 nm) as a function of the magnetic field, $B$, at low temperature. The correlation between spectroscopic results and metamagnetism has been checked by magnetization measurements carried out using inductive pick-up coils and oriented single crystals of $RbMnF_3$, $KMnF_3$ and $MnF_2$.

The PL spectrum associated with the $^4T_1 \rightarrow^6 A_1$ of each compound features not only a broad PL band but also an exciton-magnon peak and its phonon side band at low temperature. The magnetic field dependence of the exciton-magnon PL peak is presented in figure 104 in the case of $MnF_2$. Besides the Zeeman splitting exhibited by exciton-magnon lines, a salient result of this work is the drastic diminution (note the strong singularity around 10 T in the PL intensity magnetic dependence curve) of absorption and PL intensity with the magnetic field in $MnF_2$ that we associate with the well known spin-flop transition (see the $M(B)$ curve in inset). Ferromagnetic order is found to act as a $Mn^{2+}$-excitation trigger yielding exciton depopulation by pumping interruption.

Interestingly a big difference is found between the intensity variation of $MnF_2$ and $RbMnF_3$. No trace of metamagnetic transition is observed in $RbMnF_3$ up to 53 T by inductive magnetization measurements. In this case the exciton-magnon line intensity is found to decrease smoothly and continuously under applied field.

Hence, we showed that there is a close relationship between $Mn^{2+}$ PL and absorption intensities and magnetic order in these compounds. Whereas both absorption and PL appear enhanced in the antiferromagnetic phase due to exciton-magnon coupling, this mechanism is quenched in the metamagnetic phase (spin-flop phase with increasing ferromagnetic order) at low temperature.

Throughout these preliminary experiments we showed the $Mn^{2+}$ absorption and PL are suitable probes to detect metamagnetism in these ideal $Mn^{2+}$-based Heisenberg-antiferromagnet crystals.

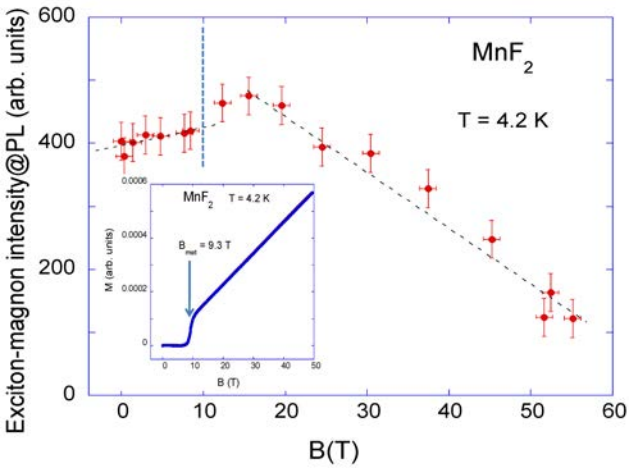


FIG. 104. *Magnetic field dependence of the exciton-magnon PL peak and spin-flop transition inset in $MnF_2$. Note the evident correlation between the singularity in the PL intensity magnetic dependence and the spin-flop transition.*

***M. Millot, J.M. Broto***
***J. Gonzalez, R. Valiente, F. Rodriguez (DCITIMAC, Univ. Cantabria, Santander, Spain)***

# Easy-axis magnetic anisotropy in SMM from hard-axis metal ions

Slow magnetic relaxation in molecular entities, especially in those known as single-molecule magnets (SMM), is an active research topic at the interface of physics and chemistry with potential applications for magnetic storage or data processing. A prerequisite is the ability of the molecular system to retain its properties when deposited on a surface. Tetrairon(III) complexes with a propeller structure behave as SMM and have shown to possess structural and electronic robustness. In order to clarify the origin of their magnetic anisotropy, an heterometallic Fe-Cr complex $[Fe_3Cr(L)_2(dpm)_6].Et_2O$, **$Fe_3Cr$**, has been synthesized and studied (where $H_3L$ = 2-phenyl-2-hydroxymethyl-propane-1,3-diol and H*dpm* = 2,2,6,6 − tetramethyl-heptane-3,5-dione). It is isomorphous to the corresponding tetrairon(III) compound (**$Fe_4$**), with Cr(III) as the central metal ion. The **$Fe_3Cr$** complex has an $S = 6$ ground state and an easy-axis magnetic anisotropy ($D < 0$) resulting in SMM behaviour. In order to fully understand the origin of the magnetic anisotropy, isomorphous Fe- and Cr-doped tetragallium(III) complexes $[Ga_4(L)_2(dpm)_6].Et_2O$, **$Ga_4$** have been prepared and studied by High-Frequency EPR (HF-EPR).

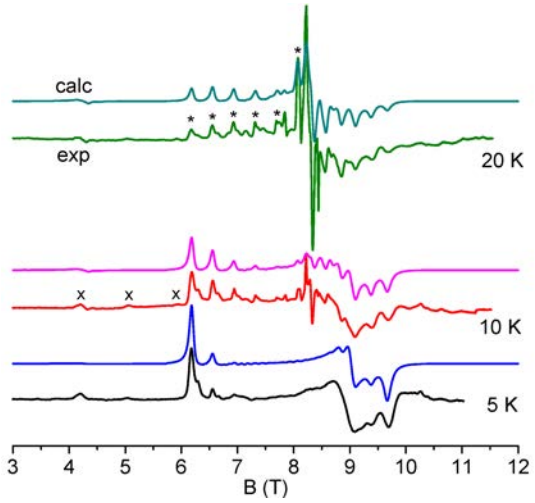


FIG. 105. *230 GHz EPR spectra of* **$Fe_3Cr$** *and best-fit simulations. The parallel transitions within the $S = 6$ state (*) and the weak bands attributable to* **$Fe_4Ph$** *(×) are indicated.*

**$Fe_3Cr$** spectra are typical of an $S = 6$ ground spin state with an easy-axis anisotropy. They were simulated using the following hamiltonian:

$$H = \mu_0 \mathbf{B}.\mathbf{g}.\mathbf{S} + DS_z^2 + E(S_x^2 - S_y^2) + B_4^0 O_4^0 \quad (9)$$

where $O_4^0$ is a Stevens operator, while D, E and $B_4^0$ are the crystal field parameters defining the anisotropy of the system. The best simulations were obtained with the following parameters (in $cm^{-1}$): D = −0.179(1), E = 0.018(1), $B_4^0 = 1.6(5) \times 10^{-6}$, together with $g_z = 1.980(5)$ and $g_x = g_y = 2.00(1)$ (figure 105). Extra signals (indicated by crosses) are also visible in the experimental spectra and are attributed to the existence of **$Fe_4Ph$** in the lattice.

**$Ga_4$:Fe** and **$Ga_4$:Cr** have been studied by HF-EPR in order to determine the single ion contribution to the magnetic anisotropy of the $S = 6$ multiplet. For both systems, spectra typical of hard-axis anisotropy (D > 0) are obtained (figure 106). Simulations of the spectra allowed determining best fit parameters; ZFS terms are found to be (in $cm^{-1}$): for **$Ga_4$:Cr** D = 0.470(5), E = 0.029(1); for **$Ga_4$:Fe** D = 0.710(5), E = 0.077(3) and D = 0.602(5), E = 0.101(3) for the two crystallographically-distinct peripheral sites.

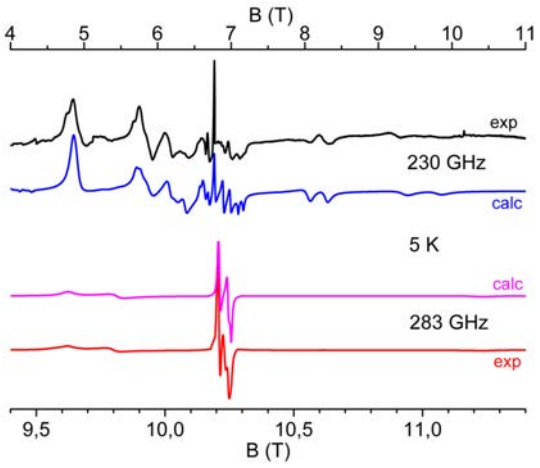


FIG. 106. *Calculated and experimental powder EPR spectra of* **$Ga_4$:Fe** *(upper curves) and* **$Ga_4$:Cr** *(lower curves).*

The ZFS tensor in ground $S = 6$ state of **$Fe_3Cr$** can be expressed as a linear combination of single-ion ZFS and dipolar tensors with coefficients calculated in the strong-exchange approximation. As the single-ion Cr(III) contribution almost cancels the dipolar term, the negative D value of **$Fe_3Cr$** is thus ruled by the peripheral Fe(III) ions and can be reproduced by setting their hard axes approximately perpendicular to the idealized threefold molecular axis [Tancini *et al.*, Chem. Eur. J. **16**, 10482 (2010)].

These findings demonstrate that SMM properties can be observed in systems comprising hard-axis metal ions only. Taking into proper account the noncollinarity of single-ion anisotropy tensors may thus be essential not only to understand magnetic quantum tunneling effects,but also to explain their anisotropy barrier.

***A.L. Barra***
***E. Tancini, M.J. Rodriguez-Douton, A. Cornia (University of Modena and Reggio Emilia, Italy), L. Sorace, R. Sessoli (University of Florence, Italy)***

# Magnetic properties of single phase nanocrystalline Dysprosium-Iron-Garnet ($Dy_3Fe_5O_{12}$)

Rare earth iron garnets (REIG) with the chemical formula $R_3Fe_5O_{12}$ exhibit magneto-optical properties suitable for applications in magneto-optical storage devices and optical communication systems. REIG materials are also promising candidates for use in high performance microwave and electrochemical devices. The garnet-ferroelectric bilayers are used as magnetooptic spatial light modulators, however, there is little known about the single phase nanocrytalline REIG garnets. Ball milling of nanocrystalline $Gd_3Fe_5O_{12}$ leads to a partial reduction of $Fe^{3+}$ to $Fe^{2+}$.

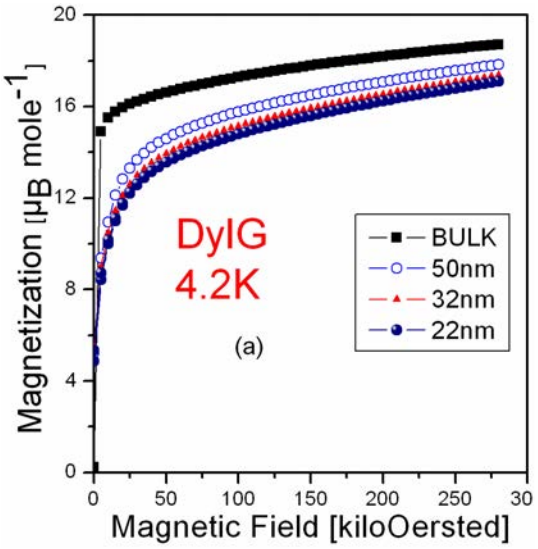


FIG. 107. *First quadrant magnetization curves for the various milled $Dy_3Fe_5O_{12}$ nanoparticles at 4.2 K.*

$Dy_3Fe_5O_{12}$ ($R_3^{3+}$ c $[Fe_2^{3+}]_a$ $(Fe_3^{3+})_d O_{12h}^{2-}$ ) particles were synthesized in polycrystalline form by the solid-state reaction technique from a mixture of $\alpha$-$Fe_2O_3$ and $Gd_2O_3$. Milling was carried out in a controlled atmosphere using a planetary ball mill. The X-ray diffractograms show that all the milled $Dy_3Fe_5O_{12}$ garnet particles retain their single phase structure ($Ia3d$ space group). The average grain size for the as prepared, 10, 20 and 30 hour milled sampled samples were 100, 50, 32 and 22 nm respectively.

$^{57}$Fe Mossbauer spectra shows that there is no evidence for the presence of $Fe^{2+}$ charge state in the as prepared garnets. On increasing the milling time, ferric and ferrous species can be identified; about $14-15$ at.% $Fe^{2+}$ content was found in the 30 hour milled sample. The grain size reduction due to milling induces the oxygen vacancies and hence some of the $Fe^{3+}$ ions are converted to $Fe^{2+}$ ions as previously reported in milled $ZnFe_2O_4$ and $Gd_3Fe_5O_{12}$ samples [Chinnasamy *et al.* J. Appl. Phys. 107, 09A512 (2010)].

The magnetization curves, $M(H)$ were measured for all the samples in the $4.2-300$ K temperature range (figure 107). They are very sensitive to the grain size. $M(H)$ for the as-prepared $Dy_3Fe_5O_{12}$ is in quasi perfect agreement with the single crystal values and this confirms that all the Fe and Dy ions are in trivalent state. When the grain size is reduced below the 50 nm (10 hours), the magnetization is strongly depedent on the applied magnetic field and no saturation is observed even at 280 kOe. The compensation temperature ($T_{romp}$) for the different nanocrystalline $Dy_3Fe_5O_{12}$ samples are only a few degrees higher than that of the as-prepared sample which indicates that the phase stability (figure 108). However, the Curie temperature ($T_C$) of the various sized nanocrystalline GdIG samples are found to be significantly higher than that of the bulk.

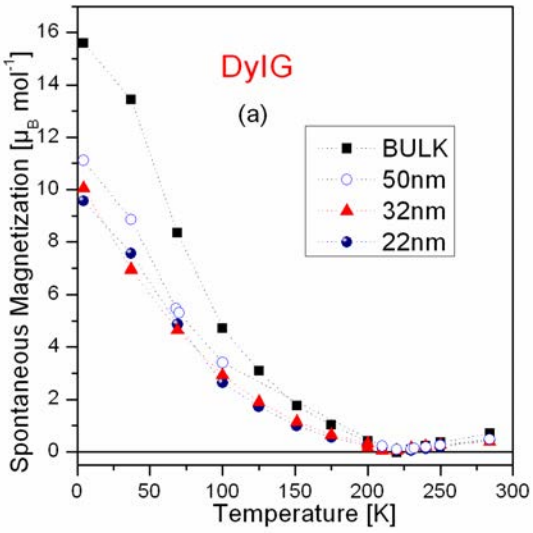


FIG. 108. *Magnetization versus temperature variation for the as prepared and milled $Dy_3Fe_5O_{12}$ samples.*

***M. Guillot***
***C. N. Chinnasamy, V. G. Harris (Dept. of Electrical and Computer Engineering, Northeastern University, Boston, USA), J. M. Greneche (Laboratoire de Physique de L'Etat Condensé, CNRS, Université du Maine, Le Mans, France)***

# Magnetic properties of $Y_{0.9}Gd_{0.1}Fe_2(H,D)_{4.2}$ compounds under very strong continuous magnetic field up to 35 T

$RM_2$ Laves phases (R= rare earth and M= Mn, Fe, Co) have been widely studied for the influence of hydrogen absorption on their magnetic properties. $YFe_2$ form hydrides with different structures derived from the C15 cubic structure and with an increase of cell volume versus H content. In $YFe_2D_x$ deuterides, the saturation magnetization measured at 4.2 K up to 230 kOe, first increases up to 3.5 D/f.u., then decreases for larger D content. For $x = 5$ there is no more ordered Fe moment. This evolution is due to a competition between the volume increase, which leads to a better localization of the Fe d orbital and favors the increases of the Fe moment and chemical Fe-D bonding which decrease the density of states at the Fermi level. $YFe_2D_{4.2}$ is ferromagnetic at low temperature and displays a sharp magnetic transition at $T_{M0} = 84$ K towards an antiferromagnetic structure. Above 84 K a metamagnetic behavior is observed. $T_{M0}$ is very sensitive to H, D composition; it is shifted to 120 K for an $H_{0.64}D_{0.36}$ mixture and 140 K for pure hydride. This difference is partly explained by the larger cell volume of the hydride due to zero point vibration difference between H and D atoms. $T_{M0}$ can also be tuned by substituting Y by other rare earth elements like Gd, Tb, Er and Lu; it decreases for Er and Lu and increases for Tb and Gd (figure 109). $T_{M0}$ remains also sensitive to the H/D isotope effect whatever the R for Y substitution.

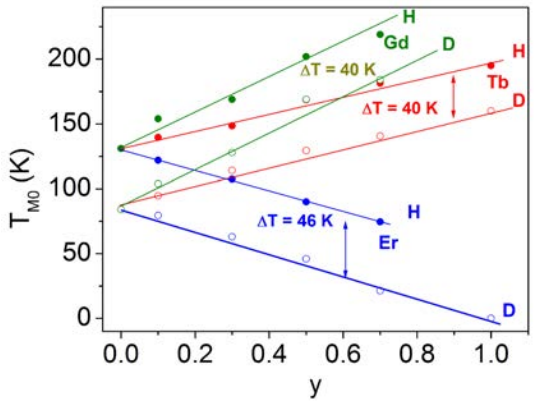


FIG. 109. *Evolution of the transition temperature of $Y_{1-x}R_xFe_2(H,D)_{4.2}$ (R=Gd,Tb,Er) compounds.*

High magnetic field measurements have been performed for $Y_{0.9}Gd_{0.1}Fe_2(H,D)_{4.2}$ compounds in the $4 - 300$ K temperature range confirming a very strong isotope effect. In $Y_{0.9}Gd_{0.1}Fe_2D_{4.2}$ the magnetization curves display a metamagnetic behavior (figure 110) and the transition is observed in the $108 - 175$ K temperatures range. On the contrary no transition is observed in the same temperature range temperature range for the corresponding hydride $Y_{0.9}Gd_{0.1}Fe_2H_{4.2}$. Note that for the Gd deuteride the transition field increases linearly versus temperature (figure 111) but with a HTR/T slope larger than for $YFe_2D_{4.2}$ showing an additional influence of the Gd substitution. These results indicate that the Y for Gd substitution is modifying the structural and magnetic properties of the hydrides and deuterides. For further details see [Guillot et al. J. Appl. Phys. **107**, 09E144 (2010)].

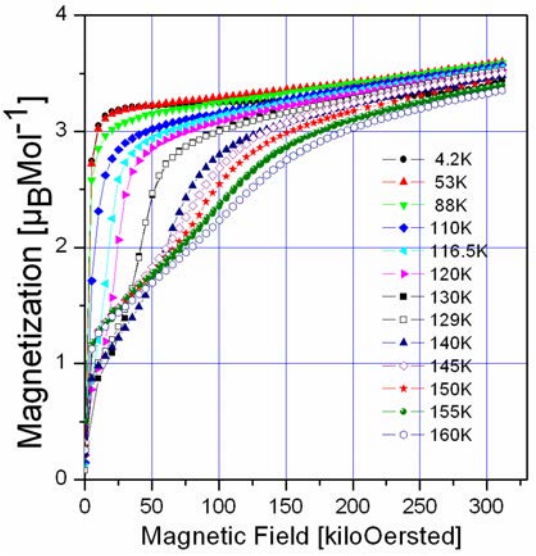


FIG. 110. *Isothermal magnetization curves of $Y_{0.7}Er_{0.3}Fe_2(H,D)_{4.2}$ compounds.*

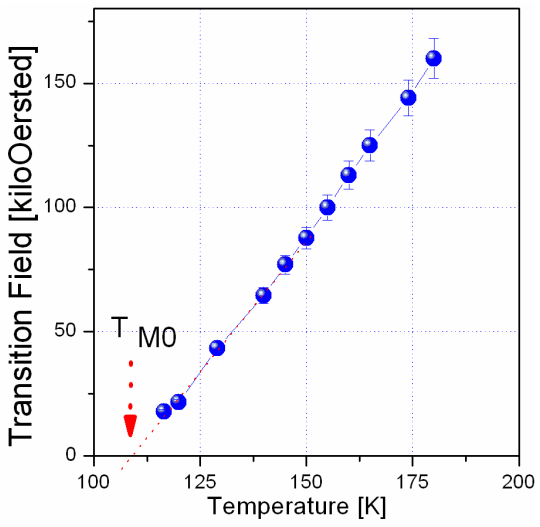


FIG. 111. *Transition field versus temperature $Y_{0.9}Gd_{0.1}Fe_2(D)_{4.2}$*

***M. Guillot***
***V. Paul-Boncour, T. Leblond (CMTR, ICMPE, CNRS and Univiversity Paris XII, Thiais, France)***

# Biology, Chemistry and Soft Matter

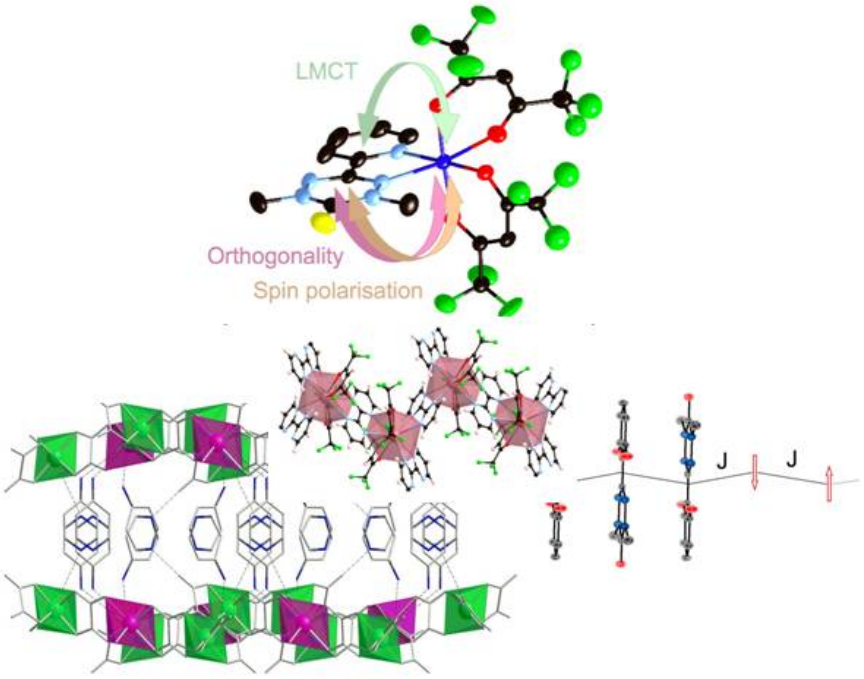

# Verdazyl radicals: Versatile tools to probe the exchange interaction

The design and the synthesis of molecular-based magnetic materials have been the subject of intense investigation over the last 20 years. Most related systems are based on metallic clusters including transition metal or lanthanide ions connected through diamagnetic ligands, the most famous one being cyanide. Using stable radicals as building blocks towards magnetic molecule-based materials is an alternative strategy. They can be used to obtain purely organic as well as hydrid compounds. This strategy has essentially been developed starting from nitroxide-based radicals.

We are currently exploring the possibilities offered by verdazyl radicals, a newcomer in molecular magnetism. This radical offers a great synthetic versatility on both the radical part and its substituent. We develop a global approach combining the experimental and theoretical exploration. As exemplified below, this back-and-forth motion between the synthesis of radical containing architectures and the theoretical investigation allows to understand the intimate mechanisms that govern the interaction between the spin bearers.

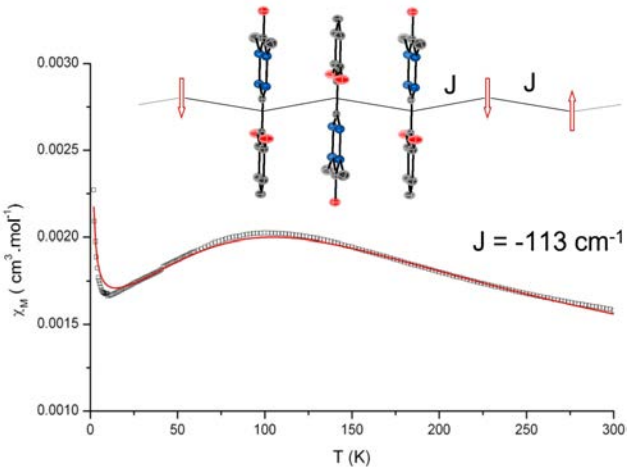


FIG. 112. *Thermal variation of the magnetic susceptibility of compound* **1**. *The solid line is the best fit of the experimental data by considering a uniform 1D model resulting from $\pi - \pi$ interactions between the radicals.*

Modifying the substituent and the charge of the radical strongly influences the crystal packing of the radical and hence the intermolecular exchange interaction. This possibility can be exemplified by comparing the structure and magnetic properties of two oxoverdazyls based compounds, the 1,5-dimethyl-3-(2'-hydroxyphenyl)-6-oxoverdazyl **1** and the perchlorate salt of 1,5-dimethyl-3-(2'-imidazolium)-6-oxoverdazyl **2** [Norel *et al.*, Polyhedron **29**, 342 (2010)]. The structural analysis of **1** reveals that radicals are closely packed in regular columns by way of $\pi$-stacking (figure 112). In contrast, the packing in **2** is definitely influenced by the protonation state of the radical substituent and shows strong lateral staggering of the organic radicals. The organisation in the solid state strongly influences the intermolecular exchange interaction between $\pi$-stacked radicals which goes from $J$ = -113 $cm^{-1}$ ($H = \Sigma - JS_iS_{i+1}$) in **1** (figure 112) to $J$ = -1.0 $cm^{-1}$ and $J'$ = -0.67 $cm^{-1}$ in **2**.

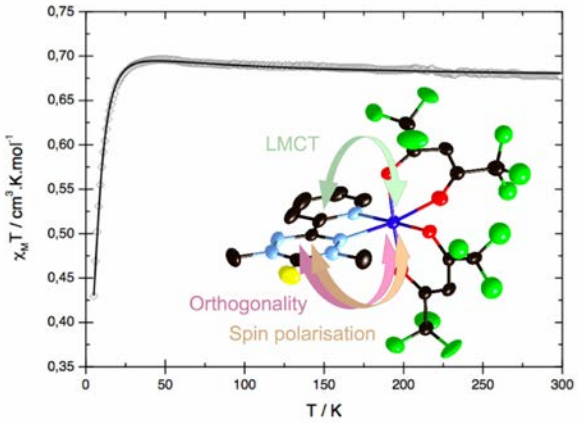


FIG. 113. *Thermal variation of the $\chi_M.T$ product of compound* **4**. *The solid line is the best fit of the experimental data. The different mechanisms governing the intramolecular exchange interaction are sketched on the structure of the complex.*

The construction of hybrid magnetic materials combining open-shell organic ligands and paramagnetic metal ions aims to exploit possibly strong metal-radical exchange interactions. In recent studies on discrete complexes [Cu(hfac)$_2$(Ovdpy)] (hfac=(1,1,1,5,5,5)hexafluoroacetylacetonate; Ovdpy= 1,5-dimethyl-3-(pyridyl)-6-oxoverdazyl), **3** [Rota *et al.*, J. Chem. Phys. **132**, 154702 (2010)] and [Cu(hfac)$_2$(Svdpy)] (Svdpy= 1,5-dimethyl-3-(pyridyl)-6-thiooxoverdazyl), **4** [Oms *et al.*, Eur. J. Inorg. Chem. (2010)], the magneto-structural correlations (figure 113) and the theoretical investigation by ab initio methods (V. Robert) afforded the identification and hierarchisation of the different mechanisms governing the metal-radical intramolecular exchange interaction beyond the usual valence-only description brought about through the Kahn's model: through Ligand-to-Metal Charge Transfer (LMCT; figure 113), the substituent of the radical brings a strong ferromagnetic contribution to the overall exchange interaction that balances the antiferromagnetic contribution arising from the spin polarisation process.

***N. Bréfuel, C. Train***
***V. Robert (Université de Strasbourg)***

# Introducing ferroelectricity in molecule-based magnets

Combining the magnetic properties of molecule-based magnets with another physico-chemical property in order to observe synergetical phenomena is one of the major trends in molecular magnetism. We have originated the observation of magneto-chiral dichroism and magnetisation-induced second harmonic generation [Train *et al.*, J. Am. Chem. Soc. **131**, 16838 (2009)] in 2D oxalate-based compounds. In solid state as well as molecular chemistry, an important effort is made to associate ferroelectricity and long-range magnetic ordering in order to observe multiferroic properties. We are currently exploring the possibilities offered by the versatility of coordination chemistry to reach this goal.

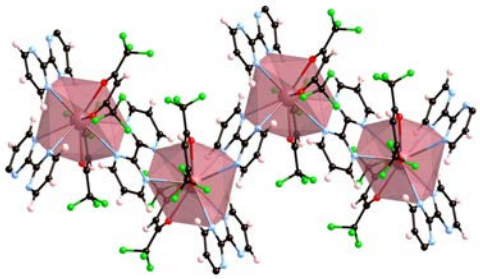

FIG. 114. *Zigzag chain of $[Ba(hfac)_2(bpm)_2]$ (hfac=(1,1,1,5,5,5) hexafluoroacetylacetonate; bpm = 2,2'-bipyrimidine).*

A first idea is to use metal ions known to favour the appearance of ferroelectric properties to construct new molecular ferroelectrics like barium(II). We have explored the association between bis(hexafluoroacetylacetonate)barium(II) and bipyrimidine derivatives [Pointillart *et al.*, CrystEngComm. **12**, 3430 (2010)]. By employing potentially bridging Lewis bases instead of chelating ligands, we have obtained three 1D coordination polymers, one of them being shown on figure 114. We demonstrate the influence of the stoichiometry and the nature of the Lewis bases on the coordination polyhedron of barium(II). This influence reflects the versatility of the coordination number of heavy alkaline-earth metal ion related to the high ionic radius of barium(II) and the non directional ionic character of the alkaline earth-ligand bonds. We show that through the bulkiness of the ligand, it is somehow possible to control this coordination number as well as the topology and the packing of the chains. Nevertheless, the three compounds crystallise in centrosymmetrical spacegroups, ruling out the presence of ferroelectricity.

A second strategy is to associate oxalate-based bidimensionnal anionic networks with polar cations. The former are known to exhibit long-range magnetic ordering for a proper choice of metal ions and to welcome a wide variety of cations in the interlayer space. The latter should favor the appearance of electric field dependent polarisation. In a first attempt, we have tried to introduce 4-aminopyridinium

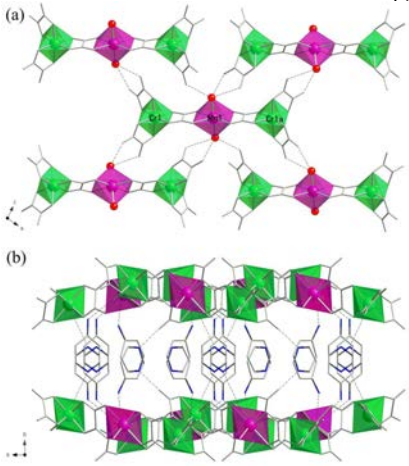


FIG. 115. *Crystal packing of $C_4[MCr_2(ox)_6(H_2O)_2]$ . 4.5 $H_2O$ along the b axis (a) and along c axis (b). In (a) dotted lines represent hydrogen bonds. The chromium and manganese surroundings are depicted as green and pink solid polyhedra.*

noted $C^+$ in oxalate-based networks [Pardo *et al.*, Dalton Trans. **39**, 4951 (2010)]. When associated with various bulky anions, this cation is indeed known to form non centrosymmetric ferroelectric crystallographic phases. By reacting $C_3[Cr(ox)_3]$ . $2H_2O$ (ox = $C_2O_4^{2-}$) with the chloride salt of manganese(II) and cobalt(II), we obtained two isostructural compounds of formula $C_4[MCr_2(ox)_6(H_2O)_2]$ . 4.5 $H_2O$. The structures of these compounds consist of discrete linear $[MCr_2(ox)_6]^{4-}$ bimetallic trinuclear units, pyridinium cations and coordinated and crystallization water molecules (figure 115). The linear trinuclear unit is built from a central trans-diaquametal(II), linked to two $[Cr(ox)_3]^{3-}$ entities by oxalate bridges. Variable-temperature magnetic susceptibility measurements indicate a weak ferromagnetic interaction between the two terminal chromium(III) and the central divalent metal ion. As previously stated in oxalate-based compounds, through the modulation of the intermolecular interactions, the choice of the cation strongly influence both the dimensionality of the final compound. In the present case, the chosen cation prevents the formation of the long-range ordered magnetic network. Moreover, the trinuclear complex does not favor a polar arrangement of the cation. Current efforts are thus devoted to synthesize new compounds using related polar precursors to get non centrosymmetric space groups and valuable dielectric properties.

***C. Train, G. L. J. A. Rikken***
***E.Pardo (University of Valencia, Spain), M. Verdaguer (IPCM, UPMC, Paris)***

# Applied Superconductivity

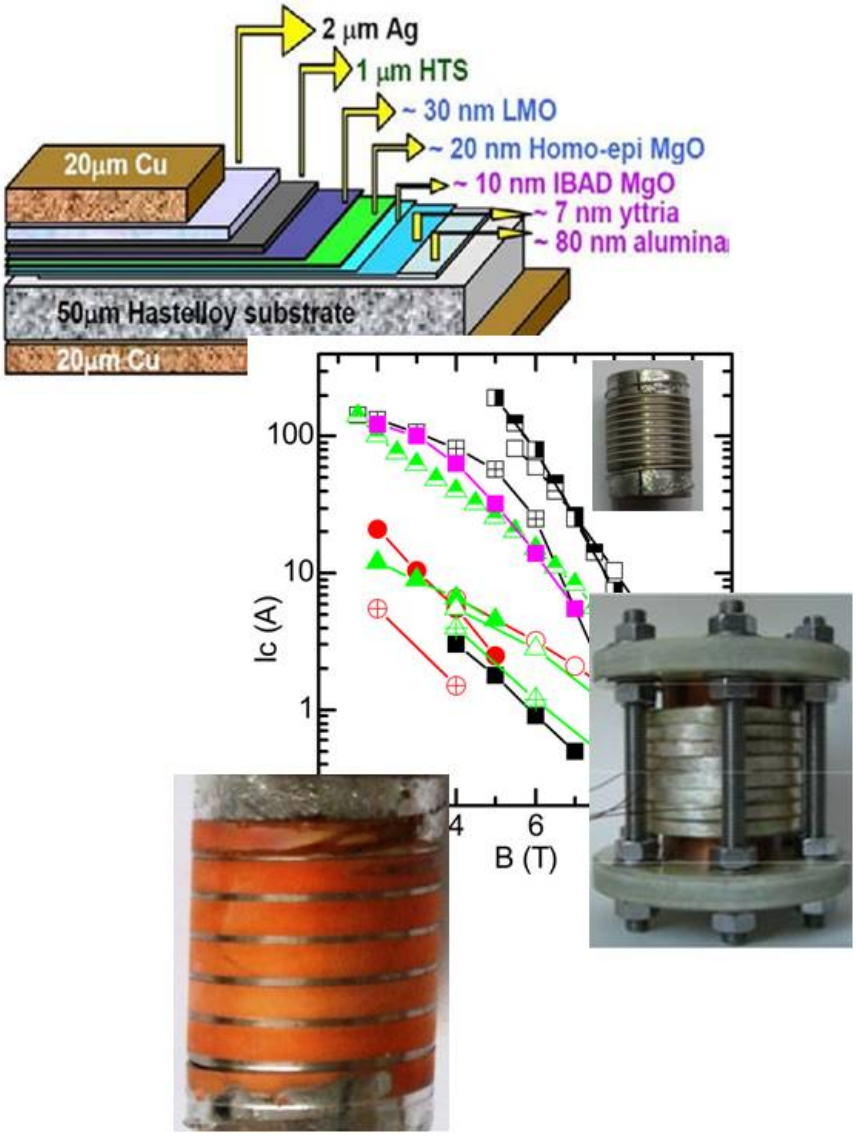

# Performance of Bi-2212 round wires

High magnetic fields are generated by circulating large electrical currents which imply large electrical power consumption and thereby high operating costs, unless flowing in a superconductor. Most superconducting magnets consist of low temperature superconductors (NbTi or $Nb_3Sn$), but they are limited to fields around 20 T by their intrinsic material properties. The main effort is now shifting to high temperature superconductors (HTSC) insert coils. This trend is encouraged by the demand for fields above 20 T and for a lower energy consumption and is now enabled by the commercial availability of HTS conductors. The ongoing focus on second generation high performance HTS conductors, such as YBaCuO coated conductors, should not put out of one's mind that first generation Bi2212 HTS conductors retain a great potential.

Small Bi2212 coils for magnetic fields of 5 T in a background field of 20 T have been realized [Weijers *et al.*, Supercond. Science Technol. **17**, 636 (2004)]. Significant improvement has been made recently by OST and Nexans to avoid leakage during heat treatment and to provide a wire with consistent performance sufficient for the design of 25 T magnets [Weijers *et al.*, IEEE Trans. Appl. Supercond. **20**, 576 (2010)]. As a clear advantage compared to YBaCuO tapes, the Bi2212 conductor is provided as a round isotropic wire ($\phi$ 0.8 mm) and can be easily incorporated into a high current cable (Rutherford).

The main issue right now is that this conductor is strain sensitive and therefore has to be wound close to its final desired shape before being heat treated to develop its superconducting properties (wind and react technique). The difficulty is that the maximum temperature (around 900 °C) determines the final critical current of the wire and that a difference of a few degrees has a drastic effect [Nast *et al.*, J. Phys.: Conf. Ser. **234**, 022026 (2010)]. The temperature must be precisely adjusted and the furnace homogeneity better than a couple of degrees.

We have measured the critical current on Bi2212 round wires provided by OST versus magnetic field for wires with a typical cross section diameter of 0.8 mm. A first series of short samples (about 3 cm long sample)was annealed at CRETA in a small, so heterogeneous, furnace following the heat treatment given by OST without any adjustment. The critical current values (*e.g.* 190 A at 4.2 K and 0 T) are less than the specification given by OST for this wire (300 A at 4.2 K and 0 T) showing the importance to have the right heat treatment (figure 116).

A 1 m length of wire wound on a barrel close to the dimension of a VAMAS was sent to OST for annealing. The wire was then transferred to a VAMAS support (figure 117) for measurement. The VAMAS-like coil values are rather consistent with the measurement on short samples (figure 118). The value at 0 T and 4.2 K is slightly higher (230 A vs 190 A), but those at higher field are lower. Further investigations are under way to understand the reason of such difference, *i.e.* heat treatment, nature of the barrel used for annealing or handling of the wire.

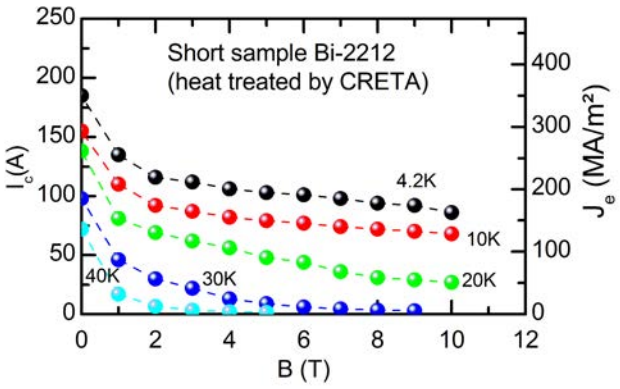


FIG. 116. *Critical current and engineering current density versus magnetic field measured on an OST Bi2212 round wire short sample annealed at CRETA.*

FIG. 117. *Bi2212 round wire and Bi2212 VAMAS coil.*

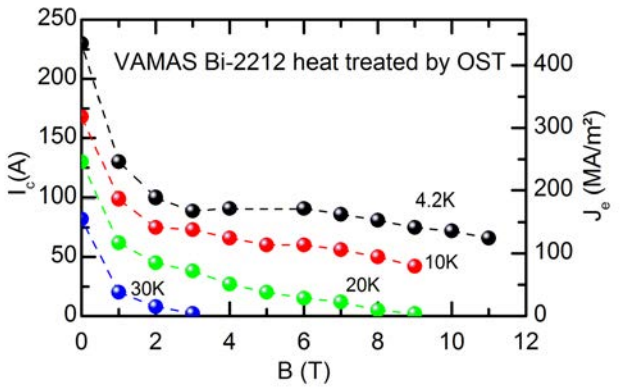


FIG. 118. *Critical current and engineering current density versus magnetic field of an OST Bi2212 round wire VAMAS annealed by OST.*

***F. Hatanian, S. Dufresnes, F. Debray, E. Mossang, X. Chaud***
***P. Tixador (Institut Néel / G2Elab, Grenoble, France), T. Lecrevisse, J.M. Rey (CEA-IRFU, Saclay, France), C.-E. Bruzek (Nexans, Paris, France)***

# Performances of commercially available YBaCuO coated conductors

Among the HTS superconductors, the second generation (2G), the YBaCuO Coated Conductors, shows very exciting performances in terms of critical current. They are now available commercially in reasonable length SuperPower® (SP), American Superconductor® (AMSC)) and manufacturing focus to provide reliable, consistent performance conductors. 2G HTS are expected to push high field magnet technology to higher field levels and to meet the demand for $25-50\,\mathrm{T}$ magnets [Markiewicz *et al.*, AIP conf. Proc. **1218**, 225 (2010)] which is beyond the possibilities offered by $Nb_3Sn$. For these reasons, we have a strong interest to follow their developments and we are involved in the characterization of such conductors in the frame of two contractual projects, the ANR project *SuperSMES* aiming at developing HTS magnet technology for high energy density SMES and the European project *EuCARD* aiming at developing a very high field HTS dipole insert.

Although effort towards round wires are made [Odier *et al.*, Supercond. Science Technol. **22**, 125024 (2009)], the 2G HTS are currently available in tape form only. We tested so far wires purchased from AMSC (344C) and SP (SCS4050). They are both elaborated following a similar architecture as the one shown in (figure 119). They consist of an inexpensive high strength metal alloy tape, Hastelloy® C-276, textured by rolling assisted biaxial texturation of substrates (RABiTS). Various layers are then deposited by techniques varying from one provider to another, on top of which the YBaCuO layer. The buffer layers protect the substrate from oxidation as well as propagate, accommodate and improve the texture so that the epitaxial texturation of the YBaCuO layer is optimized to guarantee a high critical current density. This assembly is then sandwiched between copper layers that insure protection and thermal stability.

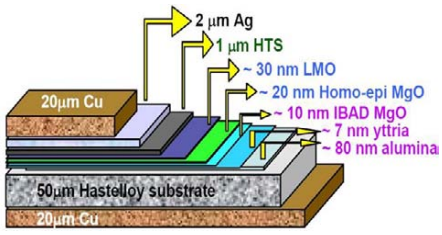


FIG. 119. *Scheme (top) of the architecture of a Superpower® YBaCuO coated conductor*

Both conductors are given for a maximal current of about 90 A at 77 K. The AMSC tape is slightly larger than the SP tape (4.4 vs 4 mm), but is twice thicker (200 vs 100 $\mu$m). As a consequence the $J_e$ is half and the bending radius twice (12.5 vs 5.5 mm). The maximum rated tensile stress, as given for $I_c$ retention greater than 95%, is more than 550 MPa for the SCS4050 (150 MPa for the 344C).

For current measurement, the conductors have been wound into a VAMAS coil (figure 120). This insures a sufficient length to inject the current into the conductor and to detect the supra-to-normal transition with the $1\mu$V/cm criterion. The measurement results are shown for both conductors at various temperatures from 77 to 20 K. One of the difficulties for characterization at lower temperature is the very high value of the currents carried by YBaCuO tapes even under high magnetic flux densities. The samples are cooled by helium gas and the heating at the current leads remains an issue.

FIG. 120. *VAMAS coil made with a 1 m length of YBaCuO coated conductor.*

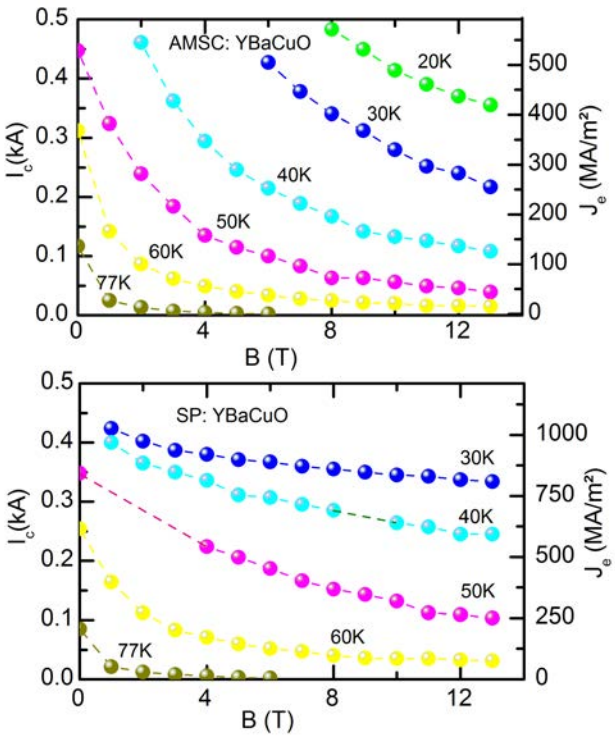


FIG. 121. *Transport critical current $I_c$ and engineering current density $J_e$ versus magnetic field at different temperatures in VAMAS configuration for two different YBaCuO coated conductors: AMSC (top) and SP(bottom).*

***F. Hatanian, S. Dufresnes, F. Debray, E. Mossang, X. Chaud***
***P. Tixador (Institut Néel / G2Elab, Grenoble, France), T. Lecrevisse, J.M. Rey(CEA-IRFU, Saclay, France)***

# Comparative investigation of YBaCuO Vamas samples

In order to produce always stronger magnetic field for different applications such as particles accelerators, MRI and NMR magnets, SMES, conductors which can transport high currents in high magnetic fields are of major importance. YBCO materials are very promising because of their large upper coercive field ($H_{c2} > 60$ T) and the capacity to carry very high current density (more than 120 A/mm$^2$ at 77 K self-field). For those reasons, LNCMI-G and CEA Saclay have a strong interest to follow their developments and are characterizing such conductors in the frame of two contractual projects. One ANR funded project called SuperSMES aiming at developing HTS magnet technology for high energy density SMES and the European project EuCARD aiming at developing a very high field HTS dipole in relation with LHC upgrades for CERN.

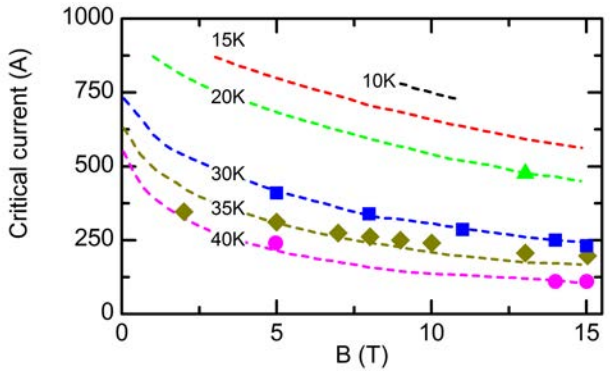


FIG. 122. *Critical current as function of magnetic field for a Vamas YBaCuO SuperPower® SCS4050. Dashed lines (Saclay data) and symbols (Grenoble data).*

Following the work made last year, the two conductors purchased from American Superconductor® (AMSC) (344C) and SuperPower® (SP) (SCS4050) were tested under high parallel field and at different temperatures.

For current measurement, the conductors have been wound into a VAMAS sample [Rey *et al.*, IEEE Trans. on Applied Superconductivity **19**, 3088 (2009)]. This insures a sufficient length to detect the superconducting-to-normal transition using the 0.1 $\mu$V/cm criterion. The samples are cooled by helium gas.

LNCMI and CEA Saclay have made complementary tests to compare the measurements and obtain a wide range of results. It is easier to make tests at high temperatures (above 45 K) on the LNCMI station, while the problem of Joule heating at lower temperature and higher current is less problematic on the CETACE station at CEA Saclay. Some comparison results are shown in figure 122 for SuperPower® SCS4050 between 10 K and 40 K.

The results show generally a good agreement between the two laboratories, however, the Joule heating seems to limit the accuracy in Grenoble for high current (see 35 K, 2 T for example). The current ramp rate at Grenoble is higher than that used in Saclay allowing a more rapid testing (about 5 s for a test in Grenoble compared to about 2 minutes in Saclay) which is necessary to limit the Joule heating because of the non-superconducting current leads used in Grenoble.

Figure 123 presents complementary work to determine the characteristic of the tape at self-field which could be very useful for critical current modelling. The testing conditions needed to ensure a good accuracy are well controlled allowing precise measurements for model development. Indeed, one of the difficulties for the low temperature characterization is the very high current value carried by YBaCuO tapes even under high magnetic flux densities (more than 880 A for SP SCS4050 and about 810 A for AMSC 344C at 20 K self-field). Moreover, due to the very high value of $H_c2$, tests at higher magnetic field (higher than 15 T) will be very interesting in determining parameters such as the maximal peak field corresponding to the maximal macroscopic pinning forces [van der Laan *et al.*, Physical Review B **77**, 104514 (2008)].

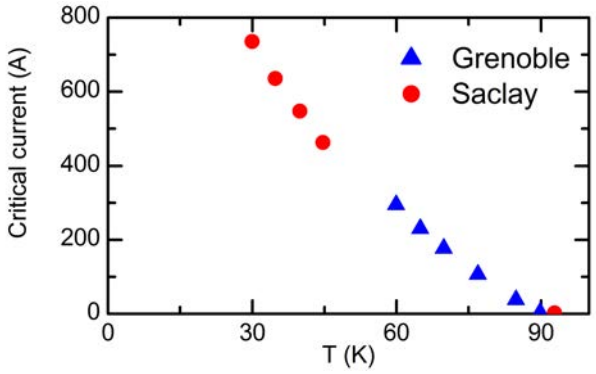


FIG. 123. *Critical current (at self-field) as a function of temperature for SuperPower® SCS 4050 YBaCuO.*

***F. Hatanian, S. Dufresnes, F. Debray, E. Mossang, X. Chaud***
***P. Tixador (Institut Néel / G2Elab, Grenoble, France), T. Lecrevisse, J.M. Rey(CEA-IRFU, Saclay, France)***

# Tests of small high critical temperature superconductor (HTS) coils under very high field for superconducting magnet development

A dedicated and rather unique cryostat (figure 124) has been especially developed to test small high critical temperature superconductors (HTS) coils in static high field magnets under various conditions (variable temperatures and various cooling conditions). After the successful tests, the cryostat will be installed and used on a large bore resistive magnet.

FIG. 124. *The CAD drawing and photograph of the VTI to be inserted in the 20 T 160 mm diameter bore resistive magnet.*

High critical temperature superconductors open extremely interesting perspectives for very high field applications such as high field magnets for nuclear magnetic resonance (NMR) or superconducting magnetic energy storage (SMES), nuclear fusion, or future colliders. The demand is high for 25 to 50 T magnets and is beyond the possibilities offered by low critical temperature superconductors, inter alia $Nb_3Sn$ whose ultimate limit is about 23 T. The increasing energy cost and the necessary sustainable development push the superconducting magnets, especially the HTS ones. When compared to resistive magnets, the power consumption of a superconducting magnet is very much less whereas its cooling power is comparable (cryo-cooler versus water cooling).

The interest for Bi-2212 round wire remains for high field applications ($J_c$ higher than 1000 MA/m$^2$ at 4.2 K and 45 T) even if their heat treatment is complicated and very delicate. Their mechanical properties are not outstanding but their main advantage is the possibility to manufacture high current Rutherford cables.

The second generation (2G) of HTS conductors, the YBaCuO coated conductors, show also very exciting performances in terms of critical currents under very high fields whereas their mechanical properties, the key issues for very high field magnets, are outstanding for the IBAD route. The 2G HTS have now produced in lengths allowing to use them in real devices.

Grenoble was at the origin of the superconducting magnet developments in France and wants to keep its leadership. Developing HTS technology will allow the LNCMI to play a major role in the construction of new economical high field magnets including the use of HTS, for in-house and external use. This is why since a few years a development program for HTS magnets has been launched. This program is supported by France through the ANR project *SuperSMES* and by the European Community through the EC project *EuCARD* for which Grenoble team leads the task about HTS insert development. This program has inter alia many experimental developments to qualify the solutions and to progress in our knowledge/understanding and know how. Aspects of the magnet technology including winding, joints, insulation, and reinforcement have to be examined as well as quench protection. To test various solutions we want to measure small coils (figure 125) under very high field (up to 20 T) to evaluate the most severe constraints for the HTS magnet without having to build a complete magnet.

FIG. 125. *YBaCuO coated conductor magnets made by 8 pancakes.*

***F. Hatanian, F. Debray, E. Mossang, X. Chaud***
***J.P. Leggeri, H. Rodenas, O. Tissot, G. Barthélémy, J. Vialle, G. Donnier-Valentin (Institut Néel, Grenoble, France), P. Tixador (Institut Néel / G2Elab, Grenoble, France)***

# Magnetic field behaviour of ex-situ processed MgB2 monofilamentary tapes

In order to develop and improve the $MgB_2$ superconducting properties in high magnetic field we study the influence of the addition of silicon carbide (SiC) and the filling density of the powder for the ex-situ powder in tube method (PIT). The last investigation is divided on two topics: (1) SiC addition and (2) powder density.

**SiC addition**: In previous work we saw how lowering the synthesis temperature of the $MgB_2$ down to 745°C increased the critical current. We have recently measured several tapes with SiC addition into the $MgB_2$ powder during the low temperature synthesis. The transport measurements do not show any appreciable improvement by SiC addition when we compare the performance of low synthesis temperature versus the high synthesis temperature (sample DT037), see figure 126.

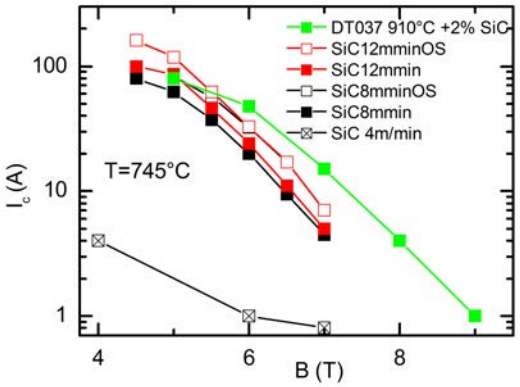


FIG. 126. *Transport critical current (IC) for different samples with SiC addition measured in magnetic field up to 9 T using a helium bath cryostat ($T = 4.2\,K$) inside a wide bore resistive magnet.*

In this context, the powder's synthesis temperature can play a crucial role, the gain of the current performance by lowering the synthesis temperature may be lost with the incomplete SiC decomposition at low synthesis temperature. This is also confirmed by X-ray data, where there is no evidence for the presence of $Mg_2Si$ (due to the SiC decomposition and subsequent reaction with Mg of the $MgB_2$).

**Powder density**: In the second topic we have focused our work on obtaining monofilamentary conductors with a high powder filling density to try an improvement of the powder connectivity. In this context, during the tape preparation, we used a hydraulic press to fill the sheath with the $MgB_2$ powders. The pressure was increased from 350 up to 1400 psi. After the filling process the samples were mechanically deformed to have several samples; respectively at 350, 700, 1100 and 1400 psi. During the measurements we have had a number of problems on the sample holder and also on the lab apparatus for the magnetic field control. For this reason only the higher and lower density samples were measured (figure 127). The density of the powders was really increased, but when the density is increased above 350 psi some cracks inside the conductor are present decreasing the current performance with further increasing density.

Some Columbus's samples were measured (figure 128). The experiments performed by Columbus superconductors in high magnetic fields are focused to evaluate the improvement of the magnetic field dependence of the critical current densities of $MgB_2$ based multifilamentary conductors.

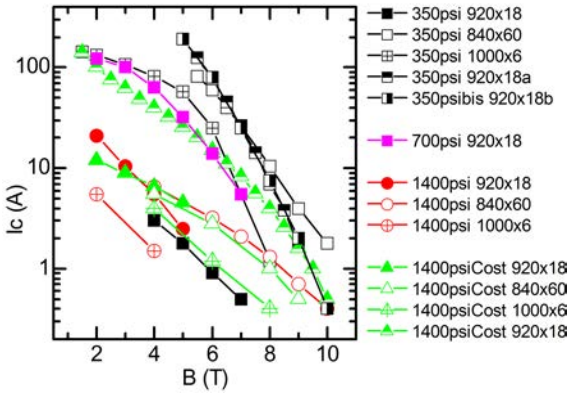


FIG. 127. *Transport critical current ($I_c$) for different samples measured in magnetic field up to 10 T using a helium bath cryostat ($T = 4.2K$) inside a wide bore resistive magnet.*

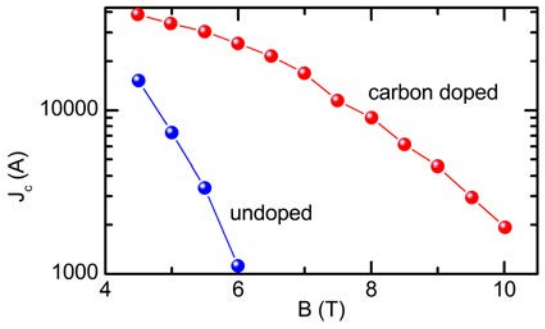


FIG. 128. *Comparison between transport critical current density of undoped and carbon doped multifilamentary conductors measured up to 10 T using a wide bore resistive magnet and a helium bath cryostat*

***X. Chaud***
***M. Vignolo, G. Romano, A. Malagoli, C. Ferdeghini, M. Putti (CNR-SPIN, Genova, Italy), S. Brisigotti, G.Grasso, A. Tumino (Columbus Superconductors S.p.A., Genova, Italy)***

# Magneto-Science

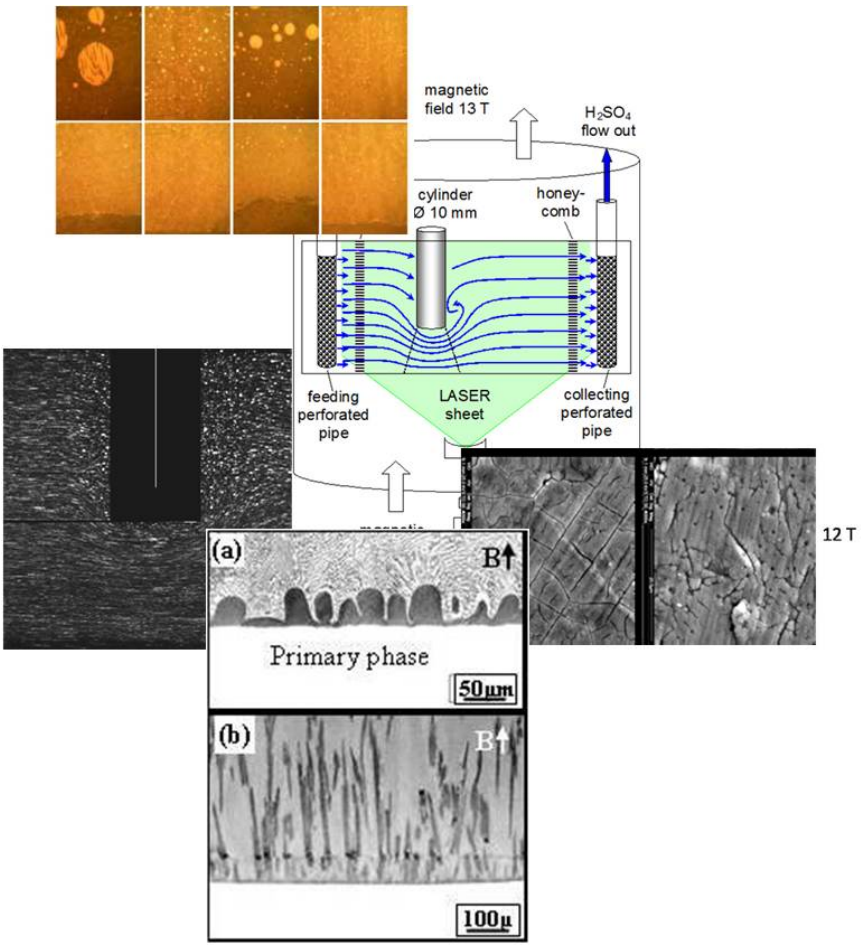

# Advanced magneto optics

In 2009-2010 we have measured for the first time the Inverse Cotton Mouton effect in a TGG ($Tb_3Ga_5O_{12}$) crystal; we improved the Axion-like particle's limits thanks to a shining wall experiment placed at ESRF; and, in the meantime, the magnetic vacuum birefringence (MVB) experiment was in progress at the LNCMI Toulouse.

**For the MVB experiment**, the main novelty of this year is the improvement by a factor of 2.5 of the finesse of our Fabry Perot cavity. This finesse is now higher than 500000 which implies that we have the cavity with the narrowest linewidth (128 Hz) in the world (for comparison LIGO, a gravitational waves interferometer in the United States, has a cavity linewidth of 160 Hz).

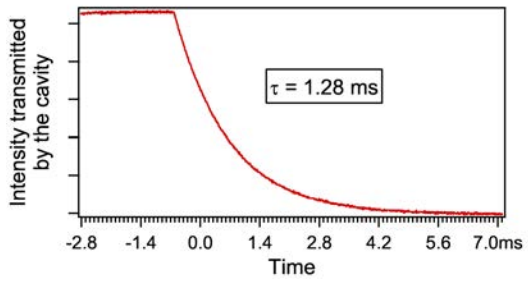


FIG. 129. *Photon lifetime in the Fabry Perot cavity deduced by an exponential decay fit of the intensity time evolution when the laser is switched off. This decay corresponds to a finesse of* 529000 *and a cavity linewidth of* 128 *Hz.*

**The Inverse Cotton-Mouton Effect (ICME)** is the magnetization induced in a medium by a non-resonant laser beam propagating in the presence of a transverse magnetic field. We performed a detailed study of the ICME in a TGG cubic crystal of 2 mm on its side, showing the dependence of the measured effect on the laser power density and polarization, and on the applied magnetic field.

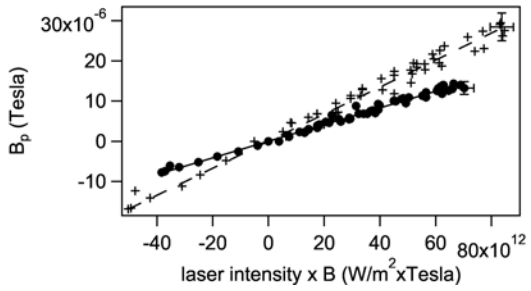


FIG. 130. *Magnetic flux density versus the product of laser power density and the applied magnetic field $B_{ext}$ for two light polarizations: parallel (+) and perpendicular (•) to $B_{ext}$. Data are fitted by linear equation.*

We showed that this magnetization is proportional to the value of the magnetic field, and to the energy density of the propagating electromagnetic waves as shown on figure 130. This certainly opens a new field of investigations of electromagnetic properties of matter. This effect has also some peculiar features that are very interesting in view of an application of ICME in optical devices (article submitted, patent pending).

**Photoregeneration using X-rays at ESRF : X-AXions (XAX).** This experimented is based on a shining wall experiment set up extended for the first time to high energy photons (X-Rays). Photons travel through a coil giving a transverse magnetic field. Some photons are converted into axions with a probability. A wall is placed after the coil in order to stop every photon, while axions cross since they hardly interact with ordinary matter. A second coil placed behind the wall converts the axions back into photons. These photons have the same energy as the initial ones and they can be detected with a suitable detector.

The experiment has been carried out at the European Synchrotron Radiation Facility (ESRF) in Grenoble. We used two different photon energies, $\omega = 50.2\,\mathrm{keV}$ and $90.7\,\mathrm{keV}$, corresponding to slightly different settings of the X-ray beamline. No excess count above background has been detected. Our limits on the axion-two photon coupling constant $g$ as a function of the axion mass $m_a$ at 95% confidence level are plotted in figure 131 which shows that we have extend limits to a parameter region where no model independent limits had been set so far. These results have been submitted for publication [Battesti *et al.*, Phys. Rev. Lett. **105**, 250405 (2010)].

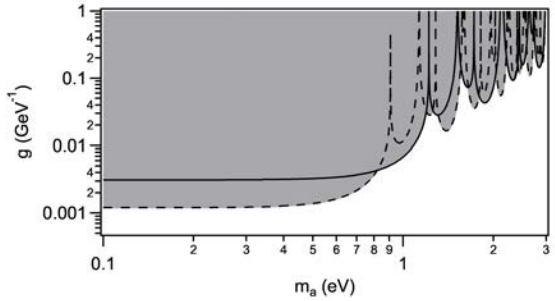


FIG. 131. *Limits on the axion two photon coupling constant $g$ as a function of the axion mass $m_a$. The areas above curves is excluded. Limits obtained with a photon energy of* 50.2 *keV (dashed line) and* 90.7 *keV (solid line).*

***P. Berceau, R. Battesti, M. Fouché, G.L.J.A. Rikken, C. Rizzo***
***A. Baranga (Beer Sheva University, Israel), C. Detlefs, T. Roth (ESRF, Grenoble)***

# Experimental study of the flow around a cylinder under a strong magnetic field

Flows around obstacles are among the most common problems encountered in the fluid mechanics literature, and cylindrical obstacles have definitely received the most extensive attention. The reason for this is that this relatively simple geometry already encompasses most of the important physical effects likely to play a role in flow around more complicated obstacles. When the working fluid conducts electricity additional effects are involved. In particular, the presence of a magnetic field tends to homogenize the flow in the direction of the magnetic field lines which leads to strong alterations of the flow patterns known from the classical non-conducting case. Since liquid metals commonly used in the magneto-hydrodynamic (MHD) experimental practice are opaque, their interior cannot be visualized, which severely hampers our understanding of magnetohydrodynamic flows.

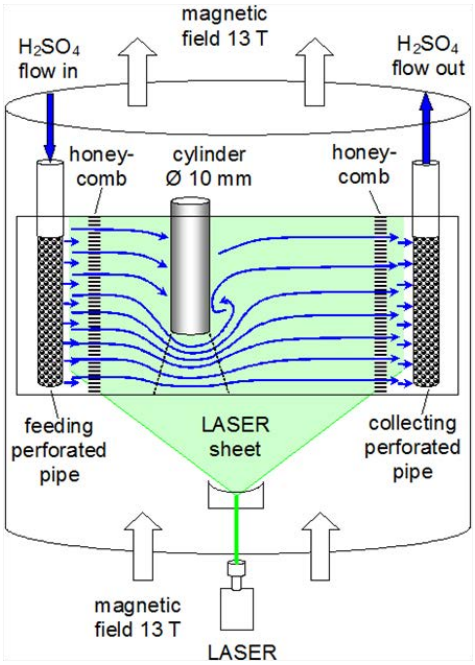


FIG. 132. *Sketch of experimental device to measure flow.*

The purpose of the present project is to demonstrate that this fundamental limitation of experimental MHD can be overcome using a large bore 13 T resistive magnet at LNCMI. This facility permits us to perform an MHD experiments with transparent electrolyte (37% aqueous solution of $H_2SO_4$) instead of opaque liquid metals. The test-section is schematically shown in figure 132. It is a straight channel with a rectangular 40×40 mm cross-section placed in a 130 mm room temperature bore of resistive magnet. Transparent Plexiglas walls of the channel allow optical observation of the flow illuminated by a laser sheet in the mid-plane of a truncated non-conducting cylinder (10 mm in diameter and 25 mm length).

For the first time the experiments will provide a direct optical access to the so-called MHD-columns which have never before been directly observed. In figure 133(a) such a column is clearly expressed as a stagnant zone attached directly below the top of the cylinder under 13 T magnetic field. In contrast, in the absence of a magnetic field (figure 133(b)) the intensive flow is sufficiently displaced toward the cylinder top. The results of numerical simulation (figure 133(c)) show that in the MHD case the stagnant zone plays a role of a quasi-solid body, which virtually elongates the cylinder along the magnetic field.

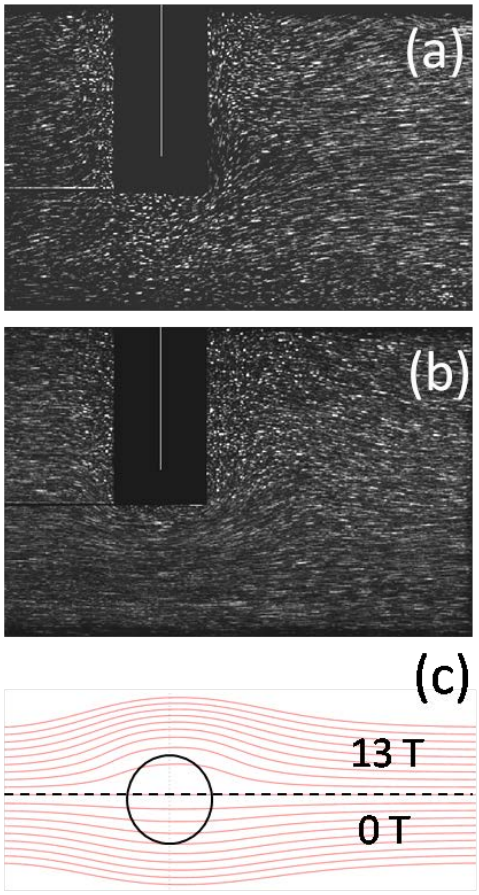


FIG. 133. *Tracer images of flow around the truncated cylinder; (a) under 13 Tesla magnetic field, Hartmann number* $Ha = 24$*, (b) without magnetic field, Reynolds number* $Re = 1$*. (c) Numerical simulation for* $Re = 1$ *of stream lines of the flow in the horizontal plane 2 mm below the top of the cylinder.*

***F. Debray***
***O. Andreev (Technische Universitt Ilmenau, Germany)***

# Solidification of hyper-monotectic Zinc-Bismuth alloy in a strong magnetic field

With the distinctive performance and the extensive application, the monotectic alloys attract much attention from researchers majoring in material and metallurgy. However, due to the immiscible gap during solidification, serious gravity segregation even a layered structure appears under traditional solidifying condition, as a result, the excellent mechanical characters of the alloy cannot be exhibited.

Recently, a new way to control the gravity segregation by superimposing a strong static magnetic field was proposed, one can even obtain homogenous Cu-90wt%Pb alloy in 12 T magnetic field, however, to hyper-monotectic alloy, superimposition of 12 T magnetic field cannot still damp the gravity segregation thoroughly, and how the strong static magnetic field affect the nucleation and growth of the second liquid phase particles as well as the movement of them is not clear up to now.

In order to investigate how the magnetic field effects the solidification of hyper-monotectic alloy, we applied a 18 T static magnetic field, to the solidifying process of Zinc-Bismuth alloy. To avoid the delamination of the alloy due to the serious gravity segregation, we quenched the sample of Zn-4wt%Bi, 5wt%Bi, 6wt%Bi, 7wt%Bi, 15wt%Bi, 30wt%Bi alloy into water in 0 T and 18 Tesla.

Figure 134 shows the longitudinal microscope image of the sample. Figure 134 shows that, when the content of Bismuth is 5-7wt%, the superimposition of 18 T magnetic field can damp the segregation remarkably, and the size of the second phase particles also is decreased, which means that the agglomeration of the second phase particles due to STOKES settlement is retarded obviously. Furthermore, to Zn-4wt%Bi alloy solidified in 18 T magnetic field, no spherical bismuth particles are found even magnifying 1000 times by microscope, which hints that the 18 T magnetic field may change its solidifying character.

To Zn-15wt%Bi and Zn-30wt%Bi alloy, due to their strong segregation trend, the 18T magnetic field still cannot damp the STOKES settlement thoroughly even by quenching way, however, no layered bismuth and zinc appears when compared to 0 T, large Bismuth block are formed in the lower half part of the sample. It is well known that the magnetic field can damp the flow and hinder the movement of particles in conductive liquid, also the diffusion due to the flow or convection can be decreased.

As we know, the size of the second phase particles in solidifying hypo-monotectic alloy is determined by the STOKES settlement, natural convection, marangoni convection and diffusion rate of solute, and the superimposition of the 18 T magnetic field can decrease the magnitude of the above parameters, which results the decrease of the size of the second phase particles. The dynamics of the nucleation and growth of the second phase particles in strong magnetic field should be studied quantitatively later.

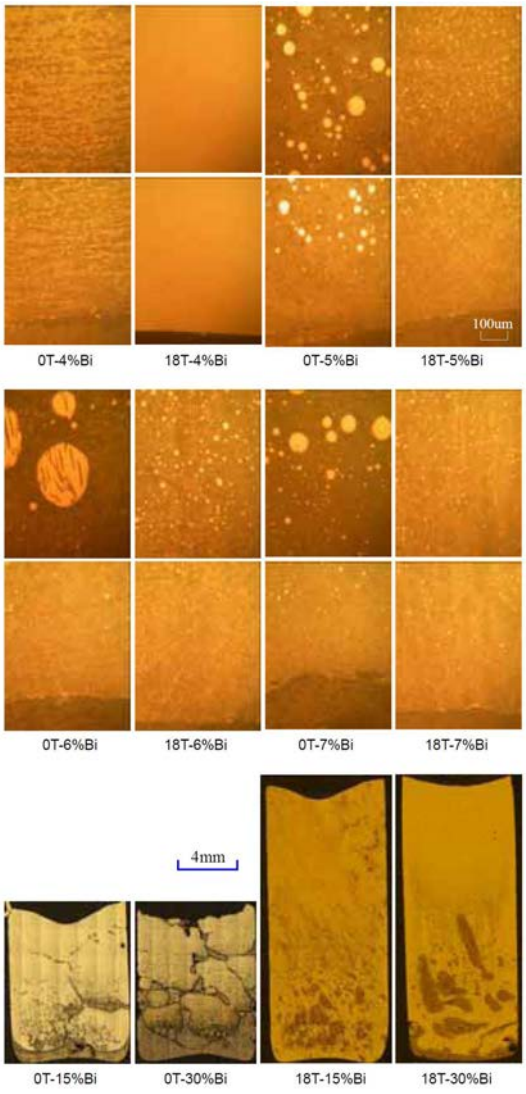


FIG. 134. *Solidifying structure of Zn-Bi alloy in 0 T and 18 T magnetic field*

***F. Debray***
***Y. Fautrelle(SIMAP, EPM, CNRS, Grenoble), Yunbo Zhong, Jiang Wang(Shanghai University, Shanghai, P.R. China)***

# A novel method to prepare aligned columnar dendrite during the solidification process under a high magnetic field

Here we present a novel method to prepare aligned columnar dendrite during the diffusion process of the Al-Cu diffusion couple under magnetic field. Figure 135 shows the microstructure near the Cu/Al interface of the sample fabricated with and without the magnetic field. The morphology of the columnar dendrite in the sample fabricated without $B$ is random array. In the sample fabricated heated to 570°C and to 610°C and held for 5 hours, and then solidified under a 16 T magnetic field, respectively, regular aligned dendrite are formed. With increasing solidification temperature, the columnar dendrites increases gradually. This implies that aligned dendrites may be produced during the diffusion process under the magnetic field.

Further, the EBSD analysis has been applied to measure the crystallographic orientation of the dendrite. The measurement (not shown here) indicates that the ≤001≥-crystal direction of the $Al_2Cu$ crystal orients along the magnetic field. In our previous work [Li *et al.*, Acta Mater. **58**, 1403 (2010)], it has been proven that the $Al_2Cu$ crystal shows remarkable magnetocrystalline anisotropy, and the ≤001≥-crystal direction is the easy magnetic axis of the crystal. The above result implies that the columnar dendrites are aligned with the easy magnetic axis, *i.e.*, along the magnetic field and that the regular $Al_2Cu$ columnar dendrite originating from the Cu/Al interface is formed during the diffusion process of the Cu/Al diffusion couple under a magnetic field. This implies that the aligned columnar dendrite can be grown by applying a high magnetic field during the diffusion process. This may open a new way to fabricate the aligned columnar dendrite under the zero temperature gradient.

The formation of the columnar dendrite during the directional solidification is attributed to the formation of the thermal undercooling in front of the solid/liquid interface. During the diffusion process under the magnetic field, initially the magnetic field may align the dendrite, and then the content of the solute in front of the dendrite will increase along with the enhancement of the diffusion. As a consequence, a concentration undercooling forms in front of the dendrite, enhancing the growth. Figure 136 shows the schematic diagram of the aligned columnar dendrite growth during the diffusion process in the A/B diffusion couple under the magnetic field. From the phase diagram of the A-B binary system it is known that a high temperature primary phase and eutectic phase exists in this system. When the A/B diffusion couple is heated above the eutectic point, the liquid eutectic phase will first form at the A/B interface. Then, along with the diffusion of the A and B atoms through the liquid eutectic, the primary phase will form at the interface and align under the magnetic field. It is not difficult to understand that with the increase of the temperature or time, the solute concentration in front of the dendrite will increase. Thus, the undercooling caused by the concentration will drive the dendrite to grow. In the Al-Cu system, the $Al_2Cu$ phase will form along with the diffusion. Owing to the magnetic crystalline anisotropy of the $Al_2Cu$ crystal, the $Al_2Cu$ phase will first be aligned with its easy magnetic axis along B, and then with the enhancement of the diffusion and the increase of the undercooling, the aligned columnar $Al_2Cu$ dendrite are formed. (figure 136).

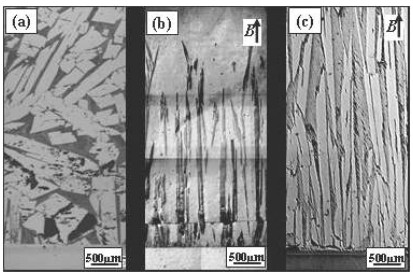


FIG. 135. *Effect of a 16 T high magnetic field on the growth of the columnar dendrite during the diffusion process of the Cu/Al diffusion couple: (a) Heated to 600°C and held for 5 hours, then solidified without the magnetic field; (b) heated to 570°C and held for 5 hours, then solidified with a 16 T high magnetic field; (c) heated to 610°C and held for 5 hours, then solidified under a high magnetic field.*

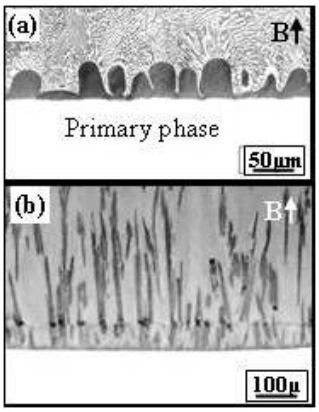


FIG. 136. *Schematic diagram of the aligned dendrite during the diffusion process under magnetic field; growth of the $Al_2Cu$ columnar dendrite from the Cu/Al interface during the diffusion process of the Cu/Al diffusion couple under the 16 T magnetic field with the increase of the diffusion time $t1$ and $t2$ (a) and (b) respectively with $t1 \leq t2$.*

***F. Debray***
***Y. Fautrelle, B. Saadi (SIMAP, EPM, CNRS, Grenoble, France), Xi Li, Z. Ren (Dep.of Mat.Eng., Shanghai University, China)***

# Hydrogen evolution on a Ni electrode in high magnetic field

Iron group metals or alloys electrodeposition is always accompanied by violent hydrogen evolution [Zabinski *et al.* Mat. Trans. **47**, 2860 (2006), Zabinski *et al.* J. Electrochem. Soc. **150** C717 (2003). An applied magnetic field parallel to the electrode surface leads to enhancement of the mass transfer through the additional convection which arises as an effect of Lorenz force and a magneto-hydrodynamic (MHD) effect. The desorption rate of hydrogen is increased in parallel magnetic field. The perpendicular field orientation case is more complicated. When a $H_2$ bubble is formed at the electrode surface the current distribution in its vicinity is distorted. The current lines are no longer perfectly normal to the electrode surface, and there is also a parallel-to-electrode component. As a consequence a Lorentz force is induced.

The Lorentz force acting in the bubble vicinity induces a localized convection close to it. This effect is analogous to a micro-MHD effect. When a magnetic field is applied perpendicular to the electrode, a localized convection introduces a hydrodynamic drag force, which acts on the hydrogen bubble. The contact angle increases, due to the drag force action, and smaller $H_2$ bubbles can be removed from the electrode surface. As a consequence, enhanced desorption of hydrogen is observed. The same effect should be observed during hydrogen evolution on metallic cathodes. The applied magnetic field may lead to faster desorption of hydrogen bubbles and hence the hydrogen evolution will be enhanced.

Experiments with magnetic field generated by large bore resistive magnet up to 12 Tesla oriented parallel to the electrode surface were performed in order to check the influence of magnetic field intensity on hydrogen evolution performance. In case of hydrogen evolution on nickel metal electrode the hydrogen evolution is increased by magnetic field *i.e.* the Tafel slope of galvanostatic polarization curve is lower. However there is no difference when magnetic field is applied parallel or perpendicular orientation. It suggests that the same mechanism of hydrogen evolution enhancement took place. It is related to the MHD effect and lowering the size of $H_2$ bubble by magnetic field action and in this way easier desorption of hydrogen from electrode surface. In case of Ni-Mo alloy, when the hydrogen evolution performance is very high due to presence of alloying metal, there is no visible effect of applied magnetic field. Both galvanostatic polarization curves for hydrogen evolution with and without presence of magnetic field show the same slope for hydrogen evolution process. It means that the hydrogen evolution is so fast that the presence of a magnetic field during experiments does not change the speed of creation nor the size of a single bubble. The hydrogen evolution enhancement by alloying element (Mo) is dominant.

It is interesting to establish if there is a minimal magnetic field intensity which changes the hydrogen evolution performance. In order to clarify the effect of magnetic field intensity on the hydrogen evolution a series of experiments with Ni metal with magnetic field from 0.3 to 12 Tesla have been performed. The results shown in figure 137 show that there is no influence of the magnetic field on hydrogen evolution performance when it is oriented parallel to the surface of electrode. The Tafel slope remains the same for the Ni metal electrode. This suggests that even magnetic field with intensity of 0.3 Tesla oriented parallel to the electrode leads to creation of MHD effect sufficient for increase hydrogen bubbles desorption from surface of electrode.

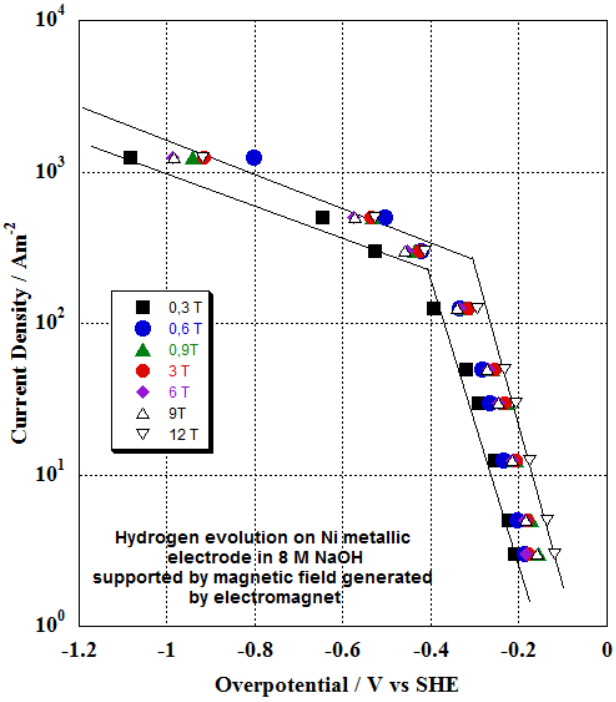


FIG. 137. *Hydrogen evolution on Ni metallic electrode in 8 M NaOH increased by a magnetic field generated by a large bore resistive magnet with intensity from* 0.3 *to* 12 *T.*

In conclusion, the magnetic field leads to increase of hydrogen evolution on metallic electrodes. The magnetic field action on hydrogen evolution is connected with MHD effect which leads to faster desorption of hydrogen bubbles from electrode surface.

***F. Debray***
***P. Zabinski, R. Kowalik, A. Jarek (AGH-University of Science and Technology, Krakow, Poland),***

# Electro-crystalization of iron group alloys under high magnetic field

During the past decades the influence of an applied magnetic field on electrochemical processes was extensively investigated. The most established impact on the electrochemical processes is the magnetohydrodynamic effect. The main driving force of the MHD effect is the Lorentz force, which arises as a cross product between the current density and magnetic flux density. This is a macroscopic effect, which induces additional stirring of the electrolyte and as a result, mass transport is increased. It was found that convection could be also introduced on a microscopic level, when a magnetic field is applied parallel to the electric field. This is due to fluctuations in the current distribution over the electrode surface, *i.e.*, so-called micro-MHD effect. The magnetic forces generated by the passage of the current and the superimposed magnetic field create additional convection which affect the morphology of the deposits. Thus, by using a magnetic field we may obtain alloys with physical properties suitable for new applications.

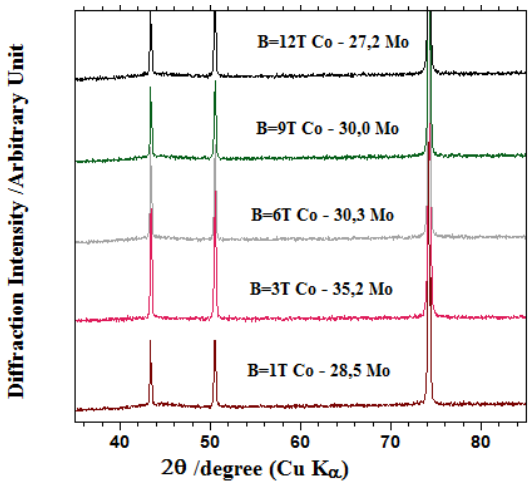


FIG. 138. *XRD diffraction pattern of Co-Mo alloys deposited with magnetic field parallel to the surface of electrode.*

A magnetic field applied parallel to the surface of the electrode generates a convection (MHD effect) of the electrolyte; it results in a laminar flow on the surface of the electrode which reduces the diffusion layer and increases the concentrations gradients. This results in change of the size of the grains and thus can also influence the texture and formation of various phases of the deposits. These various effects can be caused at the same time by the above mentioned convection but also by the magnetic properties, when the field is superimposed the growth in the direction of easier magnetization appears. Here we investigate the influence of a magnetic field applied parallel or perpendicular to the electrode during the deposition of iron group metals and alloys. XRD diffraction pattern of deposited Co-Mo alloys are presented in figure 138. The alloys show a perfectly amorphous structure. Peaks presented on the alloys XRD scans are coming from fcc structure of copper *i.e.* substrate of cathode.

Cobalt content in alloy is increased with increasing of magnetic field intensity. This could be explained by magnetic field action on hydrogen evolution. Cobalt electrodeposition is always accompanied by violent hydrogen evolution. When magnetic field is applied the size of hydrogen bubbles is smaller and they are removed faster from the surface of the electrode. In this way the cobalt partial current efficiency is increased and content of cobalt in alloy is higher. The magnetic field also influences the morphology of Co-Mo alloys. Hydrogen evolution supported by magnetic field gives a smooth surface to the alloys (figure 139). This effect is visible only for magnetic field of 6 Tesla or more.

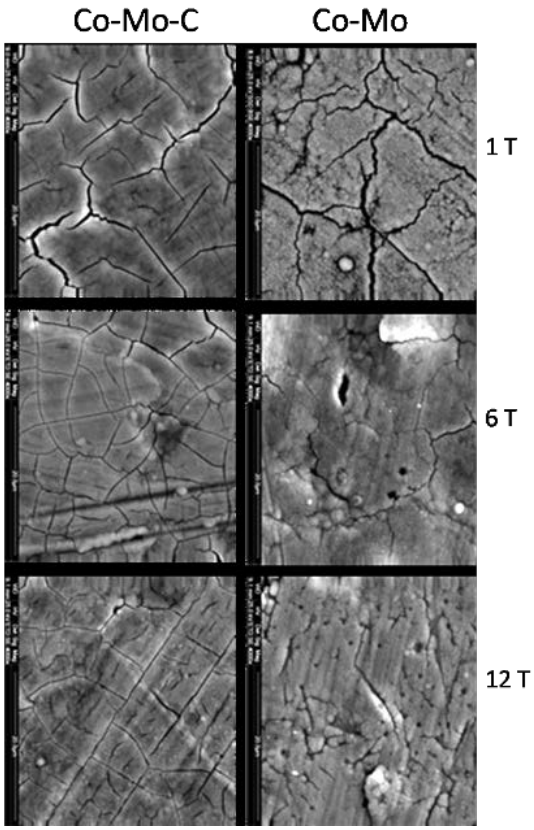


FIG. 139. *Morphology of Co-Mo alloys deposited with magnetic field parallel to the surface of electrode.*

***F. Debray***
***R. Kowalik, P. Zabinski, A. Jarek (AGH University of Science and Technology, Krakow, Poland)***

# Instrumentation

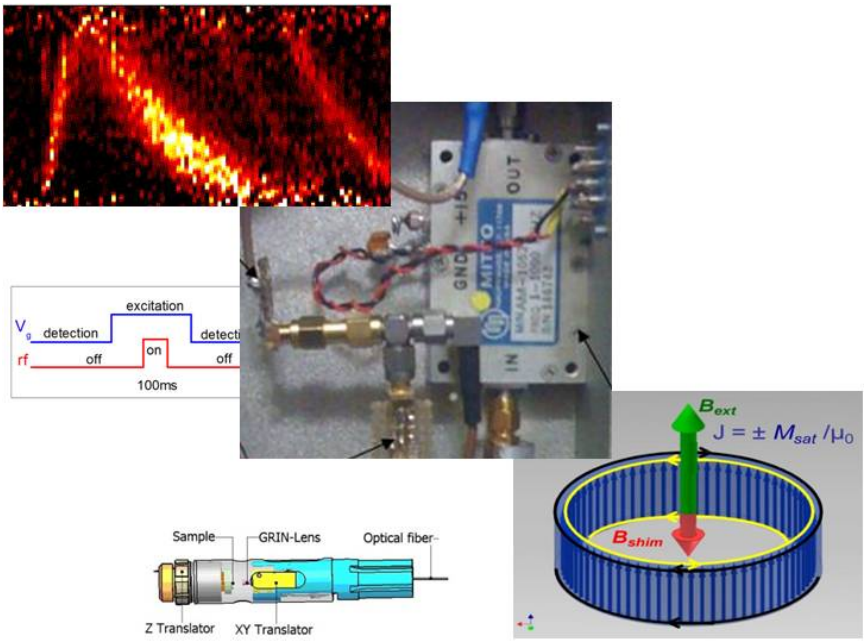

# New linear piezo motor field mapping system

The first prototype of this field mapping system has been built about 7 years ago, and is used as the standard "calibration" tool in LNCMI . This second version is currently tested. It has some improvements, compared to the first one, although its principle is the same.

## Principle

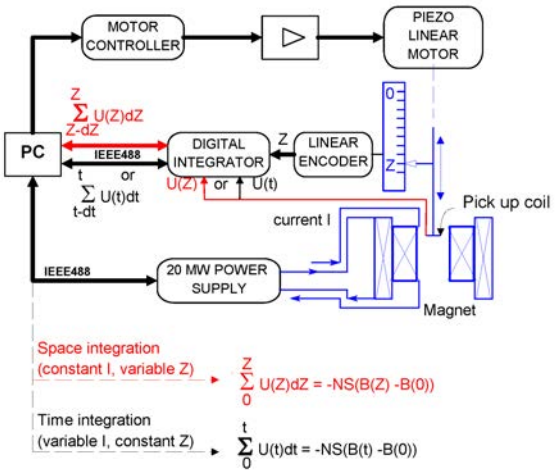


FIG. 140. *Principle of the field mapping system.*

This system uses the flux variation from a thin flat pick up coil mobile along the (vertical) axis of a magnet to calibrate (figure 140). This coil is carried by a carbon fiber tube moved by a linear piezoelectric motor. A digital integrator can receive either the signal generated by coil motion in a steady field or the signal generated by field variation in a fixed position of the coil.

## System design

This second version uses the same electronic hardware (including motor controller designed and built around a programmable digital PID microcontroller) and computer (using special control and acquisition software designed to minimize magnet current and integration drift effects) as the first one. The new mechanical part also has a new non contact incremental linear encoder and (mobile) encoder head electronic card with optical outputs. Mechanical non magnetic lightweight design uses "T" profiles assembled with high module carbon fiber parts (very low thermal expansion). The long travel stage (320 mm) is built with mobile motor and fixed driving plate. In this unusual design, static friction under motor pre-load is compensated by linear micro-rollers (with 2 mm diameter ceramic balls) and a "V" rail. Positioning precision is 5 $\mu$m, and integration can be performed under 6 mm/s speed with steps down to 10 $\mu$m. This system can be used for the vertical or horizontal measurement axis. It also uses a removable "reference" coil tube (small thin coil providing a very small field used to link mapping distances encoder zero to magnets housing top surface plane) and is well adapted to low field measurements (used to optimize laboratory magnet parts design).

FIG. 141. *Upper part of the field mapping system.*

FIG. 142. *Lower part of the field mapping system with and without the "reference" coil tube.*

***Ph. Sala, J. L. De Marinis, R. Pankow,***
***M. Deleglise, P. Hostachy, Ph. Jacquet, G. Kapoujyan (SERAS-CNRS, Grenoble)***

# Passive ferro shim: The key for homogeneous resistive high-field magnets suitable for high resolution NMR

Even though resistive high-field magnets offer the highest available fields, they are of limited use for high resolution Nuclear Magnetic Resonance (NMR) experiments. One important reason for that lies in their intrinsically lower field homogeneity as compared to superconducting magnets. Within the EuroMagNET II activity efforts are made at the LNCMI to improve the field homogeneity of resistive high-field magnets. Amongst others, this can be obtained by passive ferro shims. Compared to active shims, they offer the advantage that they reduce the center field much less (only about 0.1 T at 30 T) and that they can be more easily integrated into existing magnets.

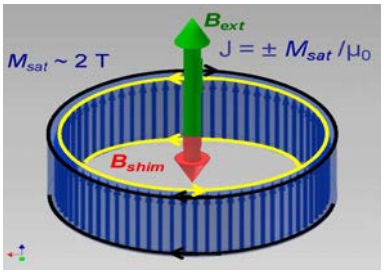


FIG. 143. *Principle of ferro shimming. The magnetic field $B_{\rm shim}$ generated by a saturated iron cylinder opposes the external field $B_{\rm ext}$.*

The principle of ferro shimming is illustrated in figure 143. Near the center of the iron cylinder with its saturated magnetization $M_{\rm sat}$ the total magnetic field $B_{\rm shim}$ generated by the iron atoms opposes the external field $B_{\rm ext}$. In a macroscopic description, the ferro shim can be modelled by two opposed current sheets with current (length) density of $J = \pm M_{sat}/\mu_0$ on the inner and outer surface of the cylinder. It can be shown analytically that a quadratic term dominates the axial field dependence near the magnet center and that this term can be compensated for a given particular value of the external field $B_{\rm ext}$ by an iron cylinder with appropriate height and wall thickness.

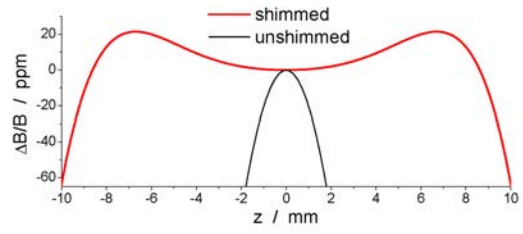


FIG. 144. *Calculated field profile along the axial direction z for the shimmed and unshimmed magnet M9. The $z^2$-term of the unshimmed magnet is $-20.2$ ppm/mm$^2$.*

In figure 144 the calculated axial field profiles for the shimmed and unshimmed magnet M9 are shown. Besides a broad homogeneous region in the center, the shimmed field profile displays two local field maxima. One of these maxima is intended to be used for a NMR spin lock, which compensates the long-term field drifts.


FIG. 145. *Realization of ferro shimming setup. The iron cylinder is mounted on a tube and can be precisely positioned in-situ by a linear and rotary stage.*

Figure 145 shows the realization of the shimming setup: the ferro shim is mounted on a non-magnetic stainless steel tube, which can be precisely positioned in-situ by a independent linear and rotary stage. The linear stage is used for precise alignment (within 0.1 mm) of the shim with respect to the magnet. In addition, the ferro shim is used to compensate "axial symmetry breaking" horizontal field gradients, mainly induced by a finite helix pitch of the inner coil. Therefore the shim is mounted in a way to be slightly off-axis in the bore of the magnet. This creates an horizontal field gradient. Using the rotary stage, the gradient by the shim can be aligned to compensate the horizontal gradient by the magnet.

The shim was validated by $^{23}$Na NMR on a saturated aqueous NaCl solution at 30 T in M9. In figure 146 a single-shot $^{23}$Na spectrum is shown that was recorded after shimming. The sample was of 4 mm diameter and of 5 mm length. The observed line width of about 10 ppm represents the total field homogeneity over this volume, which is improved by a factor of 10 in comparison to the unshimmed magnet. The shimming system was already successfully used for a first $^{25}$Mg NMR user experiment [Laurencin *et al.*, unpublished].

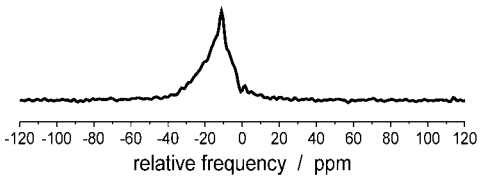


FIG. 146. *Single-shot $^{23}$Na spectrum in NaCl in saturated aqueous solution recorded at 30 T in the shimmed magnet using a sample of 4 mm diameter and 5 mm length.*

***H. Stork, S. Krämer, M. Horvatić, C. Berthier, C. Trophime, C. Mollard***

# NMR spectrometer for pulsed high magnetic fields

Today, the highest superconducting field available for commercial NMR spectrometers is 22.5 T. Although high $T_c$ superconductors hold promise to increase this value, this development is very slow and very expensive. Therefore, with 60 T pulsed magnets operating at the LNCMI Toulouse, it is a great opportunity to explore whether it is feasible to perform NMR in such high field magnets. Here a first version of a NMR spectrometer is presented.

The setup consists of three parts: the pulse generator, the "NMR box" and the signal processing.

The first part generates a RF pulse at the Larmor frequency ($F_0$) with a duration ($T_{pulse}$) which corresponds to a $\pi/2$ spin rotation. The power delivered is dimensioned as a function of the features of the resonating LC circuit and the sample's gyromagnetic ratio.

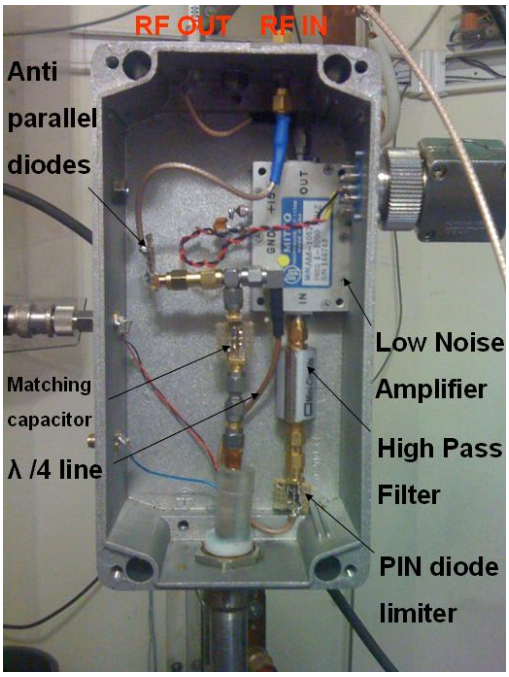


FIG. 147. *NMR setup for pulsed magnetic fields: Electronic components of the "NMR box", placed outside the pulsed magnet coil.*

The "NMR box" is used both for transmission and reception of the RF signal. An LC resonant circuit tuned to $F_0$ with high quality factor ($Q = 180$) generates the RF magnetic field and detects the free induction decay (FID) magnetization after the sample's excitation. A low noise amplifier with fast recovery time is used to detect the free induction decay correctly. A $\lambda/4$ line, a diode PIN limiter and a high-pass filter protect the low noise amplifier input during the RF pulse. The components are chosen to minimize free induction decay signal attenuation before the low noise amplifier. The signal processing unit is a down-converter of the free induction decay signal in order to analyze the signal's Fourier spectrum.
Free induction decay at 305 MHz on $^{1}$H and $^{93}$Nb respectively at 7.75 T and 30.4 T were observed. The spectrometer can be easily modified to operate at higher frequencies (up to 600 MHz) in order to work with $^{63}$Cu samples from 45 T to 60 T. The next aim is to develop this setup at very high magnetic field to explore NMR in high $T_c$ cuprates.

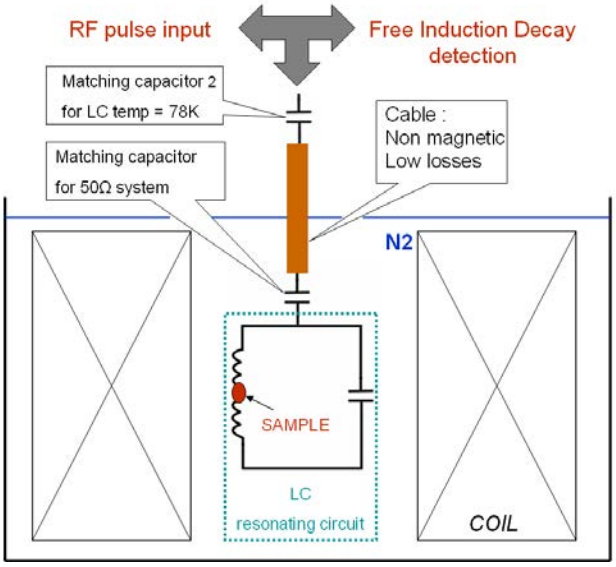


FIG. 148. *NMR setup for pulsed magnetic fields: The RF excitation coil forms part of a tuned resonant LC circuit which is placed inside the pulsed magnet coil.*

***P. Bontemps, E. Abou-Hamad, G. L. J. Rikken***

# Cryogenic developments

**Cryostat for X-ray diffraction experiments under pulsed magnetic fields:**

A top loading Helium cryostat for X-ray diffraction experiments on single crystals, under high pulsed magnetic field up to 30 T, has been developed. It is combined with a nitrogen housing dewar for the cooling of the 30 T split coil, and equipped with twelve X-ray transparent Kapton windows evenly distributed around the dewar. The Helium insert allows experiments in the temperature range between 1.4 K and 300 K. The sample holder is inserted through an air lock and is thermalised with the help of $^4$He exchange gas. The sample is located in a X-ray transparent polycarbonate capsule at the bottom of the Helium insert.

The final assembly and cryogenic performances have been first tested at the LNCMI-T, and on the beamline ID06 at the ESRF, in both "one shot" open cycle and closed cycle circulation.

FIG. 149. *(Left) Magnet and cryostat assembly on the beamline ID06 at the ESRF. (Right) Helium insert before final assembly.*

**Optical $^4$He circulation cryostat for transmission and absorption experiments under Megagauss generated high pulsed magnetic field up to** 120 **T:**

Study, assembling and test of a bottom loading, optical circulation cryostat have been performed. The principal aims of this new design are easiness, quick dismantling and possible change of the double wall vacuum insulated polycarbonate tube passing through the single turn coil which is destroyed and therefore has to be replaced after each shot. The cryostat is also equipped with two ZnSe windows at both the entrance and exit of the cryostat at room temperature and with a PVC $LH_4$-tight and easily replaceable cold window at the entrance of a thin walled polycarbonate tube delimiting the sample space. The sample is thermally linked with the liquid Helium by the 0.5 bar of $^4$He exchange gas so that the laser beam does not cross a dense liquid medium on its path between entrance and exit window ($\approx$ 650 mm long). At the exit of the circulation cryostat, a stainless steel vacuum insulated T shape part allows both evacuation of cold Helium vapors and loading of the window equipped sample holder. The vapor recovery line connection and the warm exit window are thermally disconnected from the cold vapors by a bayonet joint type connector. A base temperature of 4.5 K has been obtained at the sample place during the preliminary tests. Additional tests in real experimental context associating magnetic field pulse and laser beam are planned for the end of 2010.

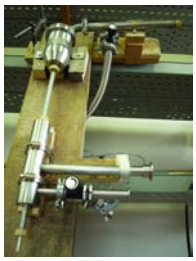

FIG. 150. *Megagauss cryostat.*

**Standard top loading double bath cryostats and experimental sites equipment:**

Two subcontractors have been chosen and trained for the assembling of standard type double bath $^4$He cryostats. These cryostats are part of the basic equipment provided in each of our ten experimental sites. They are designed for transport, magnetization and magneto-optics experiments in the temperature range from 1.5 K to 400 K under high pulsed magnetic fields up to 60 and 70 T in coils with an inner diameter bore of 13 and 27 mm, respectively. For the first time a stock of four $^4$He standard type cryostat is available in 2010 in case of cryostat damage during experiments. A rapid change of the cryostat can be performed, saving time, which is a crucial point during visitor experiments. Two supplementary standard experimental sites have been equipped with Helium recovery lines and nitrogen warmers while the Megagauss generator site has been equipped with Helium recovery line only. Final connections to the gas bag prior to compression are under way.

FIG. 151. *Standard-type double bath cryostats.*

***M. Nardone, A. Zitouni, P. Delescluse, L. Bendichou, T. Domps, S. George, F. Duc, P.Y. Solane C. Detlefs, T. Roth (ESRF, Grenoble, France)***

# Magnetization in pulsed magnetic fields

A new magnetization probe for pulsed magnetic fields has been built and tested. The probe is based on the compensated-coils technique and is made of two concentric coils, of $N_1$ and $N_2$ turns ($N_1 > N_2$), of radius $R_1$ and $R_2$ ($R_1 < R_2$), and of lengths $L_1$ and $L_2$ ($L_1 < L_2$), respectively. The two coils, which are in series and of opposite sense, permit to measure in a pulsed magnetic field an induced voltage proportional to the derivative of the magnetization $M$ (of the sample) with the time $t$. The induced voltages $U_1$ and $U_2$ on the coils 1 and 2 are given by:

$$U_1 = -\mu_0 \pi N_1 R_1^2 \cdot \frac{dH}{dt} - \frac{d\Phi_1(B_s)}{dt}, \qquad (10)$$

$$U_2 = \mu_0 \pi N_2 R_2^2 \cdot \frac{dH}{dt} + \frac{d\Phi_2(B_s)}{dt}, \qquad (11)$$

where $H$ is the pulsed magnetic field created by the magnet, $B_s$ the magnetic flux density generated by the sample, and $\Phi_i(B_s)$ the magnetic flux induced by $B_s$ through the coil $i$. A third small coil permits to adjust precisely the compensation of the coils 1 and 2 to eliminate the term related to $dH/dt$. The total induced voltage is given by:

$$U_{tot} = U_1 + U_2 = -\frac{d\Phi_1(B_s)}{dt} + \frac{d\Phi_2(B_s)}{dt}, \qquad (12)$$

and the magnetization $M$ is finally related to $U_{tot}$ by:

$$\frac{dM}{dt} = \frac{c_{cal}}{V} U_{tot}, \qquad (13)$$

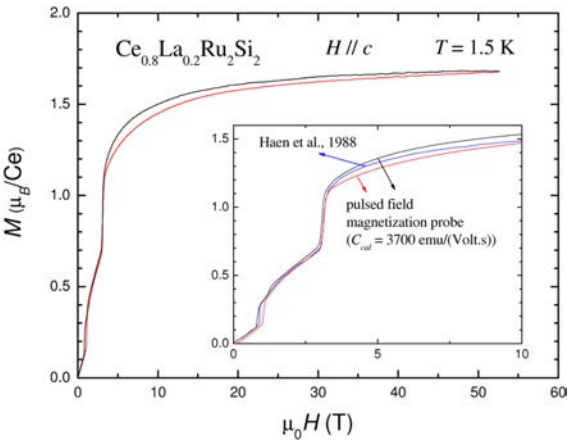


FIG. 152. *Magnetization of the heavy-fermion system $Ce_{0.8}La_{0.2}Ru_2Si_2$, for $H \parallel c$ and $T = 1.5$ K.*

where $c_{cal}$ is a calibration coefficient characteristic of the probe and $V$ the volume of the sample.

Figure 152 shows a measurement of the magnetization of a 4 mm-long sample of the heavy fermion antiferromagnet $Ce_{0.8}La_{0.2}Ru_2Si_2$ at 1.5 K and in magnetic fields $H \parallel c$ up to 53 T. Comparison with low-field magnetization data [Haen *et al.*, J. Phys. Colloques **49(C8)**, 757 (1988)] permitted to extract a calibration coefficient $c_{cal} \simeq 3700$ emu/Vs (inset figure 152). Measurements of other compounds ($Ce_{0.8}La_{0.2}Ru_2Si_2$, $CeRh_2Si_2$,...) indicated that $c_{cal}$ is smaller for smaller samples (typically, $c_{cal} \simeq 3200$ emu/Vs for 1 mm-long samples). The evolution of $c_{cal}$ as a function of the geometry of the compensated coils (figure 153) and of the size of the sample has been simulated numerically. Results of these simulations are to within 20% in good agreement with the experimental $c_{cal}$. Important efforts have also been made to improve the reproducibility of the measurements, to reduce the thermal gradients inside the cryostat, and to better estimate the sample temperature (better circulation of the gas, thermometer as close as possible to the sample etc.).

This experiment is now ready to receive visitors. New magnetization probes (with different geometries, numbers of turns, materials, etc.) will be developed to increase the signal, decrease the noise, and go to higher fields (70 – 80 T).

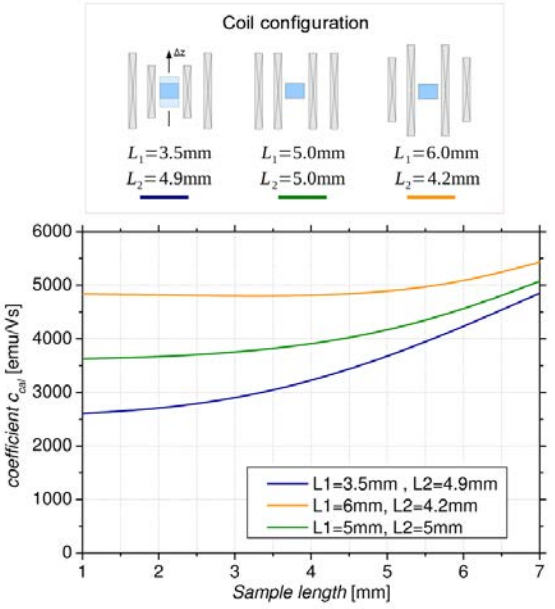


FIG. 153. *Simulated evolution of $c_{cal}$ of the magnetization probe as a function of the coil geometry and sample size.*

***G. Ballon, K. Höfner, W. Knafo***
***P. Haen, P. Lejay (Institut Néel, CNRS Grenoble), D. Aoki, J. Flouquet (SPSMS, CEA Grenoble)***

# Terahertz time-domain spectroscopy of cyclotron resonance in pulsed magnetic field

Terahertz (THz) measurements of cyclotron resonance (CR) in pulsed magnetic fields were so far mostly performed at fixed excitation frequencies. Since femtosecond-laser-pumped THz time-domain spectroscopy (TDS) systems emit and detect broadband radiation, they offer the advantage of measuring continuous spectra as has been shown at constant magnetic field. The disadvantage of these systems is the long data acquisition time required by the slow mechanical scanning of the delay stage. Here we introduce a rapid mechanical scanning, based on a rotary delay line, which enables high-speed THz TDS. We have implemented this rapid-scanning, fiber-coupled terahertz time-domain spectroscopy system that enables to perform cyclotron resonance (CR) measurements at quasi-constant magnetic field up to 40 T [Molter *et al.*, Optics Express **18**, 26163 (2010)]. We measured the CR of holes in a *p*-germanium sample and obtained in a single magnet shot 135 time-resolved cyclotron resonance spectra at a rate of 150 Hz. Figure 154 depicts the experimental set up. Broadband ultrashort THz pulses were generated and detected by using a photoconductive emitter-detector setup excited by a femtosecond fiber-laser. The emitter and the detector, based on low-temperature GaAs, were kept far enough from the magnet coil. Then, free-space propagation drives the THz signal to the sample. After reflection by a mirror on its backside, the backwards signal is separated by a beam splitter to reach the detector.

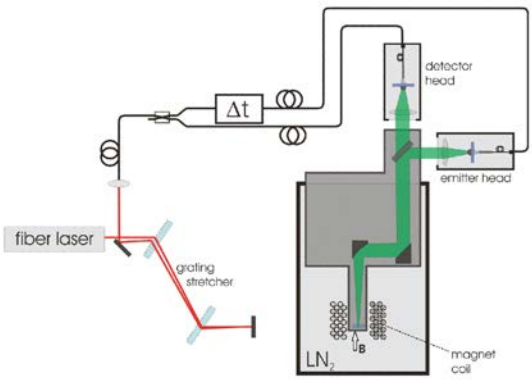


FIG. 154. *Experimental setup consisting of a commercial fiber laser, fiber coupling, and the delay line in the emitter arm. The sample is placed inside a helium cryostat inserted into the high-field magnet coil. The THz emitter and detector heads are placed outside the cryostat.*

Figure 155 shows the plot shows in the frequency domain of the THz spectra obtained by Fourier transformation of the time-domain pulses, the magnetic field versus time is displayed above. Two resonances associated to light and heavy holes CR absorption are clearly seen sweeping through the measured 0.2 – 1.2 THz spectral range. They provide the expected light and heavy holes cyclotron effective mass values of 0.04 $m_0$ and 0.3 $m_0$ respectively (figure 156). A third, weak line in-between, related to quantum effects, can be discerned.

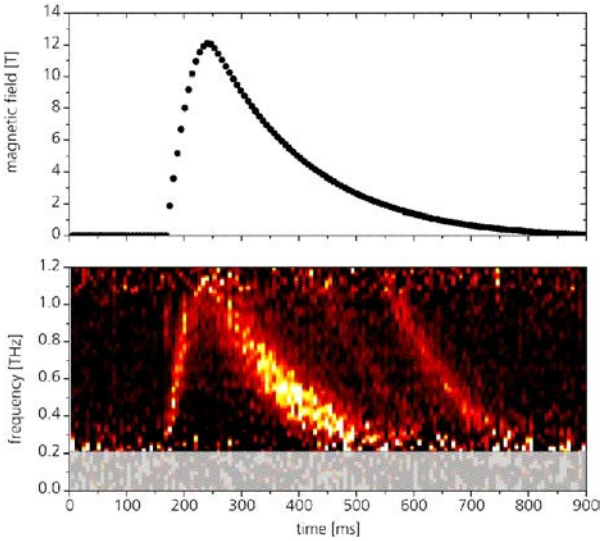


FIG. 155. *Pulsed magnet field strength (top) and evolution of THz absorbance spectra of a p-Ge crystal (bottom, color scale bar right), obtained by Fourier transform, both as a function of time. The low-frequency part below* 200 *GHz is greyed out because of a poor signal-to-noise ratio.*

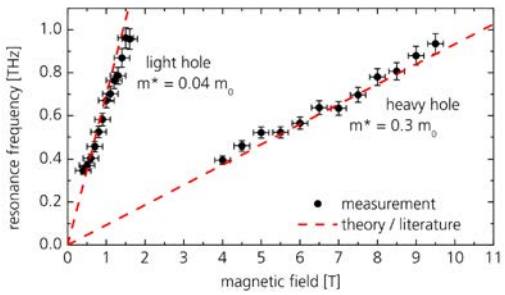


FIG. 156. *Evaluated resonance frequency of light and heavy holes vs. magnetic field, oriented along the [110] direction of the p-Ge crystal.*

Further developments now in progress are aimed at increasing the scanning speed, the intensity and the frequency range of THz pulses. This work paves the way to routine terahertz time-domain-spectroscopy at low temperatures and pulsed magnetic fields supplied by 60 T coils.

***M. Goiran, S. George, and J. Léotin,***
***D. Molter and R. Beigang (Fraunhofer Institute for Physical Measurements Techniques, Kaiserslautern, Germany) F. Keilmann (Max Plank Institute of Quantum Optics, Garching, Germany)***

# Photon correlation under high magnetic field

The photon correlation technique allows one to measure different times involved in physical processes, such as diffusion and rotational times of nano-objects. It is also a way to measure the lifetimes of excited states. We have recently implemented a photon correlation detection setup under high magnetic field. It has successfully been tested at magnetic fields up to 14 T.

Most of the optical path inside the magnet is done with the use of optical fibers in order to avoid problems due to the vibrations of the cooling system. The detection part of the setup (see Fig. 157) consists of two detectors in a Hanbury Brown and Twiss configuration [Hanbury Brown *et al.* Nature **177**, 27 (1956)]. After excitation, the luminescence of the sample is collected and separated in two paths through a beam-splitter (BS). The two beam lines are then directed to two spectrometers allowing one to either analyse the spectra by means of a CCD camera or to select a specific region of interest before detection by low background Avalanche Photodiodes (SPCM-AQR-16; Perkin-Elmer). The specificity of this technique is to allow one to correlate the arriving time of photons into one detector with respect to the other one, revealing characteristic times of the photons distribution. The use of two detectors in this configuration offers the possibility to eliminate afterpulses effects and dead-time limitations of the detectors. Additionally, one can correlate photons of different energies and polarisations. The two detectors are then connected to a time intervals analyser. One of the detection line is previously delayed in order to access to negative times.

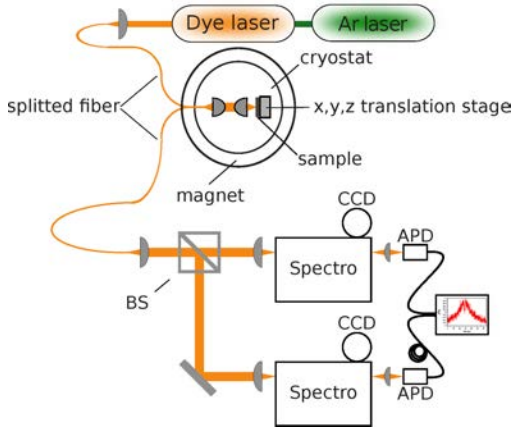


FIG. 157. *Photon correlation setup. The detection is in a Hanbury Brown and Twiss configuration. The spectral lines of interest can be selected via the spectrometers.*

In order to test our setup, we have measured the autocorrelation of the neutral exciton of a single CdTe/ZnTe quantum dot at 0 T and at 14 T. The quantum dot was excited via resonant excitation of another one in its direct surrounding. This was done by means of a CW dye laser (Rhodamine 6G). We then monitored farther in the red the luminescence of the first quantum dot. The emission line of the neutral exciton had previously been spectrally selected with the spectrometer so as to avoid the presence of any other componants at a different energy.

Fig. 158 shows the two measurements recorded at 0 T (blue curve) and at 14 T (red curve). The dip (antibunching) that can be seen around 0 delay is characteristic for sub-Poissonian statistics, when only one photon can be emitted at a time. The bunching which directly follows it at longer time scales is related to the recharging time of the quantum dot. We fitted those bunchings with a single exponential function (see the black lines on Fig. 158) and found that the recharging time of the quantum dot becomes shorter under magnetic field (21.4 ns without field, to be compared to 12.3 ns at 14 T). This effect is somehow going against intuition as one would expect the dynamics of charges to slow down when a magnetic field if applied. The understanding of this phenomenon will require further studies.

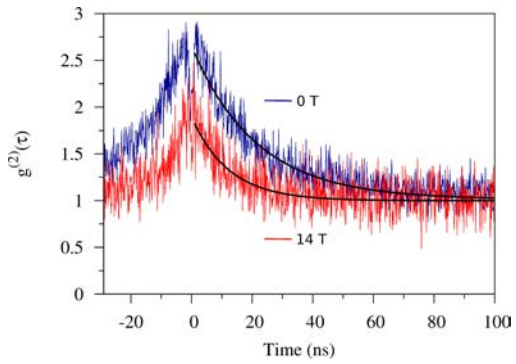


FIG. 158. *Autocorrelation measurements on a single CdTe quantum dot at 0 T (blue curve) and 14 T (red curve). Both curves were fitted (dark lines) with single exponentials, giving a decay time of 21.4 ns at 0 T and 12.3 ns at 14 T.*

Future measurements using this technique will include charge diffusion in a semiconductor and the influence of the magnetic field over those diffusion times. We would like as well to study correlation between different excitonic lines of quantum dots. Finally, this technique could be used not only to study temporal correlations, but spatial correlations as well, by detecting photons coming from two different locations on the sample.

***A. A. L. Nicolet, M. Goryca, I. Breslavetz, P. Kossacki, M. Potemski***

# Photo-current set-up to measure individual nano-objects in pulsed magnetic field

In the frame of Joint Research Activities (WP8: Nano-object measurements and local spectroscopy) of the EuroMagnet II contract, we plan to develop new measurement systems that combine optical and electrical experiments by measuring the photoconductivity of individual nano-objects in pulsed magnetic fields. The project will explore both the visible/near infrared regions of the spectrum, requiring the development of the optical fibre approach.

In figure 159, we present a schematic view of the experimental set-up that is about to be built. Laser light is coupled in a multimode optical fiber. A Graded-Index (GRIN) lens focuses the beam on the sample with a spot of about 100 $\mu$m. This optical system is fixed on an $XY$ mechanic translator who enables 1 mm displacement on each direction. The sample is glued on a ceramic and connected with gold wires on a transistor socket that can me moved on $Z$ to adjust the focal point. All this system is plugged on an insert designed for pulsed magnetic field, including a thermal sensor, a pick-up coil and five twisted pairs of wires for electrical measurements.

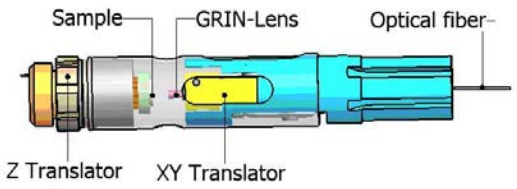


FIG. 159. *CAD design of the optical part of the sample holder.*

Such a set-up will be tested on semiconducting nanowires. In the following, we briefly describe home made silicon nanowire (Si NW) devices (see figure 160) and the first magneto-transport measurements under 60 T (figure 161). The Si NWs are single-crystal structures with diameters of several nanometers and a controllable hole and electron doping. The Si NWs were prepared by plasma-enhanced chemical vapor deposition (PECVD), using gold (Au) as a catalysis. During growth process, they can be doped by boron: $SiH_4$ + $BCl_3$. According to the concentration of $BCl_3$, the expected doping level is $n_p = 10^{19}\text{cm}^{-3}$. Nanowires were dispersed in isopropyl alcohol (IPA) from substrates by sonication and then deposited on degenerately doped Si substrate with 150 nm $SiO_2$ on the top, which was used as a gate. On the substrate there were pre-defined Au contacts made by optical-lithography. Connection to the individual Si NW was performed by electron beam lithography. The best results for electrical connection of Si NWs were obtained by Ti\Au contacts with further annealing at 300°C during 3 minutes in mixed $N_2$\$H_2$ gas.

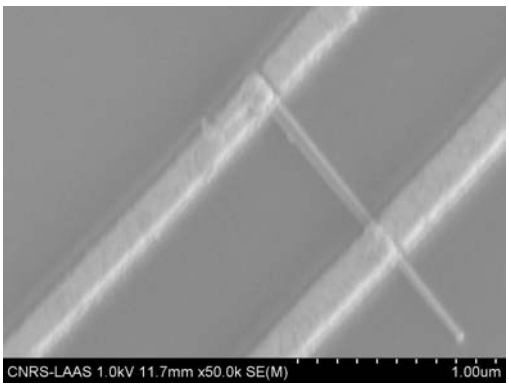


FIG. 160. *Scanning electron microscopy image of the connected Si nanowire (scale bar 1 $\mu$m).*

Measured highly $p$-doped Si WNs have no back-gate effect according to the doping level. At high magnetic field, Si NW shows a positive magnetoresistance following a square dependence. It allows us to roughly extract a carrier mobility in the range of $\mu = 30$ cm$^2$.V$^{-1}$.s$^{-1}$ and a carrier concentration $n_p = 1.1\text{x}10^{19}\text{cm}^{-3}$, in good agreement with the doping level expected from the growth process. Similar works are in progress on undoped Si NWs.

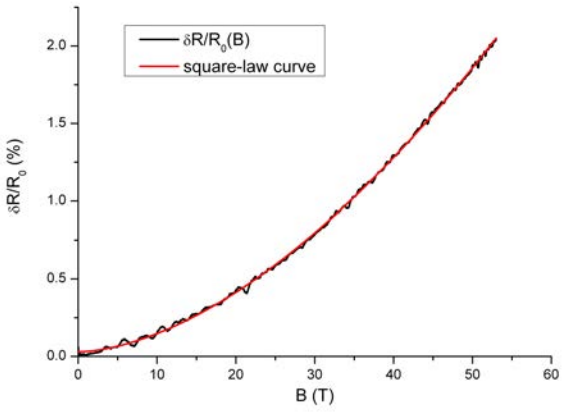


FIG. 161. *Magnetoresistance measured at 4 K on a doped Si nanowire under a perpendicular magnetic field.*

***V. Prudkovsky, S. George, W. Escoffier, J.M. Broto, M. Goiran and B. Raquet***

# Using a tunnel diode oscillator to probe quantum oscillations in pulsed magnetic fields

Radio frequency measurement technique based on tunnel diode oscillator (TDO) is very useful for the investigation of transport properties of metals for which samples have small resistance or (and) in the case where good contact-resistance are difficult to achieve.

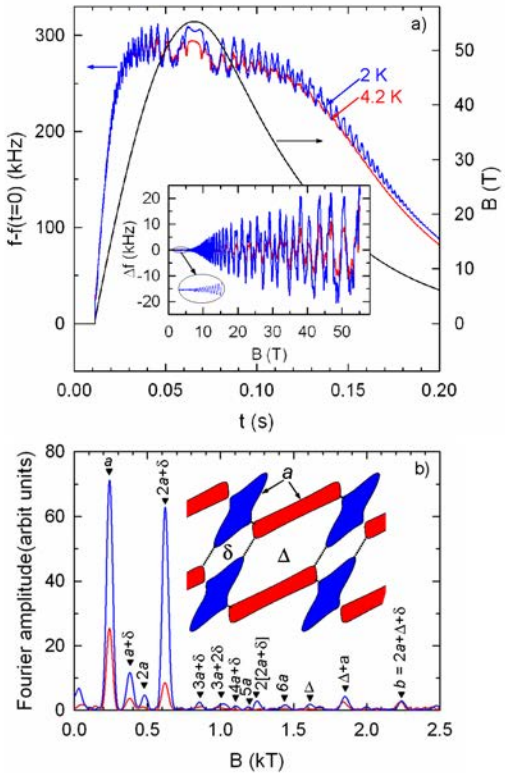


FIG. 162. *(a) Time dependence of the pulsed magnetic field and of the TDO frequency, for $B \perp$ to the conducting plane of the organic metal (BEDT-TTF)$_8$ $Hg_4Cl_{12}(C_6H_5Br)_2$. The inset displays the $B$ dependence of the background removed TDO frequency during the decreasing part of the pulse. (b) Fourier analysis of the data for $B = 15-55.3$ T. Marks are calculated with $F_\delta = 138$ T, $F_a = 240$ T and $F_\Delta = 1601$ T. The Fermi surface making explicit the labels $a$, $\delta$ and $\Delta$ is displayed in the inset. Dotted lines mark the magnetic breakdown gaps delimiting the $\delta$ and $\Delta$ pieces located in-between the compensated $a$ orbits.*

This technique has been successfully used in the past for *e.g.* detection of phase transitions and determination of Shubnikov-de Haas (SdH) oscillations spectrum in metals. However, to our knowledge, no magnetic field-dependent studies had been reported up to now even though magnetic field-dependent behaviour of SdH oscillations involves important physical parameters such as magnetic breakdown (MB) field and scattering rate. We demonstrate that these parameters can be determined from the field-dependent quantum oscillations amplitude provided oscillations are reliably detected over a large enough field range. We have considered the organic metal (BEDT-TTF)$_8$Hg$_4$Cl$_{12}$(C$_6$H$_5$Br)$_2$ with well known SdH oscillations (see [Vignolles *et al.*, Eur. Phys. J. B **66**, 489 (2008)]). The observed spectra are composed of numerous Fourier components that are linear combinations of the frequencies linked to the basic orbits labelled $a$ in figure 162 and to the $\Delta$ and $\delta$ pieces of the Fermi surface. In addition to MB orbits (such as $2a + \delta$) that are accounted for by the coupled network model and quantum interference (in particular, the $b$ oscillations), other frequency combinations due to chemical potential oscillations and (or) the formation of Landau bands (instead of discrete levels) are observed.

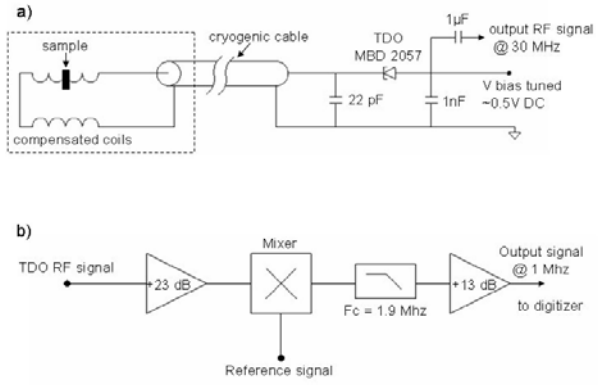


FIG. 163. *Schematic of (a) tunnel diode oscillator (TDO) circuit and (b) demodulation system. Parts inside the dotted rectangle are at $T = 4$ K.*

The device (figure 163) is an LC-tank circuit powered by a tunnel diode biased in the negative resistance region of the current-voltage characteristic, including a pair of counter-wound coils [[Drigo *et al.*, Eur. Phys. J. Appl. Phys. **52**, 10401 (2010)]]. Resistivity variations of the sample placed in one of the two coils lead, through skin depth variations, to change in the oscillator frequency. Typical data are presented in figure 162. It is shown that reliable quantitative field-dependent data can be derived provided specific data processing is conducted, in particular in the low field range. Indeed, assuming an exponential decay of the pulsed field [$B(t) = B_{max}exp(-t/t_0)$, where $t_0 = 52$ ms in the present case], the time interval ($\Delta T$) during which one quantum oscillation with frequency $F$ is covered is $\Delta T = Bt_0/F$ which goes to zero as B goes to zero, despite the exponential decay of the pulse.

***L. Drigo, F. Durantel, A. Audouard, G. Ballon***

# Pulsed resistively detected NMR

We have previously developed resistively detected nuclear magnetic resonance (RDNMR) in a GaAs/(AlGa)As 2-dimensional electron gas (2DEG) quantum Hall regime at ultra-low temperatures [Desrat *et al.* Phys. Rev. Lett. **88**, 256807 (2002)]. RDNMR is a powerful tool to probe the interaction between the electronic and nuclear spin systems. The electronic spin (**S**) and nuclear spin (**I**) couple via the hyperfine contact interaction $A\mathbf{I}.\mathbf{S}$. In an applied magnetic field ($B$), the electronic spin feels an additional effective magnetic field $B_N = A < I_z > /g\mu_B$ due to the partial polarized nuclear spins which couple to the resistance via the single particle Zeeman splitting $g\mu_B(B + B_N)$. Notably, the shift of the NMR frequency (Knight shift) gives a direct measurement of the spin polarization of the electronic system. Conventional NMR cannot generally be used in such systems because it is not sensitive enough and also requires that the substrate of the sample should be removed.

However, RDNMR has a number of limitations: It can only be used at filling factors where the sample resistance is sensitive to the Zeeman energy and the resistance of the sample is non zero. This precludes for example measuring in the close vicinity of integer filling factors where the resistance is zero or at filling factor $\nu = 5/2$ where apparently the resistance of the sample is insensitive to the single particle Zeeman energy. In addition, having a sufficiently polarized nuclear spin system requires $mK$ temperatures (due to the small nuclear spin gap) which precludes making temperature dependent measurements of, for example the electronic spin polarization.

These problems can be surmounted by implementing a gate pulsed RDNMR measurements, where the radio frequency excitation (NMR) is made at a different filling factor from the resistive detection. This technique which was developed in Japan [see *e.g.* Kumada *et al.* Phys. Rev. Lett. **99**, 076805 (2007)] has recently been implemented at LNCMI. The pulse sequence and resistive detection scheme at a fixed magnetic field are shown schematically in figure 164. Before and after the radio frequency (rf) pulse, the resistance of the sample is measured at a gate voltage $V_g$ corresponding to convenient filling factor at which we are sensitive for RDNMR. The NMR pulse is applied with a different $V_g$ corresponding to the filling factor at which we want to excite the NMR. Exciting and detecting at different times (*i.e.* different $V_g$) works because of the very slow nuclear spin relaxation time which is of the order of minutes. A typical RDNMR spectra, constructed from the measured $\Delta R$ from a large number of NMR pulses at different frequencies is shown in figure 165.

Pulsed RDNMR has a number of advantages. Absolute measurements of the Knight shift at constant magnetic field can be made using a reference measurement at a filling factor for which the system is either known to be unpolarized ($\nu = 2$) or fully polarized ($\nu = 1/3$). While the temperature bath of the dilution fridge (inset figure 165) and the nuclear spin system is almost unaffected by the rf pulse, even for the maximum power available (17 dBM). In contrast, the electronic system thermalizes rapidly during the rf pulse. The electronic temperature, estimated from the resistance of the sample during the pulse can be as high as $T \sim 1 - 2K$.

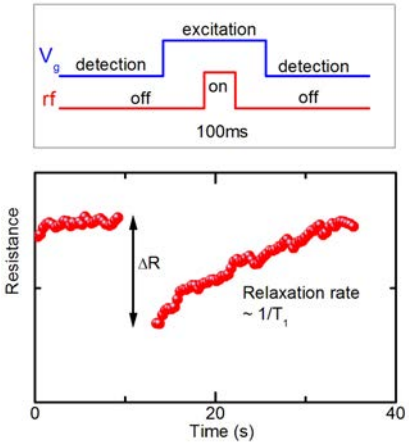


FIG. 164. *Schematic of the pulsed NMR excitation and detection protocol.*

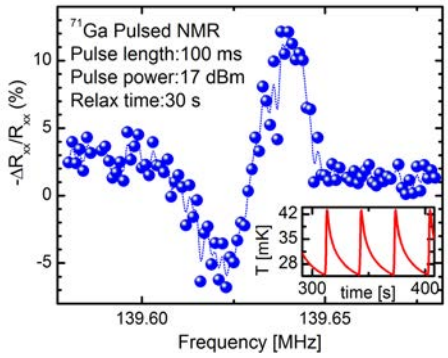


FIG. 165. *Typical pulsed resistively detected NMR spectra measured on a GaAs/(AlGa)As 2DEG in the quantum Hall regime at $T \simeq 30$ mK. Inset shows the bath temperature of the dilution fridge for a sequence of rf pulses.*

***B. A. Piot, P. Plochocka, D. K. Maude***
***M. Henini (School of Physics and Astronomy, University of Nottingham, UK), R. Airey (Department of Electrical Engineering, University of Sheffield, UK)***

# Magnet Development

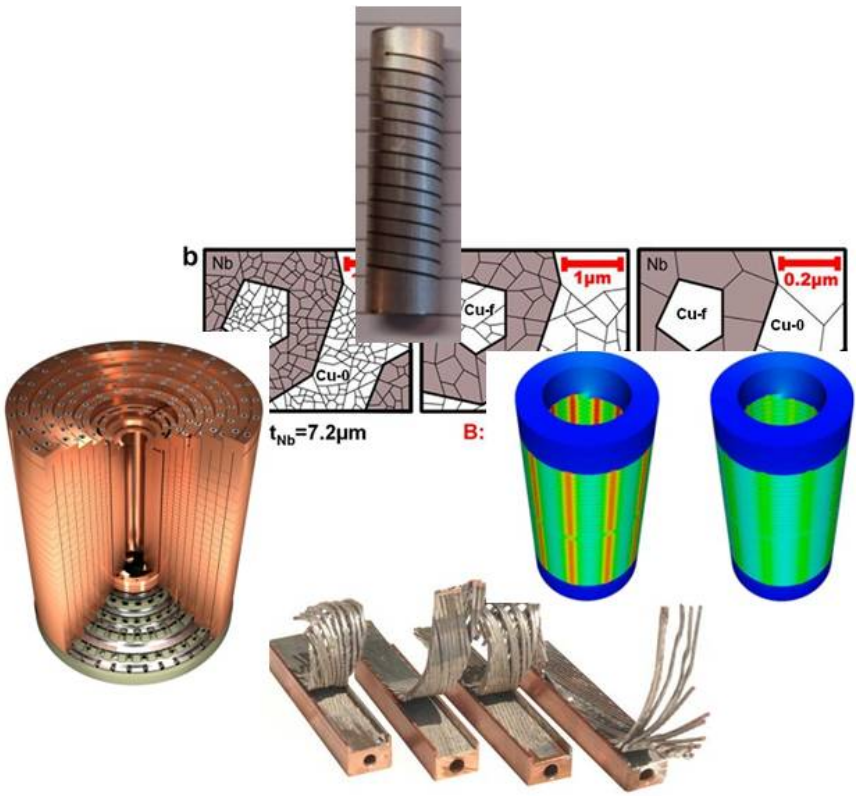

# Pulsed high magnetic field coils

**Production of user coils**

The copper-zylon coils remain the workhorse of the laboratory and their production has now become standard; parts are parameterized and can be produced in 2 weeks on the computerised milling machine, winding takes less than a week and testing a few days. Since most of the time, parts are in stock and at least 4 people have the experience to wind a coil, a standard coil can be produced in 10 days. Moreover, the policy is to have at least one standard coil in stock, in order to avoid as far as possible any delay for users after a (finally unavoidable) coil failure. Since at least one coil of each type is in stock a coil replacement after failure takes less than two days. Apart from the standard 60 T (28 mm bore) coils a few 70 T (13 mm bore) coils are now available to users.

The rapid cooling technique is generalized for all the user coils and has been improved. A prototype of a "hyper-rapid cooling" is wound and tested up to 60 T. The duty cycle is a 500 ms pulse every 30 minutes in perfect agreement with simulations.

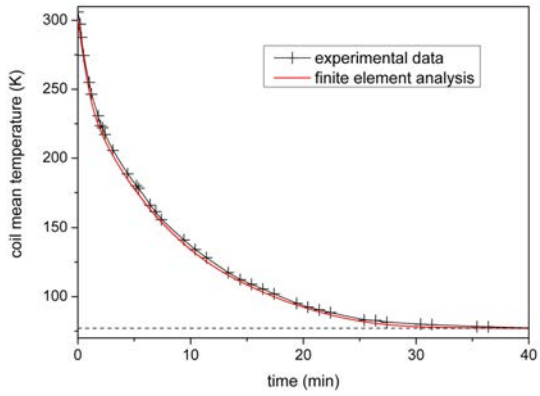


FIG. 166. *Cool-down curve for a hyper-rapid cooling 60 T long-pulse coil.*

**Special coils**

A dual-coil magnet (ARMS4) was designed for a user field of 80 T, wound and tested up to 79 T. The outer coil and the inner coil, both made with glidcop-zylon produced respectively 34 T in 170 mm and 47 T in 13 mm. The second inner coil is in progress. Its design includes developments to improve reliability. A third insert in copper/stainless steel wire zylon reinforced will be realized to increase maximum field.

Magnetic fields experiments at large user facilities (*e.g.* synchrotron and neutron beams) require a very high duty cycle. A design study of a copper stainless steel "Poly Helix" prototype is in progress in collaboration with wire-drawing workshop for the tube production and LNCMI-G for helix cutting.

A dual helix coil is under construction. It will be tested in a 20 T background field generated by a special coil based on the 5 MJ 60 T design which is under testing.

**Outlook & technical developments**

A spark-tester was installed on the winding line to control the integrity of the wire insulation during winding. Moreover, the winding machine has been modified to increase the "zylonable" diameter up to 500 mm, in order to be able to wind the 12 MJ outer coil.

Coil monitoring by comparison of pick-up coil and Rogowski probe signals permits to detect most (but not all) of the imminent coil-failures and increases the change for no loss of cryostat or sample at the end of the lifetime of a coil. This then also reduces the time to replace a defective coil.

Explo-vessels tests were continued on the high pressure rig of the Institut de Physique de Rennes. These tests will be used to determine for the first time the properties of zylon reinforcement under realistic conditions, study the influence of various impregnants and impregnation methods, and last but not least to investigate other high-strength fibres that could be used as a fall back solution in case zylon becomes no longer available.

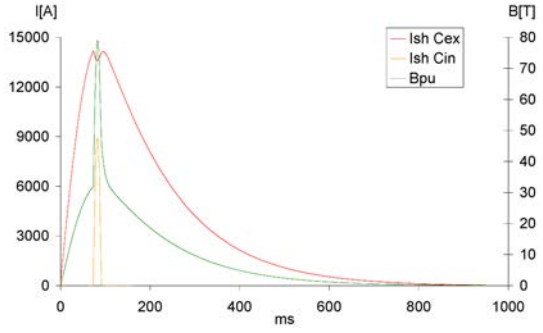


FIG. 167. *Measured field of an 80 T dual-coil system.*

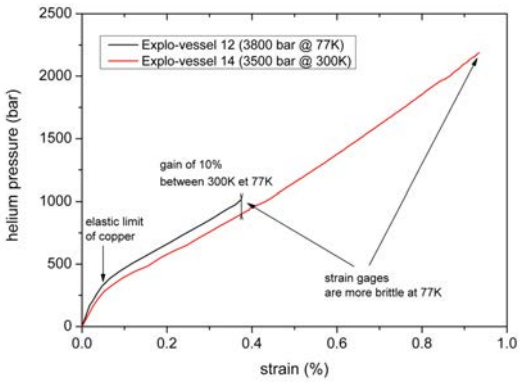


FIG. 168. *Explo-vessel results suggesting that zylon is at 77 K at least as strong as at 300 K.*

***J. Béard, J. Billette, P. Frings, F. Giquel, J.M. Lagarrigue***

# Ultra-high strength nanocomposite Cu/Nb conductors

The development of reinforced conductors, with high electrical conductivity and high strength, is essential to provide non-destructive high pulsed magnetic fields over 80 Tesla; the best compromise is obtained with copper-based continuous nanofilamentary wires (UTS = 2 GPa and $\rho = 0.6$ $\mu\Omega$.cm at 77 K). The fabrication process of these nanocomposite wires is based on severe plastic deformation (SPD) applied by accumulative drawing and bundling (ADB), leading to a multi-scale copper matrix containing up to $N = 85^4$ ($52.2\times10^6$) continuous and parallel niobium nanotubes [Vidal *et al.*, Scripta Mater. **60**, 171 (2009)].

The thermal stability of nanocomposite conductors previously described has been investigated via time-resolved in situ annealing under synchrotron high-energy X-rays at the ESRF [Dubois *et al.*, Acta Mater. **58**, 6504 (2010)]. The diffraction peak profile analysis demonstrates that internal-stress relaxation begins in the Nb nanotubes at a temperature far below the bulk recrystallization temperature and follows size specific regimes originating from a proximity effect with the nanostructured Cu matrix: the increased Cu-Nb interface surface disrupts internal-stress relaxation processes, confirming the larger thermal resistance of nanostructured materials.

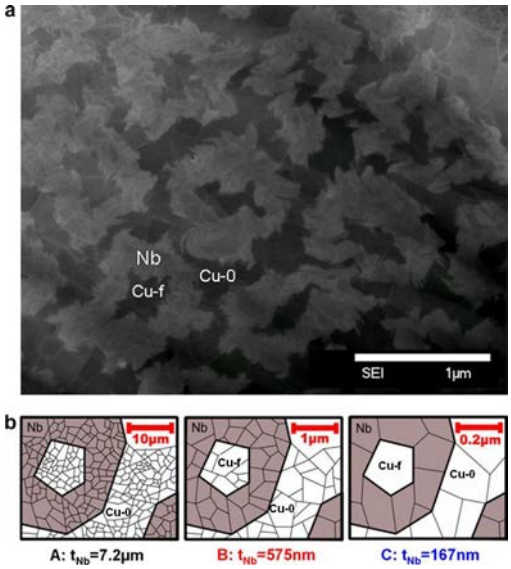


FIG. 169. *(a) TEM micrograph of a Cu/Nb where Nb nanotubes contain Cu fibres (Cu-f) and are separated by Cu channels (Cu-0). (b) Schematic of the elementary microstructure of the tested samples (A-C) with different size ($t_{Nb}$ is the Nb tube thickness).*

The first result is the unambiguous observation of the size-dependence of the onset of relaxation temperature $T^*$, observed to be strongly reduced when the microstructure size is in the nanometer range. Second, in the case of a Cu/Nb nanocomposite, three regimes are observed in the course of internal-stress relaxation:

(1) At moderate temperatures, regime 1 is observed independently of the microstructure size and is associated with a strong texture change in the Cu matrix correlated with elastic relaxation of Nb internal stresses; this interaction between the two phases is mediated by the presence of Cu-Nb interfaces, resulting in a proximity effect which favours relaxation of macrostresses.

(2) At intermediate temperatures, regime 2 is specific to nanocomposite metals and corresponds to a frustration of the normal recovery and recrystallization processes, impeded by the increased thermal resistance of Cu nano-channels; the thermal span of this regime increases with microstructure refinement.

(3) At high temperatures, regime 3 is observed independently of the microstructure size and corresponds to inter-granular events in individual phases with no further interactions.

These observations suggest that nanocomposites not only exhibit physical properties that are internal length scale dependent, but also their thermal stability is strongly affected by the microstructure size.

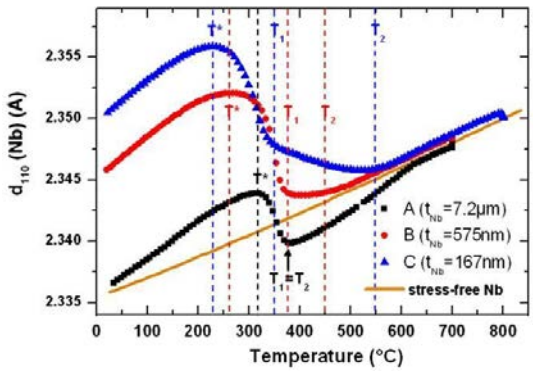


FIG. 170. *Evolution with temperature of the characteristics of the (110)Nb axial reflection for samples A-C: lattice spacing $d_{110}$(Nb) compared with expected evolution due to thermal expansion of the inter-reticular distance of {110} planes in a stress-free Nb lattice (orange line).*

***F. Lecouturier, J.B. Dubois, N. Ferreira, L. Bendichou, Ph. Delescluse***
***L. Thilly, P.O Renault (PHYMAT, Poitiers), H. van Swygenhoven, S. van Petegem (Paul Scherrer Institute, Switzerland), P. Olier (CEA-DEN-LTMEX, Saclay, France), M. Di Michiel (ESRF, Grenoble)***

# Research and development of copper stainless steel systems for conventional and poly-helix magnets

The LNCMI-Toulouse is involved since several years in the research and development of copper/stainless steel (Cu/SS) macrocomposite conductors for pulsed field magnets generating magnetic fields over 60 T. Different wires can be processed with section between 1 and 50 mm$^2$. The mechanical and electrical properties are adjusted to the magnet requirements by selecting the volume fraction of the stainless reinforcement and the work-hardening state at the end of the drawing procedure.

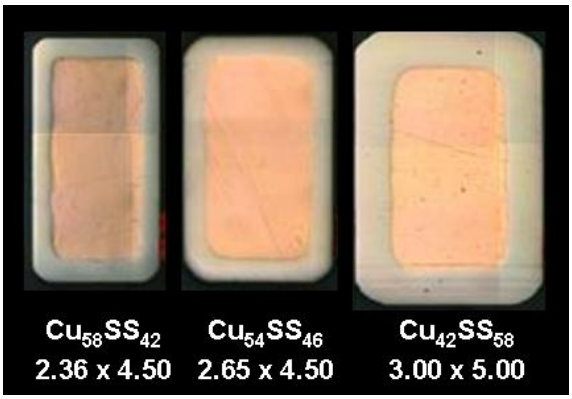


FIG. 171. *Cross section of copper/stainless steel macrocomposite conductors for pulsed magnets.*

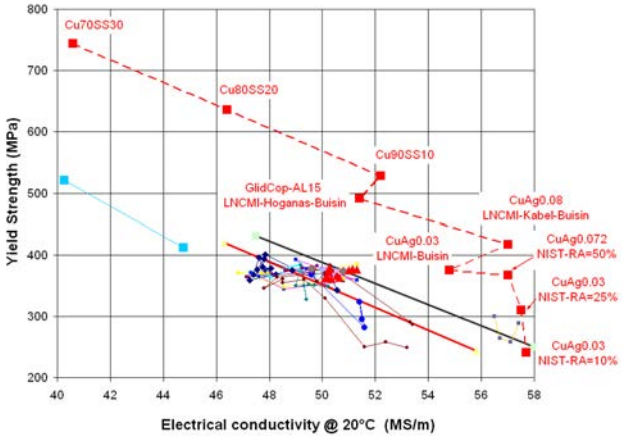


FIG. 172. *Yield strength versus conductivity for materials used in dc (solid lines) and pulsed magnets (red squares).*

Such high strength materials allow to obtain:

- 82 T in the coilin/coilex system: the development of Cu/SS wires, for the coilin, with 60% of stainless steel (UTS(77K) > 1550 MPa) and a cross section of $2.00 \times 1.25$ mm$^2$ allows to reach 82 Tesla (the LNCMI record) several months ago.

- 78 T in magnet with optimized reinforcement distribution. A few years ago, the development and production of 450 meters of Cu/SS macrocomposite conductors with 40% of stainless steel and a cross section of $2.36 \times 4.00$ mm$^2$ has been dedicated to the construction of a new type of magnet combining high strength conductors and Zylon fibers, powered by the capacitor bank of NHMFL (Los-Alamos-USA).

A new batch of Cu/SS is under development for the new coilin/coilex system which will be built at LNCMI-Toulouse.

The good compromise obtained between mechanical strength and electrical conductivity (figure 172) suggests that these composite structures can improve the performances of the poly-helix magnets, designed in LNCMI-Grenoble. Nevertheless, these composite structures have to be adapted to the geometry of poly-helix coils. A small prototype has been developed for testing the feasibility of electro-erosion cutting (figure 173). Subsequently, we have designed and produced a new real prototype, combining two poly-helix with larger dimensions which will be tested next year in pulsed environment.

FIG. 173. *Copper/stainless steel poly-helix prototype for electro-erosion cutting test.*

***F. Lecouturier, N. Ferreira, L. Bendichou, J. Billette, F. Debray***

# Pulsed energy supplies

**The 14 MJ capacitor bank**

The 14 MJ capacitor bank continues to function without any major problems. The only concern is the rather ancient (nearly 20 year old) high-voltage chargers. These chargers, over 20 of them, were produced by a company that no longer exists and some electronic replacement parts no longer exist. Several efforts to have a chargers repaired by an independent company turned out to be unsuccessful and also too expensive. We were therefore forced to conclude that the chargers have reached the end of their financially viable lifetime. We decided to replace the existing 20 chargers, two for every module, by six high-power chargers (Technix company) identical to the chargers already used on the mobile generators. The chargers will be controlled independently but are electrically in parallel. In this way the charging speed when, for instance, using only 50% of the modules, will be increased by a factor of two. When an old charger failed and no spares were left we decided to install a spare Technix charger to energize two modules; this worked very well and also resulted in much more floor space. The installation of all the new chargers will make the installation more reliable, easier to maintain and for most of the experiments result in a significant shorter charging time.

FIG. 174. *A view of the 14 MJ, 24 kV, 65 kA generator in the basement after replacing four old chargers by one Technix charger. Only one bay will be left after replacement of all the chargers.*

The summer shutdown was used to perform some major maintenance on the control system. Since most of the modifications in the last five years had to be implemented with only a few days of shut-down a lot of superfluous cables could be identified and removed. This greatly simplified the documentation and the maintenance. At the same time the software of the process-controller was streamlined and improvements of the user interface, such as dummy "test-pulse" (to test the triggering), forecast of the coil-temperature, control of safe limits for every coil, will be implemented soon or as required.

**The construction of a 1 MJ transportable capacitor bank**

The transportable generators are now in full operation. Their use and installation has become more and more user-friendly, rapid and reliable. This improvement consisted of improving hardware (IR-temperature control of the dump resistors, Wifi access, uninterruptible power supply, etc.) and improved software written by our computer engineer (Jean-Pierre Nicolin). During the intensive use and partly due to the rather harsh transport conditions we discovered two problems. Firstly the industrial-PC and the connected data-acquisition equipment did not tolerate well the repeated transport. The PC developed several problems and the SCCI type of cable for the data-acquisition became defective. During use it also became evident that the protection of an Ω-meter by a "safety-loop" was sufficient in static cases, but there was a small chance of problems during transient states that might arrive when the Windows program that served as user-interface becomes unstable. Both problems were easily solved by buying new equipment with USB connections and by transferring more of the control tasks to the process-controller, respectively. Finally we received the optical thyristors to be used in the 1 MJ generator that was temporarily running with the thyristors cannibalised from the 150 kJ generator. These thyristors were bought as parts and a new, more compact stack, was developed in-house. This stack is now ready and awaiting installation.

FIG. 175. *The, in-house developed, rapid commutation switch, for changing automatically the polarity of the field.*

**Outlook**

The most important and urgent investment is still a moderately sized (∼6 MJ) capacitor bank with a short pulse. The budget for this investment should be available before the end of 2010 and this equipment will permit us to energize coils in the 80 T range without making compromises in the design. It is foreseen that the installation will be built as two completely independent 3 MJ units. Each unit will consist of a medium size container. The use of containers has two advantages: if required one can use more than 1 MJ at remote sites (ILL, ESRF, etc.) and secondly the delivery and testing of the 6 MJ generator can start before the extension of the building has been finalized.

***P. Frings, B. Griffe, J.P. Nicolin, T. Schiavo***

# Magnet control and monitoring system

The magnet control and monitoring system is one of the crucial parts for reliable and safe operation of the LNCMI high field resistive magnets, the 24 MW power supply and the cooling system. The actual control system was installed in 1990 and it is partially based on obsolete components for which spare parts are no longer available. In order to ensure future operation and to take advantage of the latest technical evolutions, we decided to upgrade the magnet control and monitoring system. The purpose of this unit is threefold; (i) to check the integrity of the magnet using real time computation, (ii) to offer the possibility for the user to remotely start, stop and control the power supplies and (iii) to remotely control the programmable logic controller (PLC) driving the magnet cooling. The upgrade requires the replacement of the entire system; network, converter, and user control together with the development of a complete new software package. In this report we give a brief overview of the key constituents and the operating principle of the new architecture.

### Real-time operation

The most crucial issue of the magnet control and monitoring system is the timing within a complex and distributed infrastructure. Safe operation requires that the entire system has to be controlled and monitored in real time and with a time interval of 10 ms. It is important to note that *only* the surveillance avoids damaging the power supplies and magnets in case of short circuit. In this case the power supply has to be switched off as soon as possible. The crucial element of real time control is the choice of an appropriate operating System (OS). A real-time and determinist OS with low jitter and latency is required. The period of the computation realized to check a magnet is 10 ms. In view of these constraints we have chosen to work with a package called RTAI, which stands for Real Time Application Interface. This open-source project has been developed by the Dipartimento di Ingegneria Aerospaziale - Politecnico di Milano (DIAPM) [Dozio *et al.*, $6^{th}$ IEEE International Symposium on Object-Oriented Real-Time Distributed Computing, p.11 (2003)]. It is a real-time extension for a Linux kernel enabling applications with strict timing constraints. RTAI provides a deterministic response to interrupts, POSIX compliant and native RTAI real-time tasks. It consists essentially of two parts: A patch to the Linux kernel based on ADEOS (Adaptive Domain Environment for Operating Systems), which introduces a hardware abstraction layer, and a broad variety of services that can be used for real-time programming without major efforts.

### Communication

In figure 176 the operation principle of the magnet control and monitoring system is shown. It can be seen that, in addition to real time computation, exchange of remote information located in the power supplies is required, which implies also real-time communication within 10 ms. For this task we developed an in-house protocol, based on RS485 communication. For enhancing this fieldbus, we have used an optical fiber ring to share data over the whole system. Communication with cooling system is easier, because needs real-time only on a timescale of about 1 s. For this part we use an industrial network *MODBUS TCP*.

### Graphical user interface

To implement a user-friendly interface for the user control of the magnet, a framework offering a large choice of graphical component is required. We decided to use Qt, a cross platform graphical widget toolkit for the development of GUI computer programs. Our choice was based on the following reasoning: (i) its portability - it works on Windows, Linux and Mac OS -, (ii) its perpetuity - it has been used since the middle of the 90's, and (iii) the quality of the graphical components. It should be noted that Qt is extensively used in aerospace, defense, home media, IP communication, medical applications, as well as oil and gas industry.

### Perspectives

So far it has taken us three years to develop, implement and validate the different hard and software components. The new system is scheduled to be operational by February 2011. In future, a technical follow-up will be necessary to maintain it up to date and integrate the latest technical evolutions. Since the philosophy of this new system is based on a modular concept further options can be added without major efforts.

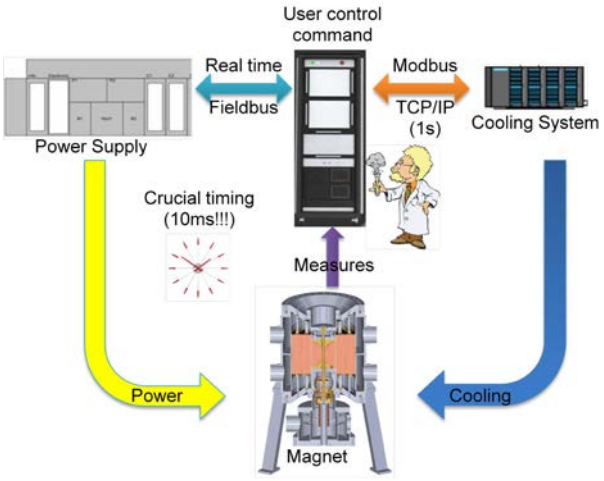


FIG. 176. *Operation principle of the* dc *magnet control and monitoring system. The user control command controls and monitors the status of magnet and power supply in real time and on a short time scale (10 ms) using a real time fieldbus (left and bottom part). Control and monitoring of cooling system is ensured on timescales of* 1 *s (right part).*

***R. Barbier, C. Grandclement, P.Petmezakis, E. Yildiz***

# The thermohydraulic loop for magnet studies

Heat transfer, together with materials, are the key issues for magnet optimization. The investigation presented here will allow to control the thermohydraulic behavior of the magnet under high field conditions.

FIG. 177. *View of the operational 40 bar hydraulic loop. Power available on this loop is 80 kW.*

Since 2009, LNCMI, with the Laboratoire des Ecoulements Géophysiques et Industriels (LEGI, CNRS INPG/UJF), have upgraded an existing hydraulic loop (Fig.177) to investigate the thermohydraulics encountered in high field magnets.

This year, hydraulic measurements have been performed on one radially cooled helix (Fig.178). The objective was to obtain the relevant hydraulic parameters in order to optimize the magnet design.

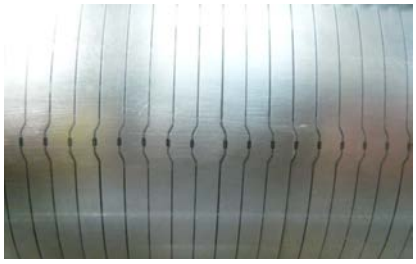

FIG. 178. *Detailed view of the coil geometry of the aluminum helix mounted on the hydraulic loop. We can see in detail the thin pitch cut, the bumps in the cut with micro-channels and the bounded insulating pieces.*

With a flow rate of 20 l/s, cavitation was not observed and the mean velocity, in the channel, is estimated to be 15 m/s with the hypothesis of a uniform distribution of the flow along the magnetic axis. Heat transfer coefficient was determined from the channel geometry and the hydraulic measurement using standard correlation. The heat transfer coefficient obtained, for the radial flow, is about 74000 $W/m^2/°C$, these values has been included in our 3D numerical model.

To refine the model, we now want to measure the departure from the equal velocity model by equipping the helix by a Doppler velocity sensor to obtain local and instantaneous velocity measurements. This type of measurement is non-intrusive and well adapted for complex hydrodynamic flow. A test section (Fig.179) under construction, will permit us to validate the velocity measurement method. After validation one sensor will be installed, at each end of the helix to estimate the gradient of velocity.

The main objective is to establish a sensitivity analysis of the water collector geometry in order to optimize the flow distribution in a radially cooled helix.

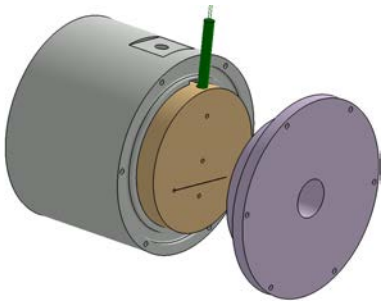

FIG. 179. *Exploded view of the test section under investigation. On the top, the small cylinder is the Doppler velocity sensor. This sensor will be positioned just above the micro-channels.*

Finally, the hydraulic loop allows to model the heat transfer mechanism in one flat thin channel using channel simulators (Fig.180).

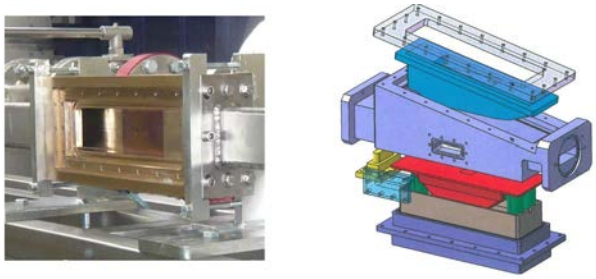

FIG. 180. *View of the existing channel simulator (left). Exploded view of the new channel simulator (right).*

***C. Auternaud, F. Debray, T. Disparti, J. Dumas, M. Kamke, J. Matera, B. Pardo, R. Pfister, C. Trophime, J. M. Tudela, E. Verney, S. Veys, N. Vidal***
***J. P. Franc, M. Riondet (LEGI, CNRS INPG/UJF, Grenoble)***

# Numerical investigations for radially cooled helices

We have performed numerical studies of radially cooled helices to improve their design. In addition to the "standard" radially cooled helix design we have also considered an "enhanced" design with additional cooling channels (micro channels) on both sides of the insulator. This second configuration is introduced to improve the cooling of the helices. Numerical modeling is based on a finite element model of the non linear electro-thermal problem which defines the temperature field and the current density distribution in the helices. The heat transfer coefficient in the cooling channels were determined during tests conducted on a hydraulic loop. Adding extra cooling channels in the design clearly reduces the maximum temperature field in the vicinity of the insulator as shown in figure 181.

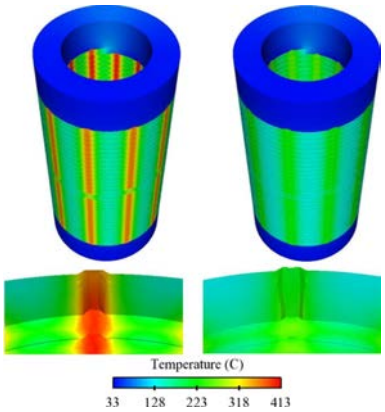


FIG. 181. *Temperature in the helix without micro-channels (left) and with micro-channels (right).*

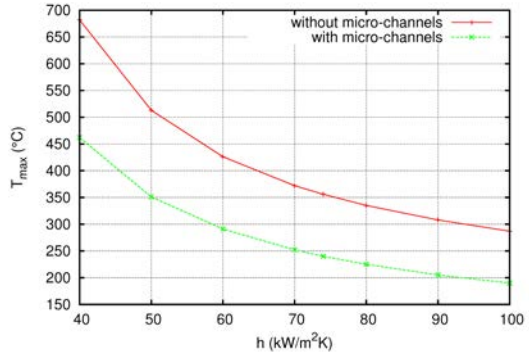


FIG. 182. *Maximum temperature vs h.*

The observed gain is about 30% compared to the "standard" configuration without micro-channels. A detailed analysis has been carried out to investigate the influence of heat transfer coefficient $h$ (figure 182). The micro-channel configuration always exhibits a lower maximum temperature.

Next we perform a sensitivity analysis to optimize the number of insulators and their shape (figure 183). The maximum angle of the insulator affects the maximum values of temperature, especially for helix without additional cooling channels. Controlling this angle is a

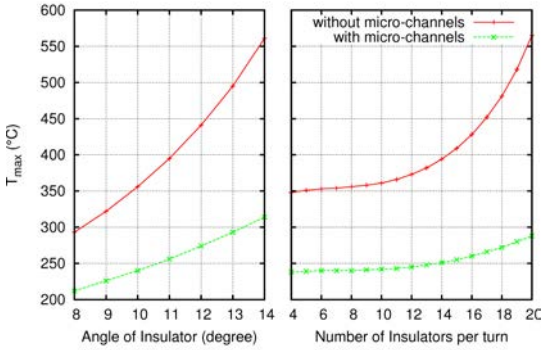


FIG. 183. *Maximum temperature vs the angular shape of the insulator (left) and versus the number of insulators (right).*

key point in magnet geometry optimization. As the cooling surface is inversely proportional to the number of insulators per turn, the maximum temperature increase with this number. This phenomenon is less pronounced for micro-channels' configuration. As a consequence we should keep this number as low as possible. To define an optimum number of insulator we have to consider a structural analysis of the helix as insulators have also a mechanical functions (they prevent a short-circuit between two consecutive turns of the helix).

In the structural analysis the magnetic and thermal loads arising from the simulations presented are applied. In the helix, stress (figure 184) remains below the elastic limit with concentration on the insulator edges.

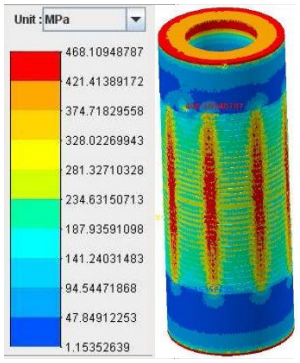


FIG. 184. *Stress distribution (MPa) in the helix without micro-channels at 34 T. Red zone corresponds to 468 MPa.*

***F. Debray, J. Dumas, B. Pardo, C. Trophime, S. Veys, N. Vidal***
***J. Giraud (LPSC, CNRS, Grenoble)***

# High field magnet development

In November 2010, LNCMI has achieved the standardization of its three 20 MW magnet sites. After the installation of a new inner housing on the oldest 20 MW site of the LNCMI (in operation since 1998) and the successful test of the new 12 helix 50 mm insert, the three version of high field helix inserts can be mounted indifferently on each of the three 20 MW sites.

FIG. 185. *Helices for the 36 T upgrade of the 35 T insert. The helix maximal temperature has been increased by 10°C in the optimization process to accept higher current densities. Current density gradient along the z-axis is increased while keeping the total power constant.*

This will help the "optimization" of the user's planning especially as the M8 site will have to be stopped in the coming years for integration of the superconducting outsert in the frame of the hybrid project. Performances of the three inserts on site M9 or M10 (outer diameter of the Bitter 1 meter) are now : 35 T in 34 mm, 29 T in 50 mm and 20 T in 160 mm. One tesla less on the M8 future hybrid site (outer diameter of the Bitter 800 mm). Tests are planned at higher field for the 50 mm version before the end of 2010. These tests have been postponed due to a default on one "river" pump of our facility that has forced us to run with limited power during November 2010 to respect the ecological limitations imposed on the temperature of the water rejected in the Isère river.

For the 34 mm version, 4 new inner helices are ready for the existing 35 T insert in order to upgrade it to 36 T (figure 185). The 35 T insert has proved is reliability with continuous operations without default since September 2009. At the end of November 2010 : 1300 hours magnet time, mean power of 8 MW for a total energy of 10 GWh. To our knowledge it is a world record as far as reliability is concerned.

In order to further increase the field to 37 T, we have developed a new insert (figure 186) in which the inner three longitudinally cooled helices will be replaced by one thick radially cooled helix. To develop this insert we have tested the efficiency of micro-channels formed directly during the cutting by electro-erosion of the helix. This helix is now under test on a 12 MW site. If successful, it will be first implemented in a 50 mm version to reach 33 T during 2011 and then on a 34 mm version to give 37 T in 2012.

FIG. 186. *A view of the future 37 T insert. A central radial helix replaces three longitudinally cooled helices. Test of this insert is foreseen end 2011.*

***C. Auternaud, F. Debray, J. Dumas, T. Disparti, M. Kamke, J. Matera, C. Mollard, R. Pfister, J.M. Tudela, D. Ponton, J. Spitznagel, C. Trophime, E. Verney, N. Vidal***

# Toward robust and reliable numerical modeling of the radially cooled helices

The temperature field distribution in the radially cooled helices has been identified as a key point of their design. Indeed the presence of insulators between turns induces hot spots in the helix. The high temperature may cause the degradation of the insulators which in turn may damage the helix. To prevent this it is essential to predict accurately the temperature field within the helix.

The temperature field $T$ in the helix is obtained by solving a non-linear electrical-thermal model. A finite element method is used to solve this problem. To obtain an accurate approximation of $T$ we have to be able to control the calculation error. It is now common practice to obtain information on the actual error present in the numerical solutions by using *a posteriori* error estimations. Basically these techniques involve post-processing numerical solutions to obtain an approximation of the error in appropriate norms. Moreover, it may be shown that some estimators bound the actual error. These estimators may also be used to drive mesh adaptation to reduce and control numerical error.

During this year we have tried to apply this approach on our electro-thermal problem. The goal is to build a more robust and reliable model for the calculation of $T$. In a first step we have reviewed and implemented some well known errors estimators :

- Error estimator based on residuals : This estimator allows us to access the error distribution on the mesh. However it does not give a good estimation of the real error;
- Hierarchical estimators : these estimators use a solution either on a finer mesh or with higher order elements to compute the error. They may give a better estimation but they are not well suited for driving mesh adaptation. A compromise should be made between the estimation of "true" error and the usability for mesh adaptation;
- Dual weighted residual (DWR) estimators : they provide a good estimate of the error and are easily used for mesh adaptation. However they require to solve a dual problem which make complex their implementation.

The implementation were based on free C++ finite element libraries (DEAL.II and FEEL++). Validations and tests have been carried out in 2D for the case of longitudinally cooled helix, as analytical expressions for the electrical potential and temperature fields may be explicated in the linear case. Our review has shown that dual weighted residuals error estimators are most suited to our purpose of accurately controlling the error even if they are more complex and more demanding on resources. They may be readily used to drive mesh adaptation.

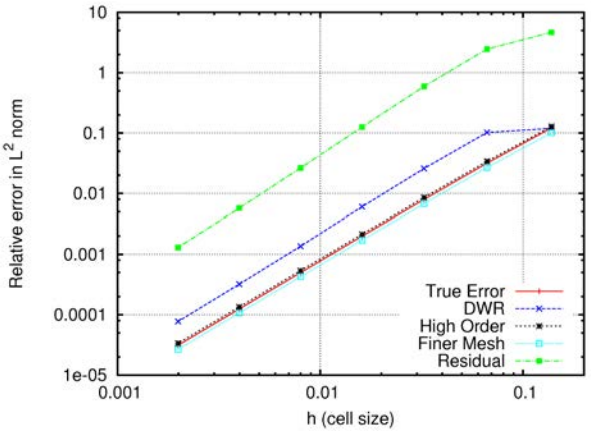


FIG. 187. *Comparison of a posteriori error estimators for $T$ in a section of a longitudinally cooled helix.*

In a second step we have developed a mesh adaption procedure. As an example we consider a section of a turn of a radially cooled helix centered on an insulator. We use the Kelly estimator to drive the mesh adaptation. With this estimator we can approximate the error on $\nabla T$. This allow us to localize zones of high gradients (see Fig. 188).

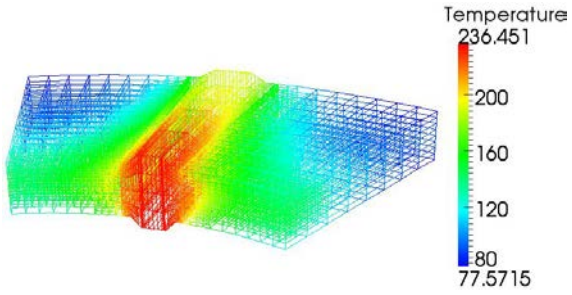


FIG. 188. *Adapted mesh for $T$ in a turn of a radially cooled helix at $I = 31$ kA.*

***B.Pardo, C.Trophime, S. Veys***
***C. Prud'homme (LJK, UJF, Grenoble),***

# Characterization of the sixty gigahertz electron cyclotron resonance ion source using megawatt magnets - SEISM prototype

LPSC Grenoble has built a 60 GHz Electron Cyclotron Resonance (ECR) ion source prototype, called SEISM. The magnetic structure design benefited from LNCMI research on split magnets, based on a radially cooled polyhelix. A dedicated test bench, appropriate electrical and water cooling environments were installed to study the validity of the mechanics, the thermal behaviour and magnetic field characteristics obtained at various current intensities (see figure 189).

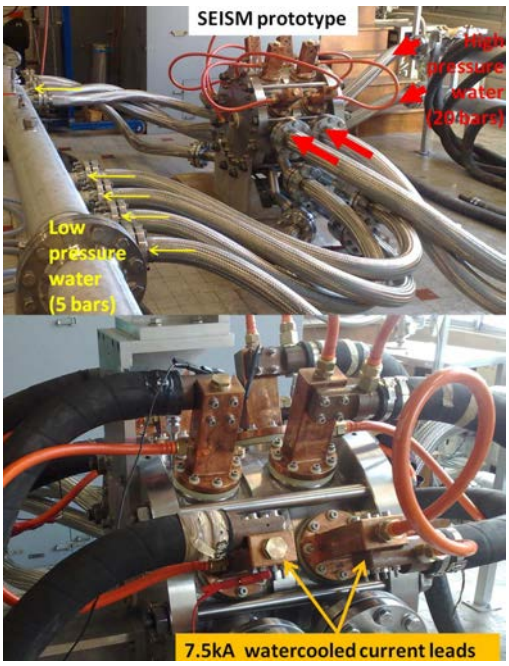


FIG. 189. *Dedicated SEISM test bench for the magnetic field measurement at half-intensity. (Top) Hydraulic circuit is parallel to M5 existing circuit. (Bottom) electrical cables are connected in series with M5 magnet.*

Hydraulic tests revealed cavitation issues when applying 7 kA on the helices, with the water speed up to 14 m/s in the radial helices slit. In order to decrease the water flow through SEISM without modifying the cooling of the M5 magnet running in parallel, stainless steel porous discs held between flanges (without soldering) were installed on the water outlets of both tanks. The water flow through the prototype was reduced by half and cavitation effects were reduced.

Thermal and mechanical resistances of the outer coil insulators were checked by inserting an endoscopic camera after forty hours of run at 7 kA applied current. Mechanical resistance was validated, as insulators were not displaced and still aligned vertically. By comparing pictures to samples of heated insulators, one estimated that temperature reached locally exceeded expectations. Alternative insulators will be investigated for magnetic field tests at full current intensity.

Direct electrical connection of SEISM to the current power supplies was validated, thus allowing to overcome the 13 kA limitation of M5 magnet. Therefore measurements could be performed for several magnetic configurations, with up to 15 kA applied on the injection and extraction coils sets. The magnetic field achieved then allows 28 GHz ECR condition (see figure 190). Magnetic field amplitude evolves linearly when increasing the current intensity, so the possibility of performing 60 GHz ECR condition at 30 kA was confirmed by extrapolation.

Discrepancies were observed between the positions measured for helices magnetic centres and those simulated with the 2D model. The resulting map seems to be displaced by about 5 mm towards the extraction, although it does not invalidate the magnetic structure. Possible reasons are investigated to eliminate future mechanical risks when increasing the current to 30 kA. Helices magnetic centres will be verified after dismounting, and 3D models taking into account non-linear effects will be simulated.

Next year, the components of the source (plasma chamber, gas and microwave injection...)will be designed. A permanent room at LNCMI is under funding request for the first plasma tests at 28 GHz.

This work was funded by EUROnu, Project Number 212372, within the European Commission Framework Programme 7 Design Study.

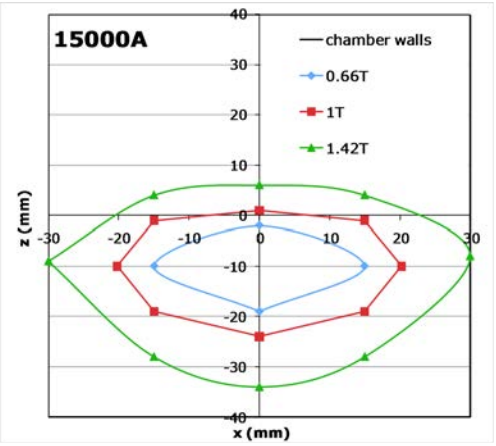


FIG. 190. *Magnetic field map measured at 15 kA: helices axis is along z and the first iso-B touching the plasma chamber walls is at 1.42 T. A closed 1 T zone is achieved, thus allowing 28 GHz ECR condition.*

***F. Debray, J. Matera, C. Trophime***
***J. Jacob, T. Lamy, M. Marie-Jeanne (LPSC, Grenoble, France)***

# Status report of the 42+T hybrid magnet project: Conductor development

The coil sub-assemblies of the hybrid magnet under construction at LNCMI-G, is composed by a resistive part made of polyhelix and bitter coils as well as a large bore superconducting one. The field contribution of each element is given in Table I. Upgrade phase scenarios to further increase the maximum field of 42 T in a 34 mm warm aperture, are also studied.

| Hybrid components | Magnetic Field |
|---|---|
| 14 series-connected helix coils | 24.5 T |
| 2 series-connected Bitter coils | 9 T |
| 37 series-connected superconducting double pancake coils | 8.5 T |

TABLE I. Subparts of the 42+T hybrid magnet.

The most important choices that have been made for the superconducting coil outsert can be summarized in four key points:

- High current to minimize the coil self-inductance and therefore to reduce the voltage levels during quenches;
- Nb-Ti/Cu Rutherford cable indirectly cooled by superfluid helium at 1.8 K;
- Insulated conductors;
- Vacuum impregnated coil with internal cooling.

The superconducting coil will consist of 37 series-connected double pancakes with 26 turns per pancake and will require a current of 7100 A to produce the design field value of 8.5 T in a 1100 mm bore diameter. This corresponds to an overall current density slightly below 30 A/mm$^2$, which is a usual value for large scale superconducting magnets. The double pancakes will be wound from a specially developed Rutherford Cable On Conduit Conductor (RCOCC) composed by a Nb-Ti/Cu Rutherford cable brazed on a Cu-Ag stabilizer. To ensure the internal cooling at 1.8 K of the fully impregnated coil winding, the stabilizer of each double pancake is equipped with a cooling channel of diameter 6 mm (figure 191) with both ends open to the static bath of pressurized superfluid He. The soft soldering of the Rutherford cable on the stabilizer is a delicate operation, which requires dedicated studies and the best attention. Several RCOCC specimens have been produced from samples of Rutherford cable with 19 strands and Cu-Ag0.04% extruded stabilizer.

The solder metal was chosen to be the same as for the strand coating (Sn96Ag3.5, melting point of 221°C). Peeling tests were performed on these samples (figure 191) to define the minimum amount of solder compatible with the mechanical constraints.

FIG. 191. *Examples of RCOCC samples after the peeling test.*

Inter-strand coupling currents should also be kept as low as possible at cryogenic temperatures to avoid quenching of the magnet during insert trips of the resistive coils. A stainless steel core of 50 $\mu$m is introduced within the Rutherford cable to obtain a contact resistance between crossing strands $R_c > 100\,\mu\Omega$. The adjacent contact resistance is governed by the amount of solder and the target is $R_a > 0.1\,\mu\Omega$. A calorimetric method has been specially developed to determine these contact resistances on selected RCOCC samples. The values obtained are in good agreement with the above expectations. The contract for the production of all unit lengths of the Nb-Ti/Cu Rutherford cable ($\sim$ 11 km) has been signed at the end of 2009 with Bruker EAS GmbH. The first unit length of Rutherford cable has been delivered at the end of 2010 for the qualification tests. If the results are conformed to the technical specification, the full production of the superconducting cable will start hereafter. The specification of the insertion of the Rutherford cable within the stabiliser has been prepared and reviewed. The call for tender will be issued beginning of 2011 at the latest. The design and the supervision of the industrial realisation of the superconducting coil, the cryostat and the related cryogenics is an ambitious project, which required various types of expertise and experience. A contract of collaboration has been signed at the end of October 2010 with the CEA/IRFU/SACM from Saclay.

***W. Joss, R. Pfister, P. Pugnat, L. Ronayette, H. Xiao***
***C. Berriaud, A. Daël, P. Fazilleau, B. Hervieu, F.P. Juster, C. Mayri, J.M. Rifflet (CEA/IRFU/SACM-Saclay, Gif-sur-Yvette, France)***

# Users of the LNCMI high magnetic field facility

### Introduction

The Laboratoire National des Champs Magnétiques Intenses is one of the large scale facilities of CNRS. It works as a research facility available both to its own researchers as well as to external users. The high field facility is open to users from 27 countries of the European Union and from the associated states (Iceland, Israel, Liechtenstein, Norway, Switzerland and Turkey) under the same conditions as users of the CNRS. Researchers from other countries can also perform their experiments at the LNCMI, but they are required to cover themselves their travel and living expenses.

### High magnetic fields and instrumentation available to the users

The LNCMI has resistive and superconducting magnets at the Grenoble site and pulsed magnets at the Toulouse site, achieving continuous magnetic fields up to 35 T and pulsed fields up to 70 T on which it is possible to install different experimental set-ups.

The technical and experimental environment also allows the user to combine very low temperatures and high pressures with very high fields. The laboratory offers a wide variety of instrumentation, allowing measurements in high magnetic fields in the following areas:

- EPR spectroscopy,
- NMR spectroscopy,
- Magnetization measurements (extraction technique, torque),
- Magneto hydrodynamics,
- Specific heat measurements,
- Magneto-transport measurements,
- Magneto-spectroscopy in the infra-red and visible area,
- Characterization of superconductors for applications.

### Access to the facility

Scientists who wish to obtain access to the resistive or pulsed magnets of the LNCMI must apply through the EuroMagNET web site (http://www.hfml.ru.nl/EuroMagNET2/). This application is drawn up according to a specific form and provides information demonstrating the relevance of the research work to be undertaken. The application is also used to ensure that the experimental conditions requested can be satisfied. Access to the superconducting magnets of the LNCMI goes through an in-house procedure, which is open all year (http://ghmfl.grenoble.cnrs.fr/spip.php?rubrique126).

### Selection Committee

All applications are examined and ranked by the EuromagNET2 selection committee, twice a year, generally in the course of December and at the end of June. The applications are ranked A, B or C. Projects rated A will be executed, those classified B are performed if the magnet time is available, and applications rated C are rejected. The ranking is made on the same basis for all applications, including those submitted by the local scientists.Accepted experiments are consequently programmed during the two semesters following this meeting. If the experiment has not been performed in this period, one has to resubmit the proposal mentioning the reasons why it could not be performed (samples not ready, *etc*). The acceptance of an application means that the entire cost of the experiment (electricity, cryogenic fluids, *etc*) will be covered by the budget of the laboratory. In the frame of the EuroMagNET2 European contract, scientists from one of the countries belonging to the European Union or to an associated state (see above) may obtain the reimbursement of their travel and living expenses (one person per project can be reimbursed).

The Selection Committee is divided into six groups; each group with a different area of expertise (Semiconductors, Metals and Superconductors, Magnetism, Magnetic Resonance, Applied Superconductors, Soft Materials). In each area there are international experts from outside the EuromagNET2 consortium, chosen from within the European Community, as well as scientists from the different high magnetic field laboratories of the EuromagNET2 consortium, whose presence ensures that a project can be technically performed in the laboratory.

### Local contact

When the applicant is informed of the acceptance of his proposal, and of the number of days scheduled for the experiment, he/she is at the same time informed of the name of his local contact in charge of facilitating his work at the LNCMI. The local contact is a research scientist or a engineer of the laboratory. If an applicant cannot identify a local contact, the laboratory management will appoint a scientist that the user can contact in order to define with him the conditions for the organization of the experimental work.

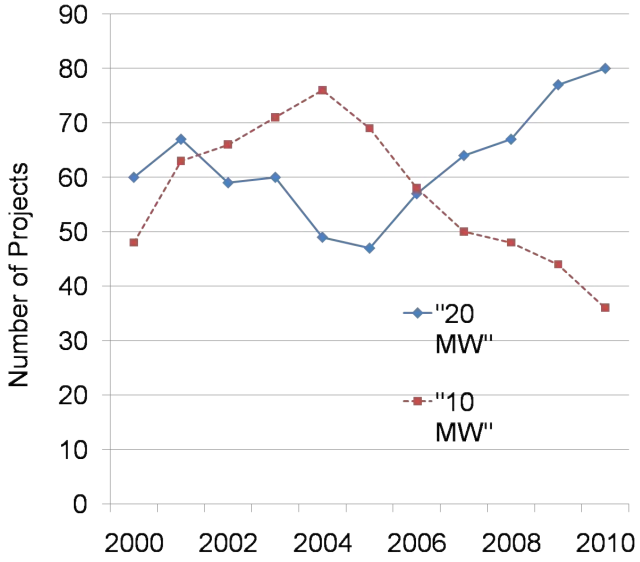


FIG. 192. *Number of LNCMI-G projects submitted to the selection committee. 20 MW refers to magnets using simultaneously the four 6 MW power supplies of the facility whereas 10 MW magnets use only two power supplies.*

### Programming the period of experiment

The schedule for utilization of the magnets is drawn up several weeks in advance and is made official at the beginning of every month. Visitors are therefore strongly urged to get in touch with their local contact, to reserve as quickly as possible the most suitable period for carrying out their experiment at the LNCMI.

### Magnet time planning

The magnets operate on a schedule, displayed monthly, taking into account the availability of staff, magnets and instrumentation. For the LNCMI-G, the installation operates outside normal working hours with professional operators. This allows the magnets to be operated 20 hours per day during the week and 11 hours per day during weekends and bank holidays. The LNCMI is shut down for maintenance during several weeks in summer and several weeks in winter. This shutdown is used for maintenance, technical interventions and upgrading and testing.

### Projects submitted during the last 10 years

An average of 180 projects are submitted annually to the EuroMagNET Selection Committee (including continuations of projects), of which there are 120 for the LNCMI-G installation and 60 for the LNCMI-T installation. Applications for the Grenoble 20 MW magnets are constantly increasing while there is a decrease in requests for 10 MW magnets. The increase in the number of requests for the 20 MW sites since 2006 is due to the commissioning of two new 20 MW magnets, configured with a 34 and 160 mm diameter bore, and partly to the increase of the field obtained (currently 35 T) on a the 34 mm bore version of these magnets (figure 192)

### Projects carried out in 2010

In 2010 the access to the Grenoble resistive magnets was possible during 41 weeks in which the laboratory has provided 2956 hours of magnet time (as of the 9th of December) to its users. Two-thirds (1979 hours) of the magnet time was consumed by the 20 MW magnets M8, M9 and M10, whereas one-third (977 hours) was consumed by the 10 MW magnets (figure 193(a)). Figure 193(b) shows the electrical power consumption of the magnets. The total power consumption of all magnets in 2010 exceeded 16 GWh. In order to try to minimize the energy costs while performing a maximum number of high field experiments the laboratory has to impose strategic planning rules for the more consuming 20 MW magnets (figure 193(b)). The Toulouse installation has provided 3800 magnet shots in 2010.

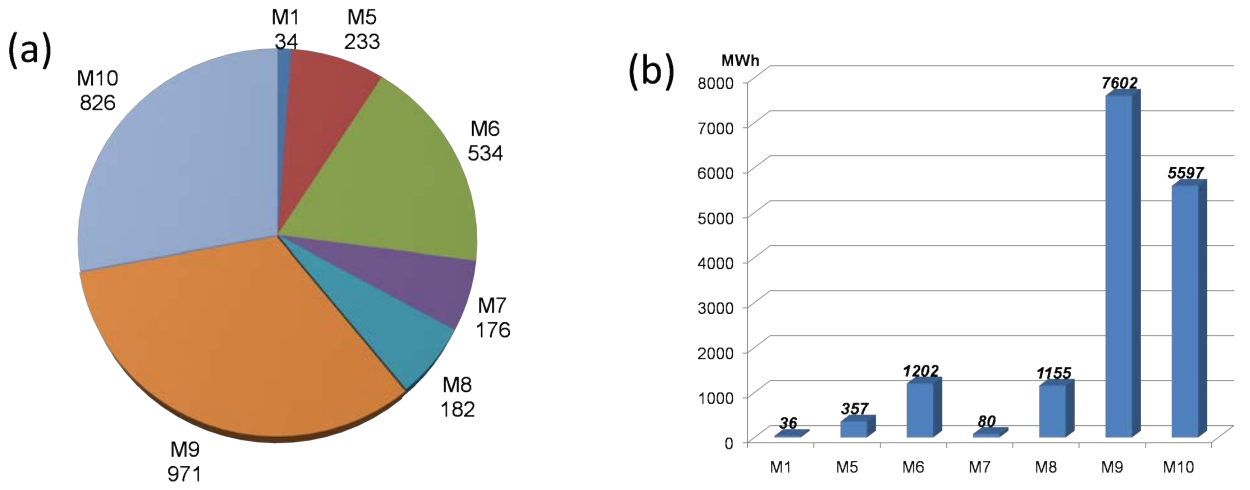


FIG. 193. *(a) Number of hours of use and (b) power consumption, of the resistive magnets at LNCMI-G from 01.01.2010 to 09.12.2010*

The left panel of figure 194 shows the country of origin of the projects that were performed on resistive and pulsed magnets in 2010. Half of the projects came from France while the other half was divided mainly between European countries. Some users also came from the USA, Canada, Russia, Brazil and China. Most scientists who have already used our facilities come back regularly, introducing and progressively forming scientists who become themselves, in turn, new users.

The projects realized in 2010 using the Grenoble resistive magnets and the Toulouse pulsed magnets are thematically distributed as shown in the right panel of figure 194.

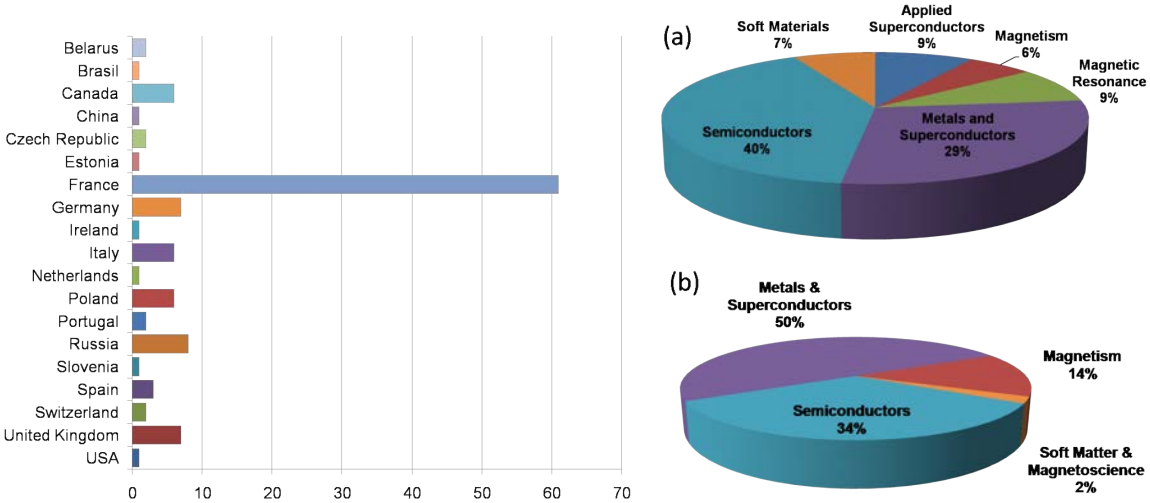


FIG. 194. *(left) Number of projects carried out at LNCMI (G+T) by country of origin. (right) Projects performed on the resistive magnets (a) and pulsed magnets (b) by area of expertise.*

## Conclusion

The technical and scientific environment of the LNCMI, adapted to research in high magnetic field, is highly appreciated by the international scientific community. A large majority of users shows great interest in the laboratory and they come regularly in order to perform their experiments, thereby strengthening collaborations between research groups. The number of projects submitted and realized at the LNCMI reached a significant number in recent years, demonstrating the international scope of the laboratory. The schedule of the Grenoble 20 MW magnets is extremely tight and it is essential to optimize the use of these magnets.

***C. Warth-Martin, O. Portugall, D. Attard, R. Graziotti, E. Mossang, A. Pic, E. Rochat, C. Vannier***

# Proposals for magnet time – Projects carried out in 2010

## APPLIED SUPERCONDUCTORS

*The $I_c - B$ dependence of Bi-2212 superconducting wires in high field at 4.2 K.*
A.Sulpice (Institut Néel-CNRS, Grenoble, France) E. Mossang (LNCMI-CNRS, Grenoble, France) C. Li (NIN, Shaanxi, China).

*High field characterizations for HTS high field inserts.*
P. Tixador (CNRS, Institut Néel, Grenoble, France), J.M. Rey (CEA Saclay, Gif sur Yvette, France), L. Porcar (CNRS, Institut Néel, Grenoble, France), J.P. Domps (CNRS, LNCMI, Grenoble, France).

*Transport properties of $MgB_2$*
M. Vignolo (CNR-INFM, Genova, Italy), A. Malagoli, G. Romano (CNR-INFM, Genova, Italy), A. Tumino, (Columbus Superconductors SpA, Genova, Italy).

*Spin hybrization in magnetic first-order phase transition materials.*
V. Amaral (Universidade de Aveiro, Departamento de Fisica e CICECO, Aveiro, Portugal), J. Amaral, S. Das, J.N. Gonalves, N.J. Silva (Universidade de Aveiro, Departamento de Fisica e CICECO, Aveiro, Portugal).

*The influence of high magnetic fields on the exchange bias of nanostructured MnIr/CoFe layers for spintronics.*
J. Ventura (IFIMUP, Alegre, Portugal), J. Araujo, A. Pereira, J. Teixeira, R. Lusche (IFIMUP, Alegre, Portugal).

*Transport properties of MgB2 based wires and tapes.*
Tumino (Columbus Superconductors SpA, Genova, Italy), S. Brisgotti, V. Cubeda, M. Palombo, S. Berta (Columbus Superconductors SpA, Genova, Italy).

## MAGNETISM

*High-field magnetoresistance of the hidden-order system $URu_2Si_2$*
W. Knafo (LNCMI, Toulouse, France), C. Proust, N. Gales (LNCMI, Toulouse, France), D. Aoki, J. Flouquet (CEA Grenoble, France).

*High-field anisotropy of hematite and goethite*
M. Dekkers (Utrecht University, Netherlands), G. Dupont-Nivet (Utrecht University, Netherlands), F. Martin Hernandez (Universidad Complutense de Madrid, Spain), J. L. Bouchez (Universite Paul Sabatier, LMTG, Toulouse, France).

*High magnetic field study of magnetic ground state of tetragonal iron chalcogenides*
R. Viennois (Institut Gerhardt, Université Montpellier II, France), E. Giannini (Université de Genève, Switzerland).

*Global ferrimagnetic ordering in $Gd_{60}Mn_{30}X_{10}$ (X = In, Al) due to the antiferromagnetic coupling between Gd and Mn atoms.*
C. Mayer (Institut de Chimie de la Matière Condensée de Bordeaux, France), B. Chev (Institut de Chimie de la Matière Condensée de Bordeaux, France).

*High field magnetization curves of $CoC_3H_6O_2$, a new 3D framework of cobalt cubanes.*
G. Viau (LPCNO - INSA Toulouse, France), L; M. Lacroix (LPCNO - INSA Toulouse, France), B. Raquet, J. M. Broto (LNCMI, Toulouse, France).

*High magnetic field study of magnetic ground state of tetragonal iron chalcogenides.*

R. Viennois (Institut Gerhardt, Université Montpellier II, France).

*Magnetization in pure and impurity doped BiCuPO Spin ladders.*
J. Bobroff (Laboratoire de Physique des Solides, Universite Paris Sud, CNRS, France), N. Laflorencie Laboratoire de Physique des Solides, Universite Paris Sud, CNRS, France), a. Mahajan A (IIT Bombay, India), B. Vignolle, W. Knafo, G. Ballon (LNCMI, Toulouse, France).

*High field magnetic properties of the $RCo_4M$ phases.*
M. Guillot (LNCMI-CNRS, Grenoble, France), O. Isnard, C. Colin (Institut Néel, UJF, Grenoble, France).

*Measurements under high magnetic fields and high pressure.*
M. Guillot (LNCMI-CNRS, Grenoble, France), O. Isnard, C. Colin (Institut Néel, UJF, Grenoble, France).

*Probing Bose-Einstein condensation in spin-1/2 alternating chain system $AgVOAsO_4$*
A.Tsirlin (Max Planck Institute for Chemical Physics and Solids, Dresden, Germany), H. Rosner, F. Weickert (Max Planck Institute for Chemical Physics and Solids, Dresden, Germany).

*Magnetic properties of $Y_{1-x}GdxFe_2D(H)_{4.2}$ compounds.*
V. Paul-Boncour (CMTR/ICMPE, CNRS and Paris 12, Paris, France), M. Guillot (LNCMI-CNRS, Grenoble, France).

## MAGNETIC RESONANCE

*High-field part of the phase diagram of novel quasi-1D Ising-like quantum antiferromagnet.*
M. Klanjsek (Jozef Stefan Institute, Ljubljana, Slovenia), M. Horvatic, Cl. Berthier, S. Krämer (LNCMI-CNRS, Grenoble, France).

*NMR study of YBCO superconductors in high magnetic fields.*
M.-H. Julien (LNCMI-CNRS, Grenoble, France), T. Wu, H. Mayaffre, Cl. Berthier (LNCMI-CNRS, Grenoble, France), D. Bonn (University of British Columbia, Department of Physics and Astronomy, Vancouver, Canada).

*Magnesium-25 solid state NMR: a new tool for the study of the environment of Mg in natural tissues.*
D. Laurencin (Université de Montpellier, Institut Charles Gerhardt, Montpellier, France), F. Fayon (CEMHTI-CNRS, Orléans, France), Ch. Gervais Stary (Université Pierre et Marie Curie, Laboratoire de Chimie de la Matire Condensée, Paris, France).

*High field Cu NMR study of the microscopic structure of the Bose-Einstein Condensate in $BaCuSi_2O_6$*
R. Stern (NICPB, Tallinn, Estonia), S. Krämer, Cl. Berthier, M. Horvatic, S. Mukhopadhyay (LNCMI-CNRS, Grenoble, France), T. Kimura (Osaka University, Osaka, Japan).

*NMR investigation of the putative FFLO phase in kappa-$(BEDT\text{-}TTF)_2Cu(NCS)_2$.*
H. Mayaffre (LNCMI-CNRS, Grenoble, France), V. Mitrovic (Brown University, Department of Physics, Providence, USA), Cl. Berthier, M. Horvatic (LNCMI-CNRS, Grenoble, France).

*NMR study of YBCO superconductors in high magnetic fields.*
M.-H. JULIEN (LNCMI-CNRS, Grenoble, France), T. Wu, H. Mayaffre, Cl. Berthier (LNCMI-CNRS, Grenoble, France).

*High-field NMR investigation of the BiCu2PO6 spin ladder.*
F. Casola (ETH, Zrich, Switzerland), T. Shiroka, H.R. Ott (ETH, Zrich, Switzerland), Ch. Regg (University College London, London, United Kingdom), M. Kenzelmann, J.F. Mesot (Paul Scherrer Institut, Villigen, Switzerland).

## METALS AND SUPERCONDUCTORS

*Upper critical magnetic field in single-crystals of $Ba_{1-x}K_xFe_2As_2$, $Ba(Fe_{1-x}Co_x)_2As_2$ and $FeTe_{0.55}Se_{0.45}$ compounds.*

V. Gasparov (Institute of Solid State Physics Russian Academy of Sciences, Russia), A. Audouard, L. Drigo (LNCMI, Toulouse, France).

*From few layer graphene to graphite.*
W. Escoffier (LNCMI, Toulouse, France), J. M. Poumirol, A. Kumar, R. Ribeiro, B. Raquet, M. Goiran (LNCMI, Toulouse, France).

*Superconductor/insulator transition in LaSrCuO.*
B. Leridon (ESPCI Paris, France).

*Ultrasound measurement in pulsed magnetic fields : elemental Bismuth beyond the quantum limit and hidden phase transition in high-Tc superconductors.*
D. Leboeuf (LNCMI, Toulouse, France), C. Proust, B. Vignolle (LNCMI, Toulouse, France), K. Behnia, B. Fauque (ESPCI Paris, France), D. Bonn (University of British Columbia, Vancouver, Canada).

*Quantum oscillations in $LaAlO_3/SrTiO_3$ interfaces in the two dimensional conduction regime.*
A. Caviglia (DPMC, University of Geneva,Switzerland), S. Gariglio, A. Fete, C. Cancellieri, J. M. Triscone (DPMC, University of Geneva,Switzerland).

*High-field magnetostriction and magnetization of heavy-fermion systems.*
W. Knafo (LNCMI, Toulouse, France), G. Ballon (LNCMI, Toulouse, France), D. Aoki, J. Flouquet (CEA Grenoble, France).

*Quantum oscillations in cuprates: the case of the electron-doped material.*
C. Proust (LNCMI, Toulouse, France), B. Vignolle, D. Vignolles, D. Leboeuf, S. Lepault (LNCMI, Toulouse, France), R. Greene (University of Maryland, USA)

*Fermi surface investigation of high Tc superconductors.*
D. Vignolles (LNCMI, Toulouse, France), C. Proust, S. Lepault, B. Vignolle (LNCMI, Toulouse, France), D. Bonn (University British Columbia, Vancouver, Canada).

*Search for the de Haas van Alphen effect in electron-doped high-Tc superconductors.*
M. Kartsovnik (Walther-Meissner-Institut, Garching, Germany), T. Helm (Walther-Meissner-Institut, Garching, Germany).

*Enhancement of quasiparticle mass close to maximum Tc in $BaFe_2(As/P)_2$.*
A. Carrington (Bristol University, UK), A. Coldea (Bristol University, UK).

*Search for metamagnetism and field induced quantum criticality in $YbCu_2Si_2$ in pulsed magnetic fields.*
D. Braithwaite (CEA Grenoble, France), A. Fernandez-Panella, L. Malone (CEA Grenoble, France).

*Magnetic oscillations in the organic metals (BEDT-TTF)$_4$MBr$_4$($C_6H_4X_2$) (M=Cd, Ni, Co, Fe, Mn, X=Cl, Br).*
R. Lyubovskii (IPCP Chernogolovka, Russia), R. Lyubovskaia (IPCP Chernogolovka, Russia), A. Audouard, D. Vignolles (LNCMI, Toulouse, France), E. Canadell (ICMAB Barcelona, Spain).

*High Field Hall Effect in YBCO.*
N. Doiron-Leyraud (Universite Sherbrooke, Canada), D. Leboeuf, J. Chang (Universite Sherbrooke, Canada) B. Vignolle, C. Proust (LNCMI, Toulouse, France), D. Bonn, R. Liang, (University of British Columbia,

Vancouver, Canada).

*Quantum Oscillations in high purity, underdoped cuprate superconductors.*
D. Bonn (University of British Columbia, Vancouver, Canada), R. Liang, B; Ramshaw, J. Day (University of British Columbia, Vancouver, Canada), B. Vignolle, C. Proust (LNCMI, Toulouse, France).

*Ultrasound and Nernst effect measurements in Bismuth in pulsed magnetic fields.*
C. Proust (LNCMI, Toulouse, France), B. Vignolle (LNCMI, Toulouse, France), K. Behnia (ESPCI Paris, France), B. Fauque, (Bristol University, UK).

*Low temperature resistivity of La-doped Bi2201.*
N. Hussey (University of Bristol, UK), P. Rourke, B. Arnold (University of Bristol, UK).

*Charge transport in bismuth and $Bi_{1-x}Sb_x$ deep in the ultraquantum regime.*
K. Behnia (LPEM-ESPCI Paris, France), B. Fauque (LPEM-ESPCI Paris, France), C. Proust, B. Vignolle (LNCMI, Toulouse, France).

*Transport properties of the iron based superconductors $Ba(Fe_{1-x}Co_x)_2As_2$.*
F. Rullier-Albenque (IRAMIS, CEA, France), H. Alloul (Université de Paris, France).

*Metal insulator transition and quantum oscillations in $(BEDT\text{-}TTF)_8Hg_4Br_{12}(C_6H_5Br)$.*
A. Audouard (LNCMI, Toulouse, France), D. Vignolles (LNCMI, Toulouse, France),R. Lyubovskii, R. Lyubovskaia (IPCP Chernogolovka, Russia), E. Canadell, (ICMAB Barcelona, Spain).

*De Haas van Alphen oscillations spectrum of the organic metal $(BEDO\text{-}TTF)_5[CsHg(SCN)_4]_2$.*
R. Lyubovskii, R. Lyubovskaia (IPCP Chernogolovka, Russia), A. Audouard, D. Vignolles (LNCMI, Toulouse, France).

*Fermi surface studies and upper critical field anisotropy in iron chalcogenites.*
A. Coldea (Bristol University, UK), P. Goddard (Oxford University, UK), A. Ganin, M. Rosseinsky (Liverpool University, UK).

*Magnetotransport in thin single crystals of graphite and graphene containing nanoholes.*
Y. Latyshev (Institut of Radioengineering and Electronics/RAS, Russia), A. Orlov (Institut of Radioengineering and Electronics/RAS, Russia), A. Sinchenko (Moscow State Engineering Physics Institute, Russia), P. Monceau (Institute Néel, Grenoble, France).

*High-field magnetization of the heavy-fermion system $Ce_{1-x}La_xRu_2Si_2$.*
W. Knafo (LNCMI, Toulouse, France), D. Vignolles (LNCMI, Toulouse, France), J. Flouquet (CEA Grenoble, France), P. Haen, P. Lejay (CNRS Grenoble, France).

*Landau States in the electronic spectrum of MWCNTs under 60 T.*
B. Raquet (LNCMI, Toulouse, France), J. M. Broto, W. Escoffier, S. Nanot (LNCMI, Toulouse, France), S. Roche (CEA Grenoble, France).

*Exploring the Fermi Surface on Iron Based Pcnitite and Chalcogenite Superconductors.*
A. Coldea (Bristol University, UK), A. Carrington, C. Andrew, A. Bangura (Bristol University, UK), P. Goddard (Oxford University, UK), A. Ganin (Liverpool University, UK).

*Specific heat on FeSeTe single crystals.*

D. Braithwaite (INAC/SPSMS/IMAPEC, CEA, Grenoble, France), Ch. Marcenat (INAC/SPSMS/LATEQS, CEA, Grenoble, France).

*Thermoelectricity and Magnetic Field Transitions in Heavy Fermion Systems.*
L. Malone (LNCMI-CNRS, Grenoble, France), G. Knebel (DRFMC/SPSMS, CEA, Grenoble, France), D. Aoki, J. Flouquet (INAC/SPSMS/IMAPEC, CEA, Grenoble, France), W. Knafo (LNCMI, Toulouse, France).

*Superconducting properties under high magnetic fields in UCoGe.*
D. Aoki (INAC/SPSMS/IMAPEC, CEA, Grenoble, France), I. Sheikin (LNCMI-CNRS, Grenoble, France), T. Matsuda, E. Hassinger, V. Taufour (INAC/SPSMS, CEA, Grenoble, France).

*Nernst effect in graphite.*
K. Behnia (LPEM-ESPCI, Paris, France), B. Fauqué (LPEM-ESPCI, Paris, France), L. Malone (LNCMI-CNRS, Grenoble, France).

*Nernst effect in high-Tc superconductors.*
J. Chang (Université Sherbrooke, Sherbrooke, Canada), N. Doiron-Leyraud, F. Laliberte, O. Cyr-Choiniere, L. Taillefer (Université Sherbrooke, Sherbrooke, Canada), R. Liang, D. Bonn (University of British Columbia, Department of Physics and Astronomy, Vancouver, Canada), K. Behnia (LPEM-ESPCI, Paris, France), C. Proust (LNCMI-CNRS, Toulouse, France).

*De Haas-van Alphen study of new superconductors $BaIr_2P_2$ and $BaRh_2P_2$.*
O. Ignatchik (Dresden High Magnetic Field Laboratory, Dresden, Germany), M. Bartkowiak (Paul Scherrer Institut, Villigen Switzerland), J. Wosnitza (Dresden High Magnetic Field Laboratory, Dresden, Germany).

*Electron confinement in $LaVO_3/SrVO_3$ superlattices.*
U. Lders (CRISMAT, Caen, France).

*Angular dependance of the Nernst effect in $Bi_{1-x}Sb_x$ for $x = 2.5\%$.*
K. Behnia (LPEM-ESPCI, Paris, France), B. Fauqué (University of Bristol, Bristol, United Kingdom).

*Pressure criticality and magnetic field induced quantum criticality: the case of $CeRu_2Si_2$.*
T. Matsuda (INAC/SPSMS, CEA, Grenoble, France), D. Braithwaite, D. Aoki, J. Flouquet (INAC/SPSMS/IMAPEC, CEA, Grenoble, France), R. Settai (University of Osaka, Osaka, Japan), L. Malone (LNCMI-CNRS, Grenoble, France), W. Knafo (LNCMI-CNRS, Toulouse, France).

*Search for metamagnetism and field induced quantum criticality in $YbCu_2Si_2$ under pressure.*
D. Braithwaite (INAC/SPSMS/IMAPEC, CEA, Grenoble, France), A. Fernandez-Panella (INAC/SPSMS/IMAPEC, CEA, Grenoble, France), L. Malone (LNCMI-CNRS, Grenoble, France).

*Normal state magnetotransport anisotropy of the electron-doped high-Tc superconductor $Nd_{2-x}CexCuO_4$.*
M. Kartsovnik (Walther-Meissner-Institut, Garching, Germany), T. Helm, W. Biberacher (Walther-Meissner-Institut, Garching, Germany).

*High-field thermoelectric response in $FeSe_{1-y}Te_y$.*
K. Behnia (LPEM-ESPCI, Paris, France), A. Pourret, B. Fauqué (LPEM-ESPCI, Paris, France), L. Malone (LNCMI-CNRS, Grenoble, France).

*Thermoelectric effects in high-$T_c$ superconductors.*
L. Taillefer (Université Sherbrooke, Sherbrooke, Canada), N. Doiron-Leyraud, J. Chang, F. Laliberté, O. Cyr-Choinière (Université Sherbrooke, Sherbrooke, Canada), D. Bonn (University of British Columbia, Department of Physics and Astronomy, Vancouver, Canada), M. Greven (University of Minnesota, Minneapolis, USA).

*Specific heat on iron pnictides and related compunds.*
Ch. Marcenat (INAC/SPSMS/LATEQS, CEA, Grenoble, France), Th. Klein, K. Hasselbach, P. Toulemonde (Institut Néel-CNRS, Grenoble, France), A.De Muer (LNCMI-CNRS, Grenoble, France), W.K. Kwok (Argonne National Laboratory, Argonne, USA), H.H. Wen, Z.S. Wang (Chinese Academy of Science, Beijing, China), D. Braithwaite (INAC/SPSMS/LATEQS, CEA, Grenoble, France).

*Angular-dependent Nernst effect in bismuth.*
B. Fauqué (LPEM-ESPCI, Paris, France), K. Behnia, Z.W. Zhu, S. Atis (LPEM-ESPCI, Paris, France), L. Malone (LNCMI-CNRS, Grenoble, France).

*The Hidden Order Phase of $URu_2Si_2$*
L. Malone (LNCMI-CNRS, Grenoble, France), J. Flouquet, D. Aoki (INAC/SPSMS/IMAPEC, CEA Grenoble, France), G. Knebel (DRFMC/SPSMS, CEA, Grenoble, France).

*De Haas-van Alphen measurements on $PrPt_4Ge_{12}$ single crystals.*
B. Bergk (Hochfeld-Magnetlabor Dresden, Dresden, Germany), A. Polakov, J. Wosnitza (Hochfeld-Magnetlabor Dresden, Dresden, Germany), H. Rosner (MPI CPfS, Dresden, Germany).

**SEMICONDUCTORS**

*Study of fractional Quantum-Hall-states other than filling-factor 1/3 in graphene in the limit of high charge-carrier-densities.*
V. Krstic (Trinity College Dublin, Ireland), S. Hansel (Trinity College Dublin, Ireland) M. Lafkioti (Max Planck Institute for Solid State Research, Stuttgart, Germany).

*Transport in individual carbon nanotubes electro-chemically embedded with transition metal clusters.*
F. Rossella (Dep. of Physics, University of Pavia, Italy), V. Bellani (Dep. of Physics, University of Pavia, Italy), B. Raquet, W. Escoffier (LNMCI, Toulouse, France), C. Soldano (CEMES, Toulouse, France).

*Determination of the dimensionality of the high mobility electron gas in the $LaAlO_3/SrTiO_3$ system.*
A. Barthélémy, M; Bibes, N. Reyren (UMP CNRS/Thales, France), B. Raquet, J.M. Broto (LNCMI, Toulouse, France).

*Disorder and magnetic edges current in Graphene Nanoribbons.*
B. Raquet (LNCMI, Toulouse, France), R. Ribeiro, J. M. Poumirol, W. Escoffier (LNCMI, Toulouse, France), H. Dai (Stanford University, USA), S. Roche (CIN2: Centre d'Investigacio en Nanociencia i Nanotecnologia, Barcelona, Spain).

*Single-object electrical transport and photoconductivity measurements under pulsed magnetic field.*
V. Prudkovsky (LNCMI, Toulouse, France), B. Raquet, M. Goiran (LNCMI, Toulouse, France).

*Field-induced Colossal Magnetoresistance in Semiconductor Quantum Wells.*
G. Gervais (McGill University, Canada).

*Edge Fingerprints and Magnetoconductance on Graphene Nanoribbons.*
B. Raquet (LNCMI, Toulouse, France), W. Escoffier, R. Ribeiro, J. M. Poumirol, J.M. Broto, M. Goiran (LNCMI, Toulouse, France),S. Roche (CEA Grenoble, France), H. Dai (Stanford University, USA).

*Quantum Hall Effect in graphene: from disordered to clean devices.*
F. Rossella (Dep. of Physics, University of Pavia, Italy), V. Bellani (Dep. of Physics, University of Pavia, Italy) W. Escoffier, J. M. Poumirol, R. Ribeiro, B. Raquet, A. Kumar, M. Goiran (LNCMI, Toulouse, France).

*Electronic properties of semiconductor nanowires : experimental study of the conductance under 60T.*
B. Raquet (LNCMI, Toulouse, France), V. Prudkovsky, M. Goiran (LNCMI, Toulouse, France)

*Photoluminescence efficiency and energy in the high mobility 2DEG. in the extreme quantum limit.*

V. Bellani Dep. of Physics "A. Volta", University of Pavia, Italy), F. Rossella, I. Colino (Dep. of Physics "A. Volta", University of Pavia, Italy), M. Goiran (LNCMI, Toulouse, France).

*Cyclotron resonance in HgTe quantum wells.*
V. Gavrilenko (Institute for Physics of Microsructures RAS, Russia), A. Ikonnikov, K. Spirin (Institute for Physics of Microsructures RAS, Russia), O. Drachenko (Forschungszentrum Dresden-Rossendorf, Germany), M. Goiran (LNCMI, Toulouse, France)

*Addressing the electronic properties of few layer graphene.*
W. Escoffier (LNCMI, Toulouse, France), B. Raquet, M. Goiran, J. M. Poumirol, A. Kumar, R. Ribeiro (LNCMI, Toulouse, France).

*High Field Magnetotransport Studies of the Quantum Interference Phenomena and Interaction Effects in Polycrystalline Tin-Dioxide Films.*
V. Ksenevich (Belarus State University, Minsk, Belarus), T. Dauzhenka (Belarus State University, Minsk, Belarus).

*Photoluminescence efficienty and energy in the high mobility 2DEG. in the extreme quantum limit.*
V. Bellani, F. Rossella (University of Pavia, Italy), F. Dionigi (University of Pavia, Italy).

*Landau Level spectroscopy of graphite.*
P. Plochocka (LNCMI, Grenoble, France), N. Ubrig, O. Portugall (LNCMI, Toulouse, France).

*Anomalous Quantum Hall effect in graphene and bi-layer graphene.*
W. Escoffier (LNCMI, Toulouse, France), J. M. Poumirol, B. Raquet, M. Goiran, J. M. Broto (LNCMI, Toulouse, France)

*Investigation of the dynamic alignement of DNA-wrapped single walled carbon nanotubes in liquid Suspension.*
J. Kono (Department of Electrical and Computer Engineering, Rice University, Houston, USA) N. Ubrig, O. Portugall (LNCMI, Toulouse, France)

*High Field Magnetotransport Properties of low-dimensional arrays of tin-dioxide nanoclusters.*
V. Ksenevich (Belarus State University, Minsk, Belarus), T. Dauzhenka, (Belarus State University, Minsk, Belarus).

*Raman experiments of interface phonons in single doped GaAs QW under high magnetic field.*
G. Martinez (LNCMI-CNRS, Grenoble, France), C. Faugeras (LNCMI-CNRS, Grenoble, France).

*Polarized magneto-Raman scattering of optical phonon in epitaxial graphene.*
C. Faugeras (LNCMI-CNRS, Grenoble, France), M. Potemski, P. Kossacki (LNCMI-CNRS, Grenoble, France).

*Polaronic effects in single doped GaAs based quantum well from a lift-off epilayer.*
G. Martinez (LNCMI-CNRS, Grenoble, France), M. Orlita, C. Faugeras (LNCMI-CNRS, Grenoble, France). Local conatct: M. Orlita.

*Magneto polaron effect in CdTe quantum wells with high mobility electron gas.*
M. Orlita (LNCMI-CNRS, Grenoble, France), M. Potemski, C. Faugeras (LNCMI-CNRS, Grenoble, France).

*Raman scattering of graphite in high magnetic fields.*
C. Faugeras (LNCMI-CNRS, Grenoble, France), M. Potemski, P. Kossacki (LNCMI-CNRS, Grenoble, France).

*Cyclotron resonance in HgTe/HgCdTe quantum wells at high magnetic fields.*

M. Orlita (LNCMI-CNRS, Grenoble, France), M. Potemski, G. Martinez, C. Faugeras (LNCMI-CNRS, Grenoble, France).

*Electrical transport phenomena in short period InAs/GaSb superlattices.*
L. Konczewicz (Groupe d'Etudes des Semiconducteurs, Université Montpellier 2, Montpellier, France), S. Contreras (Groupe d'Etudes des Semiconducteurs, Université Montpellier 2, Montpellier, France), Ph. Christol, J.B. Rodriguez, C. Cervera (Institut d'Electronique du Sud, Université Montpellier 2, Montpellier, France).

*Site-selected InAs/InP Quantum Dots in High Magnetic Fields.*
D. Dalacu (National Research Council of Canada, Ontario, Canada).

*Electron-phonon interaction in single doped GaInAs quantum well.*
G. Martinez (LNCMI-CNRS, Grenoble, France), M. Orlita (LNCMI-CNRS, Grenoble, France).

*Single-exciton energy shell structure in InAs/GaAs quantum dots.*
A.Babinski (University of Warsaw, Institute of Experimental Physics, Warszawa, Poland).

*Temperature dependance of the Quantum Hall effect in Graphene.*
E. Diez (Universidad de Salamanca, Laboratorio de Bajas Temperaturas, Salamanca, Spain), M. Amado (Universidad de Salamanca, Laboratorio de Bajas Temperaturas, Salamanca, Spain).

*Optical studies of single nanotubes.*
J. Alexander-Webber (Physics Department, Oxford University, UK), R. Nicholas (Physics Department, University of Oxford, UK).

*Novel coherent states in a quantum Hall trilayer system at Landau filling factor 1.*
G. Gusev (Instituto de Fisica da Universidade de Sao Paulo, Sao Paulo, Brasil), N. Churata Mamani (Instituto de Fisica da Universidade de Sao Paulo, Sao Paulo, Brasil), S. Wiedmann (LNCMI-CNRS, Grenoble, France).

*Effects of magnetic fields on excitonic features in optical spectra of $CuInS_2$ single crystals.*
M. Yakushev (University of Strathclyde, Department of Physics, Glasgow, United Kingdom).

*Tunnel spectroscopy of intersubband plasmons in two-dimensional electron gases.*
V. Popov (Institute of Microelectronics Technology of Russian Academy of Science, Chernogolovka, Moscow district, Russia).

*Landau level spectroscopy of graphene monolayer epitaxially grown on metallic surfaces.*
M. Orlita (LNCMI-CNRS, Grenoble, France), M. Potemski, G. Martinez, C. Faugeras (LNCMI-CNRS, Grenoble, France), A. Gruneis (University of Vienna, Vienna, Austria).

*ENDOR Spectroscopy of Magnetic Superlattices.*
A. Nogaret (University of Bath, Department of Physics, Bath, United Kingdom).

*Study of coupling in a self-assembles QD system.*
T. Kazimierczuk (University of Warsaw, Institute of Experimental Physics, Warsaw, Poland), P. Kossacki, M. Potemski, P. Plochocka (LNCMI-CNRS, Grenoble, France), M. Goryca (University of Warsaw, Institute of Experimental Physics, Warsaw, Poland).

*Magneto-optical properties of semiconductor quantum wells subject to in-plane electric field.*
J. Tucek (Institute of Physics, Faculty of Mathematics and Physics, Chares University, Prague, Czech Republic), R. Grill, M. Orlita (Charles University, Prague, Czech Republic), J. Kunc (LNCMI-CNRS, Grenoble, France), G.H. Dhler, S. Malzer (University of Erlangen-Nuremberg, Erlangen, Germany).

*Magnetotransport in high mobility electron gases on cylindrical surfaces.*
K.-J. Friedland (Paul-Drude Institute, Berlin, Germany).

*Magneto-Raman scattering of optical phonon in the graphene.*
P. Kossacki (LNCMI-CNRS, Grenoble, France), C. Faugeras, M. Potemski (LNCMI-CNRS, Grenoble, France).

*Magnetotransport in graphite.*
P. Vasek (Institute of Physics of the ASCR, Praha, Czech Republic), P. Svoboda, L. Smrcka, N. Goncharuk (Institute of Physics of the ASCR, Praha, Czech Republic).

*Polarized Raman Scattering of Bulk Graphite as a Probe for Electronic Excitations*
M. Amado (Universidad de Salamanca, Laboratorio de Bajas Temperaturas, Salamanca, Spain), C. Faugeras, P. Kossacki, M. Potemski (LNCMI-CNRS, Grenoble, France).

*Studies of Aharonov-Bohm effect on single antidot graphite structures.*
Y. Latyshev (Institute of Radio-Engineering and Electronics, RAS, Moscow, Russia), A. Orlov (Institute of Radio-Engineering and Electronics, RAS, Moscow, Russia), P. Monceau (Institut Néel-CNRS, Grenoble, France).

*Comparison of excitonic diamagnetic shift for vertical and lateral field geometry as a measure of wavefunction anisotropy.*
T. Kazimierczuk (University of Warsaw, Institute of Experimental Physics, Warsaw, Poland), P. Kossacki, M. Potemski, P. Plochocka (LNCMI-CNRS, Grenoble, France), M. Goryca (University of Warsaw, Institute of Experimental Physics, Warsaw, Poland).

*Polarized magneto-Raman scattering in the epitaxial graphene.*
M. Amado (Universidad de Salamanca, Laboratorio de Bajas Temperaturas, Salamanca, Spain), P. Kossacki, C. Faugeras, M. Potemski (LNCMI-CNRS, Grenoble, France).

*Magnetic field study of hybridized exciton states in pyramidal quantum dot molecules.*
Q. Zhu (Warsaw University, Faculty of Physics, Warsaw, Poland), A. Babinski (Warsaw University, Faculty of Physics, Warsaw, Poland), J. Szeszko (Laboratory of the Physics of Nanostructures, Ecole Polytechnique Fédérale de Lausanne, Lausanne, Switzerland).

*Field induced zero bias peak of interlayer tunneling conductance in graphite.*
Y. Latyshev (Institute of Radio-Engineering and Electronics, RAS, Moscow, Russia), A. Orlov (Institute of Radio-Engineering and Electronics, RAS, Moscow, Russia), P. Monceau (Institut Néel-CNRS, Grenoble, France).

**SOFT MATTER AND OTHERS**

*Basic Study on solidification of the Zn-30wt%Bi hypermonotectic alloy in high static field.*
Y. Zhong (Shanghai University, Shanghai, China), Y. Fautrelles (EPM Madylam, Grenoble, France), J. Wang (Shanghai University, Shanghai, China).

*Effect of a magnetic field on the dentrite morphology during solidification of Aluminium and Zinc-based alloys.*
Y. Fautrelle (SIMAP/EPM/INP, Grenoble, France), X. Li (Shanghai University, Shanghai, China).

*Hydrogen evolution in high magnetic field.*
P. Zabinski (AGH University of Science and Technology, Krakow, Poland), A. Jarek (AGH University of Science and Technology, Krakow, Poland).

*Experimental study of the flow around a cylinder under an imposed strong magnetic field*
O. Andreev (TU Ilmenau, Institute of Thermodynamics and Fluid Mechanics, Ilmenau, Germany).

*Electrocrystallization of iron group alloys under high intensity magnetic field.*
R. Kowalik (AGH University of Science and Technology, Krakow, Poland), A. Jarek (AGH University of Science and Technology, Krakow, Poland).

*Measurement of a 60 GHz ECR Ion Source prototype magnetic field.*
Th. Lamy (LPSC, Grenoble,France), M. Marie-Jeanne, L. Latrasse, Th. Thuillier, P. Sole, Ch. Fourel, J. Giraud, J.L. Vieux Rochaz, J. Jacob (LPSC, Grenoble, France).

*Effect of a magnetic field on the dendrite morphology during solidification of Aluminium and Zinc-based alloys.*
Y. Fautrelle (SIMAP/EPM/INP, Grenoble, France), X. Li (Shanghai University, Shanghai, China).

# PhD Theses 2010

1. Petr Neugebauer
   *Development of heterodyne high field / high frequency electron paramagnetic resonance spectrometer at 285 GHz.*
   Doctorat de l'Université Joseph Fourier, Grenoble
   Thèse soutenue le vendredi 15 janvier 2010

2. Steffen Wiedmann
   *Novel transport properties in multilayer electron systems.*
   Doctorat de l'Institut National des Sciences Appliquées, Toulouse.
   Thèse soutenue le vendredi 1 octobre 2010

3. Johannes Schneider
   *Electronic properties of graphite*
   Doctorat de l'Université Joseph Fourier, Grenoble
   Thèse soutenue le mardi 26 octobre 2010

4. Jean-Baptiste Dubois
   *Conducteurs nanocomposites métalliques élaborés par déformation plastique sévre ; formation et stabilité thermo-mécanique des nanostructures, propriétés induites*
   Doctorat de l'Université de Poitiers (Thèse en co-tutelle entre le LNCMI-Toulouse et le PHYMAT-Poitiers)
   Thèse soutenue le mardi 14 décembre 2010

# List of Publications 2010


[1] H. Alloul, F. Rullier-Albenque, B. Vignolle, D. Colson, and A. Forget, "Superconducting fluctuations, pseudogap and phase diagram in cuprates," Europhysics Letters **91**, 37005 (2010).

[2] M. Amado, E. Diez, D. Lopez-Romero, F. Rossella, J. M. Caridad, F. Dionigi, V. Bellani, and D. K. Maude, "Plateau-insulator transition in graphene," New Journal Of Physics **12**, 053004 (2010).

[3] Veronique Anton-Leberre, Evert Haanappel, Nathalie Marsaud, Lidwine Trouilh, Laurent Benbadis, Helian Boucherie, Sophie Massou, and Jean M. Franois, "Exposure to high static or pulsed magnetic fields does not affect cellular processes in the yeast Saccharomyces cerevisiae," Bioelectromagnetics **31**, 28–38 (2010).

[4] A. B. Antunes, C. Moure, A. Moure, and O. Pena, "Field-Induced Transitions in $RECo_{0.50}Mn_{0.50}O_3$ (RE = Dy, Eu)," Journal Of Low Temperature Physics **159**, 114–117 (2010), 9th International Conference on Research in High Magnetic Fields (RHMF 2009), Dresden, Germany, Jul 22-25, 2009.

[5] A. Balan, R. Kumar, M. Boukhicha, O. Beyssac, J. C. Bouillard, D. Taverna, W. Sacks, M. Marangolo, E. Lacaze, R. Gohler, W. Escoffier, J. M. Poumirol, and A. Shukla, "Anodic bonded graphene," Journal of Physics D-Applied Physics **43**, 374013 (2010).

[6] R. Battesti, M. Fouché, C. Detlefs, T. Roth, P. Berceau, F. Duc, P. Frings, G. L. J. A. Rikken, and C. Rizzo, "Photon Regeneration Experiment for Axion Search Using X-Rays," Physical Review Letters **105**, 250405 (2010).

[7] E. Belandria, M. Millot, J. M. Broto, E. Flahaut, F. Rodriguez, R. Valiente, and J. Gonzalez, "Pressure dependence of Raman modes in double wall carbon nanotubes filled with 1D Tellurium," Carbon **48**, 2566–2572 (2010).

[8] P. Berceau, M. Fouche, R. Battesti, F. Bielsa, J. Mauchain, and C. Rizzo, "Dynamical behaviour of birefringent Fabry-Perot cavities," Applied Physics B-Lasers And Optics **100**, 803–809 (2010).

[9] Claire Berger, Jean-Yves Veuillen, Laurence Magaud, Pierre Mallet, Valerio Olevano, M. Orlita, P. Plochocka, C. Faugeras, G. Martinez, Marek Potemski, Cecile Naud, Laurent P. Levy, and Didier Mayou, "Electronic properties of epitaxial graphene," International Journal Of Nanotechnology **7**, 383–402 (2010).

[10] Daniel Bourgault, Jeremy Tillier, Pierre Courtois, Denis Maillard, and Xavier Chaud, "Large inverse magnetocaloric effect in $Ni_{45}Co_5Mn_{37.5}In_{12.5}$ single crystal above 300 K," Applied Physics Letters **96**, 132501 (2010).

[11] A. Bourquard, D. Bresson, A. Daël, F. Debray, P. Fazilleau, B. Hervieu, W. Joss, F. P. Juster, C. Mayri, P. Pugnat, J. M. Rifflet, L. Ronayette, and C. Trophime, "A new design for the superconducting outsert of the GHMFL 42+T hybrid magnet project," IEEE Transactions on Applied Superconductivity **20**, 684 (2010).

[12] A. Bourquard, D. Bresson, A. Daël, F. Debray, P. Fazilleau, B. Hervieu, W. Joss, F. P. Juster, C. Mayri, P. Pugnat, J. M. Rifflet, L. Ronayette, C. Trophime, C. Verwaerde, and L. Villars, "The 42+T Hybrid Magnet Project at CNRS-LNCMI-Grenoble," Journal Of Low Temperature Physics **159**, 332–335 (2010), 9th International Conference on Research in High Magnetic Fields (RHMF 2009), Dresden, GERMANY, JUL 22-25, 2009.

[13] Daniel Braithwaite, Gerard Lapertot, William Knafo, and Ilya Sheikin, "Evidence for Anisotropic Vortex Dynamics and Pauli Limitation in the Upper Critical Field of $FeSe_{1-x}Te_x$," Journal Of The Physical Society Of Japan **79**, 053703 (2010).

[14] S. de Brion, M. Bonda, C. Darie, P. Bordet, and I. Sheikin, "Magnetic phase diagram of the S=1/2 triangular layered compound $NaNiO_2$: a single crystal study," Journal Of Physics-Condensed Matter **22**, 126001 (2010).

[15] L. Bryja, A. Wojs, J. Jadczak, J. Misiewicz, P. Plochocka, D. Maude, M. Potemski, D. Reuter, and A. Wieck, "Signature of Singlet-Triplet Crossing in PL in GaAs QW's," AIP Conference Proceedings **1199**, 247–248 (2010).

[16] E. Buet, J. Dubois, P. Olier, L. Thilly, F. Lecouturier, and P. Renault, "Microstructure and texture of copper/niobium composites processed by ECAE," International Journal of Material Forming **3**, 1071–1074 (2010).

[17] Haitao Cao, X. Chaud, J. G. Noudem, Cuiping Zhang, Rui Hu, Jinshan Li, and Lian Zhou, "Mechanism of seeded infiltration growth process analysed by magnetic susceptibility measurements and in situ observation," Ceramics International **36**, 1383–1388 (2010).

[18] J. Chang, R. Daou, Cyril Proust, David LeBoeuf, Nicolas Doiron-Leyraud, Francis Laliberte, B. Pingault, B. J. Ramshaw, Ruixing Liang, D. A. Bonn, W. N. Hardy, H. Takagi, A. B. Antunes, I. Sheikin, K. Behnia, and Louis Taillefer, "Nernst and Seebeck Coefficients of the Cuprate Superconductor $YBa_2Cu_3O_{6.67}$: A Study of Fermi Surface Reconstruction," Physical Review Letters **104**, 057005 (2010).

[19] C. N. Chinnasamy, J. M. Greneche, M. Guillot, B. Latha, T. Sakai, C. Vittoria, and V. G. Harris, "Structural and size dependent magnetic properties of single phase nanostructured Gadolinium-Iron-garnet under high magnetic field of 32 Tesla," Journal Of Applied Physics **107**, 09A512 (2010), 11th Joint MMM-Intermag Conference, Washington, DC, Jan 18-22, 2010.

[20] E. Cizmar, M. Ozerov, J. Wosnitza, B. Thielemann, K. W. Kraemer, Ch. Rueegg, O. Piovesana, M. Klanjsek, M. Horvatic, C. Berthier, and S. A. Zvyagin, "Anisotropy of magnetic interactions in the spin-ladder compound $(C_5H_{12}N)_2CuBr_4$," Physical Review B **82**, 054431 (2010).

[21] C. V. Colin, O. Isnard, and M. Guillot, "High magnetic field study of the anisotropy and neutron diffraction investigation of the crystal and magnetic structure of $YCo_{4.5}Ge_{0.5}$," Journal Of Alloys And Compounds **505**, 11–16 (2010).

[22] Arnaud Comment, Hadrien Mayaffre, Vesna Mitrović, Mladen Horvatić, Claude Berthier, Béatrice Grenier, and Patrice Millet, "NMR and NQR study of the tetrahedral frustrated quantum spin system $Cu_2Te_2O_5Br_2$ in its paramagnetic phase," Physical Review B **82**, 214416 (2010).

[23] R. Daou, J. Chang, D. LeBoeuf, O. Cyr-Choiniere, F. Laliberte, N. Doiron-Leyraud, B. J. Ramshaw, R. X. Liang, D. A. Bonn, W. N. Hardy, and L. Taillefer, "Broken rotational symmetry in the pseudogap phase of a high-$T_c$ superconductor," Nature **463**, 519–522 (2010).

[24] T. A. Dauzhenka, V. K. Ksenevich, I. A. Bashmakov, and J. Galibert, "Evidence of two-dimensional weak localization in polycrystalline $SnO_2$ films by high field magnetoconductance study," Journal of Low Temperature Physics **159**, 212–215 (2010).

[25] F. Debray, J. Dumas, S. Labbé-Lavigne, R. Pfister, C. Trophime, N. Vidal, F. Wilhelm, and M. Enderle, "Design study of High Field Resistive Magnets for Diffraction Experiments," IEEE Trans. on Appl. Superconduc. **20**, 664 (2010).

[26] Jan Dreiser, Oliver Waldmann, Graham Carver, Christopher Dobe, Hans-Ulrich Guedel, Hogni Weihe, and Anne-Laure Barra, "High-Frequency Electron-Spin-Resonance Study of the Octanuclear Ferric Wheel $CsFe_8$," Inorganic Chemistry **49**, 8729–8735 (2010).

[27] L. Drigo, F. Durantel, A. Audouard, and G. Ballon, "Tunnel diode oscillator-based measurement of quantum oscillations amplitude in pulsed high magnetic fields: a quantitative field-dependent study," The European Physical Journal - Applied Physics **52**, 10401 (2010).

[28] J.B. Dubois, L. Thilly, P.O. Renault, F. Lecouturier, and M. Di Michiel, "Thermal stability of nanocomposite metals: In situ observation of anomalous residual stress relaxation during annealing under synchrotron radiation," Acta Materialia **58**, 6504–6512 (2010).

[29] F. Duc, J. Vanacken, G. Zhang, W. Decelle, J. E. Lorenzo, C. Detlefs, C. Strohm, T. Roth, R. Suryanarayanan, P. Frings, and G. L. J. A. Rikken, "Direct evidence of magnetostructural phase separation in the electron-doped manganite $Ca_{0.8}Sm_{0.16}Nd_{0.04}MnO_3$ by means of high magnetic field studies," Physical Review B **82**, 054105 (2010).

[30] W. Escoffier, J. Poumirol, R. Yang, M. Goiran, B. Raquet, and J. Broto, "Electric field doping of few-layer graphene," Physica B-Condensed Matter **405**, 1163–1167 (2010).

[31] Clement Faugeras, Blaise Faugeras, Milan Orlita, M. Potemski, Rahul R. Nair, and A. K. Geim, "Thermal Conductivity of Graphene in Corbino Membrane Geometry," ACS Nano **4**, 1889–1892 (2010).

[32] C. Faugeras, P. Kossacki, D. M. Basko, M. Amado, M. Sprinkle, C. Berger, W. A. de Heer, and M. Potemski, "Effect of a magnetic field on the two-phonon Raman scattering in graphene," Physical Review B **81**, 155436 (2010).

[33] O. M. Fedorych, M. Potemski, S. A. Studenikin, J. A. Gupta, Z. R. Wasilewski, and I. A. Dmitriev, "Quantum oscillations in the microwave magnetoabsorption of a two-dimensional electron gas," Physical Review B **81**, 201302 (2010).

[34] J. Flouquet, D. Aoki, W. Knafo, G. Knebel, T. Matsuda, S. Raymond, C. Proust, C. Paulsen, and P. Haen, "Convergence of the enhancement of the effective mass under pressure and magnetic field in heavy-fermion compounds: $CeRu_2Si_2$, $CeRh_2Si_2$, and $CeIn_3$," Journal of Low Temperature Physics **161**, 83–97 (2010).

[35] J. Y. Fortin and A. Audouard, "Random walks and magnetic oscillations in compensated metals," Physical Review B **80**, 214407 (2009).

[36] M. Goiran, M. Millot, J. M. Poumirol, I. Gherasoiu, W. Walukiewicz, and J. Leotin, "Electron cyclotron effective mass in indium nitride," Applied Physics Letters **96**, 052117 (2010).

[37] M. Goryca, P. Plochocka, T. Kazimierczuk, P. Wojnar, G. Karczewski, J. A. Gaj, M. Potemski, and P. Kossacki, "Brightening of dark excitons in a single CdTe quantum dot containing a single $Mn^{2+}$ ion," Phys. Rev. B **82**, 165323 (2010).

[38] D. S. Grachtrup, M. Bleckmann, S. Sullow, B. Willenberg, H. Rakoto, Y. Skourski, and J. A. Mydosh, "High field magnetization of $UPt_2Si_2$," Journal of Low Temperature Physics **159**, 147–150 (2010).

[39] M. Guillot, V. Paul-Boncour, and T. Leblond, "Magnetic properties of $Y_{0.7}Er_{0.3}Fe_2(H,D)_{4.2}$ compounds under continuous magnetic field up to 35 Tesla," Journal Of Applied Physics **107**, 09E144 (2010), 11th Joint MMM-Intermag Conference, Washington, DC, Jan 18-22, 2010.

[40] G. M. Gusev, E. B. Olshanetsky, Z. D. Kvon, N. N. Mikhailov, S. A. Dvoretsky, and J. C. Portal, "Quantum hall effect near the charge neutrality point in a two-dimensional electron-hole system," Physical Review Letters **104**, 166401 (2010).

[41] G. M. Gusev, Yu. A. Pusep, A. K. Bakarov, A. I. Toropov, and J. C. Portal, "Magnetic-field-induced transition in a wide parabolic well superimposed with a superlattice," Physical Review B **81**, 165302 (2010).

[42] Walt A. de Heer, Claire Berger, Xiaosong Wu, Mike Sprinkle, Yike Hu, Ming Ruan, Joseph A. Stroscio, Phillip N. First, Robert Haddon, Benjamin Piot, Clement Faugeras, Marek Potemski, and Jeong-Sun Moon, "Epitaxial graphene electronic structure and transport," Journal Of Physics D-Applied Physics **43**, 374007 (2010).

[43] T. Helm, M. V. Kartsovnik, I. Sheikin, M. Bartkowiak, F. Wolff-Fabris, N. Bittner, W. Biberacher, M. Lambacher, A. Erb, J. Wosnitza, and R. Gross, "Magnetic Breakdown in the Electron-Doped Cuprate Superconductor $Nd_{2-x}Ce_xCuO_4$: The Reconstructed Fermi Surface Survives in the Strongly Overdoped Regime," Phys. Rev. Lett. **105**, 247002 (2010).

[44] Ko-ichi Hiraki, Masatsugu Kitahara, Toshihiro Takahashi, Hadrien Mayaffre, Mladen Horvatic, Claude Berthier, Shinya Uji, Hisashi Tanaka, Biao Zhou, Akiko Kobayashi, and Hayao Kobayashi, "Evidence of Charge Disproportionation in lambda Type BETS Based Organic Superconductors," Journal Of The Physical Society Of Japan **79**, 074711 (2010).

[45] A. Ikonnikov, S. Krishtopenko, V. Gavrilenko, Y. Sadofyev, Y. Vasilyev, M. Orlita, and W. Knap, "Splitting of Cyclotron Resonance Line in InAs/AlSb QW Heterostructures in High Magnetic Fields: Effects of Electron-Electron and Electron-Phonon Interaction," Journal Of Low Temperature Physics **159**, 197–202 (2010), 9th International Conference on Research in High Magnetic Fields (RHMF 2009), Dresden, Germany, Jul 22-25, 2009.

[46] J. Jadczak, L. Bryja, P. Plochocka, A. Wojs, J. Misiewicz, M. Potemski D. Maude, D. Reuter, and A. Wieck, "The observation of exciton-cyclotron resonance in photoluminescence spectra of a two dimensional hole gas," Journal of Physics: Conference Series **210**, 012043 (2010).

[47] Johannes Jobst, Daniel Waldmann, Florian Speck, Roland Hirner, Duncan K. Maude, Thomas Seyller, and Heiko B. Weber, "Quantum oscillations and quantum Hall effect in epitaxial graphene," Physical Review B **81**, 195434 (2010).
[48] T. Jungwirth, P. Horodyská, N. Tesařová, P. Němec, J. Šubrt, P. Malý, P. Kužel, C. Kadlec, J. Mašek, I. Němec, M. Orlita, V. Novák, K. Olejník, Z. Šobáň, P. Vašek, P. Svoboda, and Jairo Sinova, "Systematic Study of Mn-Doping Trends in Optical Properties of (Ga,Mn)As," Physical Review Letters **105**, 227201 (2010).
[49] T. Kazimierczuk, A. Golnik, P. Wojnar, J. A. Gaj, and P. Kossacki, "Clustering in a self-assembled CdTe/ZnTe quantum dot plane revealed by inter-dot coupling," Physica Status Solidi B-Basic Solid State Physics **247**, 1409–1412 (2010).
[50] T. Kazimierczuk, M. Goryca, M. Koperski, A. Golnik, J. A. Gaj, M. Nawrocki, P. Wojnar, and P. Kossacki, "Picosecond charge variation of quantum dots under pulsed excitation," Physical Review B **81**, 155313 (2010).
[51] L. Kilanski, M. Gorska, W. Dobrowolski, E. Dynowska, M. Wojcik, B. J. Kowalski, J. R. Anderson, C. R. Rotundu, D. K. Maude, S. A. Varnavskiy, I. V. Fedorchenko, and S. F. Marenkin, "Magnetism and magnetotransport of strongly disordered $Zn_{1-x}Mn_xGeAs_2$ semiconductor: The role of nanoscale magnetic clusters," Journal of Applied Physics **108**, 073925 (2010).
[52] M. Klanjsek, H. Mayaffre, C. Berthier, M. Horvatic, B. Chiari, O. Piovesana, P. Bouillot, C. Kollath, E. Orignac, R. Citro, and T. Giamarchi, "Luttinger liquid physics in the spin ladder material $CuBr_4(C_5H_{12}N)_2$," Physica Status Solidi B-Basic Solid State Physics **247**, 656–658 (2010), International Conference on Quantum Criticality and Novel Phases, Dresden, Germany, Aug 02-05, 2009.
[53] T. Klein, D. Braithwaite, A. Demuer, W. Knafo, G. Lapertot, C. Marcenat, P. Rodière, I. Sheikin, P. Strobel, A. Sulpice, and P. Toulemonde, "Thermodynamic phase diagram of $Fe(Se_{0.5}Te_{0.5})$ single crystals in fields up to 28 tesla," Phys. Rev. B **82**, 184506 (2010).
[54] W. Knafo, D. Aoki, D. Vignolles, B. Vignolle, Y. Klein, C. Jaudet, A. Villaume, C. Proust, and J. Flouquet, "High-field metamagnetism in the antiferromagnet $CeRh_2Si_2$," Physical Review B **81**, 094403 (2010).
[55] Peter Kopcansky, Natalia Tomasovicova, Martina Koneracka, Milan Timko, Vlasta Zavisova, Nandor Eber, Katalin Fodor-Csorba, Tibor Toth-Katona, Aniko Vajda, Jan Jadzyn, Eric Beaugnon, and Xavier Chaud, "The structural instabilities in ferronematic based on liquid crystal with negative diamagnetic susceptibility anisotropy," Journal Of Magnetism And Magnetic Materials **322**, 3696–3700 (2010).
[56] G. Koutroulakis, M. D. Stewart, Jr., V. F. Mitrovic, M. Horvatic, C. Berthier, G. Lapertot, and J. Flouquet, "Field Evolution of Coexisting Superconducting and Magnetic Orders in $CeCoIn_5$," Physical Review Letters **104**, 087001 (2010).
[57] K. Kowalik, F. J. Teran, P. Plochocka, J. Kunc, D. K. Maude, M. Potemski, K. J. Friedland, R. Hey, K. H. Ploog, G. Karczewski, and T. Wojtowicz, "Exchange driven spin splitting of fully occupied Landau levels measured using polarization resolved photoluminescence spectroscopy," AIP Conference Proceedings **1199**, 249–250 (2010).
[58] R. B. G. Kramer, V. S. Egorov, A. G. M. Jansen, and W. Joss, "Condon-domain phase diagram and hysteresis size for beryllium," Physical Review B **82**, 075101 (2010).
[59] A. Kumar, J. M. Poumirol, W. Escoffier, M. Goiran, B. Raquet, and J. C. Pivin, "High magnetic field induced charge density waves and sign reversal of the Hall coefficient in graphite," Journal of Physics-condensed Matter **22**, 436004 (2010).
[60] J. Kunc, K. Kowalik, F. J. Teran, P. Plochocka, B. A. Piot, D. K. Maude, M. Potemski, V. Kolkovsky, G. Karczewski, and T. Wojtowicz, "Enhancement of the spin gap in fully occupied two-dimensional Landau levels," Physical Review B **82**, 115438 (2010).
[61] A. Laslo, C. V. Colin, O. Isnard, and M. Guillot, "Effect of the M/Co substitution on magnetocrystalline anisotropy and magnetization in $SmCo_{5-x}M_x$ compounds (M=Ga;Al)," Journal Of Applied Physics **107**, 09A732 (2010), 11th Joint MMM-Intermag Conference, Washington, DC, Jan 18-22, 2010.
[62] L. Latrasse, M. Marie-Jeanne, T. Lamy, T. Thuillier, J. Giraud, C. Fourel, C. Trophime, F. Debray, P. Sala, and J. Dumas, "SEISM: A 60 GHz cusp electron cyclotron resonance ion source," Review Of Scientific Instruments **81**, 02A324 (2010), 13th International Conference on Ion Sources (ICIS'09), Gatlinburg, TN, SEP 20-25, 2009.
[63] Y.U. I. Latyshev, A.P. Orlov, E.G. Shustin, N.V. Isaev, W. Escoffier, P. Monceau, C.J. van der Beek, M. Konczykowski, and I. Monnet, "Aharonov-Bohm effect on columnar defects in thin graphite and graphene," Journal of Physics: Conference Series **248**, 012001 (2010).
[64] F. Luckert, M. V. Yakushev, C. Faugeras, A. V. Karotki, A. V. Mudryi, and R. W. Martin, "Diamagnetic shift of the A free exciton in $CuGaSe_2$ single crystals," Applied Physics Letters **97**, 162101 (2010).
[65] T. T. A. Lummen, C. Strohm, H. Rakoto, and P. H. M. van Loosdrecht, "Mapping the magnetic phase diagram of the frustrated metamagnet $CuFeO_2$," Physical Review B **81**, 224420 (2010).
[66] M. Matsuda, K. Ohoyama, S. Yoshii, H. Nojiri, P. Frings, F. Duc, B. Vignolle, G. L. J. A. Rikken, L. P. Regnault, S. H. Lee, H. Ueda, and Y. Ueda, "Universal magnetic structure of the half-magnetization phase in Cr-based spinels," Physical Review Letters **104**, 047201 (2010).
[67] M. Millot, J. M. Broto, S. George, J. Gonzalez, and A. Segura, "Electronic structure of indium selenide probed by magnetoabsorption spectroscopy under high pressure," Physical Review B **81**, 205211 (2010).
[68] M. Millot, J. M. Broto, J. Gonzalez, and F. Rodriguez, "Trigonal field acting at the $Cr^{3+}$ $^2E$ states in ruby from magneto-optical measurements under high pressure," Physical Review B **81**, 075120 (2010).
[69] M. Millot, S. George, F. Hatami, W. T. Masselink, J. Leotin, J. Gonzalez, and J. M. Broto, "Photoluminescence of InP/GaP quantum dots under extreme conditions," High Pressure Research **29**, 488–494 (2009).
[70] M. Millot, R. Tena-Zaera, V. Munoz-Sanjose, J. M. Broto, and J. Gonzalez, "Anharmonic effects in ZnO optical phonons probed by Raman spectroscopy," Applied Physics Letters **96**, 152103 (2010).
[71] O. A. Mironov, M. Goiran, J. Galibert, D. V. Kozlov, A. V. Ikonnikov, K. E. Spirin, V. I. Gavrilenko, G. Isella, M. Kummer, H. von Kanel, O. Drachenko, M. Helm, J. Wosnitza, R. J. H. Morris, and D. R. Leadley, "Cyclotron resonance of extremely conductive 2D holes in high Ge content strained heterostructures," Journal of Low Temperature Physics **159**, 216–221 (2010).

[72] D. Molter, F. Ellrich, T. Weinland, S. George, M. Goiran, F. Keilmann, R. Beigang, and J. Léotin, "High-speed terahertz time-domain spectroscopy of cyclotron resonance in pulsed magnetic field," Optics Express **18**, 26163 (2010).
[73] S. Nanot, R. Avriller, W. Escoffier, J. M. Broto, S. Roche, and B. Raquet, "Propagative Landau states and Fermi level pinning in carbon nanotubes," Physical Review Letters **103**, 256801 (2009).
[74] S. Nanot, M. Millot, B. Raquet, J. M. Broto, A. Magrez, and J. Gonzalez, "Doping dependence of the G-band Raman spectra of an individual multiwall carbon nanotube," Physica E-Low-Dimensional Systems & Nanostructures **42**, 2466–2470 (2010).
[75] P. Neugebauer and A. L. Barra, "New cavity design for Broad-band Quasi-Optical HF-EPR spectroscopy," Appl. Magn. Reson **37**, 833 (2010).
[76] A. Nogaret, J. C. Portal, H. E. Beere, D. A. Ritchie, and C. Phillips, "Microwave Induced Forward Scattering in a Multi-channel Magnetically Confined Quantum Wire," AIP Conference Proceedings **1199**, 345 (2010).
[77] A. Nogaret, P. Saraiva, B. Dai, and J. C. Portal, "Control of spin currents with double spin resonance," Physica E-Low-Dimensional Systems & Nanostructures **42**, 926–928 (2010), 18th International Conference on Electronic Properties of Two-Dimensional Systems, Kobe, Japan, Jul 19-24, 2009.
[78] Lucie Norel, Lise-Marie Chamoreau, and Cyrille Train, "Modulation of intermolecular exchange interaction in organic radical based compounds: Magneto-structural analysis of phenol and imidazolium substituted oxoverdazyl radicals," Polyhedron **29**, 342 (2010), 2009 Young Investigator Special Issue.
[79] H. Ohta, O. Portugall, N. Ubrig, M. Fujisawa, H. Katsuno, E. Fatma, S. Okubo, and Y. Fujiwara, "Photoluminescence measurement of Er,O-Codoped GaAs under a pulsed magnetic field up to 60 T," Journal of Low Temperature Physics **159**, 203–207 (2010).
[80] E. B. Olshanetsky, Z. D. Kvon, G. M. Gusev, N. N. Mikhailov, S. A. Dvoretsky, and J. C. Portal, "Weak antilocalization in HgTe quantum wells near a topological transition," JETP Letters **91**, 347–350 (2010).
[81] Olivier Oms, Jean-Baptiste Rota, Lucie Norel, Carmen J. Calzado, Rousselière, Héléne, Cyrille Train, and Vincent Robert, "Beyond kahn's model: Substituent and heteroatom influence on exchange interaction in a metal-verdazyl complex," Eur. J. Inorg. Chem. (2010).
[82] M. Orlita, C. Faugeras, G. Martinez, S. A. Studenikin, and P. J. Poole, "Electron-phonon interactions in a single modulation-doped GaInAs quantum well," Euro Phys. Lett. **92**, 37002 (2010).
[83] M. Orlita and M. Potemski, "Dirac electronic states in graphene systems: optical spectroscopy studies," Semiconductor Science And Technology **25**, 063001 (2010).
[84] Emilio Pardo, Cyrille Train, Rodrigue Lescouezec, Kamal Boubekeur, Eliseo Ruiz, Francesc Lloret, and Michel Verdaguer, "Synthesis, crystal structure and magnetic properties of two oxalato-bridged dimetallic trinuclear complexes combined with a polar cation," Dalton Transactions **39**, 4951–4958 (2010).
[85] Emilio Pardo, Cyrille Train, Rodrigue Lescouezec, Yves Journaux, Jorge Pasan, Catalina Ruiz-Perez, Fernando S. Delgado, Rafael Ruiz-Garcia, Francesc Lloret, and Carley Paulsen, "Single chain magnet behaviour in an enantiopure chiral cobalt(II)-copper(II) one-dimensional compound," Chemical Communications **46**, 2322–2324 (2010).
[86] A. Patanè, N. Mori, O. Makarovsky, L. Eaves, M. L. Zambrano, J. C. Arce, L. Dickinson, and D. K. Maude, "Manipulating and Imaging the Shape of an Electronic Wave Function by Magnetotunneling Spectroscopy," Phys. Rev. Lett. **105**, 236804 (2010).
[87] O. Pena, A. B. Antunes, V. Gil, C. Moure, and S. de Brion, "Spin reversal, magnetic domains and relaxation mechanisms in Er(Co,Mn)$O_3$ perovskites," Thin Solid Films **518**, 5666–5669 (2010), International Symposium on Functional Materials for Non-Volatile Memories, Beijing, Peoples R China, Sep 03-05, 2007.
[88] J. A. A. J. Perenboom, P. Frings, J. Beard, B. Bansal, F. Herlach, T. Peng, and S. Zherlitsyn, "Optimization of large multiple coil systems for pulsed magnets," Journal of Low Temperature Physics **159**, 336–340 (2010).
[89] A. P. Petrovic, Y. Fasano, R. Lortz, C. Senatore, A. Demuer, A. B. Antunes, A. Pare, D. Salloum, P. Gougeon, M. Potel, and O. Fischer, "Real-Space Vortex Glass Imaging and the Vortex Phase Diagram of $SnMo_6S_8$," Physical Review Letters **103**, 257001 (2009).
[90] B. A. Piot, J. Kunc, M. Potemski, D. K. Maude, C. Betthausen, A. Vogl, D. Weiss, G. Karczewski, and T. Wojtowicz, "Fractional quantum Hall effect in CdTe," Physical Review B **82**, 081307 (2010).
[91] Fabrice Pointillart, Kamal Boubekeur, Patrick Herson, and Cyrille Train, "Barium one-dimensional coordination polymers from barium $\beta$-diketonates and 2,2'-bipyrimidine derivatives," CrystEngComm. **12**, 3430–3436 (2010).
[92] J. M. Poumirol, A. Cresti, S. Roche, W. Escoffier, M. Goiran, X. R. Wang, X. L. Li, H. J. Dai, and B. Raquet, "Edge magnetotransport fingerprints in disordered graphene nanoribbons," Physical Review B **82**, 041413 (2010).
[93] J. M. Poumirol, W. Escoffier, A. Kumar, M. Goiran, B. Raquet, and J. M. Broto, "Electron-hole coexistence in disordered graphene probed by high-field magneto-transport," New Journal of Physics **12**, 083006 (2010).
[94] J. M. Poumirol, W. Escoffier, A. Kumar, B. Raquet, and M. Goiran, "Impact of disorder on the $\nu$=2 quantum Hall plateau in graphene," Physical Review B **82**, 121401 (2010).
[95] T. A. Prikhna, W. Gawalek, Ya. M. Savchuk, N. V. Sergienko, V. E. Moshchil, V. Sokolovsky, J. Vajda, V. N. Tkach, F. Karau, H. Weber, M. Eisterer, A. Joulain, J. Rabier, X. Chaud, M. Wendt, J. Dellith, N. I. Danilenko, T. Habisreuther, S. N. Dub, V. Meerovich, D. Litzkendorf, P. A. Nagorny, L. K. Kovalev, Ch. Schmidt, V. S. Melnikov, A. P. Shapovalov, A. V. Kozyrev, V. B. Sverdun, J. Kosa, and A. V. Vlasenko, "Nanostructural Superconducting Materials for Fault Current Limiters and Cryogenic Electrical Machines," Acta Physica Polonica A **117**, 7–14 (2010), International Scientific Workshop on Oxide Materials for Electronic Engineering Fabrication, Properties and Applications, Lviv, Ukraine, JUN 22-26, 2009.
[96] Pascal Puech, Sbastien Nanot, Bertrand Raquet, Jean-Marc Broto, Marius Millot, Abdul Waheed Anwar, Emmanuel Flahaut, and Wolfgang Bacsa, "Comparative raman spectroscopy of individual and bundled double wall carbon nanotubes," Physica Status Solidi B , 1–6 (2010).
[97] D. Raabe, P.-P. Choi, Y. Li, A. Kostka, X. Sauvage, F. Lecouturier, K. Hono, R. Kirchheim, R. Pippan, and D. Embury, "Metallic composites processed via extreme deformation: Toward the limits of strength in bulk materials,"

MRS Bulletin **35**, 982 (2010).

[98] S. Raymond, W. Knafo, J. Flouquet, F. Bourdarot, and P. Lejay, "Quantum criticality of $Ce_{1-x}La_xRu_2Si_2$: The magnetically ordered phase," Physica Status Solidi B-Basic Solid State Physics **247**, 700–702 (2010).

[99] C. Rizzo, A. Dupays, R. Battesti, M. Fouche, and G. L. J. A. Rikken, "Inverse Cotton-Mouton effect of the vacuum and of atomic systems," Europhysics Letters **90**, 64003 (2010).

[100] Maria Jesus Rodriguez-Douton, Andrea Cornia, Roberta Sessoli, Lorenzo Sorace, and Anne-Laure Barra, "Introduction of ester and amido functions in tetrairon(III) single-molecule magnets: synthesis and physical characterization," Dalton Transactions **39**, 5851–5859 (2010).

[101] Jean-Baptiste Rota, Carmen J. Calzado, Cyrille Train, and Vincent Robert, "Microscopic origins of the ferromagnetic exchange coupling in oxoverdazyl-based Cu(II) complex," Journal Of Chemical Physics **132**, 154702 (2010).

[102] P. M. C. Rourke, A. F. Bangura, C. Proust, J. Levallois, N. Doiron-Leyraud, D. LeBoeuf, L. Taillefer, S. Adachi, M. L. Sutherland, and N. E. Hussey, "Fermi-surface reconstruction and two-carrier model for the Hall effect in $YBa_2Cu_4O_8$," Physical Review B **82**, 020514 (2010).

[103] S. Sakarya, W. Knafo, N. H. van Dijk, Y. K. Huang, K. Prokes, C. Meingast, and H. von Lohneysen, "Characterization of the weak itinerant ferromagnetic order in single-crystalline UIr," Journal of the Physical Society of Japan **79**, 014702 (2010).

[104] J. M. Schneider, N. A. Goncharuk, P. Vasek, P. Svoboda, Z. Vyborny, L. Smrcka, M. Orlita, M. Potemski, and D. K. Maude, "Using magnetotransport to determine the spin splitting in graphite," Physical Review B **81**, 195204 (2010).

[105] J. M. Schneider, M. Orlita, M. Potemski, and D. K. Maude, "Comment on "Consistent Interpretation of the Low-Temperature Magnetotransport in Graphite Using the Slonczewski-Weiss-McClure 3D Band-Structure Calculations" Reply," Physical Review Letters **104**, 119702 (2010).

[106] J. Scola, W. Noun, E. Popova, A. Fouchet, Y. Dumont, N. Keller, P. Lejay, I. Sheikin, A. Demuer, and A. Pautrat, "Spin reorientation induced by a very high magnetic field in domain-structured $YFeO_3$ films: Emergence of perpendicular anisotropy," Physical Review B **81**, 174409 (2010).

[107] A. Serafin, A. I. Coldea, A. Y. Ganin, M. J. Rosseinsky, K. Prassides, D. Vignolles, and A. Carrington, "Anisotropic fluctuations and quasiparticle excitations in $FeSe_{0.5}Te_{0.5}$," Physical Review B **82**, 104514 (2010).

[108] Rikio Settai, Keisuke Katayama, Hiroshi Muranaka, Tetsuya Takeuchi, Arumugam Thamizhavel, Ilya Sheikin, and Y. Onuki, "Superconducting properties in $Rh_{17}S_{15}$ under magnetic field and pressure," Journal Of Physics And Chemistry Of Solids **71**, 700–703 (2010), 15th International Symposium on Intercalation Compounds, Beijing, Peoples R China, May 11-15, 2009.

[109] H. Shishido, A. F. Bangura, A. I. Coldea, S. Tonegawa, K. Hashimoto, S. Kasahara, P. M. C. Rourke, H. Ikeda, T. Terashima, R. Settai, Y. Onuki, D. Vignolles, C. Proust, B. Vignolle, A. McCollam, Y. Matsuda, T. Shibauchi, and A. Carrington, "Evolution of the Fermi surface of $BaFe_2(As_{1-x}P_x)_2$ on entering the superconducting dome," Physical Review Letters **104**, 057008 (2010).

[110] H. G. Silva, A. M. Pereira, J. M. Teixeira, J. M. Moreira, G. N. Kakazei, J. P. Araújo, Yu. G. Pogorelov, J. B. Sousa, M. E. Braga, B. Raquet, H. Rakoto, C. Gatel, E. Snoeck, S. Cardoso, and P. P. Freitas, "Magnetic field strength and orientation effects on co-fe discontinuous multilayers close to percolation," Physical Review B **82**, 144432 (2010).

[111] M. Stern, P. Plochocka, V. Umansky, D. K. Maude, M. Potemski, and I. Bar-Joseph, "Optical Probing of the Spin Polarization of the $\nu = 5/2$ Quantum Hall State," Physical Review Letters **105**, 096801 (2010).

[112] R. Stoyanova, A. L. Barra, M. Yoncheva, E. Zhecheva, E. Shinova, P. Tzvetkova, and S. Simova, "High-Frequency Electron Paramagnetic Resonance Analysis of the Oxidation State and Local Structure of Ni and Mn Ions in Ni,Mn-Codoped $LiCoO_2$," Inorganic Chemistry **49**, 1932–1941 (2010).

[113] Tetsuya Sugawara, Noriaki Kimura, Haruyoshi Aoki, Florence Levy, Ilya Sheikin, and Taichi Terashima, "Anomalous Behavior of the Upper-Critical-Field in Heavy-Fermion Superconductor $CeRhSi_3$," Journal Of The Physical Society Of Japan **79**, 063701 (2010).

[114] Masashi Takigawa, Takeshi Waki, Mladen Horvatic, and Claude Berthier, "Novel Ordered Phases in the Orthogonal Dimer Spin System $SrCu_2(BO_3)_2$," Journal Of The Physical Society Of Japan **79**, 011005 (2010).

[115] E. Tancini, M. J. Rodriguez-Douton, L. Sorace, A. L. Barra, R. Sessoli, and A. Cornia, "Slow Magnetic Relaxation from Hard-axis Metal Ions in Tetranuclear Single-Molecule Magnets," Chem. Eur. J. **16**, 10482 (2010).

[116] F. J. Teran, M. Potemski, D. K. Maude, T. Andrearczyk, J. Jaroszyński, T. Wojtowicz, and G. Karczewski, "Quantum Hall states under conditions of vanishing Zeeman energy," Physical Review B **82**, 245120 (2010).

[117] M. Tropeano, M. R. Cimberle, C. Ferdeghini, G. Lamura, A. Martinelli, A. Palenzona, I. Pallecchi, A. Sala, I. Sheikin, F. Bernardini, M. Monni, S. Massidda, and M. Putti, "Isoelectronic Ru substitution at the iron site in $SmFe_{1-x}Ru_xAsO_{0.85}F_{0.15}$ and its effects on structural, superconducting, and normal-state properties," Physical Review B **81**, 184504 (2010).

[118] N. Ubrig, J. Shaver, A. N. G. Parra-Vasquez, M. Pasquali, J. Kono, J. A. Fagan, and O. Portugall, "Dynamic alignment of single-walled carbon nanotubes in pulsed magnetic fields," Journal of Low Temperature Physics **159**, 262–266 (2010).

[119] R. Valiente, M. Millot, F. Rodriguez, J. Gonzalez, J. M. Broto, S. George, S. Garcia-Revilla, Y. Romanyuk, and M. Pollnau, "$Er^{3+}$ luminescence as a sensor of high pressure and strong external magnetic fields," High Pressure Research **29**, 748–753 (2009).

[120] P. Vasek, P. Svoboda, V. Novak, M. Cukr, Z. Vyborny, V. Jurka, J. Stuchlik, M. Orlita, and D. K. Maude, "Anisotropic Magnetoresistance of GaMnAs Ferromagnetic Semiconductors," Journal Of Superconductivity And Novel Magnetism **23**, 1161–1163 (2010).

[121] A. Vasiliev, O. Volkova, I. Presniakov, A. Baranov, G. Demazeau, J.-M. Broto, M. Millot, N. Leps, R. Klingeler, B. Buchner, M.B. Stone, and A. Zheludev, "Thermodynamic properties and neutron diffraction studies of silver ferrite $AgFeO_2$," Journal of Physics: Condensed Matter **22**, 016007 (2010).

[122] S. I. Vedeneev, B. A. Piot, and D. K. Maude, "Magnetic field dependence of the superconducting energy gap in $Bi_2Sr_2CaCu_2O_{8+\delta}$ probed using break-junction tunneling spectroscopy," Physical Review B **81**, 054501 (2010).

[123] Thengarai S. Venkatakrishnan, Shaon Sahoo, Nicolas Brefuel, Carine Duhayon, Carley Paulsen, Anne-Laure Barra, S. Ramasesha, and Jean-Pascal Sutter, "Enhanced Ion Anisotropy by Nonconventional Coordination Geometry: Single-Chain Magnet Behavior for a $[\{(Fe^{II}L\}_2\{Nb^{IV}(CN)_8\}]$ Helical Chain Compound Designed with Heptacoordinate $Fe^{II}$," Journal Of The American Chemical Society **132**, 6047–6056 (2010).

[124] Q.Y. Wang, G.F. Jiao, G.Q. Liu, X.M. Xiong, S.C. Yan, P.X. Zhang, A. Sulpice, E. Mossang, Y. Feng, and G. Yan, "Fabrication and properties of multifilamentary $MgB_2$ wires by in-situ powder-in-tube process," Physica C: Superconductivity **470**, 1415 (2010), proceedings of the 22nd International Symposium on Superconductivity (ISS 2009).

[125] Zhe Wang, Wu Shi, Hang Xie, Ting zhang, Ning Wang, Zikang Tang, Xixiang Zhang, Rolf Lortz, Ping Sheng, Ilya Sheikin, and Albin Demuer, "Superconducting resistive transition in coupled arrays of 4 Angstrom carbon nanotubes," Physical Review B **81**, 174530 (2010).

[126] S. Wiedmann, G. M. Gusev, O. E. Raichev, A. K. Bakarov, and J. C. Portal, "Microwave zero-resistance states in a bilayer electron system," Physical Review Letters **105**, 026804 (2010).

[127] S. Wiedmann, G. M. Gusev, O. E. Raichev, A. K. Bakarov, and J. C. Portal, "Crossover between distinct mechanisms of microwave photoresistance in bilayer systems," Physical Review B **81**, 085311 (2010).

[128] S. Wiedmann, G. M. Gusev, O. E. Raichev, A. K. Bakarov, and J. C. Portal, "Microwave induced magnetoresistance oscillations and inelastic scattering time in double quantum wells," Physica E-Low-Dimensional Systems & Nanostructures **42**, 1075–1077 (2010), 18th International Conference on Electronic Properties of Two-Dimensional Systems, Kobe, Japan, Jul 19-24, 2009.

[129] S. Wiedmann, G. M. Gusev, O. E. Raichev, A. K. Bakarov, and J. C. Portal, "Thermally activated intersubband scattering and oscillating magnetoresistance in quantum wells," Phys. Rev. B **82**, 165333 (2010).

[130] S. Wiedmann, N. C. Mamani, G. M. Gusev, O. E. Raichev, A. K. Bakarov, and J. C. Portal, "Integer and fractional microwave induced resistance oscillations in a 2D system with moderate mobility," Physica E-Low-Dimensional Systems & Nanostructures **42**, 1078–1080 (2010), 18th International Conference on Electronic Properties of Two-Dimensional Systems, Kobe, Japan, Jul 19-24, 2009.

[131] S. Wiedmann, N. C. Mamani, G. M. Gusev, O. E. Raichev, A. K. Bakarov, and J. C. Portal, "Magneto-intersubband oscillations in triple quantum wells," Physica E-Low-Dimensional Systems & Nanostructures **42**, 1088–1090 (2010), 18th International Conference on Electronic Properties of Two-Dimensional Systems, Kobe, Japan, Jul 19-24, 2009.

[132] A. M. Witowski, M. Orlita, R. Stępniewski, A. Wysmołek, J. M. Baranowski, W. Strupiński, C. Faugeras, G. Martinez, and M. Potemski, "Quasiclassical cyclotron resonance of Dirac fermions in highly doped graphene," Phys. Rev. B **82**, 165305 (2010).

[133] M. V. Yakushev, F. Luckert, C. Faugeras, A. V. Karotki, A. V. Mudryi, and R. W. Martin, "Excited states of the free excitons in $CuInSe_2$ single crystals," Applied Physics Letters **97**, 152110 (2010).

[134] Tomoka Yamaguchi, Jean-Pierre Costes, Yukana Kishima, Masaaki Kojima, Yukinari Sunatsuki, Nicolas Brefuel, Jean-Pierre Tuchagues, Laure Vendier, and Wolfgang Wernsdorfer, "Face-Sharing Heterotrinuclear $M^{II}$ $Ln^{III}$ $M^{II}$ (M = Mn, Fe, Co, Zn and Ln = La, Gd, Tb, Dy) Complexes; Synthesis, Structures and Magnetic Properties," Inorganic Chemistry **49**, 9125 (2010).

[135] Huan Yang, Benoît Fauqué, Liam Malone, Arlei Antunes, Zengwei Zhu, Ctirad Uher, and Kamran Behnia, "Phase diagram of bismuth in the extreme quantum limit," Nat. Comm. **1**, 1–5 (2010).

[136] Xianping Zhang, Dongliang Wang, Zhaoshun Gao, Lei Wang, Yanpeng Qi, Zhiyu Zhang, Yanwei Ma, Satoshi Awaji, Gen Nishijima, Kazuo Watanabe, Eric Mossang, and Xavier Chaud, "Doping with a special carbohydrate, $C_9H_{11}NO$, to improve the $(J_c - B)$ properties of $MgB_2$ tapes," Superconductor Science & Technology **23**, 025024 (2010).

[137] Xiaoqing Zhou, B. A. Piot, M. Bonin, L. W. Engel, S. Das Sarma, G. Gervais, L. N. Pfeiffer, and K. W. West, "Colossal Magnetoresistance in an Ultraclean Weakly Interacting 2D Fermi Liquid," Physical Review Letters **104**, 216801 (2010).

## Collaborating External Laboratories

**Belarus**
Belarus State University, Dept Phys. SC & Nanoelectronics, BY-Minsk : 40
Belarus State Univ. Research Institute of Physicochemical Problems, BY-Minsk: 40
Scientific-Practical Material Research Centre of the Belarus National Academy of Science, Minsk: 42

**Belgium**
INPAC, Leuven : 75

**Brazil**
Instituto de Física de São Carlos da Universidade de São Paulo, São Carlos: 21, 27
Instituto de Física da Universidade de São Paulo : 21, 29, 30
Universidade de São Paulo : 72

**Canada**
Institute of Microstructural Sciences, NRC, Ottawa : 24, 24, 46
University of British Columbia, Vancouver : 62, 65, 66
University of Sherbrooke : 62, 65

**China**
Dep.of Mat.Eng., Shanghai University : 98
Shanghai University, Shanghai : 97

**Columbia**
Departamento de Química, Universidad del Valle, Cali : 36

**Croatia**
University of Zagreb : 72

**Czech Republic**
Charles University, Prague 39
Institute of Physics ASCR,v.v.i.,Prague: 38, 39

**Estonia**
NICPB, Tallinn : 74

**France**
CEA-DEN-LTMEX, Saclay : 116
CEA/IRFU/SACM-Saclay, Gif-sur-Yvette : 87, 88, 89, 125
CEA-SPSMS, Grenoble : 50, 53, 54, 55, 56, 58, 59, 107
Centre de Spectrométrie Nucléaire et de Spectrométrie de Masse (CSNSM), Orsay : 13
CMTR, ICMPE, CNRS and Univiversity Paris XII, Thiais : 79
CRISMAT, CNRS, Caen : 41
ESPCI, Paris : 54
ESRF, Grenoble : 75, 95, 106, 116
Groupe d'Etude des Semi-conducteurs, Université de Montpellier II, Montpellier : 24, 35
INAC/SPSMS-CEA, Grenoble : 73
INP-Grenoble, Grenoble : 3
Institut d'Electronique du Sud, Université de Montpellier II, Montpellier : 35
Institut Néel, CNRS Grenoble : 107, 58, 75, 90
Institut Néel / G2Elab, Grenoble : 87, 88, 89, 90
IPCM, UPMC, Paris : 84
Laboratoire de Physique de L'Etat Condensé, CNRS, Université du Maine, Le Mans : 78
LCC, Toulouse : 49
LEGI, CNRS INPG/UJF, Grenoble : 119

**Switzerland**
EPFL, Lausanne : 73
Paul Scherrer Institut, Villigen : 60, 116

**Ukraine**
Institute of Semiconductor Physics, NAS of Ukraine, Kiev : 29, 30

**United Kingdom**
Clarendon Laboratory, University of Oxford : 4
Department of Electrical Engineering, University of Sheffield, Sheffield : 112
Department of Physics, SUPA, Strathclyde University, Glasgow, UK : 42
School of Physics and Astronomy, University of Nottingham, Nottingham : 36, 112
University of Bristol, Bristol : 32, 63
University of Cambridge, Cambridge : 32, 62

**USA**
Brown University, Providence : 73
Dept. of Electrical and Computer Engineering, Northeastern University, Boston : 78
Georgia Tech., Atlanta : 8, 9, 12
University of California at Berkeley, Berkeley : 12

# Author Index
## (Contributors of LNCMI to this annual report)

CONTINUOUS MAGNETIC FIELDS
LNCMI-G, CNRS
25 rue des Martyrs, B.P. 166
38042 GRENOBLE cedex 9 - France
Tel. : +33 (0)4 76 88 10 48
Fax : +33 (0)4 76 88 10 01

PULSED MAGNETIC FIELDS
LNCMI-T, CNRS
143 avenue de Rangueil
31400 TOULOUSE - France
Tel. : +33 (0)5 62 17 28 60
Fax : +33 (0)5 62 17 28 16

lncmi.direction@lncmi.cnrs.fr
http://www.lncmi.cnrs.fr





Création : Anne-Claire LECOMTE, www.studiographisme.fr - Impression : COQUAND - LA TYPO
Photos : CNRS Photothèque ; LNCMI ; CNRS Photothèque / Martin HYTCH ; CNRS Photothèque / Denis MOREL ; LNCMI / Baptiste VIGNOLLE ; CNRS Photothèque / Stéphane BECHU.